About the thermomechanical behavior of thermoplastic composites under critical temperature conditions: a multiscale numerical analysis and experimental characterization

David Philippe

▶ **To cite this version:**

David Philippe. About the thermomechanical behavior of thermoplastic composites under critical temperature conditions: a multiscale numerical analysis and experimental characterization. Engineering Sciences [physics]. Normandie Université, 2023. English. ⟨NNT : ⟩. ⟨tel-04523937⟩

HAL Id: tel-04523937

https://hal.science/tel-04523937v1

Submitted on 27 Mar 2024

HAL is a multi-disciplinary open access archive for the deposit and dissemination of scientific research documents, whether they are published or not. The documents may come from teaching and research institutions in France or abroad, or from public or private research centers.

L'archive ouverte pluridisciplinaire **HAL**, est destinée au dépôt et à la diffusion de documents scientifiques de niveau recherche, publiés ou non, émanant des établissements d'enseignement et de recherche français ou étrangers, des laboratoires publics ou privés.

HAL Authorization

Normandie Université

THESE

Pour obtenir le diplôme de doctorat

Spécialité Mécanique

Préparée au sein de l'INSA Rouen Normandie

About the thermomechanical behavior of thermoplastic composites under critical temperature conditions: a multiscale numerical analysis and experimental characterization

Manuscrit provisoire de

David PHILIPPE

Soutenance prévue le 21 Novembre 2023 devant le jury composé de		
M. Redouane ZITOUNE	Professeur des Universités - University Paul Sabatier Toulouse	Rapporteur
M. Damien HALM	Professeur des Universités - ISAE-ENSMA Poitiers	Rapporteur
M. Cédric HUCHETTE	Ingénieur de recherche - ONERA	Examinateur
M. Lucien LAIARINAN-DRASANA	Directeur de recherche - Mines ParisTech PSL	Examinateur
M. Yann CARPIER	Ingénieur de recherche - SEGULA Technologies	Examinateur
M. Benoit VIEILLE	Professeur des Universités - INSA Rouen Normandie	Directeur de thèse
M. Fabrice BARBE	Professeur des Universités - INSA Rouen Normandie	Co-directeur de thèse

Thèse dirigée par Benoit VIEILLE et Fabrice BARBE, au Groupe de Physique des Matériaux, CNRS UMR 6634

INSA INSTITUT NATIONAL DES SCIENCES APPLIQUÉES ROUEN NORMANDIE

ED 591 PSIME

GPM Groupe de Physique des Matériaux

TABLE OF CONTENTS

NOTATIONS

Acronyms

DIC	Digital Image Correlation
DMA	Dynamic Mechanical Analysis
DSC	Differential scanning calorimetry
FE	Finite Element
PEEK	Polyetheretherketone
PPS	Polyphenylene Sulfide
QI	Quasi-isotropic
RVE	Representative Volume Element
TGA	Thermogravimetric Analysis
TP	Thermoplastic
TS	Thermoset
RT	Room Temperature
UD	Unidirectional

Symbols

α	Pyrolysis degree
α_{ab}	Absorptivity
α_{th}	Thermal expansion coefficient
c_p	Specific heat capacity
$\underline{\underline{C}}$	Stiffness tensor
χ	Cristallinity rate
d	Numerical density
Δt	Numerical time increment
E	Young's modulus

E'	Storage modulus
E_{ac}	Activation energy
ε	Mechanical strain
ϵ_{emi}	Emissivity
f_a	Adaptation function
F	Mechanical force
F^u	Force to failure
G	Shear modulus
G_N	Nucleation rate
h	Thermal convection coefficient
h_d	Dissociation latent heat
h_e	Evaporation latent heat
h_m	Melting latent heat
η	Volume fraction or viscosity parameter
L_g	Gasification latent heat
λ	Thermal conductivity isotropic)
$\underline{\lambda_y}$	Thermal conductivity tensor (anisotropic)
$\overline{\overline{m}}$	Mass
μ	Poisson's ratio
N	Number of finite elements
ω	Numerical weight
p	Porosity formation probability
P_{int}	Internal pressure
p_{growth}	Growth probability
Q	Thermal energy
R	Molar gas constant
ρ	Volumetric density
RE	Relative error
σ	Mechanical stress
σ^u	Stress to failure
t	Time
T	Temperature
T_0	Room temperature
T_d	Thermal decomposition onset
T_g	Glass transition temperature
T_m	Melting temperature
τ_{tr}	Transmittance
W	Heat flux

Subscripts

a	Air

cl	Composite laminates
f	Fiber
fb	Fiber bundle
g	glass(y)
m	Matrix
p	Porosity
rub	Rubbery
w	Water

Superscripts

a	Air
ax	Axial
d	Decomposed
e	Elasticity
imp	Imposed
ini (or 0)	Initial
L	Longitudinal
p	Plasticity
r	Radial
ref	Reference
T	Transverse
ve	Viscoelasticity
vp	Viscoplasticity
w	Water

INTRODUCTION

Contents

Context of study

Nowadays, one of the most recurrent issue in the industry is the mass reduction of the different structures. It is especially the case in the transportation industry (among which is the aerospatial) since a lighter aircraft can drastically reduce the fuel consumption. To that effect, polymer matrix-based is a more and more serious candidate to replace metallic alloys in structural parts of an airplane. Its low weight and excellent specific mechanical properties (properties divided by the density of the material) justify the exponential trend which has been observed in its use over the past 50 years, see Fig. 1. The mass percentage has indeed increased slowly until the mid-80', before a drastic increase and exceeding 50% in the last aircraft generation (Boeing 787 and A350). The main composite family used are Carbon Fiber Reinforced Polymers (CFRP). The distribution of the various materials in the Boeing 787 can be observed on Fig. 2. CFRPs constitute the bulk of the plane, while the metallic alloys are still sparsely used for strategic parts which require a higher thermomechanical capacity than those obtained with CFRPs.

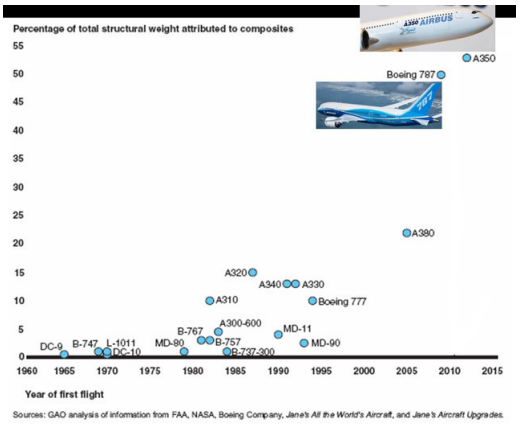

Figure 1. – Evolution of the mass percentage of composite material in civil aircrafts from 1965 to 2015 (Loukil, 2013)

However, as the massive use of composite materials in structural design remains rather recent, their behavior is still not as well understood as the one of metallic alloys. It is especially the case in extreme conditions in which the matrix component will often act as the weak link of a CFRP, e.g. for high temperature exposure the polymer matrix is far more sensitive to degradation than carbon fibers or metals.

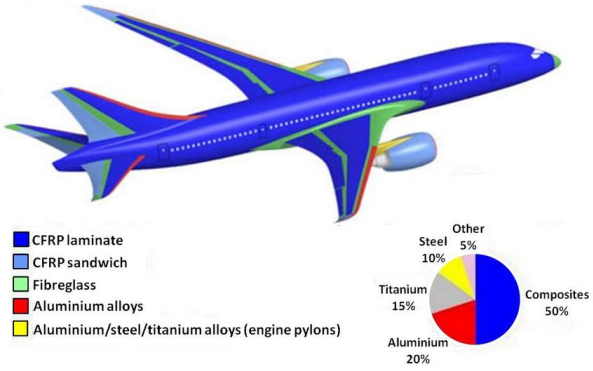

Figure 2. – Distribution of the different material categories in the Boeing 787 structure in terms of mass percentage. Data of 2009 (Naghipour, 2011)

Generalities on composite materials

A material is referred to as composite when it results from the assembly of various constituents (see Fig. 3). These constituents can be categorized into two categories, the first one being continuous and unique while the other is discontinuous and can be multiple (Jean-Marie, 2012). They are respectively called matrix and reinforcements. The mixture usually provides advantageous properties compared to the constituents the constituents, which would be impossible by considering only a raw material. Indeed, the matrix is used to create the required shape while the reinforcements insure the mechanical properties (stiffness and strength). Fig. 4 highlights the mechanical differences in the matrix and fibers. Thus, composite materials have a strongly heterogeneous and anisotropic mechanical behavior.

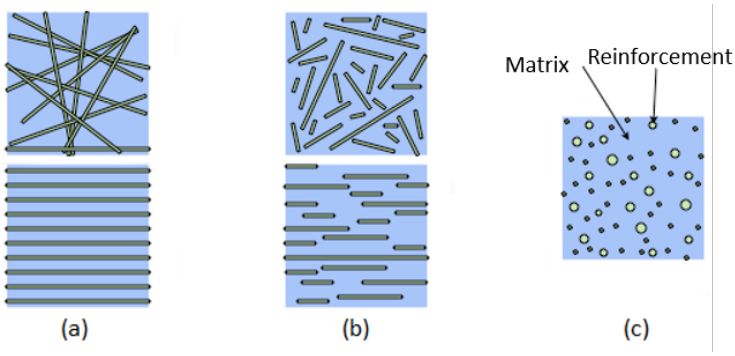

Figure 3. – Composite material structure: (a) long fibers, (b) short fibers, (c) particular (Gendre, 2011)

Although many matrix and reinforcement families exist, the focus will be set in this study on polymer matrix combined with fiber bundle reinforcements to obtain laminated composites.

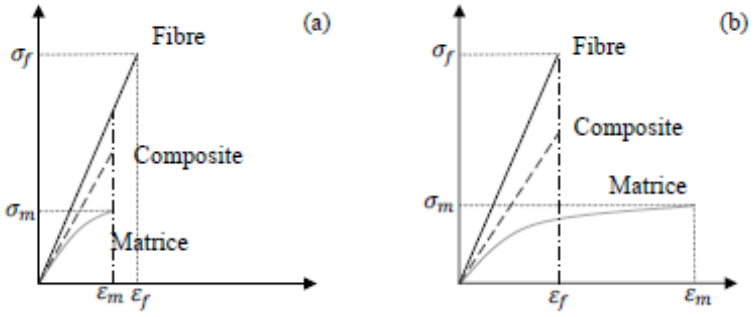

Figure 4. – Stress / strain schematic curves representing the axial tensile loading of a fiber-matrix composite : (a) $\epsilon_f > \epsilon_m$; (b) $\epsilon_f < \epsilon_m$ (Aucher, 2011)

Polymer matrix

Comparison thermoset - thermoplastic

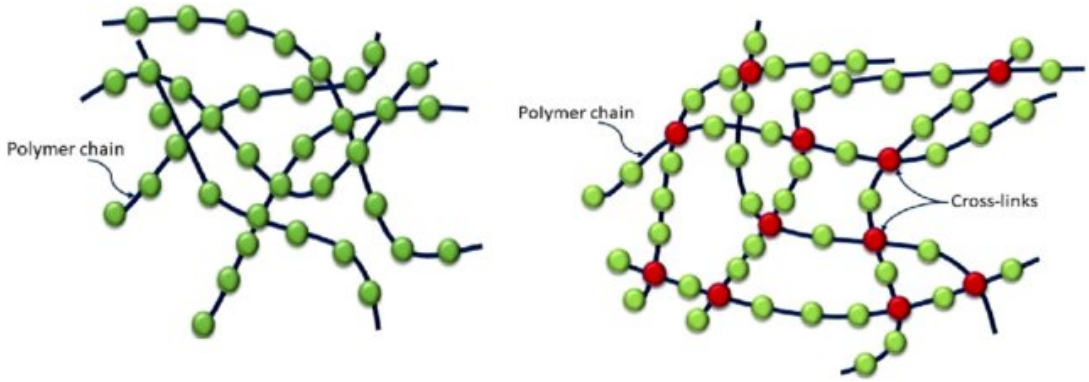

Figure 5. – Various polymer macromolecular chains (Kazemi et al., 2021)

Polymers can be divided into two categories:

— When the macromolecular chains form a three-dimensional structure, the polymer is qualified as thermoset (TS), as shown in Fig. 5. They have been extensively used fore more than forty years in the aerospace industry because of their good performance, low price and processability;

— When the macromolecular chains possess only two extremities (often with smaller lateral branches), the polymer is qualified as thermoplastic (TP). They have been increasingly considered for applications in aeronautics over the last decades due to the good resistance to high temperatures, the thermoforming possibility, the recycling nature and overall improvements on the processing of the TP (short cycles in particular).

The advantages of TP over TS polymers for composite matrix consideration are summarized on Table 5(Berreur et al., 2002).

		TS (*e.g.*, epoxy)	TP (*e.g.*, PPS)
Processing	Shelf life	Limited	Unlimited
	Storage	Refrigeration	No refrigeration
	Processing T°C	Low	High
	Processing viscosity	Low	High
	Processing Time	Long	Short
	Assembly	Adhesive/Bolted	Welded/Adhesive/Bolted
	Processing cost	Relatively low	Overall processing cost generally higher
	Recycling	Under certain conditions	Possible
Performance	Glass transition temperature	Higher	Lower
	Moisture resistance	Lower	Excellent
	Fire resistance	Lower	Hardly flammable
	Impact resistance	Limited	Relatively good
	Fracture toughness	Limited	Better

TABLE 5. – Pros and cons of TS and high performance TP composites in terms of processing and performance (Bouscarrat, 2019)

Crystalline phase

Contrary to TS polymers, crystalline phase areas can be observed in some parts of a TP macromolecular structure (usually from 10% to 50%, it can never be fully crystalline (Haudin, 2008)), see Fig. 6. It happens at a temperature of "crystallization" when the chains get closer to one another. The spatially fixed areas represent a phase called amorphous. A TP polymer is then called semi crystalline when both of these phases are included. TP polymers include (without being exhaustive) PPS, PEEK, PEK or PPA.

Contrary to amorphous polymers, the crystalline phase is not affected by the glass transition (see Section 1.2.1). Hence, semi-crystalline polymers have a better tolerance to high temperatures.

Fiber bundles and stacking sequence

A fiber bundle (or yarn) is an entity composed of a majority of fibers distributed within a small amount of matrix used to ensure the cohesion of the thin fibers. These bundles are spatially embedded within the matrix according to various sequences called weave patterns (see Fig. 6). Each weave pattern has specific mechanical behavior. All the fiber bundles architectured according to a pattern compose a ply. The plies can be stacked to form a laminates (see Fig. 7). More details on the possible arrangements are provided in Section 1.2.3

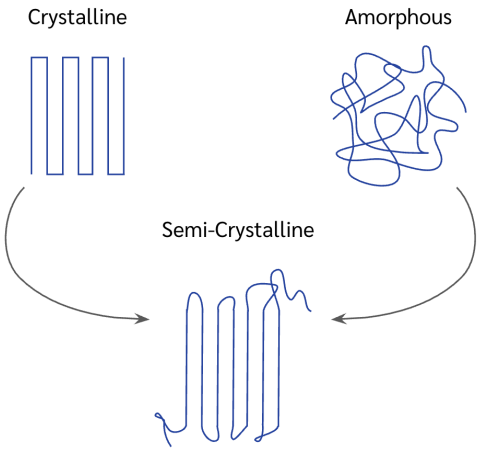

TABLE 6. – Schematics of the amorphous, semi-crystalline and crystalline composites

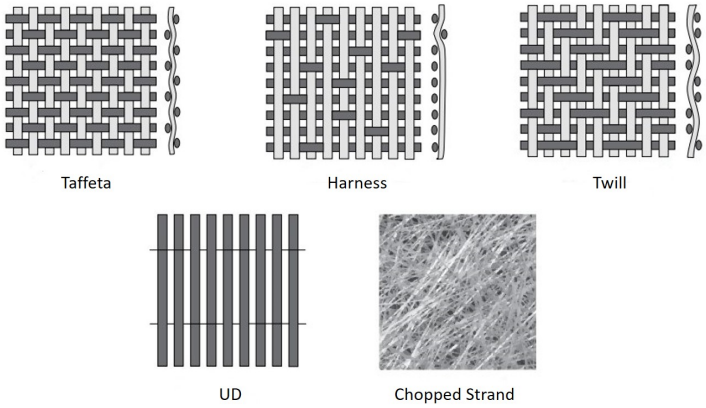

Figure 6. – Examples of fiber bundle possible weave patterns (Samaro, 2022)

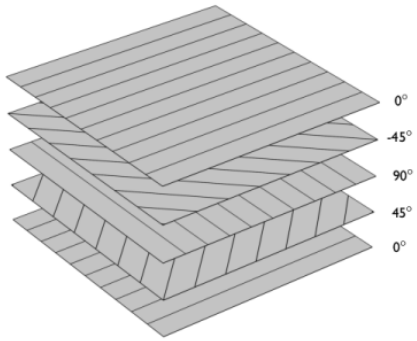

Figure 7. – Examples of a stacking sequence (Stacking sequence, 2023)

Context of the study

Under critical service conditions, aeronautical structural parts consisting of polymer matrix composite materials may be exposed to intense sources of thermal energy leading to high thermal gradients. Although these fire scenarios are quite rare, they immediately imply drastic human consequences should the aircraft not be able to perform landfall and evacuate the passengers before the failure of its structural integrity. One of the latest occurrences of such an accident goes back to May 2019 in Moscow when the crash of an airplane caused the death of 41 passengers and crew members, see Fig. 8.

Figure 8. – Aircraft crash causing the death of 41 people in May 2019

It is then necessary to understand the response of CFRP to thermal exposure as they represent a large majority of the volume of the structure. This thermal exposure consists of an anisothermal transient thermal problem combining solid state transitions, solid-liquid transitions and decomposition of the polymer matrix with rapid kinetics. The encountered temperature ranges from the ambient to the temperature of the thermal decomposition onset of the polymer ($\approx 450°C$ (Ma et al., 1988) for Polyphenylene Sulfide) and above. The capacity of the composite to sustain a thermomechanical load then depends on the degradation of the composite constituent properties, first and foremost those of the polymer matrix especially when it comes to high temperature conditions. The analyses of the interactions between mechanics and thermal transfers taking place under such conditions rely on very specific experimental means. Indeed, it is necessary to reproduce these critical operating conditions of composite materials intended for applications in aircraft engine. To this end, an approach based on both experimental and numerical analyses enables both a better understanding of the involved physics, and the development of a model to predict the progressive degradation of the state of the material.

A large variety of work have studied this response, as presented in 1, but without explicitly accounting for the influence of the thermal decomposition on the thermomechanical properties of the laminates. This work builds on the study performed by Carpier (Carpier et al., 2021) within the AEROFLAMME project which aims at understanding the response of laminated composite materials when exposed to a critical fire scenario.

Figure 9. – 5-harness satin weave pattern. Each color represents a fiber bundle

Material

The polymer matrix of the CFRP considered in this study is the Polyphenylene Sulfide (PPS) which is a thermoplastic semi-crystalline polymer. Its use is justified by its common use for aeronautical parts as well as its good thermal stability.
The CFRP composite studied (C/PPS) is laminated and assembled through 7 layers following a 5-harness satin weave pattern (see Fig. 9) according to two different stacking sequences: quasi-isotropic and $\pm 45°$ oriented (see Section 1.2.3 for the details). It is to be noted that the $\pm 45°$ oriented laminates were only experimentally investigated. The volume fraction of fiber and matrix is the same 50%.

The PPS used in this study was created by the company Hexcel and named the Fortron 0204 while the carbon fibers (T300 3K) were supplied by Toray. The C/PPS laminate was assembled by Soficar.

Objectives of the study

Carpier mainly focused on the impact of thermal exposure for temperatures up to the melting point, results which should be consolidated and extended up to temperatures above the onset of the thermal decomposition and taking into account the associated phenomena. To do so, a multi-scale modelling developed based on experimental analysis is used to assess the consequences of the thermal degradation and decomposition at the microscopic level on property and structural alterations at the mesoscopic level, the ply level and the macroscopic one. The influence of high temperatures on the thermomechanical behavior of the laminates could then be determined and compared with the numerical results.

Manuscript outline

As it is explained in the bibliographic review of Chapter 1, the exposure to a high temperature, no matter the thermal agression (homogeneous furnace, heat flux, flame), leads to a degradation of the thermomechanical properties of the composites and a progressive decomposition of its matrix through pyrolysis. For high enough temperatures (see Section 1.2.2), the carbon fibers behavior is affected, although it will only be briefly tackled as it will be the focus of further works.
The estimation of the effect of temperature on the thermal properties (conduction, thermal expansion, specific heat) and the mechanical ones (stiffness, viscous behavior) on the constituents of the C/PPS laminates will be presented in Chapter 2 through experimental measurements. The selected modelling constitutive laws will also be depicted. In order to extend the temperature limit of the model previously developed by Carpier (from 450°C up to 600°C and above), Chapter 3 will present the thermal decomposition modelling of QI laminates based on an experimental qualitative and quantitative overview of the processes. Experiments were used as a database for the development of a Finite Element model. This model replicates the various phenomena and introduces porosities within the matrix based on a probabilistic approach following the pyrolysis reaction . Finally the multi-scale impact of both the thermal degradation and the thermal decomposition on the residual thermomechanical properties of the QI laminates will be analysed in Chapter 4. The influence of flame exposure as well as the corresponding modelling will be tackled, along with a preliminary study on the thermomechanical response of the ±45° laminates.

CHAPTER 1

LITERATURE REVIEW: THERMOMECHANICAL BEHAVIOR OF COMPOSITE LAMINATES UNDER FIRE EXPOSURE

Contents

When considering the thermomechanical coupling of a composite material at high temperatures, the influence of various thermal-dependant mechanisms might need to be looked into. They can mainly be divided into three parts according to the material state at which they occur i.e. not degraded, degraded and finally degraded and decomposed (Table 1.1). Another distinction to make is the nature of the temperature loading leading to their appearance, whether it is a homogeneous or heterogeneous one.
On the one hand, a homogeneous loading induces a similar temperature throughout the material. Although it is an assumption rarely fulfilled in industrial applications, it allows several mechanisms to be highlighted such as, in order of appearance as the temperature increases, thermal expansion, thermomechanical property degradation, damage, viscous behavior, and lastly the pyrolysis mechanism and the induced porosity formation.
On the other hand, a heterogeneous temperature can be brought by the exposition of one (or multiple) surface(s) of the material to a heat flux such as a fire. The temperature is therefore higher along the contact surfaces than it is within the material, hence the appearance of new phenomena namely thermal transfers, thermomechanical property gradients and, when a fire is considered, oxidization. Moreover, this loading case tends to increase the aforementioned mechanisms, as fire exposure induces new chemical reactions (such as the heat release rate evolution depicted by (Mouritz and Gibson, 2006), or the piloted ignition due to pyrolysis gas acting as fuel and flame transfer presented by (Hull and Baljinder, 2009)).
It is brought to the attention of the reader that the studies about C/PPS behavior are not numerous and the literature review will occasionally focus on other materials with similar thermomechanical trends.

In order to investigate the thermomechanical behavior of a laminates, two aspects usually need to be dealt with, which are running experimental tests and numerically modelling its behavior. Both of these fields are strongly connected since experimental results are necessary to determine the appropriate numerical models. Furthermore, simulations allow the user to study various phenomena within the material, which is difficult to achieve from tests. A thermomechanical study therefore preferably presents a duality with a constant interaction between experimental and numerical data. These two fields are therefore presented throughout this bibliographic overview, beginning with the experimental means required to achieve the thermomechanical characterization.

Material state	Not degraded	Degraded	Degraded / decomposed
Associated phenomena	Damage Viscous behavior Thermal transfers Thermal expansion	Thermal property degradation Mechanical property degradation Damage Viscous behavior	Porosity formation Pyrolysis Oxidization
Modelling	Mesostructure model Thermal model Constitutive relations	Property degradation relations	Pyrolysis model Porosity growth

TABLE 1.1. – Review of thermomechanical phenomena - Homogeneous temperature phenomena - Heterogeneous temperature phenomena

1.1. Experimental means

A great amount of experimental means are required in order to thermomechanically characterize a material. They vary according to the level of representativity of the critical service conditions when the composite is subjected to both a flame and a mechanical loading (Fig. 1.1). Five levels can be distinguished depending on the specimen scale:

— The first level represents experimental means in which only a thermal loading is applied. These therefore provide information about thermal properties, such as thermal expansion, thermal conductivity, specific heat capacity or pyrolysis kinetics.
— The second level initiates the thermomechanical loading. It allows thermomechanical properties of the material (such as stiffness, viscous behavior, damage) under homogeneous temperature to be determined.
— The third level completes the previous one by including a heterogeneous temperature.
— The fourth level reproduces as precisely as possible the critical conditions by introducing a flame.
— Finally, the last level represents at full scale the critical service conditions which are usually not reproduced in a laboratory.

The first four levels will be further detailed in the coming parts. It is to be noted that the properties introduced are further described in Sections 1.2.3 and 1.3.1.

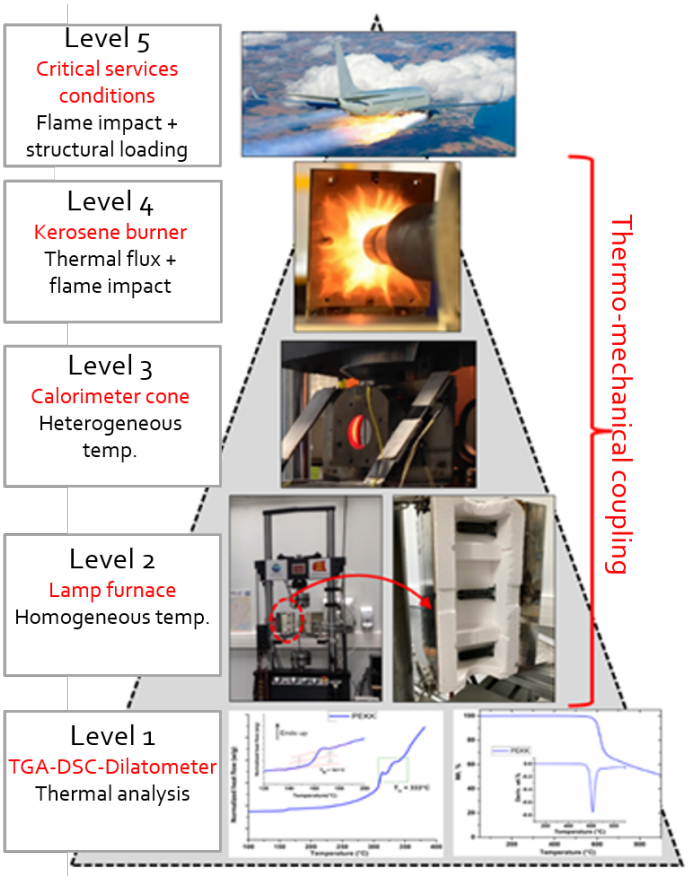

Figure 1.1. – Presentation of the five representativeness levels for thermomechanical coupling experimental study

1.1.1. Thermal property determination

Thermal conductivity

Let us begin with the most difficult property to identify at high temperatures in TP (see Section 1.3.1) as well as the one the greatest amount of experimental means to identify it. Thermal conductivity can be measured through a number of ways, divided into three classes: steady-state, time-domain and frequency-domain as is reviewed by (Wang et al., 2019).

Steady-state In steady-states methods, the thermal conductivity measurement is conducted at a temperature stable over time. This provides results easier analyzed, with the downside of requiring a well-engineered experimental set-up, which can quickly cause errors if it is well enough built. Among the most common methods are the absolute technique and the parallel conductance method (Zhao et al., 2016).

Time-domain Time-domain methods are transient techniques and perform a measurement as the material is heating up. Its main advantage is to produce results quite quickly since the temperature does not have to stabilize, at the cost of a data analysis more difficult. Among these methods one can find the laser flash method, the transient plane source or the transient line source, although the most common method is the transient hot wire (Assael et al., 2015).

Frequency-domain Frequency-domain methods are mainly based on the 3ω-method (Rowe, 2006). Its principle is to fluctuate the heating based on a frequency. However, complex to apprehend.

Thermal expansion

The thermal expansion coefficient is often evaluated through dilatometry tests, using a dilatometer (Fig. 1.2) (Nawab et al., 2013). Its principle is to place the sample on a furnace and gradually increase the temperature whilst imposing a slight compression through the pushrod just high enough to let the material progressively expand. The thermal expansion coefficient is that way measured by lasers in the most modern ones.

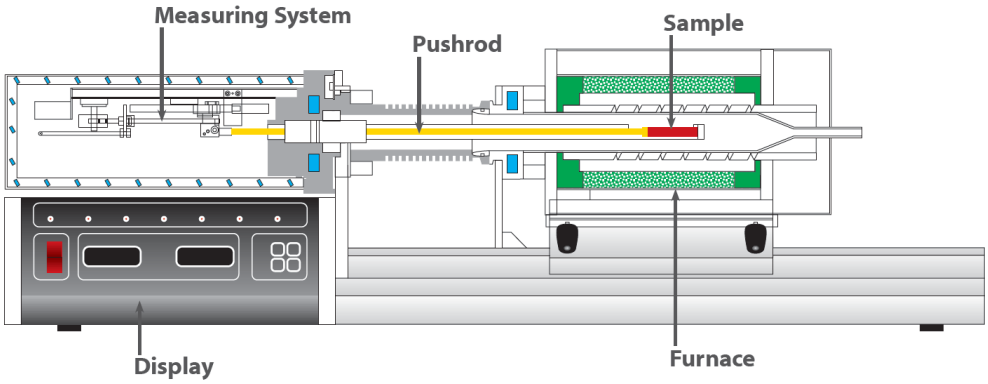

Figure 1.2. – General principle of a dilatometer (Linseis, 2021)

Specific heat capacity

The specific heat capacity is commonly determined by Differential Scanning Calorimetry (DSC) tests. Two DSC types can be found (Höhne et al., 1983):

— The heat-flux DSC consists of placing the sample and a reference in the same furnace and submit them to the same heat flux (dQ/dt), examining the heat-up rate (dT/dt) of the materials.

— The power differential DSC consists of the reverse, meaning that the sample and the reference are placed on separate furnaces and a same heat-up rate is requested while examining the response in terms of heat flux provided.

The specific heat c_p is ultimately calculated by:

$$c_p = \frac{1}{m}\frac{dQ/dt}{dT/dt} \tag{1.1}$$

It appears that the c_p calculation directly depends on the mass of the sample. Or it was previously shown that this mass strongly decrease during the decomposition process. It therefore seems necessary to also measure the mass loss whilst the DSC tests are carried. (Cheng et al., 2020) achieved this by combining DSC tests with Thermogravimetric analysis (TGA). TGA consists in placing a small sample (usually a few milligrams) in a heating device and monitoring the mass loss throughout the decomposition process.

When studying the thermomechanical behavior, one of the main aspects is to choose an appropriate heat source according to the purpose of the study. It is unnecessary to use a flame or a heterogeneous temperature which would complicate the process of property identification and behavior understanding if a homogeneous temperature is enough to identify these properties.

1.1.2. Exposure to isothermal conditions

In order to impose a homogeneous temperature, a high temperature lamp furnace can be used in which the temperature is progressively increased within the confines of the furnace, the heating coming from electrical resistances. Once the desired temperature is reached, it is held for a certain amount of time before applying the mechanical loading to make sure that the temperature is completely homogeneous within the material.

1.1.3. Exposure to a heat flux

However, it is necessary to consider heterogeneous temperature conditions to properly reproduce the thermal gradient representative of a fire exposure. In order to study the influence of an anisothermal heat source, the choice of the nature of the heat flux is essential. Depending on the required scale and phenomena to highlight, three main possibilities appear: a cone calorimeter, a laser ray and a flame.

Cone calorimeter

Among the anisothermal heat sources, the most used is the cone calorimeter, as described Fig. 1.3, and its use can be found on studies by (Mouritz and Mathys, 2000; Gibson et al., 2004; Luche et al., 2011; Legrand et al., 2020; Vincent et al., 2019; Halm et al., 2017). This experimental set-up applies a heat flux on one of the sides of the samples, and the thermomechanical coupling can be performed. It is as well possible to visually follow the response to the thermomechanical loading through a camera.

This experimental set-up is ideal for testing large samples, and to remove the complexification induced by fire exposure. However, the imposed heat flux is usually limited to values lower than 75kW/m^2. This limitation is a drawback when compared to the FAA regulations requiring a 115kW/m^2 heat flux.

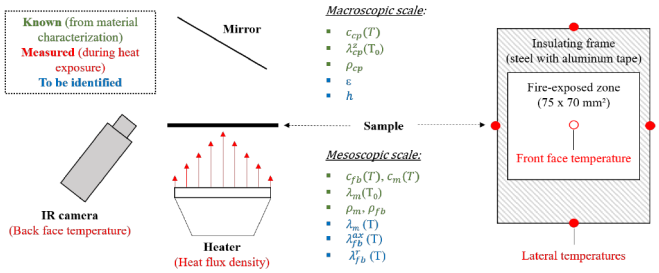

Figure 1.3. – Cone calorimeter diagram (Carpier et al., 2022)

Laser ray

In order to increase the heat flux level, several studies use a laser ray such as (Westover, 2012; Swanson and Wolfrum, 2018; Sihn et al., 2023) or the ONERA laboratory through the BLADE bench (see Fig. 1.4) (Leplat et al., 2016). This method allow heat fluxes over 200kW/m^2 to be reached. However, the degradation area is very limited , which is not fully representative of critical service conditions in fire.

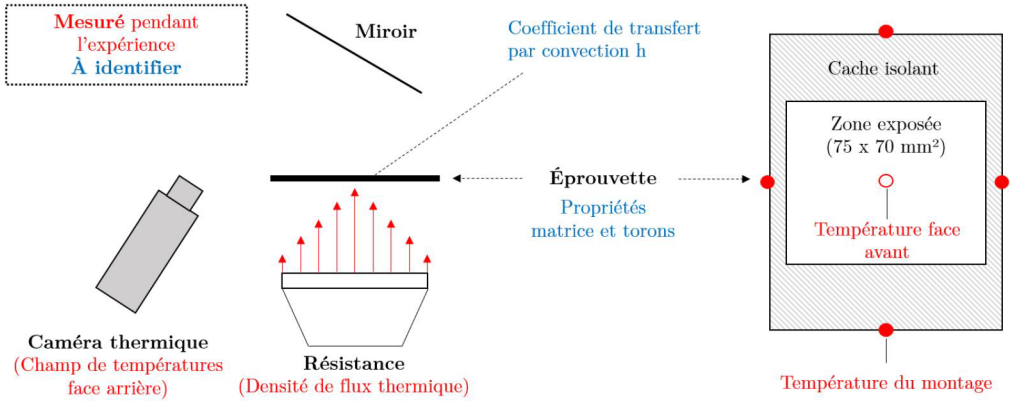

Figure 1.4. – BLADE laser bench of the ONERA (Leplat et al., 2016)

Miniaturized burner

Lastly, a miniaturized burner can be used to replicate as precisely as possible a fire exposure as performed by (Braiek et al., 2020) who used two rows of five burners. The heat flux level required by the FAA can be reached, and larger samples can be used than with the laser ray. As a drawback, some technical difficulties appear such as the measurement of the heat flux or insuring the homogeneity of the flame.
When a composite laminates is subjected to a fire, a series of phenomena occur from the thermal decomposition along with others specific to an impinging flame. This process is represented on Fig. 1.5.

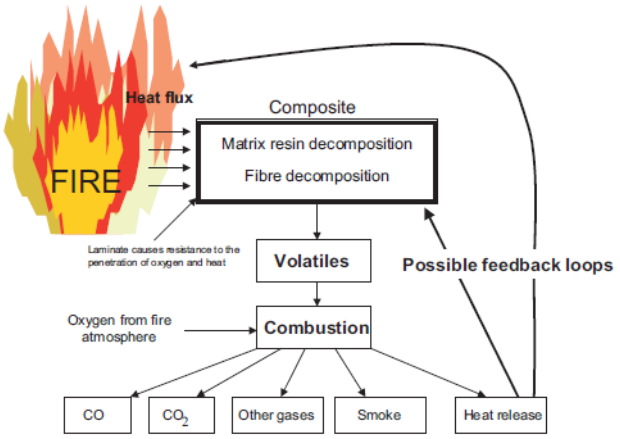

Figure 1.5. – Reaction to a fire exposure of a polymer composite (Mouritz and Gibson, 2006)

These specific reactions, although following similar tendencies, can be altered by the nature of the flame. Two main families can be determined:

— Hydrocarbons, such as kerosene or propane, which are traditionally used as fuel source
— Hydrogen, which has seen a massive increase of its prospects in the past years in many fields. However, possible leaks in high-pressure hydrogen containment unit may lead to fire exposure.

Hydrocarbon flame The influence of the mainly used hydrocarbons (kerosene and propane) were studied by (Chazelle et al., 2019). Several differences were noted:

— A curvature of the exposed surface without char formation for the propane flame, with the reverse for the kerosene;
— A higher temperature of the back surface and mass loss for the propane (see Fig. 1.6)

Hydrogen flame Although it has not been studied as extensively as the hydrocarbon ones so far, a few studies were carried out on the properties of hydrogen flames, which will be briefly presented as an introduction for future considerations. (Choudhuri and Gollahalli, 2003) found that it was easier to work with mixed hydrogen-hydrocarbon fuel as hydrogen is difficult to store and has a tendency to self-ignite. It was shown that the percentage of hydrogen in the mixture highly modifies the properties of the flame, such as the flame length, the convective time scale and the char volume, which all decreases as the hydrogen volume increases (Fig. 1.7).

(Schefer et al., 2006) focused on the radiant fraction, defined as the fraction of the total chemical heat release that is radiated to the surroundings. Their results showed that the flame residence time (depicting the time that a fuel particle spends in the flame, and hence the severity of the flame) is higher within the hydrogen flames for similar radiant fraction (Fig. 1.8). A material exposed to a hydrogen flame is therefore more severely impacted.

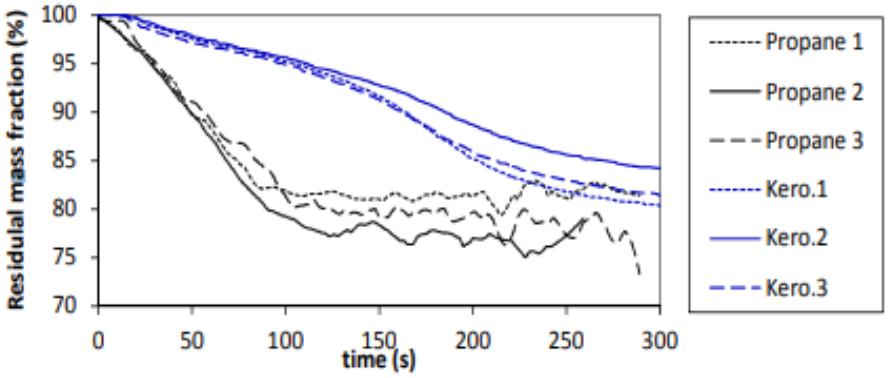

(a)

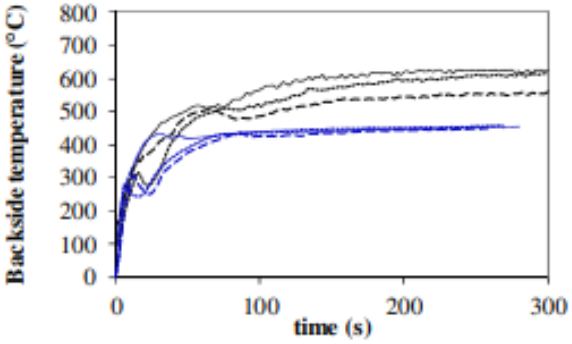

(b)

Figure 1.6. – Comparison of the influence of kerosene and propane flames on the evolution of the thermal state of C/epoxy laminates. (a) Back side temperature, (b) residual mass (Chazelle et al., 2019)

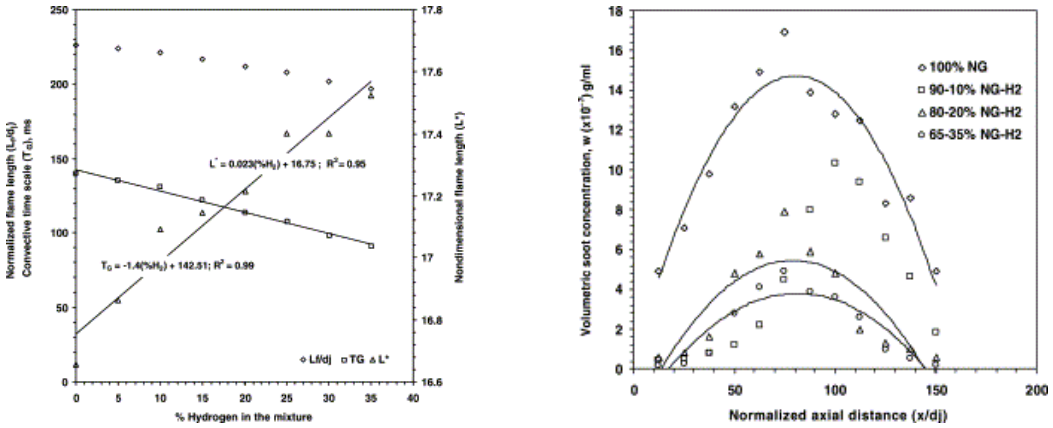

(a) (b)

Figure 1.7. – Evolution of the mixed hydrogen-hydrocarbon flame characteristics according to the amount of hydrogen. (a) Flame length and convective time scale, (b) char content (Choudhuri and Gollahalli, 2003)

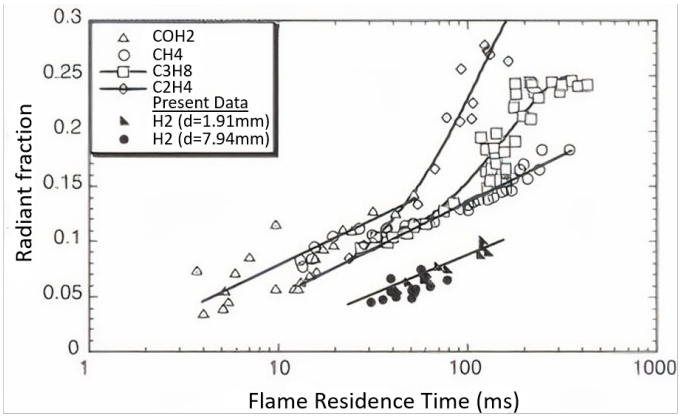

Figure 1.8. – Evolution of the radiant fraction over flame residence time for various hydrocarbon and hydrogen jet flames (Schefer et al., 2006)

1.2. Thermomechanical behavior - homogeneous temperature

Despite the fact that a homogeneous temperature is unlikely to be encountered in service, its simplicity makes it a perfect way to highlight the phenomena detectable through this mean without the interferences that fire exposure can cause. This therefore allows to tackle the response to a thermomechanical loading in a first time.

The thermomechanical behaviors of matrix and fibres are highly different at room temperature, and the differences even enhance as the temperature increases. While the thermomechanical properties of carbon fibers do not vary much within the temperature range considered (up to the thermal decomposition temperature and above), TP ones greatly depend on it.

1.2.1. Matrix behavior

Characteristic temperatures of the matrix

When a semi-crystalline TP polymer is considered, various characteristic temperatures of transition appear which have a major impact on the internal structure of the material which is translated to its properties, see Fig. 1.9. The three primary transitions are the glass transition (at the temperature T_g) which influences the amorphous phase, the melting (at T_m) altering the crystalline phase, and finally the thermal decomposition (at T_d). They can be experimentally determined by different methods, such as Differential Scanning Calorimetry (DSC), Dynamic Mechanical Analysis (DMA) or dilatometry. The values of these temperatures are listed in Table 1.2 for PPS and PEEK.

Resin	T_g	T_m	T_d	degree of crystallinity (%)
PPS	90°C	280°C	450°C	10 - 60
PEEK	143°C	343°C	575°C	0 - 40

TABLE 1.2. – (Walther, 1998; Patel et al., 2010; Montaudo et al., 1994)

T_g represents the transition from a glassy state of the polymer to a rubbery one. When the temperature reaches T_g, the heat energy stored becomes sufficient to break apart some of the weak bonds and therefore increase the chain mobility of the amorphous phase. It is to be noted that the majority of studies do not go above this temperature.as the use of TP polymers is mainly limited to temperatures below T_g. It has been shown that the presence of carbon fibers nested within the matrix can increase the glassy temperature up to 40% for the PPS (Walther, 1998). In the case of a woven laminates, this increase can apply to the fiber bundles.

During the melting phase, strong intermolecular bonds within the crystalline phase begin to be destructed. The crystalline phase ultimately disappears and it only remains an amorphous phase. It is to be noted that unlike the glass transition, this one is not bound to a unique tem-

perature since it highly depends on the size of the crystalline areas. The melting temperature is therefore spread across a range centered around T_m.

Finally, during the thermal decomposition, the covalent bonds holding the molecular chains together are fractured, leaving smaller molecules, decomposition gas and a carbon residue (Mouritz and Gibson, 2006). The various decomposition phenomena will be presented further within Section 1.2.1.

Concerning the thermomechanical behavior, different phenomenologies can be observed as temperature increases:
— Elasto-viscoplasticity and damage up to T_m
— Decomposition process which mainly relies on the pyrolysis of the matrix and the nucleation, growth and coalescence of porosities above T_d
— Thermal degradation highly affecting the thermomechanical properties of the TP matrix
The combination of these phenomena creates a complex interaction mixing various behaviors. They are detailed thereafter.

Thermal degradation

The thermal degradation of the matrix can be described as a process by which the exposure to a heat source causes a deterioration of several properties (such as the thermomechanical ones) of the material. This is amplified for $T > T_g$ and $T > T_m$. Once the melting point is temperature, the residual stiffness drastically decreases.

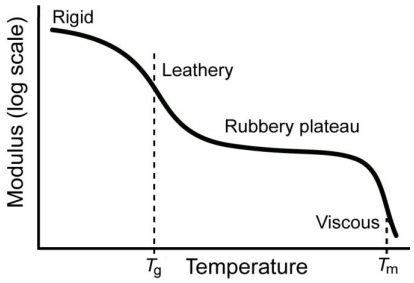

Figure 1.9. – Temperature influence on a thermoplastic's stiffness (AZO Materials, 2018)

Viscosity

When applying a mechanical loading to a polymer, it will first behave in an elastic manner. However, as the strains increase, the viscous behavior might appear, which represents the influence of time, strain-rate and temperature on the response of the material (see the first steps of Fig. 1.10). The viscous strain can be separated into two contributions under constant strain / stress loading: a reversible portion called viscoelasticity and an irreversible one called viscoplasticity (Fig. 1.11).

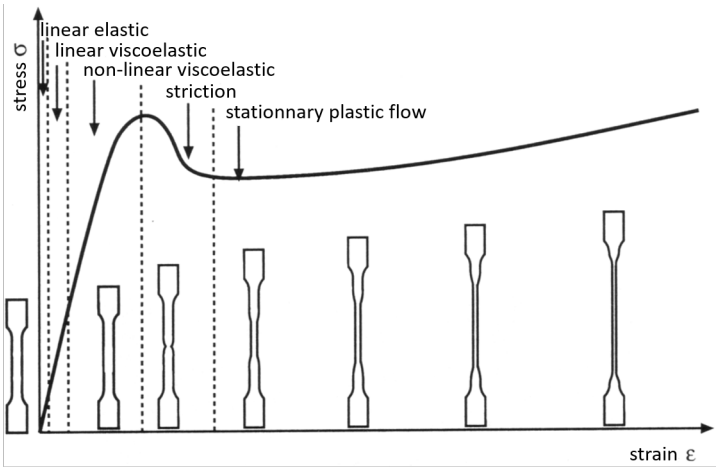

Figure 1.10. – Characteristic response in traction of a thermoplastic polymer (Christian, 1993)

Viscoelasticity Due to the organic nature of the polymer, a progressive recovery will take place through the viscoelastic behavior (Carbillet, 2005). It results from macromolecular movement without bond rupture and two domains can be observed according to the stress / strain state applied. First, the viscoelasticity can be estimated as linear which is adequate for low loading levels and is even then a somewhat idealized response. It can also be non-linear which is a more realistic as the operation loadings are often higher than the linearity limit.

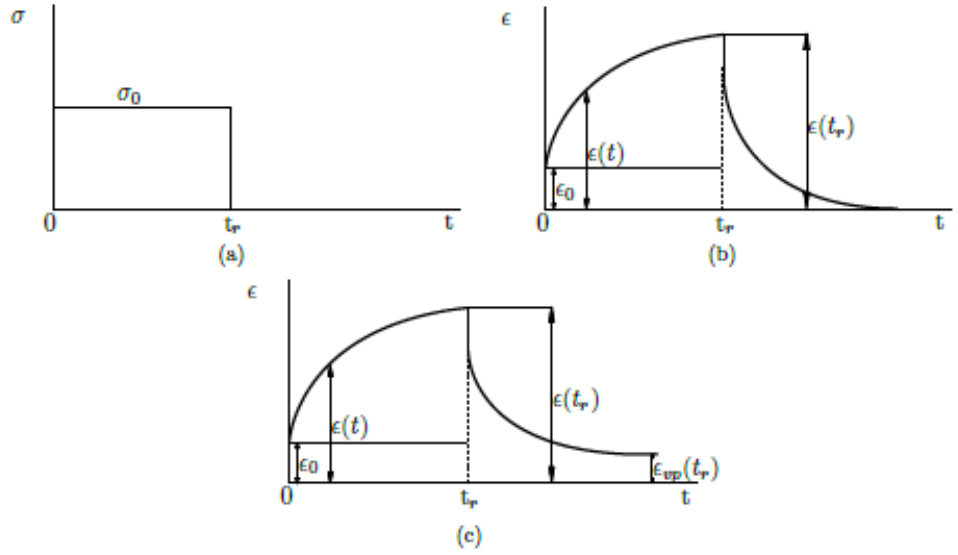

Figure 1.11. – (a) Idealized creep test and responses (b) viscoelastic (c) elasto-viscoplastic (Bouscarrat, 2019)

Viscoplasticity Contrary to viscoelastic strains, viscoplastic strains are irreversible. During this process, bonds between macromolecules are reorganized, therefore creating a time-dependant irreversible transformation.
Among the various experimental means available to highlight the viscous effects, two appear to be mainly used which are Dynamic Mechanical Analysis (DMA) and creep / relaxation tests. Experimental means and viscous behaviors will be presented further in Section 1.1.

Thermal decomposition

Once the temperatures reach the onset of T_d, the decomposition occurs as the received thermal energy is high enough to break apart the covalent bonds insuring the molecular chains integrity. Although thermoplastic materials are composed in various ways, their decomposition process follows a similar global chemical reaction in which the polymer is transformed into carbon residue and pyrolysis gases (Mouritz and Gibson, 2006).

$$\text{Polymer} \rightarrow \text{Carbon residue} + \text{Pyrolysis gases}$$

During this process, porosities filled with pyrolysis gas therefore appear embedded within the material. The combination of carbon residue (around 85% to 98%) with aromatic-alaphatic compounds is called char. It can possess a cristalline phase and an amorpheous one, is highly porous, and further information, such as its composition, is available in (Duquesne and Bourbigot, 2009). The polymer are categorized according to the amount of char produced (Duquesne and Bourbigot, 2009). PPS can be categorized among the large char producers (Kourtides et al., 1979). Subreactions and subproducts are however numerous at solid, liquid and gas states during the four different steps of the decomposition (Beyler and Hirschler, 2002) and are extremely difficult to isolate. The thermal decomposition process taking place in a laminates is summarized in Fig. 1.12. One can note that the presence of polymer-rich zones directly influences the spatial distribution of the local decomposition state in the laminates.

The thermal decomposition progress is often followed by the study of the mass loss originating from the gaseous phase transformation of the matrix. This mass loss evolution over various characteristics (such as time, temperature and heat rate) has been widely studied in TP polymers (Moldoveanu, 2005; Yao et al., 1991; Ma et al., 1988; Patel et al., 2011a; Levchik et al., 1999). An example of the evolution of the residual mass of a TP polymer (PEEK) both pure and within a laminates over temperature is shown on Fig. 1.13 under N_2 atmosphere and in air.

The quantification of the porosity content can be performed through various means which are further presented in Section 3.1.1

Influence of matrix composition

As previously stated, TP polymers consist of two phases, an amorphous one and a crystalline one. Usually, the degree of crystallinity χ (defined as the volume ratio of the crystalline phase within the material) is situated within the 10-50% range. However, this amount can vary according to the considered TP, and the same material can be obtained in various configurations according to its fabrication process.

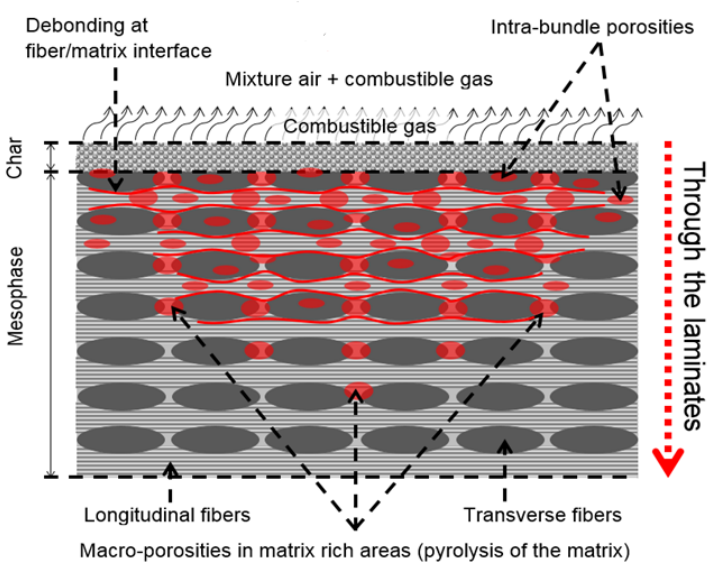

Figure 1.12. – Schematics of the thermal decomposition process in polymer-based laminates

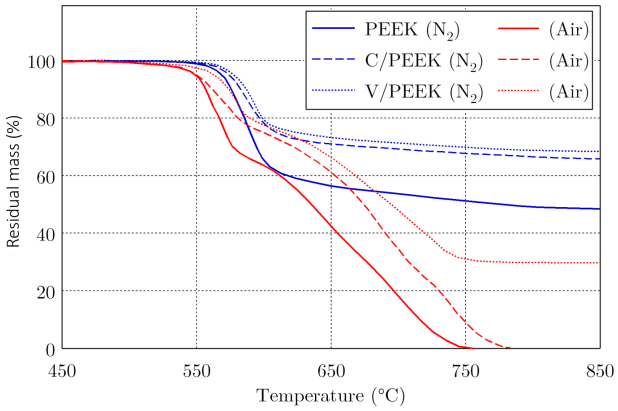

Figure 1.13. – Evolution of the residual mass of a thermoplastic-based laminates throughout the thermal decomposition of the polymer matrix (Patel et al., 2011b)

The degree of crystallinity is the major matrix composition parameter which needs to be looked into since it has a significant impact on its thermomechanical properties. Fig. 1.14 depicts a generalized TP Young's modulus behavior over temperature and the effect of increasing cristallinity. It can be seen that it does not affect the modulus when considering lower temperature than T_g. However, for temperatures above and up to T_m, increasing the degree of crystallinity will lower the stiffness due to the T_g transition phase. This can easily be explained considering that the glass transition is associated with the amorphous phase. This advantage ceases after the melting of the matrix considering that afterwards both phases are degraded. The plateau after the glass transition due to the semi-crystalline structure can be observed for other mechanical character-

istics in general, such as tensile strength as was found by (Reifsnider and Caset, 1998; Loverich et al., 2000; Feih et al., 2007b).

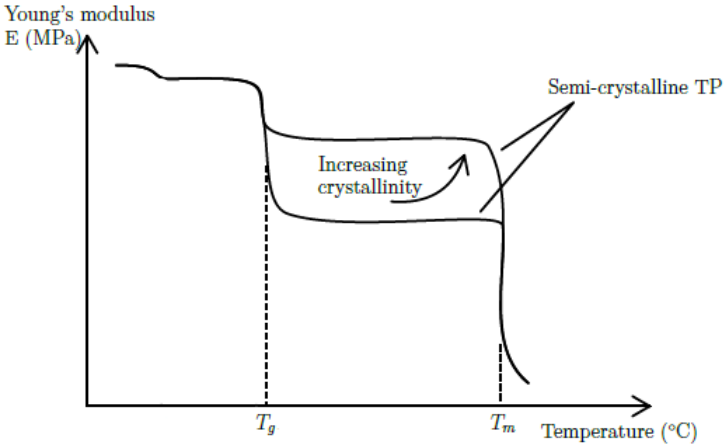

Figure 1.14. – Evolution of a TP's Young's modulus according to temperature and degree of crystallinity (Combette and Ernoult, 2005)

For comparison purposes, a precise knowledge of the crystallinity degree is then required. It can mainly be obtained with three techniques: X-ray diffraction, DMA and DSC (Hermans and Weidinger, 1961; Kolařík and Pegoretti, 2006).

1.2.2. Changes in the behavior of carbon fibers

Although the TP matrix undergoes various phenomena which greatly influence its thermomechanical behavior, the variation considering the response of carbon fibers is much more restricted, at least at the temperature / mechanical loading ranges considered in this study.

Considering the loading to which the composite material is subjected in application, the stresses are lower than the yield stress of carbon fibers. Their behavior can therefore be estimated as linear elastic (Guo et al., 2021). Furthermore, the influence of temperature on the thermomechanical behavior can be neglected (Fig. 1.15) since a decrease in Young's modulus of only 1.5% can be observed at $1000°C$ for instance (Sauder et al., 2002).

These assumptions are valid in the absence of oxidization, which occurs following the reaction:

$$\text{Fiber (or char)} + O_2 \rightarrow CO_2(g) + H_2O(g) + \text{Volatiles} + \text{Solid residue}$$

(Feih and Mouritz, 2012) showed that this oxidization starts at around 500°C, at a slow rate which increases with temperature.

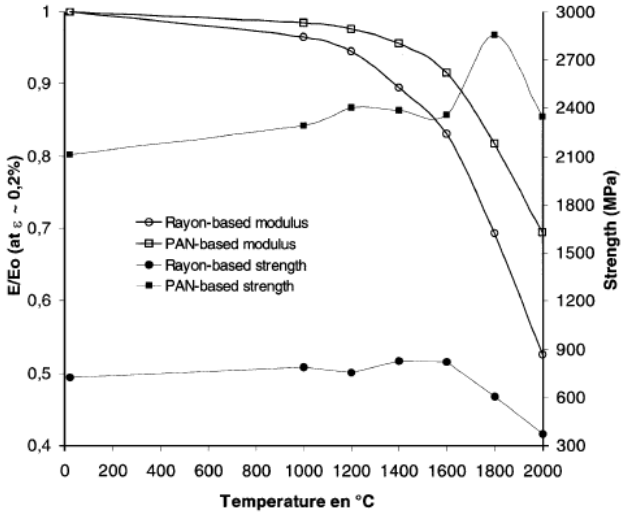

Figure 1.15. – Evolution of carbon fibers Young's modulus across a temperature range (Sauder et al., 2002)

1.2.3. Composite laminates behavior

Stacking sequence

Since the thermomechanical behavior of fibers and matrix are drastically different, a particular attention is paid to determining the most efficient way to assemble these two components within the plies. Three basic stacking sequences and their interest will be presented: unidirectional (UD) and quasi-isotropic (QI) having an industrial application and $\pm 45°$ highlighting the behavior of the matrix.

Unidirectional Unidirectional composites consist of an assembly of plies containing fibers following only one direction. UD fiber-reinforced composites have been widely used in the aeronautical industry due to its good strength / weight ratio and its simplicity. It is an extremely anisotropic material limiting its applications. The composite shows great longitudinal properties since its behavior is dominated by the fibers. However, the transverse properties are governed by the matrix as well as the loading transfers. These two aspects can not meet the expectations to actually carry a structural role, limiting the use of this kind of laminates to applications in which it can be safely assumed that the loading is only applied in one direction.

Quasi-isotropic To overcome their anisotropic behavior, quasi-isotropic composites have been developed. Their principle is to assemble plies with different fiber orientations so that the overall response gets closer to an isotropic one. Such materials are therefore more versatile and highlight their stiffness for different loading conditions. The contribution of the matrix is in this way limited which becomes more and more beneficial as the temperature increases since the matrix is more subject to temperature-related variations.

±45° Finally, a laminate consisting of ±45° oriented fibers can be used. This material has the specificity to have a matrix-dominated response when an axial loading is applied, highlighting the phenomena specific to the matrix, such as viscosity, damage and high temperature dependence.

The bulk of the presented work focuses on the QI laminates, however a preliminary study on the ±45° to assess further the influence of the chemico-physical transformations of the matrix was performed.

However, one should however not limit oneself to these examples, since many reinforcement distribution can be found and are often designed specifically for an industrial application.

Thermomechanical behavior

Stiffness The thermomechanical behavior of both matrix and fibers have been developed for steady-state temperatures. However, when they are assembled the interactions at the phases interfaces induce new variations. This influence on the stiffness is shown in Fig. 1.16. Although the matrix stiffness is very low after its melting, the fiber properties at T_m are almost unchanged and the matrix degradation can therefore not fully account for the significant decrease. The laminate stiffness loss originates from the interface stiffness loss as well. It has been shown that the higher the temperature becomes, the lower the stiffness decrease is.

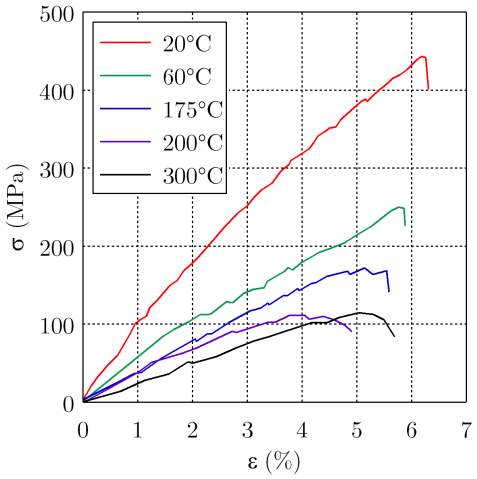

Figure 1.16. – Isothermal stress / strain curves of Glass/PP serge at various temperatures under tensile loading (Gibson et al., 2010)

A similar trend was found by (Carpier, 2018) on QI C/PPS who showed a strong decrease up to the matrix melting (Fig. 1.17.)

Failure The influence of thermal degradation on the failure in compression was widely studied. (Grape and Gupta, 1998) and (Aucher, 2011) showed that at low temperatures, the fracture

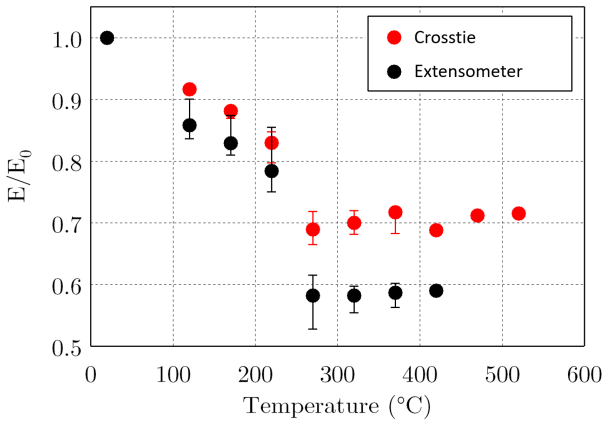

Figure 1.17. – Isothermal evolution of the axial stiffness of QI C/PPS over temperature (Carpier et al., 2020a)

occurs through shear of the fiber bundles parallels to the loading and longitudinal cracks of the matrix. As temperature increases, the longitudinal cracks appear less which progressively lowers the shear angle. Finally, for temperatures around T_g, the mechanism stabilizes in the form of buckling areas, leaving a residual stiffness to the material. (Alan, 2006) and (Nawaz, 2011) showed the large tensile strength decrease over temperature of various polymer-based composites.

Thermal expansion and density As well as its mechanical behavior, various properties of the composite are affected by a temperature increase. Among these parameters are the thermal expansion coefficient and the density which are both necessary to characterize the thermomechanical behavior of the matrix and are difficult to estimate experimentally (see Section 1.1).

Density evolution with temperature is often neglected or estimated to follow the evolution of the residual mass of the composite using an Arrhenius-type law (Biasi et al., 2014). This point of view assumes that the transformation is iso-volumetric i.e. the thermal expansion is neglected. Although this hypothesis is widely spread, it might result in some inaccuracies as the thermal expansion reaches high levels at high temperatures (see Section 2.3.1).

The thermal expansion coefficientα_{th} can be expressed as the dimension evolution of the component over temperature (Eq. 1.2), with β a characteristic dimension of the material such as its volume or a representative length.

$$\alpha_{th}(T) = \frac{1}{\beta}\left(\frac{\partial \beta}{\partial T}\right)_p \tag{1.2}$$

The thermal expansion process differs between the matrix and the fibers since the matrix deforms in an isotropic way, whereas the thermal expansion of carbon fibers has to be separated

into two categories being the axial and the radial ones (Fig. 1.18a). (Pradère, 2004) showed that the radial expansion is much more elevated than the axial one, due to their much higher axial strength, and presents an almost linear evolution with temperature. On the contrary the axial coefficient is negative up to around 600°C and then becomes positive. Although it might seem unexpected, it can be explained by the competition between the axial expansion of the crystalline network which induces a radial contraction through Poisson's effect, and the radial expansion within carbon plans (Sauder, 2001).

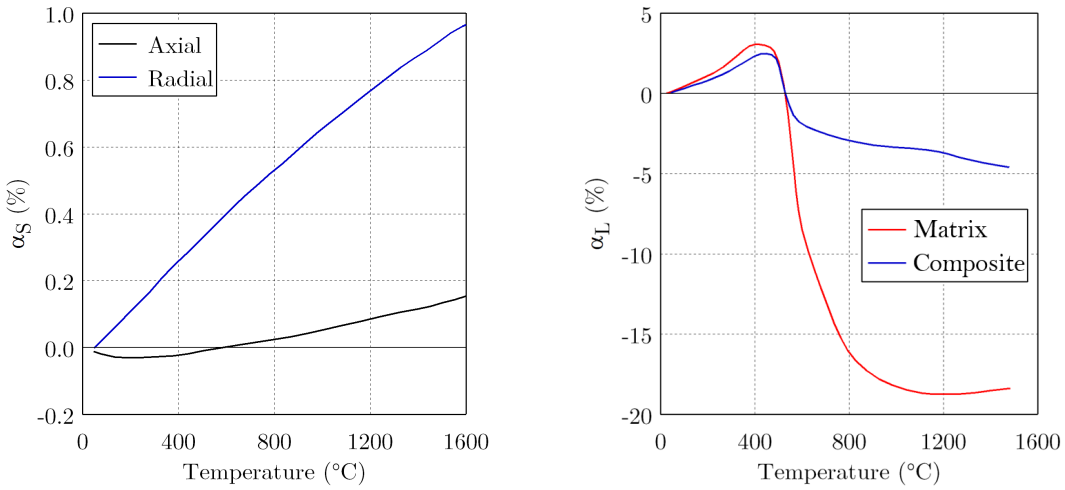

Figure 1.18. – Evolution of the thermal expansion over temperature of (a) carbon fibers (Pradère et al., 2009; Pradère, 2004) and (b) polymer matrix / CFRP (Schulte-Fischedick et al., 2007)

(Schulte-Fischedick et al., 2007) showed that the evolution of the thermal expansion of a polymer matrix increases in an almost bilinear trend from RT to T_m and from T_m to T_d before a drastic collapse leading to a contraction state, see Fig. 1.18b. The CFRP composite follows a similar behavior (softened by the fibers) with the exception of the absence of the plateau at the highest temperatures.

Thermally activated damage in PPS

Given the thermomechanical resistance of fibers compared to the one of the TP matrix in the temperature / loading conditions considered, the majority of damage mechanisms can either affect the matrix or the interface between the components. Semi-crystalline polymers and CFRP can be studied through several scales (from the molecular scale to the macroscopic one), and may presents various morphologies (amorphous and crystalline phases), a large variety of damage mechanisms can appear. To this end, these mechanisms are precisely described in (Schirrer, R. and Fond, C., 1995; Blaise, 2011; Chaudemanche, 2013). Three physical damage mechanisms are assumed as the principal ones: crazing (Friedrich, 1983; Plummer et al., 1994), nucleation

and growth of cavities (Humbert et al., 2010; Pawlak et al., 2013) and the appearance of shear bands (Friedrich, 1983).

Cavitation within the matrix and at the fiber/matrix interface In the following part, the focus will be set on the cavities (or porosities) which are of particular interest in this study since they originate from both mechanical and thermal sources. Cavities which appear within the matrix are pores filled by gas (either air or pyrolysis gas). There is therefore no internal structure which implies no load transfer as well as a disruption in the thermal properties of the material from the interface solid / gas. These cavities can either pre-exist in the initial microstructure or they can appear throughout the lifetime of the material and are usually measured in terms of a porosity content (ratio of the porosity volume to the material volume). It is to be noted that the lower the amount of impurities is in the initial state, the more spread the cavitation process during mechanical loading is likely to occur (Rozanski et al., 2011). On one side these porosities can appear when subjected to mechanical loading (favored by triaxiality (Addiego et al., 2010; Rosenberg et al., 2011)), on the other side it also depends on other factors such as strain rate (Pawlak and Galeski, 2008) or, more importantly for this study, temperature (Castagnet et al., 2000):

- For $T < T_d$:
  - The high disparity of thermal expansion coefficients between the matrix and fibers can lead to strain incompatibility. Both of these discontinuities may cause the decohesion at the interfaces which will fasten the appearance of cracks within the matrix and the laminates, ultimately causing delamination.
  - (Atreya and Agrawal, 2002) showed that phase changes such as glass transition and melting require energy which can slow down the temperature increase inhomogeneously within the laminates.
- For $T < T_d$, most of the damage originates from pyrolysis's direct or side effects:
  - On the surface, a thin layer of decomposed material will form itself. The unrestrained pyrolysis gas is highly inflammable, and will therefore self-ignite at a sufficient temperature. It creates another source of damage similar to what is described in Section 1.3.
  - Within the material, the gases will not have the capacity to break free from the material and will therefore gather in an ever-growing amount of cavities. These embedded porosities filled with pyrolysis gas will contribute to the volumetric expansion due to their high pressure.

The damaging effect of the appearance of porosities can also be summarized according to the scale of study (Bonnet, 2005):

- Microscopic scale: fiber / matrix decohesion
- Mesoscopic scale: intra-laminar cracks, fiber fracture
- Macroscopic scale: delamination

Various experimental means are available for precisely detecting porosities, such as X-Ray tomography. This method is often used in the literature by (Poulet, 2017b) or (Gigliotti et al., 2018) for example.

Deformation mechanisms of along with structural effects Apart from porosities, other mechanisms may damage the material and irreversibly alter its structure. Fig. 1.19 represents failure tensile tests of QI C/PPS up to thermal decomposition.

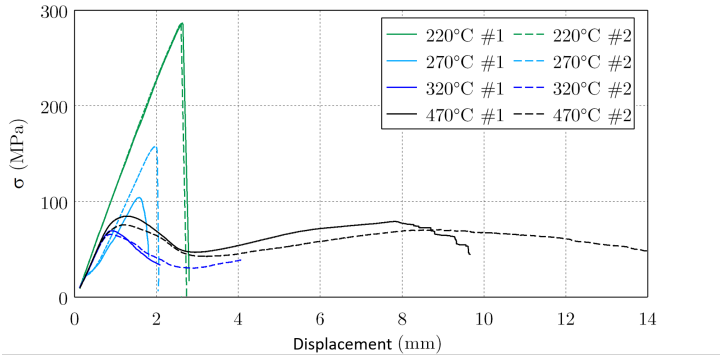

Figure 1.19. – Tensile response of C/PPS with a QI lay-up for different temperatures of exposure (Carpier, 2018)

(Carpier, 2018) showed the different trends and fracture stress according to the temperature which are based on various structural effects (Carpier, 2018):

- At 220°C, the behavior is quasi-linear with a slight change at 180 MPa due to the typical matrix cracking appearing in the overlapping yarn areas (Osada et al., 2003). The brittle fracture occurs through the 0° fibres whose maximum strain is limited and reveals a weak interface bond between fibres and matrix (Fig. 1.20).
- At 270°C, the behavior remains mostly brittle linear, with an inflexion at 25 MPa more pronounced due the local crushing of the yarns in the overlapping sections. Furthermore, the density of cracks is higher.
- At $T > T_m$, the melted matrix does not ensure the cohesion of the fiber network within the yarns and of the yarns within the plies.
  - The fibers are no longer stretching homogeneously, allowing the yarns to transversely contract and elongate much more. These two unusual behaviors result in the striction and the rotation of the 0° fiber bundles (Fig. 1.21). It leads to a generalized striction of the 0/90° plies which will increase further the bending stresses in the overlapping areas. It ultimately leads to a state in which the 90° yarns are intensively crushed by the 0° ones, creating an intense delamination and a curved surface (Fig. 1.22).
  - The yarns are free to rotate, and will reorient themselves towards the direction of the loading. It affects not only the 90° yarns within the 0/90° plies, but especially the ±45° plies. The fiber bundles then rotate (creating a shear effort) up until they touch each other, therefore ending the rotation (Lomov et al., 2008) and increase the general stiffness of the composite (Totry et al., 2010).

  (Selezneva et al., 2011) showed that these two phenomena, striction and reorientation, have an increasing effect with temperature and are primary responsible for the non-fracture behavior above the melting temperature (Fig. 1.19). The entire process is summarized in Fig. 1.23. They can be quantified through post-mortem observations (Vieille and Taleb,

2011). Table 1.3 summarizes fiber reorientation of C/PPS at 120°C for creep tests at 40, 60 and 100 MPa in terms of total, residual and reversible rotation as was found by (Bouscarrat, 2019). It shows at high stresses a large reversible rotation and a significant residual one. A majority of the rotation will then disappear upon unloading, but almost 40% will remain. This drastically influences the structural integrity of the laminates.

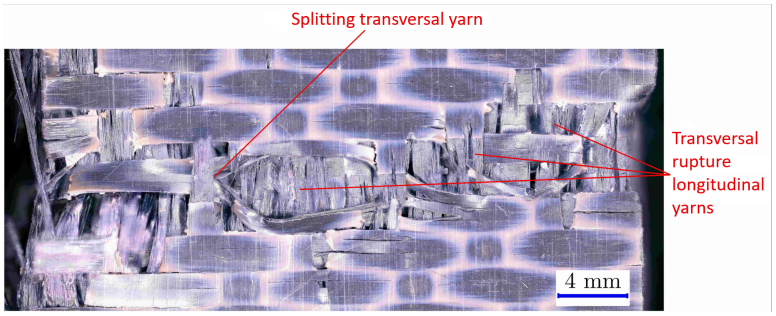

Figure 1.20. – Fracture facies in tension at 220°C (Carpier, 2018)

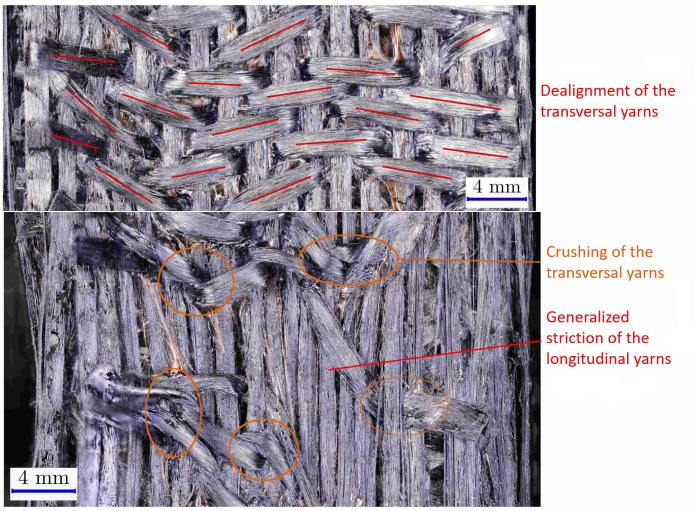

Figure 1.21. – Optical microscopy observations of the striction and rotation occuring in the 090° plies during a tensile loading (Carpier, 2018)

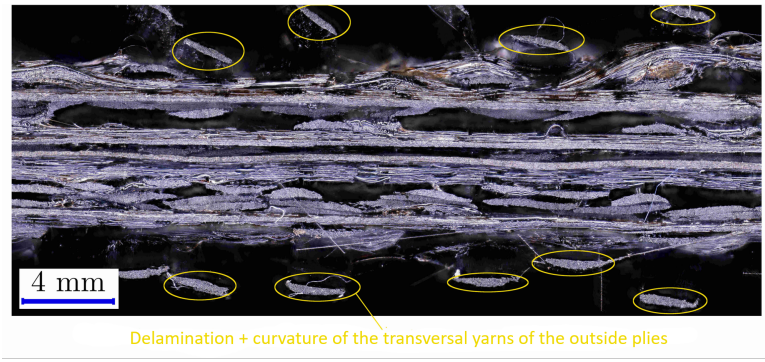

Figure 1.22. – Through-the-layer optical microscopy observation after failure in tension at 470°C (Carpier, 2018)

	40 MPa		60 MPa		100 MPa	
	Avg	Std	Avg	Std	Avg	Std
Total rotation (°)	1.3	0.9	3.5	1.2	9.5	1.4
Residual rotation (°)	0.5	0.7	1.3	0.8	3.6	0.2
Reversible rotation (°)	0.9	0.3	2.1	0.4	5.9	1.3

TABLE 1.3. – Summary of the total, residual and reversible rotation of C/PPS at 120°C after creep tests

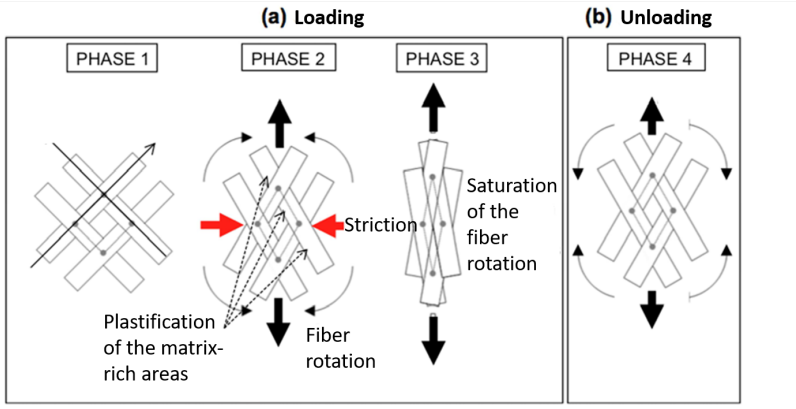

Figure 1.23. – Summary of the striction / reorientation processes (Aucher, 2011)

1.3. Thermomechanical behavior - heterogeneous temperature

In the case of a fire exposure, one face of the laminates is exposed to a high source of thermal energy. This results in a high through-the-thickness thermal gradient as illustrated in Fig. 1.24.

The previous section provided some insight on the influence of temperature on the behavior of the composite. These effects can be extended to the heterogeneous case considering that the disparity of temperature induces extremely different responses within the different areas of the material. These discontinuities are amplified by the characteristic variation of the components (fiber, matrix, char) as well as their evolution with temperature. Furthermore, local irregularities such as porosities can drastically alter the resistance of the material. Therefore, the thermal transfers leading to large temperature gradients need to be considered to account for the fire response of composite laminates.

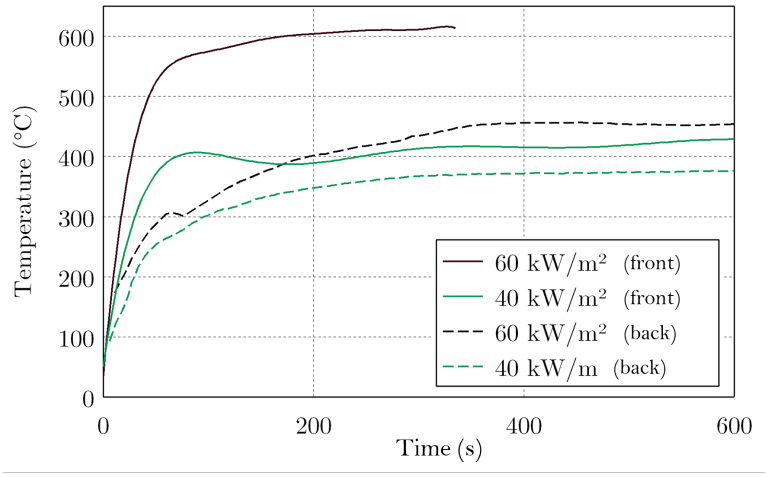

Figure 1.24. – Temperature difference between the exposed and back faces of a QI C/PPS laminates for different heat flux levels (Carpier, 2018)

1.3.1. Thermal transfers

When a radiant heat flux is imposed on one face, the temperature increases through the thickness by conduction and exchanges with the outside environment at its boundaries through heat radiation and convection. Overall, when considering the energy conservation, the process can be expressed as the following (Lagrée, 2023):

$$\text{temporal variation} = \text{flux term} + \text{internal creation/dissipation}$$

These phenomena are translated by the following equation Eq. 1.3

$$\frac{\partial E}{\partial t} = \vec{\nabla}.(\underset{\sim}{\lambda}\vec{\nabla}T) + p \tag{1.3}$$

with $\underset{\sim}{\lambda}$ the thermal conductivity tensor and p a source term.
This equation is the one usually used in composite subjected to a heat flux, along with the boundary conditions (in our case heat radiation and convection). By assuming that the temporal energy variation is obtained by a temperature change and that specific heat and the density do

not depend on the time, it leads to:

$$\rho C_p \frac{\partial T}{\partial t} = \vec{\nabla}.(\underset{\sim}{\lambda}\vec{\nabla}T) + p \tag{1.4}$$

This equation is based on two properties: the thermal conductivity and the thermodynamics.

Thermodynamic properties

In order to elevate its temperature, a material requires an energy source, which can be quantified as an energy Q to elevate the temperature from an initial T_1 up to T_2. In the case of the carbon fibers, this can be translated to:

$$Q = \int_{T_1}^{T_2} mc_p dT \tag{1.5}$$

As the matrix undergoes several transition, additional terms must be added. Elevating its temperature above the decomposition onset requires an energy depending on various latent heats (Stoliarov and Walters, 2008):

$$Q = \int_{T_0}^{T>T_d} mc_p dT + m\delta h_m + m\delta h_d + m\delta h_e \tag{1.6}$$

with δh_d the latent heat of chemical dissociation and δh_e the latent heat of the evaporation of the decomposition products. These two terms can be difficult to separate and can be grouped as the pyrolysis latent heat (Frederick Jr. and Mentzer, 1975). However, Q is usually not determined with 1.6 since it is much easier to use thermogravimetry tests under different heat flux (Staggs, 2004).
The specific heat capacity values at room temperature are not always provided by the constructor. It is the case of the T300 fibers used, at a value of 800J.kg^{-1}.K^{-1}. It is unfortunately not the case of PPS, although it was estimated at 1020J.kg^{-1}.K^{-1} by (Plastics and rubber, 2004). It is to be noted that the specific heat is not an anisotropic value, hence the one of the composite can be calculated through a mixture law.
The evolution of the value for C/PPS and its different components over temperature was estimated by (Carpier, 2018) up to the thermal decomposition (Fig. 1.25). It is important to notice that the specific heat presented also include the melting latent heat, therefore artificially increasing the c_p around the melting temperature. It can be observed that apart from the peak around T_m, the specific heat follows an almost linear evolution at a rate of 2.6J.kg^{-1}.K^{-2}, as it was expected from (Stoliarov et al., 2009). As for the fibers, a similar trend is observed, albeit with an increase rate slightly lower.

Thermal conductivity

The thermal conductivity coefficient λ represents the ability of the material to diffuse heat without matter movement. Contrary to the specific heat capacity, in a composite material the conductivity is strongly anisotropic, especially in carbon fibers. Indeed, (Schuster et al., 2008)

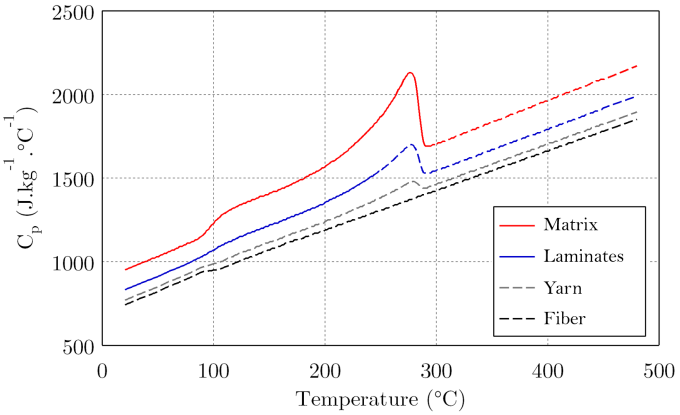

Figure 1.25. – Evolution of the specific heat capacity of the C/PPS and its components (full line: experimental values, dash line: calculated values) (Carpier, 2018)

showed that their thermal conductivity coefficient at room temperature is around ten times higher in the axial direction than in the radial one (100 $W.m^{-1}.K^{-1}$ against 10 $W.m^{-1}.K^{-1}$) . It is however isotropic for the PPS, with values estimated between 0.19 $W.m^{-1}.K^{-1}$ and 0.29 $W.m^{-1}.K^{-1}$ which is much lower than the one of the carbon fibers.
The experimental determination of the value for the matrix at high temperatures is challenging because of their softening or even melting. That is why λ is rarely found at temperatures higher than 150°C in the literature. For semi-crystalline polymers, the amorphous phase has an increasing thermal conductivity up to the glass transition temperature before decreasing as explained by (Eiermann, 1964). The trend of the crystalline phase however varies depending on the material. It is therefore not possible to generalise this behavior to all TP polymers. It was nonetheless determined by (Carpier, 2018) that the conductivity of the PPS decreases after the glass transition. As for the carbon fibers, the lack of studies and contradictory results make it hard to conclude on the evolution of their conductivity with temperature (Pradère et al., 2009).

Given the anisotropic thermal conductivity of the fibers, the axial and radial properties need to be studied separately. The axial conductivity of the composite can be easily calculated with a parallel mixture law:

$$\lambda_c^{ax} = \lambda_m V_m + \lambda_f^{ax}(1 - V_m) \tag{1.7}$$

A series mixture law such as Eq. 1.8 can be used to assess the radial conductivity, but it only provides a lower limit. Although the true value is often close from this one, it is not always the case. There are however specific models available according to the specific features of the composite (Progelhof et al., 1976).

$$\lambda_c^r = \frac{\lambda_f^r \lambda_m}{\lambda_f^r V_m + \lambda_m(1 - V_m)} \tag{1.8}$$

Whatever the choice, the evolution over temperature is usually considered linear up to the

decomposition temperature because of the difficulty to experimentally measure it. It is sometimes found piecewise linear with intermediate temperatures chosen for instance as T_g and T_m (Carpier, 2018). Once the material starts decomposing, the conductivity is often approximated by a mixture law based on the pyrolysis degree. Finally, once the material is decomposed, its conductivity is calculated using a third-order polynomial (Henderson et al., 1987).

Emissivity coefficient

When a radiant heat flux is applied to the material, its temperature increase highly depends on its radiative properties: the emissivity ϵ_{emi}, the absorptivity α_{ab} and the transmittance τ_{tr} and the reflectance ρ (dependent of the temperature and the wave length). They characterize whether the material will reflect, absorb or transmit the heat flux or not. They are linked by the following relations

$$\epsilon + \alpha_{ab} + \rho = 1 \epsilon = \frac{(1-\rho)(1-\tau)}{1-\rho\tau} \tag{1.9}$$

Materials can be classified according to their radiative properties. A material which would absorb all of the radiation is called a black body ($\alpha_{ab} = 1$), although it is not really obtainable in application. The true distinction is therefore whether the material transmits or not. If it does not, it is called an opaque body. If it does, it is a (semi)-transparent body. Finally, if the properties do not depend on the length wave of the radiation, it is called a grey body.
The heat flux emission W from a body varies according the temperature and the Stephan-Boltzmann law:

$$W = \epsilon \sigma T^4 \tag{1.10}$$

with $\sigma_{SB} = 5.670x10^{-8}$ W.m^{-2}.K^{-4} the Stefan-Boltzmann constant and ϵ the total emissivity over the wave length range.

1.3.2. Thermomechanical response

Because of the induced thermal gradient, the thermomechanical behavior of the composite presents some differences.

Influence of the thermal expansion and processing debonding

As it was previously described, the properties of the matrix / fibers couple highly changes with the variation of temperature. Over the property gradient within the laminates resulting from the heterogeneous temperature, the thermal expansion ones are the most impactful damage source (Feih et al., 2007a; Chang, 1986). (Fahmy and El-Lozy, 1974) observed that a 200°C heat-up is sufficient for cracks and delamination to appear due to thermal stresses, both being strongly influenced by structural imperfections. These imperfections originate from the heating during the processing which induces a large deconsolidation, as depicted by (Amedewovo et al., 2023). The influence of porosity formation during processing on the mechanical properties (interlaminar shear strength, transverse strength and stiffness) was estimated by (Fisher et al., 2023) and (Zhang et al., 2022). Even at low porosity contents (< 2.5%), a clear decrease of the mechanical

properties is observed. This is especially the case under compression loading, which is confirmed by (Liu et al., 2011). Furthermore, the apparition of thermally insulating gaseous areas lowers the thermal exchanges through the laminates.

Overall, the knowledge of α_{th} is often overlooked and dismissed as neglectful (usually chosen as a constant, which is strongly disputed by Fig. 1.18b) whereas it highly participates to delamination and porosity formation.

Internal pressure induced by the thermal decomposition

When the temperatures exceeds T_d, the new porosities originating from the thermal decomposition appear. As they combine with the ones from the thermal expansion, large networks of cavities form. The pyrolysis gas is then free to (i) escape from the laminates if they are connected to the outside environment, or (ii) move through the laminates and exert high internal pressure on the components. Although this internal pressure is difficult to quantify, (Hariharan et al., 1990) observed a large increase at the start of the decomposition as the pyrolysis gas appear 1.26. The laminates consequently swells, and the porosities grow larger. As a result, an increasing amount of gas can escape, which is confirmed by a steep lowering of the pressure.

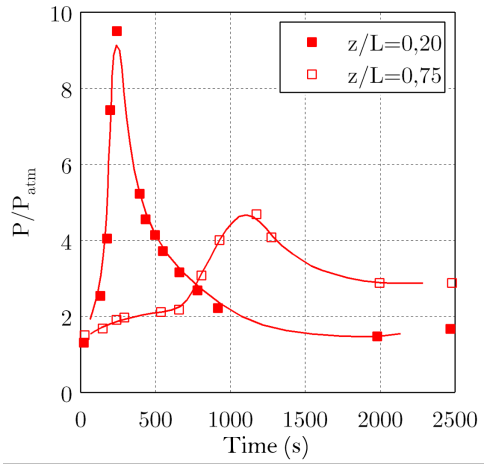

Figure 1.26. – Evolution of the internal pressure within a laminates over time due to the pyrolysis of the matrix (Hariharan et al., 1990)

The following parts are based on Carpier's work (Carpier, 2018) since very little information can be found in the literature about tensile/creep behavior of TP polymers at high temperatures under coupled thermomechanical loading. In addition, it deals with the same material (C/PPS) as the one studied here.

Tensile behavior

When investigating the behavior of a material, the simplest loading to apply to a material is a tensile test. Fig. 1.27 shows tensile tests carried on QI C/PPS at two heat flux levels (40kW.m^{-2} and 60kW.m^{-2}) representing respectively a maximum temperature at the exposed surface of 401°C and 582°C. It is to be noted that contrary to homogeneous temperature, in the present case the stress state is not similar in the material due to the thermal gradient. The curves therefore require to be plotted in terms of applied force against displacement.

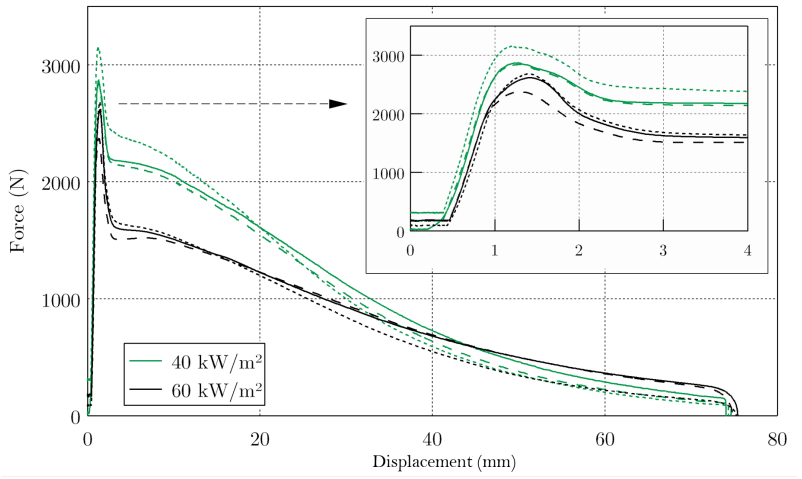

Figure 1.27. – Tensile curves of C/PPS at $40kW.m^{-2}$ and $60kW.m^{-2}$ heat flux (Carpier, 2018)

Given that at these temperature levels the matrix is molten, the load bearing capability is almost only provided by the 0° plies. The response is at first linear elastic up to 2.4 and 3.1 kN respectively before starting to decrease partially due to the striction. The differences from the homogeneous temperature mainly come from the thermal gradient. The striction phenomena quite differ from the homogeneous case. Because of the thermal gradient, strong discontinuities appear at the interface between the exposed area and the opposed one, becoming the preferred localization of striction initiation. This results in a much more important striction: 55% vs 40% in homogeneous conditions.

Although tensile tests allow to quickly obtain a general idea about the behavior of a material, especially its failure mechanisms, they are not representative of the stress distribution within laminates subjected to fire conditions. Structural parts are usually subjected to constant forces making creep loading more relevant to be considered.

Creep behavior

When considering a creep test under heterogeneous temperature, two phases are distinguished. First, the transitory phase takes place during which the mechanical deformation is driven by the thermal degradation. Secondly, when the thermal discontinuities become less drastic, creep be-

comes the prominent mechanism and the material enters a steady phase.
Considering at the response of QI C/PPS in tensile creep tests, different behavior appear according to the applied stress at 60kW.m^{-2} (Fig. 1.28). For creep stresses higher than 37% of σ_u (failure stress at RT, σ_u = 532 MPa), the fracture happens before 60s due to an elongation higher than the one of fracture of the 0° fibers. This process is similar to the one of homogeneous temperature, the difference being that the failure only occurs in the plies below the melting temperature.
For lower stress levels, the composite resists long enough for the temperature to increase up to the level of pyrolysis and oxidization. oxidization is the main factor for the following strain increase. Indeed, (Feih and Mouritz, 2012) showed that it progressively the diameter of the carbon fibers, lowering their rigidity. At some point, the fiber bundles become unable to withstand the mechanical loading, hence fracturing. This creates a "strain jump" as the strain brutally increases. It is to be noted that the following ply (at ±45°), can act as a thermal shield for the others 0/90° plies, allowing them to keep their good resistance for a longer time. The plies gradually fail, ultimately resulting in C/PPS laminates failure.

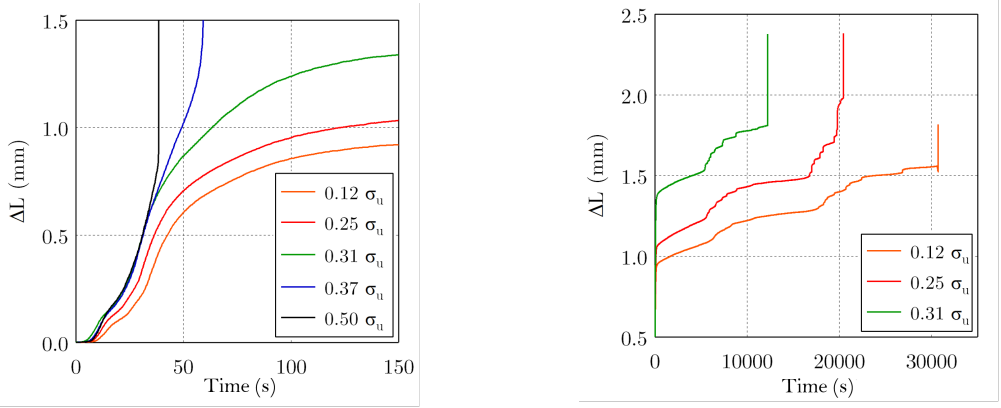

Figure 1.28. – Creep response of C/PPS laminates subjected to a 60 kW.m^{-2} heat flux (QI case)(Carpier, 2018)

Damage factor

Considering the evolution of the mechanical property, a damage factor is classically defined from the evolution of the axial stiffness (Ladeveze and LeDantec, 1992):

$$d = 1 - \frac{E}{E_0} \tag{1.11}$$

E can be estimated in creep tests as the secant modulus E_{sec}:

$$E_{sec} = \frac{\sigma_{creep}}{\epsilon_{mec}}$$

with ϵ_{mec} the mechanical strain obtained by removing the thermal strain (estimated by imposing a neglectful compression) to the total strain. It finally gives the following expression:

$$d(t) = 1 - \frac{\epsilon_0}{\epsilon_{mec}} \tag{1.12}$$

The evolution of d during creep tests (Fig. 1.29) shows the separation between the transition and the steady phases (inflexion around 150s). It therefore appears that this factor is a good indicator of the mechanical state of the material.
Although the temperature influence on various mechanisms and characteristics was not fully extensive, the reader can refer to other references for better description (Carpier, 2018; Aucher, 2011; Bouscarrat, 2019; Nawaz, 2011; Walther, 1998).

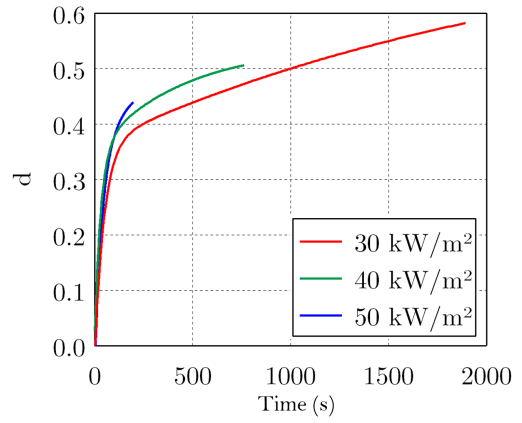

Figure 1.29. – Evolution of the damage factor as a function of time in QI C/PPS laminates for different heat flux densities (Carpier, 2018)

1.4. Numerical modelling

The other approach to study the thermomechanical coupling is a numerical one which relies upon the experimental work to identify the different parameters of the model.

1.4.1. Model scales

Thermomechanical modelling usually relies on three modelling scales:

— The macroscopic scale is used to represent the entirety of the geometry of a material so that the macroscopic structural effects can be identified. The material properties of such a model are estimated by considering the composite material as a homogeneous assembly with orthotropic properties. (Sihn et al., 2023) simulated the thermomechanical behavior of CFRP composites using this approach.Although certain phenomena can be characterized at a macroscopic scale (such as convection or emissivity), the vast majority

of the mechanical phenomena are localized in small part of the material as was presented earlier. It would not be relevant to increase the refinement of the geometry at such a big scale since the calculations would take far too long to process.

— The second approach consists of modelling the laminates at the ply level, as did (Rizk et al., 2018, 2019). In this intermediate approach, each ply is considered homogeneous. Although more representative than the macroscopic scale, it still does not include localized phenomena

— The final approach is to consider a small part of the material in which the fiber bundles and the matrix are separately represented, as well as their properties. This is the mesoscopic point of view used in works such as (Biasi, 2014; Biasi et al., 2014). In such a model the fiber bundles are considered homogeneous given that the fibers are not explicitly represented (it would require a microscopic scale).

The macroscopic scale and ply-level modelling are mostly used in the industry given that the behavior of the whole structure needs to be studied. However, the mesoscopic approach is often used to have a better understanding of the phenomena happening within the material. Once the scale is chosen, the various constitutive laws governing the thermomechanical behavior of the composite can be determined.

1.4.2. Thermal behavior

Temperature-dependence and thermal model

As it has been depicted throughout this review, the various thermal properties of the constituents evolve with temperature. This temperature-dependence is often considered in the literature, although not necessarily for all of the parameters. Indeed, as they are difficult to identify experimentally, it is sometimes chosen to neglect their dependence to temperature. As an example, (Halm et al., 2017) and (Rizk et al., 2019) chose to do so for the thermal conductivity while (Biasi, 2014; Biasi et al., 2014) and (Sihn et al., 2023) decided to account for all of the dependencies.

While most of the studies consider heat transfers to occur following the usual heat equation, more advanced equations have been developed to account for the specificities of ploymer-based composites exposure to high temperatures. Among them, (Biasi et al., 2014), building on the work of (Henderson et al., 1985; Henderson and Wiecek, 1987), developed a model taking into account the polymer phase changes, the pyrolysis gas movement within the laminates, internal pressure induced and the chemical reaction of the thermal decomposition.

Pyrolysis

In order to quantify the evolution of the pyrolysis and to model it, the pyrolysis reaction advancement of the polymer is usually experimentally assessed by the pyrolysis degree α:

$$\alpha = \frac{m - m^{ini}}{m^{ini} - m^{d}} \tag{1.13}$$

with m^{ini} and m^{d} the initial and decomposed masses after the pyrolysis. Its rate is often

modelled by a multiplicative decomposition depending on the temperature and the pyrolysis degree (Day and Budgell, 1992; Vyazovkin and Wight, 1999; Budrugeac, 2000):

$$\frac{d\alpha}{dt} = k(T)\, f(\alpha) \tag{1.14}$$

with k an Arrhenius-type law:

$$k(T) = Aexp\left(-\frac{E_{ac}}{RT}\right) \tag{1.15}$$

A, E_{ac} and $f(\alpha)$ are model parameters which require to be identified based on the experimental results. Two approaches may be considered:

— Modelistic: It is based on the assumption that the pyrolysis kinetics can be represented by a conversion function $f(\alpha)$ whose general expression is chosen among a large range of possibilities. The simplest one is $f(\alpha) = 1 - \alpha$. The differential equation is then solved and (A, E_{ac}) is identified.

— Model-free: This methods first determines the value of E_{ac} which then leads to the identification of $f(\alpha)$ and A.

These two methods and their advantages / disadvantages are precisely described in (Carpier, 2018).

1.4.3. Mechanical behavior

The constitutive relations presented will only focus on the mesoscopic approach given that it is much more delicate to identify all of its variable than the macroscopic one.

The mechanical strain tensor within composites can be additively decomposed into four contributions in order to study its non-linear behavior: elasticity, plasticity, viscoelasticity and viscoplasticity. Under the assumption of small strain, it reads:

$$\underset{\sim}{\varepsilon} = \underset{\sim}{\varepsilon}^{e} + \underset{\sim}{\varepsilon}^{p} + \underset{\sim}{\varepsilon}^{ve} + \underset{\sim}{\varepsilon}^{vp} \tag{1.16}$$

As it was previously stated, the behavior of yarns and matrix are extremely different both in terms of resistance at room temperature and impact of high temperatures. Although the behavior of the fiber bundles can be approximated as linear elastic, the viscosity of the matrix is often considered given its dependence on temperature and loading speed (González and LLorca, 2007; Zhang et al., 2010; Totry et al., 2010; Vaughan and McCarthy, 2011; Canal et al., 2009; Yang et al., 2012). No plasticity model will be presented here as they are rarely used at high temperatures.

Linear elasticity

Even for the matrix, while the strain/stress within the material is low enough, its response is linear elastic. This behavior is usually reproduced with Hooke's law which stipulates that the strain tensor $\underset{\sim}{\varepsilon}$ is directly proportional to the stress tensor $\underset{\sim}{\sigma}$ through the stiffness tensor $\underset{\sim}{C}$ (Eq. 1.17)

$$\underset{\sim}{\sigma} = \underset{\sim}{C}\underset{\sim}{\varepsilon} \tag{1.17}$$

Viscoelasticity

Contrary to elasticity, there is a part of the strain energy which is lost or dissipated through viscoelasticity, phenomenon known as the hysteresis (Fig. 1.30). On this figure, the hysteresis is the area in the center of the loop.

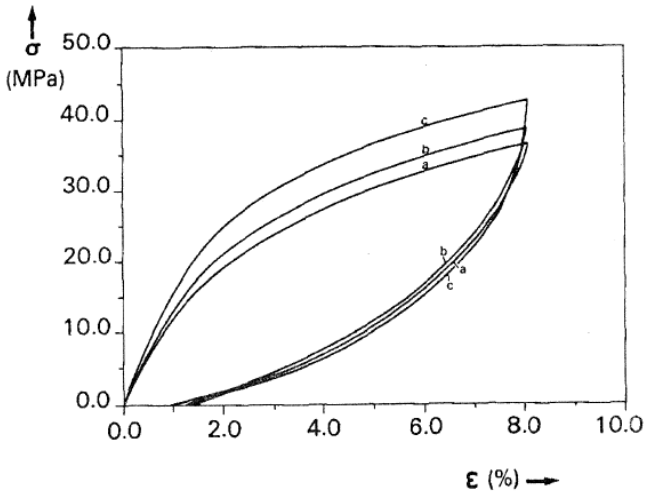

Figure 1.30. – Hysteresis curves of a viscoelastic material at different strain rates (Van Hartingsveldt and Van Aartsen, 1991)

The viscous mechanism is often considered in the literature for temperatures up to T_g, as it significantly alters the thermomechanical behaviour of the matrix (Hirsekorn et al., 2022). Several models account for the viscoelastic behavior. The most used ones are described thereafter.

Rheological models Rheological models are models describing the viscoelastic behavior of materials using an assembly of springs and dampers. The springs are reproducing the linear isotropic linearity from Hooke's law (Eq. 1.18)

$$\sigma = E\varepsilon \qquad \text{with E the Young Modulus} \tag{1.18}$$

As for the dampers, they represent the time-dependant viscous behavior. This is accounted for by Newton's law (Eq. 1.19)

$$\sigma = \eta\frac{d\varepsilon}{dt} \qquad \text{with } \eta \text{ a viscous parameter} \tag{1.19}$$

This components are then assembled either in series or in parallel, thus providing a combination of the multiple possibilities. Two elementary models appear: Maxwell model consisting

of a spring and a damper in series, and Kelvin-Voigt model using these two elements in parallel (Fig. 1.31)

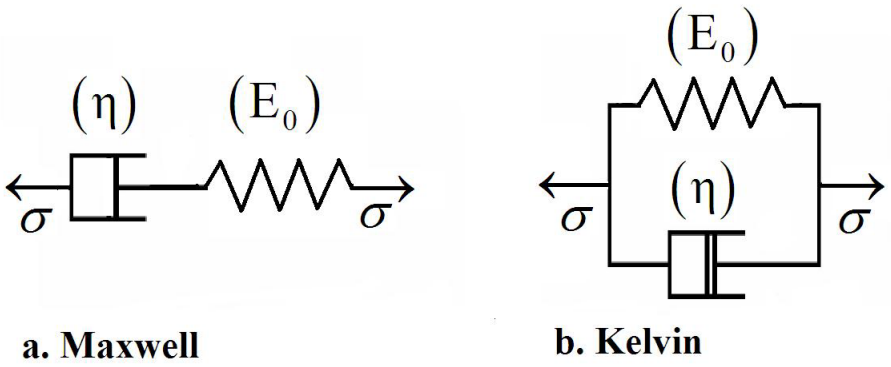

Figure 1.31. – Rheological models of Maxwell and Kelvin-Voigt

The following stress/strain relations are obtained:

— Maxwell:

$$\frac{d\varepsilon}{dt} = \frac{1}{E}\frac{d\sigma}{dt} + \frac{\sigma}{\eta} \tag{1.20}$$

— Kelvin-Voigt

$$\sigma = E\varepsilon + \eta\frac{d\varepsilon}{dt} \tag{1.21}$$

Both of these models are appropriate to a first approach in order to obtain a general idea of the viscoelastic behavior. However, for more precise results, these two models can either be combined together or be reproduced multiple times.
The combination of a Maxwell and a Kelvin-Voigt models gives a Maxwell model with an additional spring, called the Standard linear solid rheological model used in works such as (Christöfl et al., 2020; Plaseied and Fatemi, 2008; Takagi et al., 2008; Ge et al., 2012).

The other type of combination is to reproduce the same model multiple times. This is called a generalization. It originates from the fact that a polymer does not relax at a single relaxation time as it is the case in the previous models. To overcome that, N Maxwell models can be assembled in parallel, therefore including N relaxation times creating the Generalized Maxwell model (GM), widely used in the polymer modelling (Papanicolaou and Zaoutsos, 2019; Zerbe et al., 2017; Dörr et al., 2017). It can be further improved by including a free spring as well (Fig. 1.32). The equations therefore incorporate N first-order differential equations which can be associated by the superposition theorem.

Although intrinsically easy to implement, the rheological models may necessitate a great amount of parameters depending on the complexity of the generalisation. Furthermore, this approach does not precisely models multiaxial loadings and is only considering the linear aspect of viscoelasticity. These limitations need to be kept in mind throughout the modelling process.

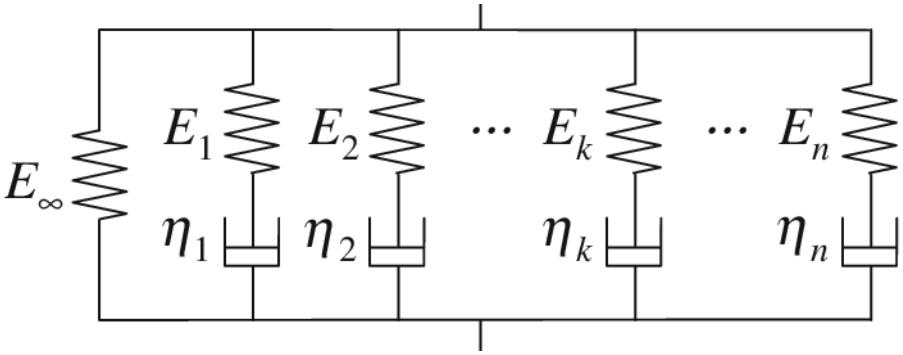

Figure 1.32. – Generalized Maxwell rheological model (Chae et al., 2010)

Spectral model and others An alternative to the rheological model is to choose a spectral formulation. This approach considers various relaxation times, the difference being that the viscosity parameters are linked between them by continuous functions (Marcin, 2010). The assembly of functions creates a spectrum, which can be weighted by various spectral distributions, such as rectangular, triangular or Gaussian (Remy-Petipas, 2000). It was also proven by (Boubakar et al., 2003) to be more reliable under multiaxial loadings . This approach was chosen in the PhD works of W. Albouy (Albouy, 2013). Other models can be found in the literature, such as the Schapery model (Schapery, 1969) and Mooney model (Somarathna et al., 2020).

Micromechanical models

The micromechanical models are numerical models usually used to describe the behavior of porous materials. These models take into account parameters representing the porosity volume fraction within the material, as well its evolution through nucleation, growth and coalescence. It provides a way to consider the influence of porosity on the damage behavior of a material (mainly on metal alloys, but adapted to polymers as well).
The Gurson Tvergaard Needleman (GTN) model (Needleman and Tvergaard, 1984) is a frequently used example of these micromechanical models (Cayzac, 2014; Poulet, 2017a). Although they are used for mechanical behavior purposes, it could be assumed that the models can be altered to replicate the porosity formation due to the thermal decomposition of the polymer matrix. However, the porosity content is only a global variable and does not explicitely represent the porosities locally and their influence on the thermomechanical behavior. Such a limitation would considerably decrease the representativity of the model, especially during a fire / heat flux exposure in which a gradient of temperature - and hence of porosity content - is induced.

1.4.4. Thermomechanical model developed by Carpier

In the previous works carried by (Carpier et al., 2022) on QI laminates, a mesoscopic approach was used considering a representative volume element (RVE) (see Fig. 1.33) and temperature-dependent thermomechanical properties (linear elastic behavior for the matrix and thermal behavior of matrix and fiber bundles). The thermal properties were determined either by (i) direct

experimental identification (specific heat, thermal expansion, emissivity), and (ii) by reverse identification (genetic algorithm) trying to numerically replicate temperature fields obtained with a cone calorimeter (conductivity, convection coefficient). More details on the modelled domain and the thermomechanical properties are provided in Section 2.2. Fig 1.34 shows the two-step decrease in the axial stiffness of the laminates (normalized by the stiffness at the initial state). The simulation precisely reproduces the experimental stiffness loss during the phase transitions (glass transition and melting).

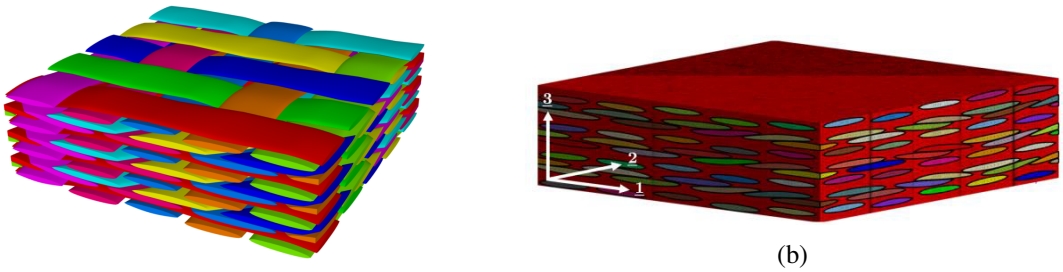

(a) (b)

Figure 1.33. – Woven meso-structure of the RVE: (a) as generated with Texgen, (b) as meshed for the finite elements analyses (Carpier et al., 2022).

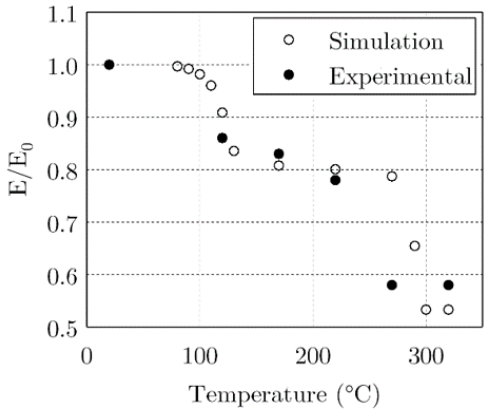

Figure 1.34. – Comparison experimental / numerical of the evolution of the normalized axial stiffness of QI C/PPS laminates with temperature (Carpier et al., 2022)

A heterogeneous thermal loading case was then reproduced. Given that the modelling did not account for the thermal decomposition of the matrix, a criterion was to consider temperatures lower than T_d. To that end, one surface of the laminates was exposed to a 20kw/m^2 heat flux. Fig. 1.35 shows the temperature evolution (up to 370°C) within the various plies as well as the induced axial stiffness. It appears that the glass transition (which is almost instantly reached) highly decreases the stiffness of every ply within the first 20s. However the second drop due to the melting occurs at various times according to the localization of the plies in respect of the exposed surface.

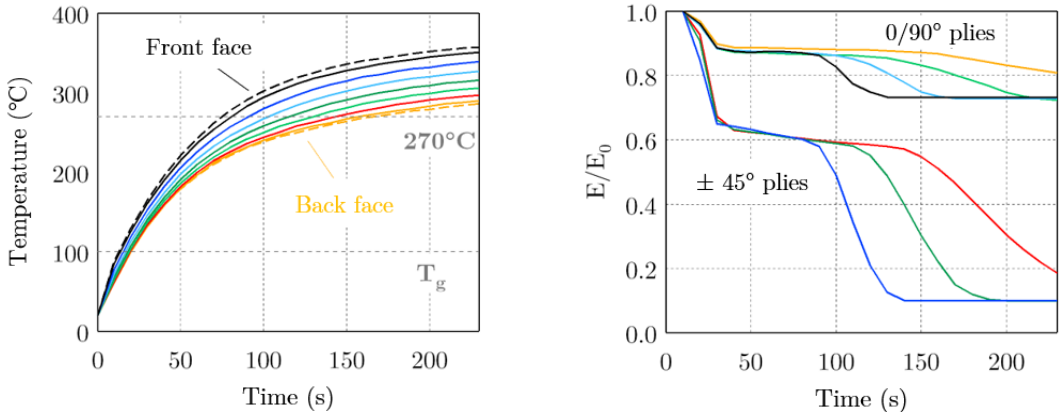

(a) (b)

Figure 1.35. – Influence of a 20kw/m^2 heat flux exposure on the thermomechanical behavior of the different plies of QI C/PPS laminates. (a) Evolution of the average temperature over time, (b) evolution of the normalized axial stiffness over time (Carpier et al., 2022)

As a result of the alternated thermal degradation of the plies, the axial strain increases progressively during a 60MPa tensile load combined with the 20kw/m^2 heat flux (see Fig. 1.36(a)). Furthermore, the stress distribution between the plies evolves as a function of time. The plies oriented according to 0/90° and ±45° sequences have similar contributions during the initial times as they all have similar stiffnesses (see Fig. 1.36(b)). However, as the temperature increases in the plies near the exposed surface, their mechanical contribution is redistributed to the back ones.

(a) (b)

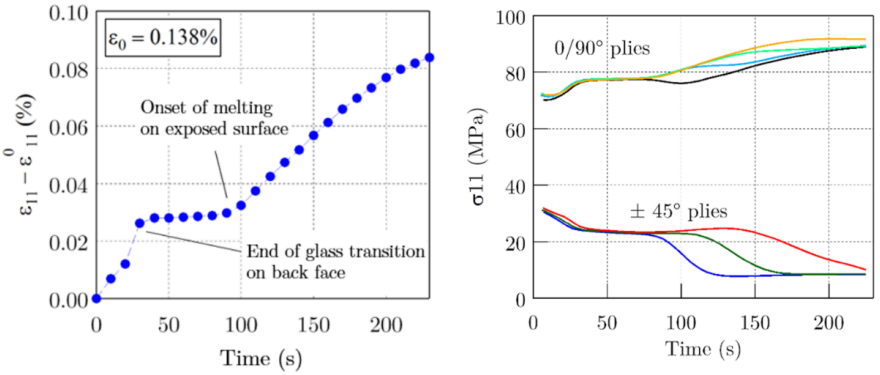

Figure 1.36. – Thermomechanical response of QI C/PPS laminates under a coupled 20kw/m^2 heat flux and a 60MPa axial tensile loading. (a) Evolution of the axial strain (after removal of the initial strain at room temperature), (b) evolution of the axial stress in the different plies (Carpier et al., 2022)

This model can then precisely investigate the influence of temperatures up to the melting of the matrix, with an insight in the stress and strain distribution within the laminates when considering the mesoscale approach. However, its temperature range is limited and does not include temperatures which would occur during an exposure to a heat flux more representative of a fire scenario. The pyrolysis of the matrix must be considered in order to account for the temperature-dependence behavior of TP-based composites.

They were implemented and proved to accurately replicate the experimental pyrolysis degree (see Fig. 1.37).

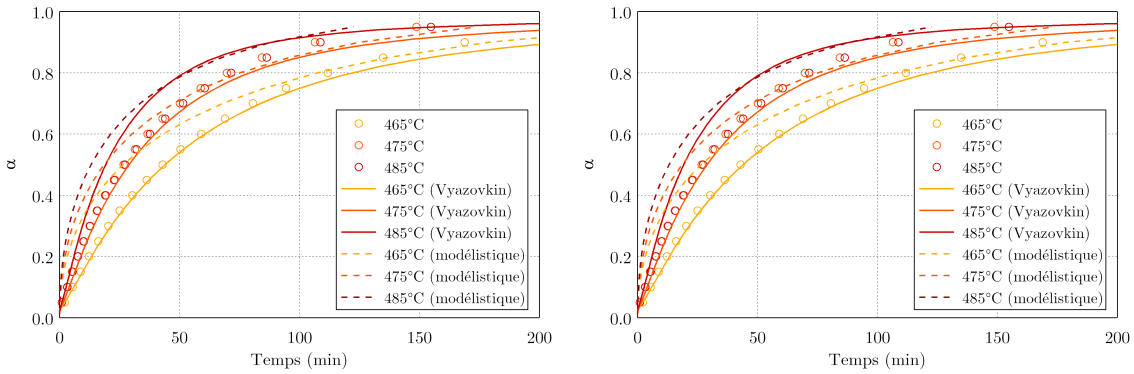

(a) (b)

Figure 1.37. – Comparison of the pyrolysis degree as obtained experimentally and numerically through the modelistic and model-free (Vyazovkin) approaches. (a) From 465°C to 485°C, (b) From 500°C to 545°C (Carpier et al., 2022)

Fig. 1.38 shows the gradient of the temperature field and the corresponding pyrolysis degree for a 50kw/m^2 heat flux during 150s.

The pyrolysis degree-based approach can characterize the advancement of the decomposition reaction, however it does not provide a modelling directly driven by by the formation of porosities and their content. Indeed, it only accounts for mass loss which does not consider the gas remaining trapped within the laminates. Furthermore, the thickness expansion due to the internal pressurization is not considered.

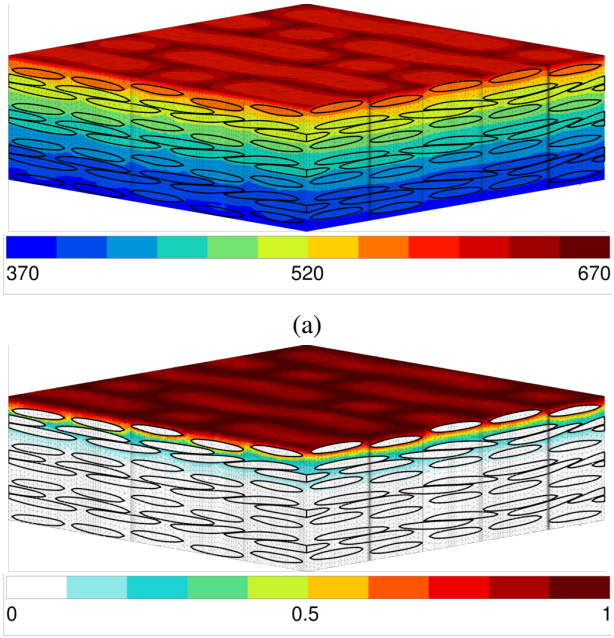

Figure 1.38. – Influence of the exposure to a 50kw/m^2 heat flux on the top surface during 150s on the thermal decomposition state of the C/PPS laminates. (a) Temperature field, (b) pyrolysis degree field (Carpier et al., 2022)

1.5. Conclusion

This literature review showed the importance of considering the thermal degradation of the matrix when exposed to high temperature conditions (phase changes, thermomechanical property degradation, porosity formation). As it has been presented, the thermomechanical behavior of TP polymers and PPS have been precisely studied for temperatures below the glass transition. However the phenomena were not well documented for temperatures representative of a fire scenario, especially in terms of the numerical modelling (temperatures above T_d = 450°C and up to 1100°C). Carpier (Carpier et al., 2022) proposed a first numerical approach reproducing the thermomechanical behavior of C/PPS QI laminates to tackle this lack of knowledge. This model can be used for temperatures up to the onset of the thermal decomposition by considering a linear elastic mechanical behavior for the matrix. Several research areas can be proposed to extend the predictive capabilities of this model.
At temperatures lower than the matrix melting, it was shown that the viscous behavior of the matrix has a large contribution to the mechanical response. A viscous model could hence be included in the model. In order to account for the behavior at higher temperatures, several improvements should be performed first experimentally and then numerically based on the experimental data:

— Identify the thermomechanical properties of the constituents temperatures above the on-

set of polymer decomposition (450°C) where the polymer undergoes a third transformation (after glass transition and melting), inducing large variations in its thermomechanical properties.

— Experimentally characterize the thermal decomposition phenomena and the porosity formation mechanisms.

— Quantify the porosity formation kinetics and propose a numerical adaptation of the process

The obtained model could then perform coupled thermomechanical simulations for higher heat fluxes and simulate the behavior of TP-based laminates subjected to fire conditions.

CHAPTER 2

EXPERIMENTAL ANALYSIS AND MODELLING OF THE THERMOMECHANICAL PROPERTY DEGRADATION

Contents

As it as been depicted in the literature review, the thermomechanical response of CFRP laminates at high temperature is usually limited to temperatures below T_d (including (Carpier, 2018). At higher temperatures, the laminates' behavior is strongly altered due to the matrix decomposition leading to porosity formation (and char production although not investigated during this study). These porosities induce large thermomechanical property gradients within the laminates. In order to predict the behavior of composite laminates subjected to a heat flux or a flame, it was necessary in a first time to conduct tests to estimate the influence of temperature on the various thermomechanical properties of the C/PPS constituents. It is indeed a prerequisite to the building of a numerical model faithfully representing the response of the laminates. It is to be reminded that the scope of this numerical study is focused on QI laminates. As a first step, this chapter focuses on the determination of the degradation of the thermomechanical properties for temperatures starting below the onset of the thermal decomposition of the matrix. Although the ultimate purpose is to include in the modelling the thermal and mechanical consequences of polymer pyrolysis, lower temperature considerations are necessary to accurately simulate the early stage of fire exposure.

2.1. Presentation of the model

2.1.1. Structural modelling

The large discrepancies between the matrix and the fiber bundles in terms of thermomechanical behavior, combined with the objective to address problems in the presence of severe thermal gradient, has led to consider a mesoscopic scale based on the previous work of Carpier et al. (Carpier et al., 2022). A three-dimensional mesoscopic numerical model of QI laminates was hence created using the software TexGen (Sherburn, 2007) which represents explicitly matrix and fiber bundles whose geometrical characteristics are presented in Table 2.1. The model volume was limited to a quarter of a representative volume element (RVE) (for computation time considerations) which represents a $3.7 \times 3.7 \times \times 2.2\text{mm}^3$ domain and its geometry is presented on Fig. 2.1. The chosen representative volume was selected as to reproduce the volumetric distribution of fiber and matrix (50% each). The volume was also meshed using TexGen and a discretization was performed with the same parameters as the ones used by Carpier since it was found sufficient for a convergence of the thermomechanical response. The consequence of mesh refinement on the thermal decomposition will be further discussed in Section 3.3.2

Geometry	Dimension (mm)
Length/width	3.7
Ply thickness	0.312
Fiber bundle width	1.31
Fiber bundle thickness	0.162
Fiber bundle spacing	1.46

Meshing parameters	QI
Elements	C3D4
Number of nodes	133 990
Number of elements	754 080

TABLE 2.1. – Geometrical and meshing characteristics of the numerical models of the QI laminates

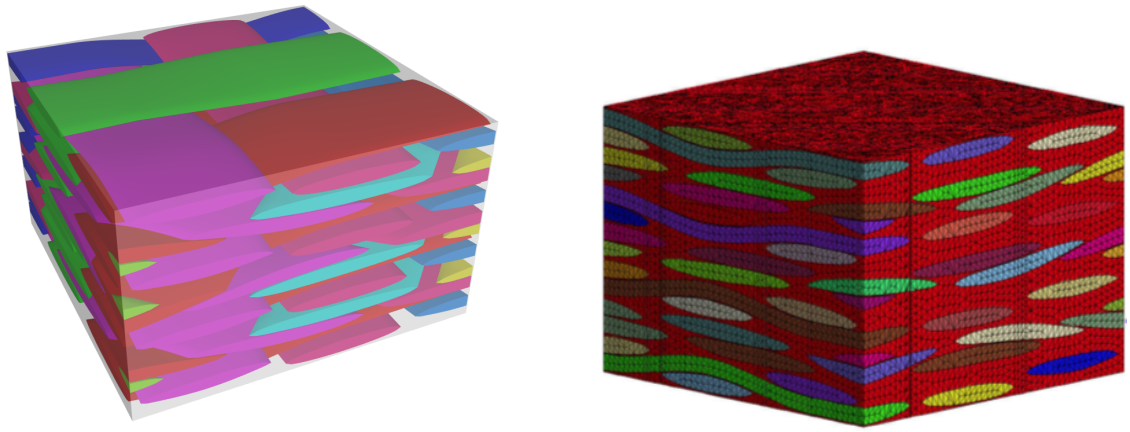

(a) QI geometry (b) QI mesh

Figure 2.1. – Geometry and mesh of the 1/4 RVE QI numerical model. Colors represent different fiber bundles

2.1.2. Thermal transfer modelling

The various thermal transfers considered for the modelling of the thermal response to a heat flux applied on one surface of the laminates are summarized in Fig. 2.2:

— The heat flux applied on one surface is equal to the emitted heat flux times the absorptivity
— Planar and through-the-thickness conduction
— Convection and radiation on the opposed surface
— Only radiation on the exposed surface as the heat flux is an imposed condition
— Adiabatic behavior on the sides as the model sample is considered to be embedded within a much larger laminate.

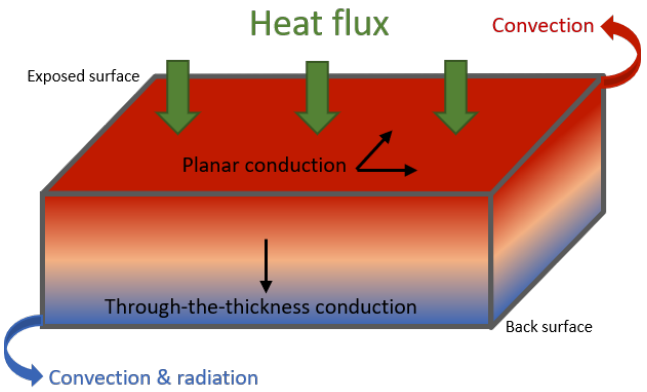

Figure 2.2. – Schematics of the modelled thermal transfers to reproduce the thermal response of a laminate to a heat flux applied on its upper surface

The thermal radiation is modelled by a Stefan-Boltzmann law in which the radiated heat flux W_r is calculated as:

$$W_r = \epsilon_{emi}\sigma\left(T^4 - T_{out}^4\right) \tag{2.1}$$

with $\sigma = 5.670x10^{-8}W.m^{-2}.K^{-4}$ the Stefan-Boltzmann constant, $\epsilon_{emi} = 0.9$ the emissivity of the laminates (as is often considered for CFRP (Pering et al., 1980)) and T_{out} the temperature of the environment.

The heat flux exchange through convection is modelled by:

$$W_{conv} = h\,(T - T_{out}) \tag{2.2}$$

with h the convection coefficient. Its evaluation is discussed in Section 2.3.3

The following work considers that the densities of both the fiber bundles and the matrix, alongside the emissivity and the convection coefficient are constant and unaltered by temperature changes.

The thermal degradation of the thermomechanical properties of PPS and C/PPS was previously investigated by Carpier (Carpier, 2018). The following sections present the obtained temperature evolutions: (i) values identified by Carpier, or (ii) new values with more accurate representativity of high temperature behavior, especially above T_m. The discussion on the thermomechanical properties of the porosities resulting from the thermal decomposition of the matrix will be further discussed in Section 3.3.4 and Section 4.2.2 as the focus of this chapter is set on the original constituents (matrix and fiber bundles).

It is important to note that the properties were identified for temperatures either up to T_m or T_d (depending on the parameters) and then kept constant due to the difficulty to accurately determine them for higher temperature levels.

2.2. Mechanical properties

2.2.1. Matrix behavior

The mechanical behavior of the matrix can be introduced with different material model according to the temperature range of the simulations, the nature of the loading the required level of accuracy:

In order to model the temperature-dependence of the mechanical behavior, one should ideally account for the viscosity of the matrix (with viscoelastic or elasto-viscoplastic models) along with working in large strain formulation. It could replicate more accurately the structural modifications of the laminates such as fiber bundle rotation. However, linear elasticity coupled with small strain formulation was chosen for this study as a first step towards a comprehensive modelling and to focus on the thermal decomposition mechanisms.

The identification of an elasto-viscoplastic model for the PPS matrix is presented in Appendix A at 120°C as a proof of concept.

Elastic behavior modelling

The characterization of the evolution of the matrix stiffness E_m over temperature is of the utmost importance as the thermal degradation will highly influence the load transfers within the laminates. This characterization was experimentally performed by Carpier (Carpier et al., 2022) and extrapolated using Mahieux phenomenological model. It reads:

$$E_m(T) = (E_g - E_{rub})exp\{-\left(\frac{T}{T_g}\right)^{m_g} + E_{rub}exp\{-\left(\frac{T}{T_m}\right)^{m_m} \tag{2.3}$$

with E_g and E_{rub} the elastic moduli at the glassy and rubbery states, and m_g and m_m the Weibull parameters. Fig. 2.3 shows the identified and extrapolated evolution of E_m as a function of temperature.

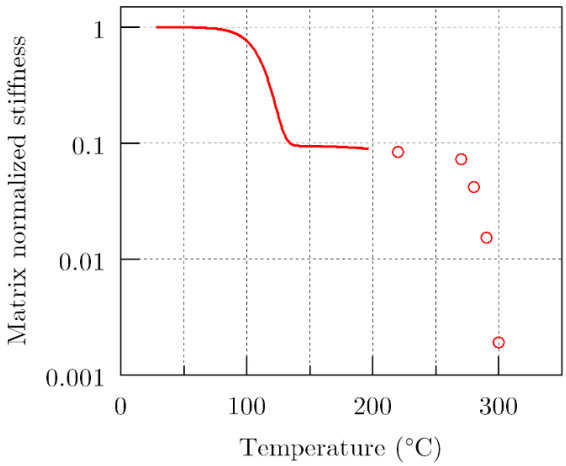

Figure 2.3. – Evolution of the polymer matrix Young modulus according to temperature in the range $[T_0, 300°C]$. The continuous line refers to both DMA results and Mahieux model. Dots represent predictions from the Mahieux model in the range of unavailable DMA results (Carpier, 2018)

For temperatures higher than T_m, the liquid was modelled as a solid material with an extremely low stiffness of 1MPa.

2.2.2. Yarn behavior

The Chamis model provides an efficient mean to describe the effective isotropic transverse elasticity of a fiber bundle (Chamis, 1989). This approach is based on the hypothesis that each bundle of the composite material can have its mechanical behavior approximated to the one of a uni-directional ply which contains the same matrix volume ratio (in the present case $\eta_m = 17\%$). Both the fibers and the matrix are considered as linear elastic. Following this assumption, the transverse orthotropic mechanical properties of the bundles are as follows (where L stands for longitudinal properties and T for transverse ones):

$$E_y^L = E_f^L V_f + E_m V_m \tag{2.4}$$

$$E_y^T = \frac{E_m}{1 - \sqrt{V_f}\left(1 - \frac{E_m}{E_f^T}\right)} \tag{2.5}$$

$$G_y^{LT} = \frac{G_m}{1 - \sqrt{V_f}\left(1 - \frac{G_m}{G_f^{LT}}\right)} \tag{2.6}$$

$$G_y^{TL} = \frac{G_m}{1 - \sqrt{V_f}\left(1 - \frac{G_m}{G_f^{TL}}\right)} \tag{2.7}$$

$$\nu_y^{LT} = \nu_f^{LT} V_f + \nu_m V_m \tag{2.8}$$

$$\nu_y^{TL} = \frac{E_T}{2G_t^{TL}} - 1 \tag{2.9}$$

The constituent properties as well as the resulting parameters for the fiber bundles is presented in Table 2.2 for room temperature.

Parameter	Matrix value
E_m (GPa)	2.6
G_m (GPa)	1.0
ν_m	0.36

Parameter	Fiber value	Yarn value
E^L (GPa)	231.0	192.2
E^T (GPa)	28.0	15.0
G^{LT} (GPa)	24.0	7.9
G^{TL} (GPa)	10.7	5.7
ν^{LT}	0.26	0.28
ν^{TL}	0.30	0.30

TABLE 2.2. – Linear elasticity parameters of the constituents at room temperature, as used in the Chamis model (Chamis, 1989)

2.2.3. Chamis model verification

As the Chamis model relies on specific hypotheses (notably the equivalence of a fiber bundle effective behavior to that of a ply with unidirectional fibers), one may question the accuracy of the approach, especially when the temperature increases and the matrix becomes degraded. It was chosen to compare its accuracy on the predicted fiber bundle mechanical properties to the ones obtained with a full field approach. To do so, a fiber bundle was reproduced by explicitly representing 7μm-wide fibers and matrix in a square 3D extruded domain. An example of the created geometry in 2D is shown in Fig 2.4 with the following features:

— The fiber shape:
  — Circular: The circular shape is presented in Fig. 2.4a. It is representative of an ideal fiber. However such an approach only allows a theoretical fiber density up to $\frac{\pi}{4}$ =

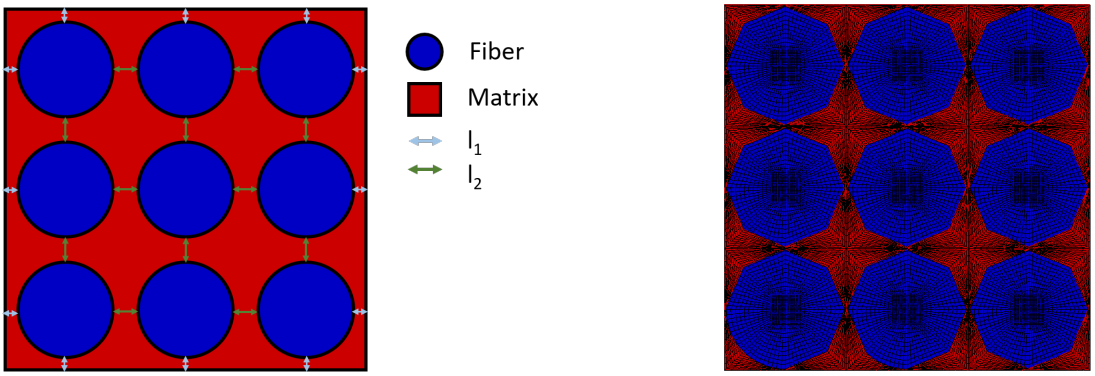

(a) Circular shape geometry

(b) Circular shape mesh

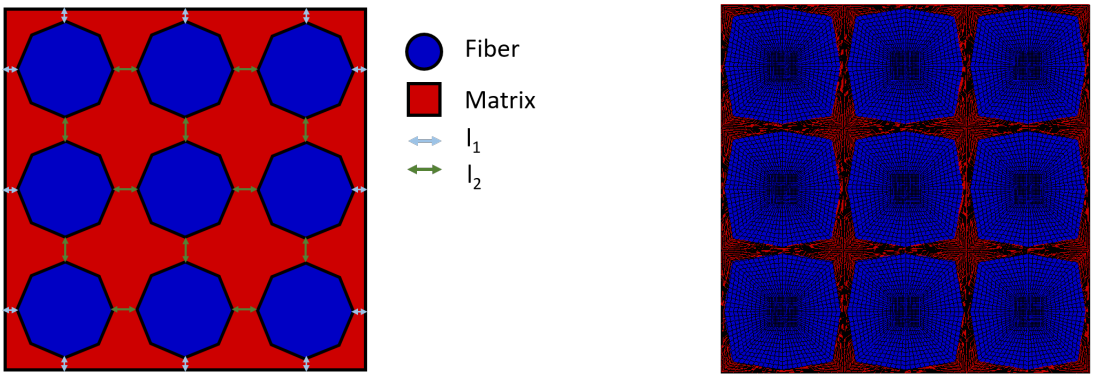

(c) Octagonal shape geometry

(d) Octagonal shape mesh

Figure 2.4. – Two-dimensional view of fiber bundle modelling geometry examples representing 3x3 fibers with the corresponding meshes

78.5%. It is even less in numerical modelling as two fibers cannot be directly in contact for meshing purposes (it lowers the maximum fraction to around 75%). It is therefore not possible to reproduce the 83% fiber volume fraction of the actual fiber bundles. This difference can be explained by the fact that fibers are not perfectly circular and ordered within the fiber bundles.

— Octagonal: The octagonal shape is presented on Fig. 2.4c Its main advantage is to allow for higher fiber densities, although not being fully representative of the fiber structure.

— The number of fibers

— The distance between the fibers l_2 and to the edges l_1, which cannot be too low as requirement of the Finite Element meshing. These two values determine the fiber density. The two meshes presented were created with:

$$\begin{aligned} l_2 = 2l_1 = &\quad 0.2\mu\text{m for the circular shape, giving a fiber density of 72.3\%} \\ l_2 = 2l_1 = &\quad 0.4\mu\text{m for the octagonal shape, giving a fiber density of 76.7\%} \end{aligned} \tag{2.10}$$

The influence of these parameters is discussed thereafter.

Number of fibers In order to limit the calculation times, it is necessary to use as few fibers in the model as possible, while still remaining precise enough. In Fig. 2.5, we first check that the conditions of periodicity are well respected in the full-field modelling: considering a single cell of the periodic medium (a square with a single central fiber) leads to the same results as in a domain with 3x3 elementary cells. The axial stress and strain presented in Fig. 2.5 correspond to the axial stress and strain averaged over the domain of simulation. The tension is exerted in the direction perpendicular to the plane of Fig. 2.4. The matrix is assigned an isotropic linear elasticity and the fibers are assigned an isotropic transverse elasticity described by the moduli listed in Table 2.2.
Thus, one may conclude that a single fiber embedded within the matrix is enough to reach convergence for the full field model. This single fiber approach was then used in the sequel of the study.

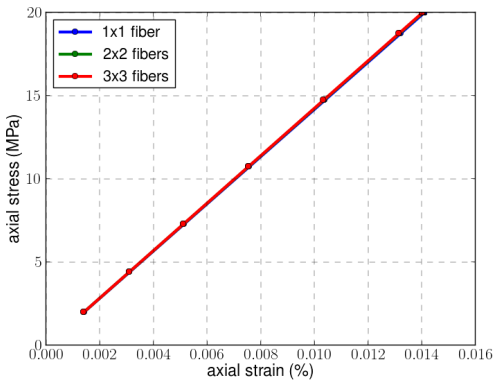

Figure 2.5. – Influence of the number of fibers considered for an explicit representation of a fiber bundle on the mechanical response

Fiber volume fraction As the circular fiber volume fraction is limited to about 75%, it was necessary to verify whether considering a lower density than the actual 83% would affect the results or not.
The influence of the fiber volume fraction on the accuracy of Chamis model was assessed using the octagonal geometry and varying l_1 and l_2 (see Fig. 2.6). Tensile loading simulations showed very little differences in the axial stiffness, confirming that it was possible to assess Chamis model accuracy using the circular shapes.

Chamis model accuracy assessment The two main loading directions of the simulated laminates are axial (for the $0/90°$ plies) and shear (for the $\pm 45°$ plies). Shear loading was modelled by applying to the upper surface in Fig. 2.4 a tension in transverse direction of the

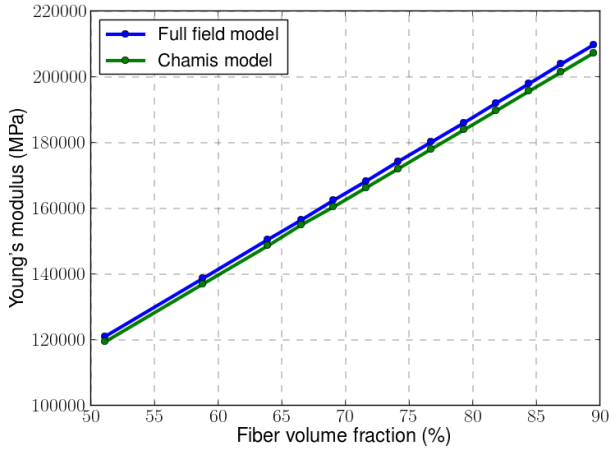

Figure 2.6. – Influence of the fiber volume fraction within a fiber bundle on Chamis model accuracy

fiber. Chamis model was validated for these two loading cases as it shown in Fig. 2.8 which show small differences with the full-field simulations (around 4% for the axial stiffness and 10% for the transverse one).

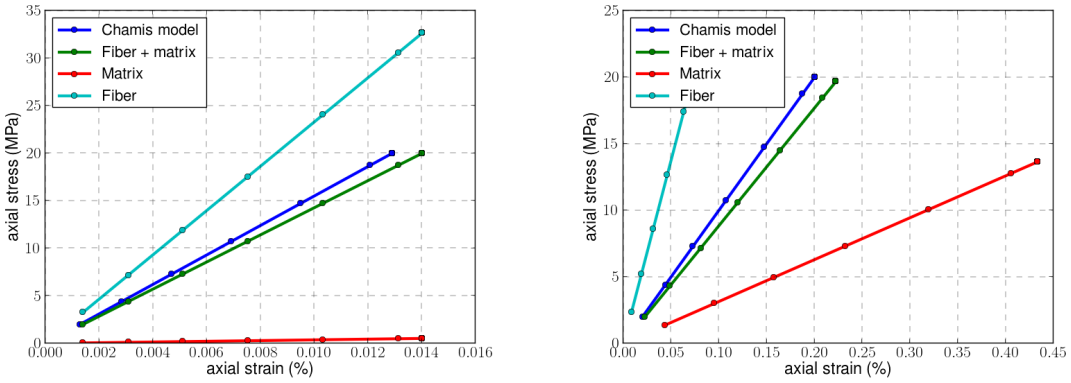

(a) Axial loading

(b) Shear loading

Figure 2.8. – Comparison of axial the stress/strain obtained from full-field model and Chamis model at room temperature

2.3. Thermal properties

In order to perform simulations introducing a heterogeneous temperature through the thickness resulting from a heat flux (see Fig. 2.2), one must properly characterize the thermal proper-

ties and their temperature dependences to accurately predict the evolution of the thermal gradient in the laminates. These properties concern four different characteristics, namely the thermal expansion, the thermal heat capacity, the thermal conductivity and the thermal convection. They are highly dependent on the nature of the constituent (matrix, fiber or fiber bundle).

The thermal transfers were modelled by the heat equation for each constituent. Due to the anisotropy of the fiber bundles, the equation is expressed in two different ways:

— For the matrix:

$$\rho_m(T)\, c_{p_m}(T) \frac{\partial T}{\partial t} = \lambda_m(T) \nabla^2 T \tag{2.11}$$

— For the fiber bundles:

$$\rho_{fb}(T)\, c_{p_{fb}}(T) \frac{\partial T}{\partial t} = \nabla \left(\underline{\underline{\lambda_{fb}}}(T) \nabla T \right) \tag{2.12}$$

with $\underline{\underline{\lambda_{fb}}}$ the thermal conductivity tensor expressed in the local coordinate system as:

$$\underline{\underline{\lambda_{fb}}} = \begin{bmatrix} \lambda_y^{ax} & 0 & 0 \\ 0 & \lambda_y^{r} & 0 \\ 0 & 0 & \lambda_y^{r} \end{bmatrix} \tag{2.13}$$

The list of the properties and the involved parameters is summarized in Table 2.3 with the indexes m for matrix, fb for fiber bundle , ax for axial and r for radial in the local coordinate system of the yarn. Each of these parameters evolves differently with temperature.

	Property	Matrix coefficient	Yarn coefficient
Material properties	Thermal expansion	$\alpha_{th,m}$	$\alpha^{ax}_{th,fb}$, $\alpha^{r}_{th,fb}$
	Thermal heat capacity	c_{p_m}	$c_{p^{ax}_{fb}}$, $c^{r}_{p_{fb}}$
	Thermal conductivity	λ_m	λ^{ax}_{fb}, λ^{r}_{fb}
Interface property	Thermal convection	h	

TABLE 2.3. – List of the model thermal properties and the associated coefficients

These parameters and their temperature-evolutions have been determined by Carpier (Carpier et al., 2022) for the range $[T_0, T_m]$, however additional tests were performed for a better representation of the physical meaning (with the exception of the thermal conductivity which remained similar to what was previously obtained, see Section 2.3.4):

— The assumption of a constant thermal expansion coefficient with temperature has been questioned in Section 2.3.1 using dilatometry tests.

— The temperature limit on the thermal heat capacity has been extended above the melting point using a coupled DSC-TGA method in Section 2.3.2.

— The estimation of the thermal convection coefficient has been reviewed in Section 2.3.4.

The following Sections 2.3.1 to 2.3.4 tackle the methods carried out to obtain the parameters. Each experimental method has a temperature limit to ensure the validity of the measurements.

The properties were kept constants and equal to the last measured value for temperatures higher than the limit. The heating phase of the sample is usually conducted under air. Three different atmospheres were considered during the tests:

— Air: The air atmosphere is the most representative atmosphere when the sample is exposed to a heat source. An exception may be found in the contact surface of the flame in the fire scenario as the gazes resulting from the kerosene combustion and the thermal decomposition of the laminates could highly alter the composition of the atmosphere locally. This exception can however be supposed negligible as the purpose of this study was not to investigate the fluid-dynamics interactions at the boundaries.

— N_2: Nitrogen is an inert gas. The thermal degradation and decomposition process can then be studied without the influence of oxidization.
— Vacuum: The vacuum atmosphere is also inert one, which allows to verify the conclusions obtained from the previous ones.

2.3.1. Thermal expansion

Dilatometry tests were performed by the UCCS Laboratory in Lille, using a Netzsch DIL 402 dilatometer from room temperature up to 250°C for pure PPS testing, and up to 450°C for C/PPS laminates with a heating rate of 5K.min^{-1}. The maximum temperature was set at the onset of the thermal decomposition as the porosity formation process would disrupt the measurements. As the thermal expansion of the fiber bundles is constant over the considered temperature range (as described in Section 1.2.3), the focus was set on the PPS matrix. Three PPS samples were used under air and N_2 atmospheres and one under vacuum. In order to estimate if the laminate expansion is in agreement with the results obtained on the matrix, three additional C/PPS QI laminates samples were dilated under nitrogen. The resulting evolution of the thermal expansion with temperature for these three configurations for PPS is presented in Fig. 2.9 with a 95% confidence interval.

Overall, the results show that the assumption of a constant value is not correct, especially for temperatures above the glass transition. Indeed, in all three configurations the thermal expansion coefficient follows a similar trend:

— An almost steady coefficient for temperatures up to the onset of the glass transition at a value in the order of magnitude of the previous value set at $52.2\ 10-6\text{K}^{-1}$
— A sudden drop during the glass transition which remains inconclusive due to the complexity of the physico-chemical phenomena taking place. The glass transition occurs at temperatures close to the expected 90°C
— A major increase afterwards up to 130 to 150°C, which can originate from the structural alteration of the amorphous phase leading to an increase in the mobility of the molecular chains
— A progressive stabilization at a value between $300\ 10-6$ and $500\ 10-6\text{K}^{-1}$ which is 6 to 10 times higher than the previous assumption. The stabilization is followed by a lowering tendency as the temperature approaches T_m.

However, despite the similar trends, differences can be observed between the configurations. First of all, contrary to air, a major disparity resulted from the three samples exposed to nitrogen,

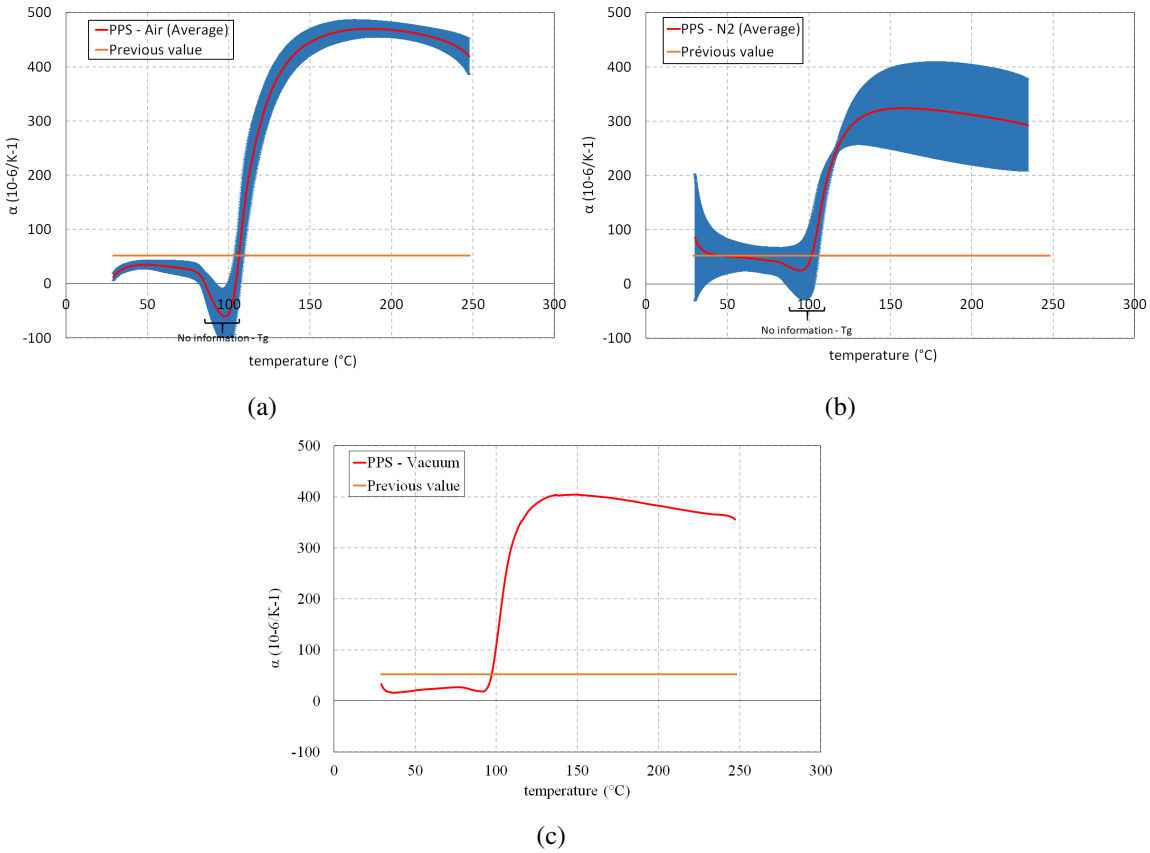

Figure 2.9. – Evolution of the thermal expansion of the PPS matrix with temperature (average and 95% confidence interval) under: (a) air, (b) N_2 and (c) vacuum

making definite conclusions not fully reliable. Furthermore, extra two samples were tested but resulted in inconsistent data while the error source was not identified.
The drastic evolution both during the glass transition and for higher temperatures still seems to be limited in the absence of oxygen. The oxidization might therefore increase the thermally-induced expansion. The vacuum curve is included within the error range of the nitrogen one, which could confirm the importance of oxidization.

Results on the C/PPS laminates show a smoothed, softened behavior up to T_m compared to the plain PPS polymer ones (see Fig. 2.10). The decrease at the glass transition is much less significant, while the following increase is almost linear up until T_m. Fiber bundles then inhibits the expansion of the material as the value at 250°C barely exceeds 100 $10-6\mathrm{K}^{-1}$. The coefficient then drastically increases as the matrix is gradually transformed into liquid before slightly decreasing at the approach of T_d.

The values under air were used as an input for $\alpha_{th,m}$. The coefficients $\alpha^{r}_{th,fb}$ and $\alpha^{ax}_{th,fb}$ were

evaluated from a mixture law:

$$\alpha_{th,fb}^{r,ax} = \alpha_{th,m} V_m + \alpha_{th,f}^{r,ax}(1 - V_m) \tag{2.14}$$

where the fiber thermal expansion coefficients $\alpha_{th,f}^{r}$ and $\alpha_{th,f}^{ax}$ were extracted from $fig : alpha_carbon_fibers$

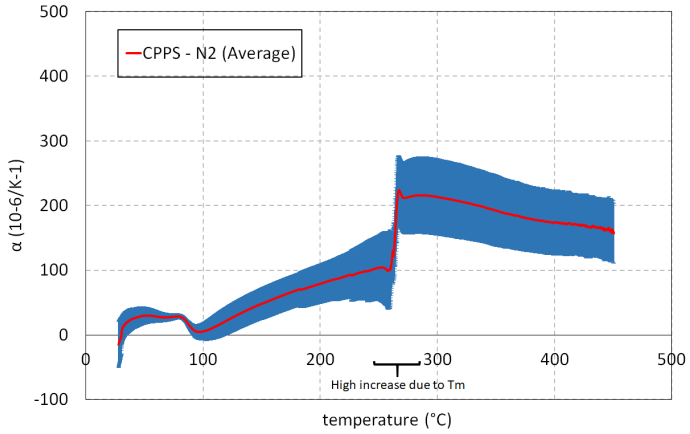

Figure 2.10. – Evolution of the thermal expansion of the C/PPS QI laminates over temperature in an air based atmosphere (average and 95% confidence bands)

2.3.2. Thermal heat capacity

A coupled DSC-TGA at a heating rate of 10K/min (see Section 1.1.1 for the method) was used to assess the thermal heat capacity of the matrix and the laminates undair air and nitrogen atmospheres for temperatures up to 500°C. Preliminary calibration tests showed a good repeatability of the results, hence only one sample was used in each configuration. The apparent constant and almost linear increase is disrupted at about T_m due to the melting of the matrix (see fig. 2.11). It is worth noting that the curves represent the combination of both the specific heat and the melting latent heat. The estimated melting latent heats h_m are presented in Table 2.4. The bi-linear shaped thermal capacities appear higher in presence of oxidization as the oxide layer may act as a thermal insulator. This coupled mechanism is applicable for temperatures up to 500°C.

Configuration	$h_m\,(J/g)$
PPS - air atmosphere	36
PPS - N_2 atmosphere	49
C/PPS - air atmosphere	12
C/PPS - N_2 atmosphere	19

TABLE 2.4. – Melting latent heats obtained with coupled DSC-TGA for PPS matrix and C/PPS laminates under air / N_2

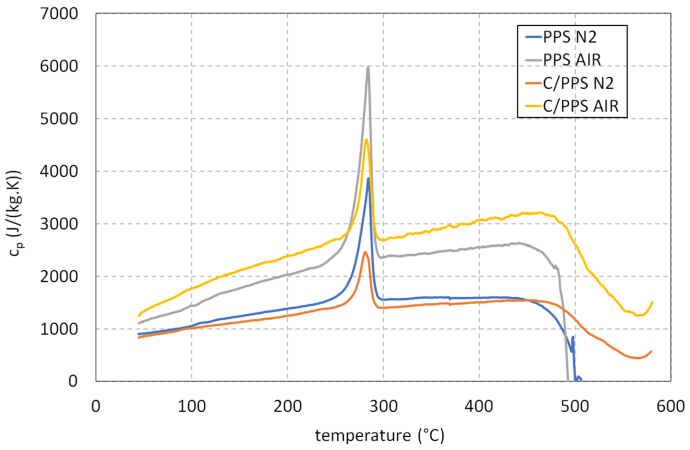

Figure 2.11. – Temperature-dependence of the thermal heat capacity of the PPS matrix and C/PPS QI laminates under air / N_2 at 10K/min

Knowing the densities of the matrix and the fiber bundles and the equi-volumetric distribution of matrix and fiber bundles, the thermal heat capacity of a fiber bundle can be approximated by means of a linear mixture rule:

$$c_{p,fb}(T) = \frac{\rho_m + \rho_{fb}}{\rho_{fb}} \left(c_{p,cl}(T) - \frac{\rho_m}{\rho_m + \rho_{fb}} c_{p,m}(T) \right) \tag{2.15}$$

The corresponding curve is presented on Fig. 2.12.

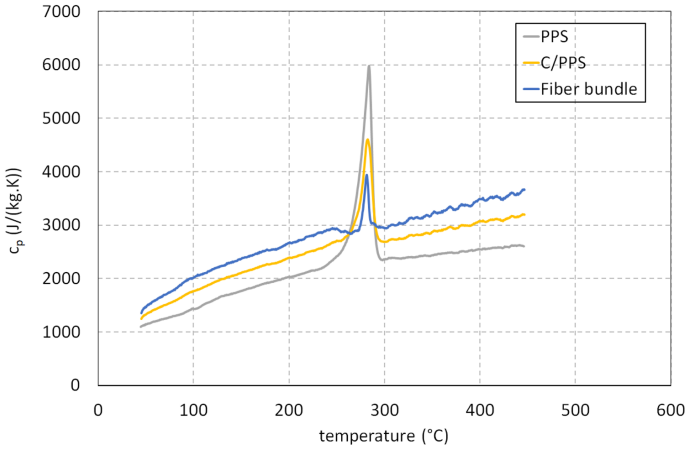

Figure 2.12. – Temperature-dependence of the thermal heat capacity of the PPS matrix, the C/PPS QI laminates and the calculated-fiber bundles under air (Eq. 2.15)

It was chosen not to directly reproduce the phase transformation, but rather to artificially include the melting latent heat within the specific heat. The temperature-evolution of the specific heat was fitted as linear before and after melting, and the raw experimental data was kept for the

phase transition (see Fig. 2.13a and 2.13b).

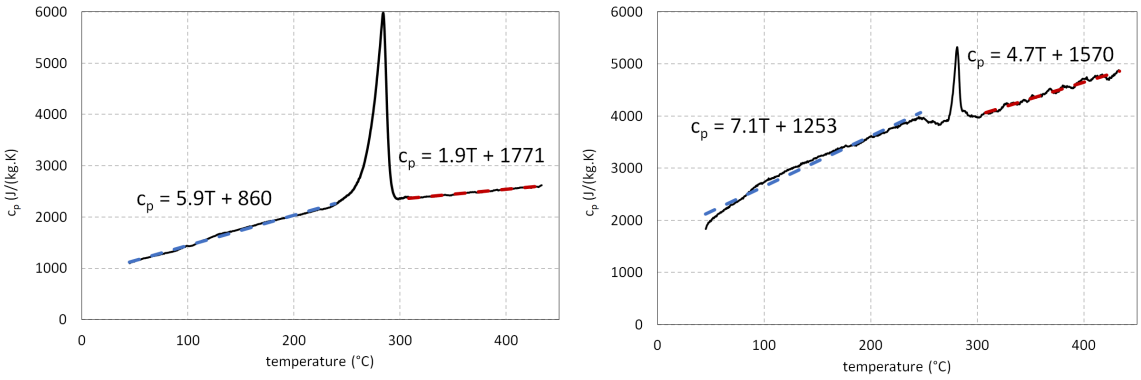

(a) (b)

Figure 2.13. – Modelling of the temperature-dependence of the thermal heat capacity under air with a bilinear approximation and the corresponding coefficients (a) of the PPS matrix, (b) of the fiber bundles

It is to be noted that the specific heat increase rate is of $5.9\text{J.kg}^{-1}.\text{K}^{-2}$, which is much higher than the value discussed in Section 1.3.1. The difference may stem from the accuracy provided by coupling DSC and TGA tests.

2.3.3. Thermal convection

The tthermal convection coefficient h at the opposed surface was chosen considering four successive steps:

— (Carpier et al., 2022) obtained $h = 2\text{W.m}^{-2}.\text{K}^{-1}$ using reverse identification on calorimeter cone experimental data, and used this value for his simulations. The opposed surface was vertical and no air extractor included.

— The theoretical calculation of the Rayleigh number associated with the calorimeter cone problem showed a laminar air flow at the opposed surface. It was followed by the determination of Nusselt number using the approach from (Ostrach, 1952) which led to an approximation of h around $8\text{W.m}^{-2}.\text{K}^{-1}$.

— When exposed to fire using small scale burners, the opposed surface is horizontal and oriented upwards. Without air extractor influence, literature values usually range from $5\text{W.m}^{-2}.\text{K}^{-1}$ to $12\text{W.m}^{-2}.\text{K}^{-1}$ in works such as (Cain and Lattimer, 2009) and (Biasi, 2014).

— When working with an air extractor (as is the case of the burner in this study), a small airflow impacts the laminates on the opposed surface. Hence the convection coefficient must be increased to account for this forced convection. h is often approximated using the equation (The Engineering ToolBox, 2003):

$$h = 10.45 - v + 10\sqrt{v} \tag{2.16}$$

with v the relative speed between the opposed surface and air. Considering a small air flow of the order of 1m.s^{-1}, one obtains $h = 20\text{W.m}^{-2}\text{.K}^{-1}$ which is the value considered during this study.

2.3.4. Thermal conductivity

Finally, the thermal conductivity of the constituents was kept identical to the ones identified by Carpier (Carpier et al., 2022) for $T \in [T_0, T_d]$. It is based on the assumption that:

— The axial conductivity of the fiber bundles was estimated by a mixture law as discussed in Section 1.3.1. λ_{fb}^{ax} varies linearly as a function of temperature from 86W/m/K to 133 W/m/K at $T = T_d$.

— The matrix conductivity and the radial conductivity of the fiber bundles follow trilinear curves with a change in the linear coefficient during the glass transition and melting of the matrix. The changes with temperature are presented in Fig. 2.14.

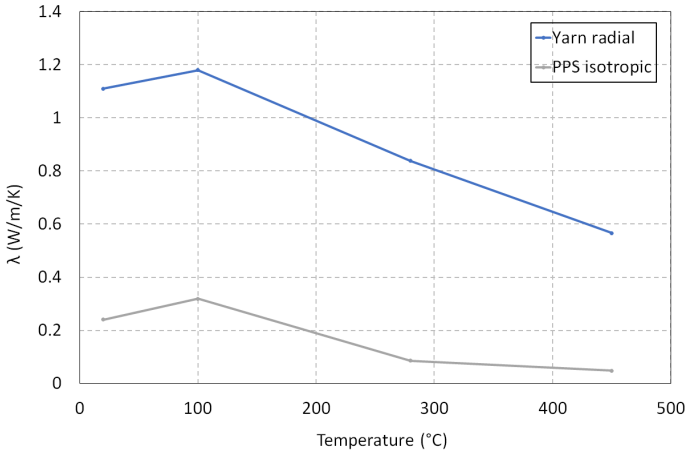

Figure 2.14. – Evolution of the PPS matrix and radial carbon fiber bundle thermal conductivity with temperature

2.4. Conclusion

The objective of this chapter was to estimate the influence of temperature on the thermal degradation of the thermomechanical behavior of the constituents of C/PPS laminates. It was shown that the matrix has a significant viscous response which is exacerbated as the temperature increases. Firstly, an elasto-viscoplasticity model was developed based on creep tests at 120°C which accurately reproduces the strain evolution with time. It was however chosen to model the behavior of both matrix and fiber bundles with linear elasticity, as described in (Carpier et al., 2022). Indeed, the main mechanical behavior investigated in this study is the stiffness which significantly decreases within the temperature range upwards of T_d.
Secondly, the various thermal properties required by the modelling (convection, conduction,

thermal heat capacity, thermal expansion, radiation exchanges) have been identified by Carpier. These values were used if the temperature range and accuracy were acceptable or else they were updated with more adequate methods. These values were kept constant for temperatures higher than the maximum at which they were identified.

CHAPTER 3

MODELLING OF THE THERMAL DECOMPOSITION OF THE MATRIX: CASE OF QI LAMINATES

Contents

The thermomechanical characterization performed by (Carpier, 2018) and the new measurements carried during this study have been described in Section 1.4.4 and in the previous Chapter. It lead to the validation of a thermomechanical model for temperatures ranging from room temeprature up to T_d. In order to extend the model temperature range, this chapter describes the meso-structure changes in the laminates along with the thermal decomposition process of the polymer matrix. Such an explicit decomposition representation is a pre-requisite to any investigation into the evolution of the thermomechanical behavior under the circumstances of a fire. As temperature increases and exceeds T_d, the pyrolysis of the matrix becomes a dominant mechanism. During the process, cavities form, filled with pyrolysis gas. It can be characterized according to its kinetics, as it is discussed in Section 1.4.2.

However, these studies do not consider the influence of the presence of cavities within the structure, although they drastically alter both the structural and the thermomechanical behavior of the laminates (Carpier et al., 2020b). From a structural viewpoint, the cavities induce the presence of high-pressure gas pockets which, as they expand, introduce an increase in the volume of the macro-structure through peeling. This behaviour is even more amplified by the fact that there is less matrix to ensure the load transfer within the laminates. As a consequence on the thermomechanical properties, the behaviour of the material is dramatically altered since solid matter is replaced by gas. During fire exposure, time-dependent thermal gradients within the laminates will lead to a disparity of matrix states at the scale of a ply. Such local variations can be considered at a mesoscopic scale by means of the explicit representation of the matrix and fiber bundles arrangement previously described in Chapters 1 and 2.
This experimental and numerical study focuses on understanding the phenomena in the core of the material. Therefore, the oxidization of both char and fibers in addition to the pyrolysis decomposition observed experimentally by (Vieille et al., 2015) on the borders of the thermally exposed sample, due to direct contact with oxygen, was not investigated.

This chapter first presents an experimental study of the porosity formation along with the quantification of the pyrolysis reaction kinetics according to the porosity content within the QI laminates rather than in terms of mass loss. In order to model the porosity formation, models such as GTN which account for porosity content to describe damage in a solid material only consider the porosity content as a global variable, which is not compatible with the numerical model's ultimate usage of accounting for local thermal gradients combined with swelling. As a result, this chapter then presents an original proposal explicitly representing the porosity formation inside the matrix of the laminates mesostructure. It is performed by progressively transforming finite elements of matrix into porosities. Numerical models for nucleation and growth are presented. Finally, the swelling induced by porosity formation and by delamination are tackled.

The results of this chapter (except for Sections 3.3.5 and 3.3.3) are the subject of (Philippe et al., 2023).

3.1. Experimental characterization

3.1.1. Measurement methods

Experimental protocols were considered to comprehend the kinetics associated with the porosity formation, both at qualitative and quantitative levels:

— Qualitative analyses: Optical microscopy, X-Ray tomography
— Quantitative analyses: Geometrical measurements, mass measurements, densitometry

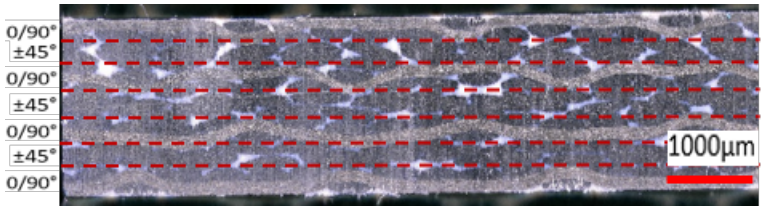

Figure 3.1. – QI C/PPS stacking sequence

The qualitative study focuses on the spatial distribution, shape and dimensions of porosities according to time of aggression while the quantitative one aims at measuring the amount of porosities within the laminates.The perfect analysis would result in a further understanding of both the explicit spatial distribution of the porosities and the amount of porosities in the laminates, which is the case of X-Ray tomography. However it was restrained to qualitative considerations. Indeed, the cost of analysis is not compatible with the current objectives of a modelling development and with the timelines of this PhD work: it requires a large amount of samples to cover the representative time and temperature ranges involved in the decomposition of the laminates.

Therefore, in order to constitute the reference set of experimental measurements necessary for a comprehensive identification, a more simple and efficient experimental protocol was applied to determine experimentally the porosity content (a volume fraction), noted $\eta_p(t, T)$.

As the composite material is subjected to thermal decomposition, the nucleated porosities induce the presence of high-pressure gas pockets which, as they expand, introduce an increase of the volume of the macro-structure through the peeling of laminates plies. The volume increase (quantitative) and porosity distribution (qualitative) were studied by the experimental means described thereafter. Stationary and isothermal conditions were considered: samples are deposited in a muffle furnace (Nabertherm, inside volume inertia of $29 \times 30 \times 18\text{cm}^3$) at a stabilized temperature T; given the thermal inertia of the furnace (temperature back to the setpoint in less than 10 seconds) and the small dimensions of the samples, the time of heating of the sample is considered negligible compared to the characteristic times of the decomposition analyses ($\sim$ 1min) and the sample can reasonably be assumed to reach the target temperature instantaneously and uniformally. Each measurement was repeated three times on three different samples giving a

reference value of the porosity content at time t and temperature T, noted $\eta_p^{ref}(t,T)$, as well as its variance. The protocol is detailed in Section 3.1.2.

Five different experimental techniques were employed: (i) mass loss (ii) densitometry (iii) geometry (iv) optical microscopy observation (v) X-Ray tomography. They can be divided into two categories: on the one hand (i), (ii) and (ii) rely on measurements of samples before and after they were subjected to thermal aggression. This allows the porosity content to be calculated as the ratio of porosity volume over the final volume after swelling. On the other hand, (iv) and (v) rely on post-mortem observations in which the porosities are directly detected by visual means. All five experimental methods are detailed below.

Mass loss

This technique is solely based on mass measurements. The mass of the sample is measured before and after thermal exposure. Let us note (i) $m_{\#}^{\star}$ the mass of the considered material # (either fiber, matrix or composite laminates) at the state defined by $\star$ (either initial or decomposed), (ii) η_m^{ini} and η_f^{ini} the volume fractions of matrix and fibers within the laminates at the initial state, and (iii) ρ_m and ρ_f the densities of the matrix and the fibers. The porosity content can be expressed as:

$$\eta_p = \left(1 - \frac{m_{cl}^d}{m_{cl}^{ini}}\right)\left(\frac{m_m^{ini} - m_m^d}{\rho_m} + \frac{m_f^{ini} - m_f^d}{\rho_f}\right)\frac{\eta_m\rho_m + \eta_f\rho_f}{m_{cl}^{ini} - m_{cl}^d} \tag{3.1}$$

In the present case, since $\eta_m = \eta_f = 0.5$, and by considering that the mass loss only comes from the matrix, Eq.3.1 can be simplified into:

$$\eta_p = \frac{\left(1 - \frac{m_{cl}^d}{m_{cl}^{ini}}\right)\left(\rho_m + \rho_f\right)}{2\rho_m} \tag{3.2}$$

Its main drawback is that it does not provide any information on the swelling of the laminates.

Densitometry

This technique uses a densitometric scale. It consists in measuring the weight of a sample in the air then in water and then in applying Archimedes formulas in order to determine the density. With m_{cl}^a the mass of the composite laminates in the air, m_{cl}^w the mass in water and ρ_a, ρ_w the density of respectively air and water, the density of the sample is

$$\rho_{cl}^d = \frac{m_{cl}^a}{m_{cl}^a - m_{cl}^w}\left(\rho_w - \rho_a\right) + \rho_a \tag{3.3}$$

The density of the sample is calculated before and after thermal exposure. Knowing both its density and its mass, its volume can be determined and the volume difference originates from the porosity formation. The results are however strongly influenced by edge effects as the edges become thicker than the center. Indeed, after a 5 minute exposure at 530°C, the thickness

increase is mainly located within five millimetres from the edges and up to 30% higher. The density is therefore lower on these parts of the sample and it can reduce the laminates density down to a value lower than 1. In this case, the density formula from Eq. 3.3 is then altered and given by 3.4.

$$\rho_{cl}^{d} = \frac{m_{cl}^{a}\rho_{w}}{m_{cl}^{a} - m_{cl}^{w}} \tag{3.4}$$

Noting ρ_{cl}^{ini} and ρ_{cl}^{d} the initial and final densities of the sample, the porosity content finally reads:

$$\eta_{p} = \frac{m_{cl}^{d}/\rho_{cl}^{d} - m_{cl}^{ini}/\rho_{cl}^{ini}}{m_{f}^{ini}/\rho_{f}} \tag{3.5}$$

Geometry

This technique is based on the measurement of the initial (V_{cl}^{ini}) and final volumes (V_{cl}^{d}) of the samples. The porosity volume is finally obtained by adding the contributions of both the closed and open porosities (see Section 3.2.1 for the open/closed distinction). The contribution of the former is the volume difference between pristine and post-exposure states. This accounts for the swelling of the material. The contribution of the latter is the mass lost during the process as the pyrolysis gas escape. Ultimately, the porosity content reads

$$\eta_{p} = \frac{V_{cl}^{d} - V_{cl}^{ini}}{V_{cl}^{d}} + \frac{m_{cl}^{ini} - m_{cl}^{d}}{\rho_{m} V_{cl}^{d}} \tag{3.6}$$

Edges effects (increase in thickness on the borders) may affect the measurements, similarly to densitometry. However they were avoided by measuring the dimensions at the center of the sample.

Optical microscopy

This technique relies on destructive observations. Once the sample has been thermally decomposed, it is cut into 3mm-height slices. These profiles are then observed and captured using a 3D numerical microscope (KEYENCE VHX-500). Images are finally numerically treated in order to compute the porosity surface fraction. This method highly depends on both the localisation of the cut and the segmentation threshold chosen by the user. Furthermore, the black/white threshold presents some subjectivity as it is set by the user to detect the porosities where they are likely to appear.

X-Ray tomography

This technique uses 3D reconstruction (softwares 3D slicer or Avizo ®) of tomography slices (EasyTom 150, 9.5μm, 150kV) to isolate and dissociate the porosities within the material. As for the optical microscopy method, a segmentation threshold is used, with the same drawback.

But since the whole volume is considered, the disparity between measurements is reduced.
After comparison of these techniques, it was chosen to quantify $\eta_p(t,T)$ using the geometry based method for the case of homogeneous thermal exposure. X-Ray tomography and optical microscopy were however used to analyze the porosity formation process from a qualitative standpoint. It is to be noted that the technique based on geometrical measurements is relevant only for scenarii of homogeneous temperature. In the case of decomposition gradients, tomography and microscopy have to be used in a quantitative way, with a special attention to the representativity of the results in terms of edge effects as well as 2D projection in the microscopy method.

3.1.2. Experimental analysis protocol

Throughout the experimental analyses, the following protocol was applied:
— Preparation of $25 \times 25 \times 2.2\text{mm}^3$ samples (water cutting, cleaning, drying)
— Initial measurements (geometry, mass measured three times and averaged)
— Exposure in the muffle furnace at the setpoint temperature
— Removal of the sample after a given exposure time
— Post-mortem measurements at the center of the samples to prevent edge effect influence
— Use of three samples for each (time,temperature) set

Temperatures and times of exposure were carefully chosen to provide the wider possible range of results. Thermal decomposition tests were carried out for the following constant temperatures:
— 465°C: onset of the thermal decomposition (Ma et al., 1988)
— 500°C and 530°C: intermediate temperatures
— 600°C: temperature limit for post-mortem observations

Exposure times were set at various times highlighting the primary kinetics changes up to 15 minutes (FAA standards resistance time (Federal Aviation Administration, 2023)).

3.2. Experimental results

3.2.1. Qualitative analyses on porosity formation

Qualitative considerations based on optical observations confirmed that porosity formation highly depends on time and temperature at various levels as can be seen on Fig. 3.2 for observations obtained in a central slice.

Overall, the porosities progressively replace the virgin matrix and tend to form pockets of localized pyrolysed areas. As they appear, porosities can be classified into two categories: (i) open porosities which are connected to the external environment either directly or by a network of voids created during the progressive decomposition of the matrix within the laminates; the pyrolysis gases generated inside these porosities can then escape from the porosities; (ii) closed porosities which remain trapped within the material and are still filled with pyrolysis gases.

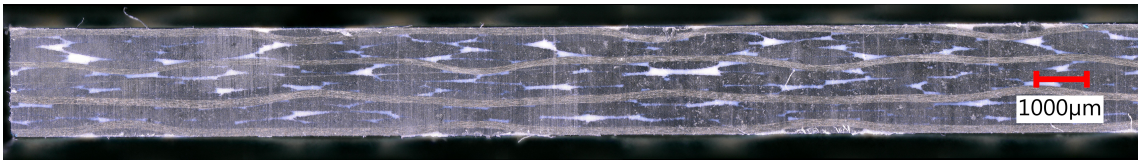

(a) Virgin sample

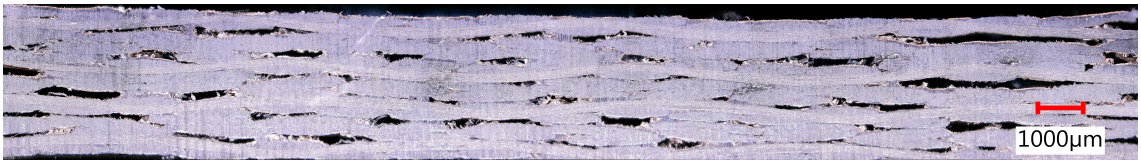

(b) 465°C – 7min – Porosity content: 28.6%

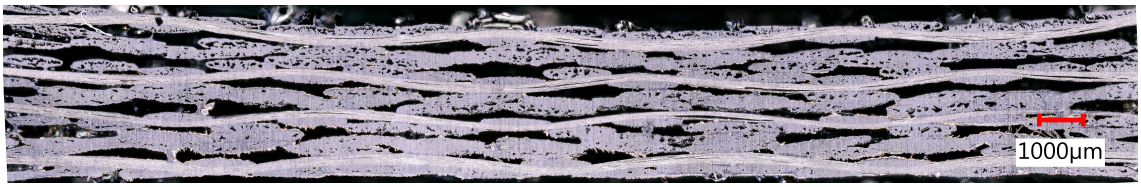

(c) 530°C – 7min – Porosity content: 43.2%

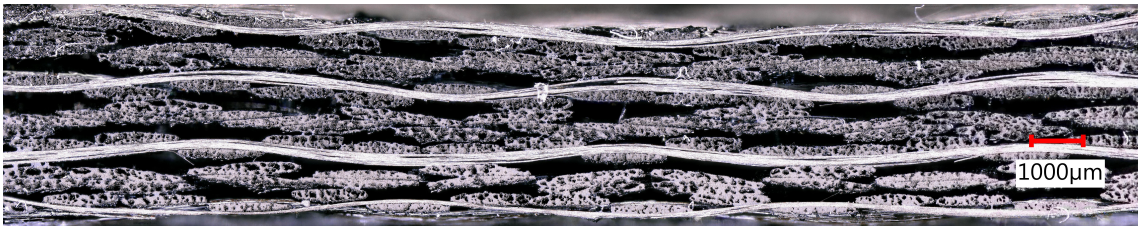

(d) 600°C – 5min – Porosity content: 54.8%

Figure 3.2. – Optical microscope observations of thermally decomposed QI C/PPS laminates under homogeneous thermal exposure at different temperatures and instants

Their influence on the geometrical changes of the laminates also vary. Whereas closed porosities tend to induce a homogeneous swelling of the material (due to internal pressure), open ones disrupt this homogeneity along the borders of the sample. Indeed, the escape of the gases is an abrupt process making the swelling far more important at the edges of the composite than in the middle, making it less thick in the center.

The process of porosity formation can be described by three consecutive mechanisms: (i) nucleation, mostly within matrix-rich areas, (ii) growth and coalescence of these porosities and (iii) decohesion at the fiber bundle / matrix interface. Although the porosities originating from on one hand (i) and (ii), and on the other hand from (iii) do not have the same nature (the firsts are filled with gas while the other only consist of voids), they will not be differentiated throughout this study. It results in interconnected porosities over the whole length of the sample, therefore connecting them to free edges which releases the pyrolysis gas.

As temperature increases, the thermal decomposition state progresses. However it is not a linear evolution since at high temperatures (beginning at 530°C and clearly visible at 600°) new areas of porosities appear within the fiber bundles, resulting in a severe fiber bundles / matrix debonding. These intra-bundle porosities may result from three mechanisms: (i) the decomposition of the polymer matrix constituting the fiber bundle (volume fraction of 17%), (ii) the debonding of the fibers and (iii) oxidization of the fibers due to the air flux and the oxygen which is released as the polymer matrix decomposes into gas (Grange, 2018). The onset of this phenomenon can be observed on Fig. 3.2 at 600°C. Besides, the time of exposure at a given temperature mainly contributes to continue the process of porosity formation already in place, without introducing new ones.

For a better understanding of the porosity distribution, X-Ray tomography observations are used to perform a 3D numerical reconstruction of the samples (Fig. 3.3). Afterwards, internal porosities can be extracted by setting a greyscale threshold. To set aside the edge effects, porosities are extracted from the center of the sample. It is observed in this particular example that the porosity distribution is rather homogeneous (each color distinguishing a separate porosity), which was expected for a homogeneous thermal exposure. However, this technique is more relevant in the case of a non uniform thermal exposure (e.g. one-face flame impact) since it is expected that the thermal gradients induce a significant porosity gradient through the thickness.

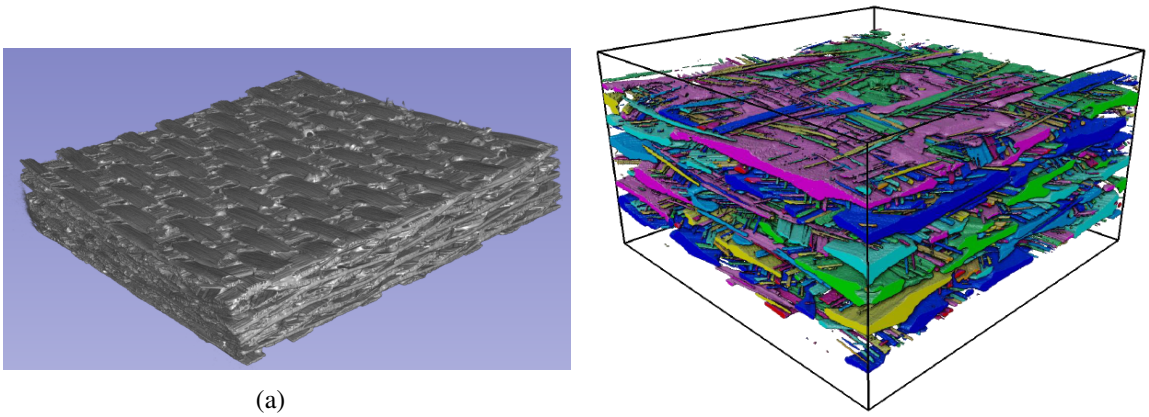

(a) (b)

Figure 3.3. – 3D reconstruction from tomography slices obtained from C/PPS laminates - 25 × 25mm^2 - 530°C - 7min - Porosity content: 42%. (a) Whole sample, (b) extracted porosities. Colors correspond to porosity network

3.2.2. Quantitative analyses on porosity formation

As explained in Section 3.1.1, the porosity content was determined according to various times and temperatures. Although the initial matrix volume represents 50% of the initial volume of the laminates, porosity content goes over 50% since the final volume gets larger and since it can

be reasonably assumed that the carbon fiber volume remains unchanged.

The time evolution of the porosity content $\eta_p(t,T)$ is depicted in Fig. 3.4 for temperatures of 465°C, 500°C, 530°C and 600°C for the laminates. Results show a similar trend of evolution for all considered conditions: a rapid increase during the first minutes and then a saturation to an asymptotic value depending on the temperature of treatment. However a major limitation for numerical modelling was observed at 7 minutes. It was the direct consequence of the sudden thickness drop at 5 minutes for temperatures of 530° and higher (see Fig. 3.5(a) in which the final thickness is normalized by the initial one). As the temperature and time of exposure became too elevated, structural damage made the laminates unable to withstand such a swelling which resulted in a collapse of the material. The swelling appeared to be limited to a maximum factor of 1.7 of the initial thickness in every scenario, confirming the above-mentioned maximum expansion of the laminates before collapse. Since the porosity volume determination highly depends on the thickness, its collapse strongly decreases η_p. However the mass loss increase (Fig. 3.5(b)) compensates the thickness decrease in the porosity content calculation (Eq. 3.1). As a result, the porosity content remains steady.

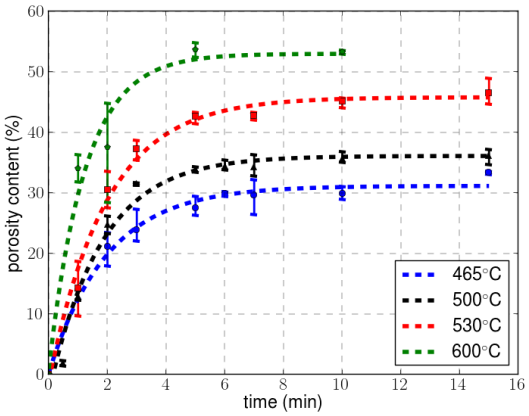

Figure 3.4. – Evolution over time of porosity content in QI laminates for different temperatures of exposure, as measured with the geometry-based method

Considering that the mechanisms leading to the collapse of the laminates are not fully understood yet, it was chosen to limit the exposure time to 5 minutes in the numerical modelling for temperatures above 500°C.

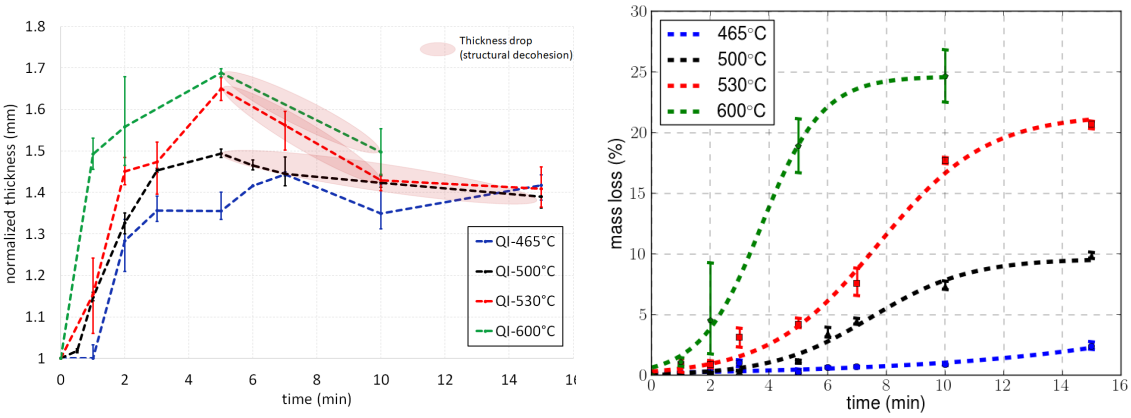

(a) Sample thickness

(b) Sample mass loss

Figure 3.5. – Evolution over time of the geometry-based method characteristic quantities (thickness and mass) in QI laminates for different temperatures of exposure

3.3. Numerical modelling

3.3.1. Domain of computation

The large discrepancies between the matrix and the fiber bundles in terms of thermomechanical behavior and thermal decomposition process (Fig. 3.2) has led to consider a mesoscopic scale based on the previous work of Carpier et al. (Carpier et al., 2022). A three-dimensional mesoscopic numerical model of the composite was hence created (using the software TexGen (Sherburn, 2007)), representing explicitly matrix and yarns in 1/28th of a RVE, i.e. a volume of $1.7 \times 1.03 \times 2.20\text{mm}^3$ (cf. Fig. 3.6 (a) and (b)). To start the analyses, the dimensions of study were set to get a fine discretization (5,000,000 elements), and the location of the subdomain was chosen to have the same volume fraction of matrix as in the laminates. The mesh refinement is depicted on Fig. 3.6 (c) with a zoom on the subdomain. Further analyses on sensitivity to mesh size are presented in Section 3.3.2. Finite Element calculations were performed using Z-Set (Z-set, 2023).

3.3.2. Nucleation of the porosities

As a first approach, it was chosen to focus on the porosity nucleation mechanism out of the three possible mechanisms, viz. nucleation, growth and coalescence, and interface decohesion. Two main reasons motivated this choice: it is the first step of the porosity formation and a compromise between computation time and modelling complexity. The other mechanisms will be discussed in Section 3.3.3 and Section 3.3.5.

In the numerical model, the porosity formation and the swelling mechanisms at a given in-

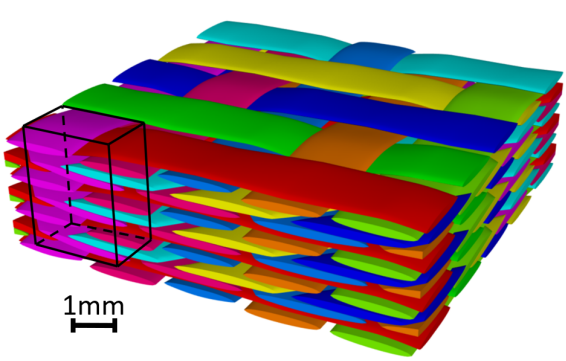

(a) RVE and selected subdomain

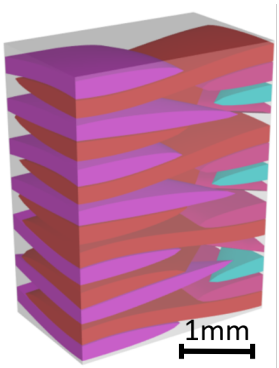

(b) QI 1/28th subdomain

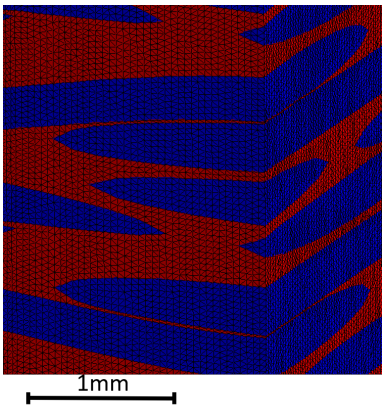

(c) Zoom on the subdomain mesh

Figure 3.6. – 3D mesoscopic numerical model of the laminates. Colors are used to differentiate the fiber bundles

stant of the decomposition are introduced according to two successive steps: first the formation of porosities and then their swelling (explained in Section 3.3.4). In order to reproduce the nucleation of porosities, the numerical separation of the nucleation and swelling processes is performed by using an intermediate normalization of the experimental η_p according to the thickness of the samples. The normalized η_p^{ref}, noted η_p^*, then represents the porosity content in a sample which would have been brought back to its initial thickness before swelling.

The modelling applies to a subdomain of computation which is embedded within the laminates. No difference is made between closed porosities at the core and open porosities along the edges. With such a representation and since the volume fraction of matrix in the subdomain is equal to that of the laminates, the kinetics of porosity formation within the subdomain can be assumed to be representative of that of the laminates with large dimensions. As a corollary to these working hypotheses, the kinetics of porosity formation is solely characterized by the volume fraction of porosities inside the subdomain.
The nucleation was implemented as mesh elements of matrix progressively turning into gas

based on a probabilistic law depending on time and temperature.

Probability based kinetics model

For sake of clarity at this stage of the presentation, the kinetics model is presented in the model configuration of a fixed temperature T (so that no dependence on T is mentioned yet; it is introduced in a second step) and of a mesh made up of matrix and porosity elements exclusively. Let $N_m(t)$ and $N_p(t)$ denote the numbers of matrix elements and porosity elements at the instant t, within a set of $N_m^0 = N_m(t=0)$ matrix elements at the initial instant. Owing to conservation, the following equality holds:

$$N_m(t) \; + \; N_p(t) \; = \; N_m^0 \qquad \forall\, t \geq 0 \tag{3.7}$$

Noting $\dot{N}_p(t)$ the rate of production of porosity elements at time t, the number of produced porosities within the time interval $[t, t+\Delta t]$ is

$$\Delta N_p(t) = \dot{N}_p(t)\,\Delta t \tag{3.8}$$

If each matrix element is assigned a probability p to transform into a porosity within $[t, t+\Delta t]$ and assuming that $N_m(t)$ is very large, the complete set of random draws over the $N_m(t)$ candidate elements leads to the following expected number of produced porosities:

$$\Delta N_p(t) = p N_m(t) \tag{3.9}$$

The combination of Eq. 3.8 and 3.9 enables to define p according to a function $G_N(t)$ -depending only on time- and to the time duration Δt:

$$\frac{p}{\Delta t} = G_N(t) \qquad \text{where} \quad G_N(t) = \frac{\dot{N}_p(t)}{N_m(t)} \tag{3.10}$$

Assuming that all the elements have the same volume, the rate of porosity content $\dot{\eta}_p(t)$ and the volume fraction $\eta_p(t)$ at an instant t can be expressed by:

$$\dot{\eta}_p(t) = \frac{\dot{N}_p(t)}{N_m^0} \qquad \eta_p(t) = \frac{N_p(t)}{N_m^0} \tag{3.11}$$

The combination of Eq. 3.7, 3.10 and 3.11 leads to the following partial differential equation, of which the volume fraction of porosity $\eta_p(t)$ is solution:

$$\dot{\eta}_p(t) = G_N(t)\left(1 - \eta_p(t)\right) \qquad \forall\, t \geq 0 \tag{3.12}$$

By repeating the reasoning from Eq. 3.7 to Eq. 3.13 for a different temperature, one obtains the following partial differential equation to describe the temperature-dependent kinetics model of

porosity formation:

$$\begin{aligned} &\dot{\eta}_p(t,T) = G_N(t,T)\left(1-\eta_p(t,T)\right) \qquad \forall t \geq 0,\ \forall T \geq T_\mathrm{d} \\ &\text{where} \quad G_N(t,T) = \frac{p(t,T,\Delta t)}{\Delta t} \end{aligned} \tag{3.13}$$

A similar approach is regularly used in theoretical physics to study the evolution of particle decay over time. It emanates from the theory of radioactive decay which was first developed by Rutherford and Soddy in 1902 (Rutherford and Soddy, 1902). The G_N factor is then a constant decay rate and an explicit expression of η_p can be obtained (proportional to $exp(-G_N t)$).
From Eq. 3.13 it follows that, given a time discretisation in terms of Δt (not necessarily constant), the kinetics is completely described from the probability $p(t,T,\Delta t)$. There thus only remains to attribute an analytical form to $p(t,T,\Delta t)$ -or alternatively $G_N(t,T)$-, after which Eq. 3.13 can be numerically solved to approximate $\eta_p(t,T)$ under the assumption of a very large set of matrix elements. This is under concern in Section 3.3.2.
In the particular case of a constant time increments Δt, a closed form of $\eta_p(t)$ can be obtained. Let us note $t^{(k)} = k\Delta t$ the time at the k-th increment, $p^{(k)} = p\left(t^{(k)}\right)$ the corresponding probability, and $\eta_p^{(k)}$ the corresponding porosity content. After the definition of η_p and p, $\eta_p^{(k)}$ can be described by the following recursive sequence:

$$\begin{cases} \eta_p^{(0)} = 0 \\ \eta_p^{(k+1)} = \left(1-p^{(k+1)}\right)\eta_p^{(k)} + p^{(k+1)} \end{cases} \tag{3.14}$$

As to illustrate with $t^{(3)} = 3\Delta t$: $\eta_p^{(3)} = p^{(1)}+p^{(2)}+p^{(3)}-p^{(1)}p^{(2)}+p^{(2)}p^{(3)}+p^{(1)}p^{(3)}+p^{(1)}p^{(2)}p^{(3)}$
Let $C_{i,k}$ denote the set of possible combinations of i elements out of k and let us note $c \in C_{i,k}$ any of these combinations. From a recurrence analysis, it can be shown that the volume fraction at the time $t^{(k)}$ is:

$$\eta_p(k\Delta t) = \sum_{i=1}^{k} (-1)^{i+1} \sum_{c \in C_{i,k}} \prod_{j \in c} p^{(j)} \tag{3.15}$$

If, further, the probability $p^{(k)}$ is set constant over time increments, Eq. 3.15 is simplified into:

$$\eta_p(k\Delta t) = \sum_{i=1}^{k} (-1)^{i+1} \binom{k}{i} p^{(i)} \qquad \text{with} \quad \binom{k}{i} = \frac{k!}{i!\,(k-i)!} \tag{3.16}$$

As for $\eta_p(t,T)$ determined from Eq. 3.13, the assumption pertaining to the closed form of Eq. 3.16 is that the number of matrix elements is very large. This closed form has been retained as the reference asymptotic kinetics law, noted $\eta_p^\infty(t,T)$, for the analyses of the effect of domain size and mesh refinement in Section 3.3.2.

Probabilistic law

According to Eq. 3.13, if the expression of $G_N(t,T)$ (or alternatively $p(t,T,\Delta t)$) is prescribed, then the temperature dependent evolution of the porosity content can be described completely. One way to build up $G_N(t,T)$ would be to derive it from the classical partial differential equation

describing pyrolysis kinetics (cf. (Flynn and Wall, 1966)). This equation gives the rate of the degree of thermal decomposition $\dot{\alpha}(t,T)$ according to a temperature dependent rate factor in the form of an Arrhenius function and to a reaction model depending on α. As detailed in (Carpier et al., 2021), the identification of the decomposition kinetics of the polymer matrix can be made from different approaches, more or less consistent with the involved physics, and all of them are based on thermogravimetric analyses of the polymer matrix.
In the present work it is purposely chosen to develop a model from macroscale measurements of thermally-induced mass and dimensions evolutions. Along with this choice, the main role assigned to $G_N(t,T)$ is to enable the reproduction of a macroscale phenomenology from a microscale mechanism -porosity nucleation- on a wide range of temperatures. Given the extant of scales and the spectrum of thermomechanical properties to deal with in this model, a pragmatic choice is made for the construction of $G_N(t,T)$: it can be a phenomenological function calling on as few parameters as possible and necessarily positive.
According to experimental results at each considered temperature T, the rate of porosity content $\dot{\eta}_p(t,T)$ is maximal at $t=0$ and monotonously decreases over time until $\eta_p(t,T)$ reaches a saturation value. This evolution corresponds to a probability of nucleation which itself should be maximal at $t=0$ and then would continuously decrease to zero over time. The form of $G_N(t,T)$ proposed in Eq. 3.17 enables to reproduce this trend:

$$G_N(t,T) = \frac{A(T)}{t+B} \tag{3.17}$$

$A(T)$ depends on the temperature while B correspond to a constant (positive) characteristic time. $A(T)$ should describe the dependence to T, potentially non linear, using as few parameters as possible. In order to adapt the conditions for an efficient identification of these parameters, a first round of analyses was performed at a reference temperature T^{ref} in the medium range of considered temperatures ($T^{ref} \in [T_d, 600°\mathrm{C}]$), at which a comprehensive set of mechanisms is involved in the phenomenon of decomposition. This preliminary functional analysis has led to the expression of $G_N(t,T)$ provided in Eq. 3.18. The parameters and their respective roles are reported in Table 3.1. The provided values result from the identification which is explained in Section 3.3.2. Fig. 3.7 shows the evolution of p over time for different temperatures.

$$G_N(t,T) = \frac{a_1 + a_2\left(\dfrac{T-T_d}{T^{ref}-T_d}\right)^b}{t+\tau} \tag{3.18}$$

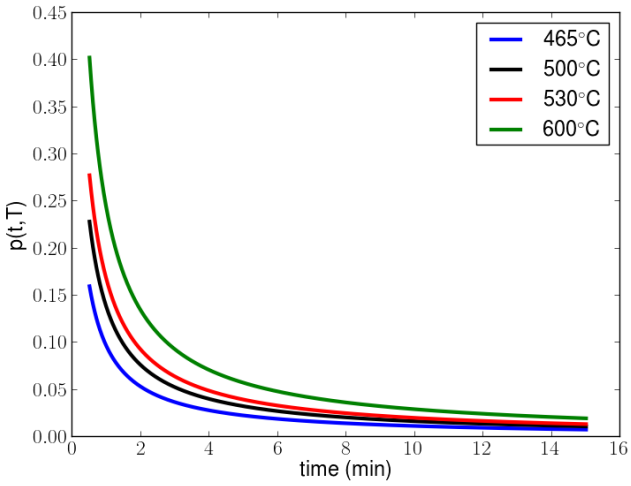

Figure 3.7. – Evolution of the nucleation probability p over time for different temperatures

Parameter	Unit	Value	Main role
a_1	No unit	0.205	Affects G_N for $T = T^{ref}$
a_2	No unit	0.139	Dependence of G_N to T
τ	Time (s)	15	Time shift at the initial time
b	No unit	1.15	Dependence of $\frac{\partial G_N}{\partial T}$ to T
T^{ref}	Temperature (°C)	530	Reference temperature

TABLE 3.1. – Parameters used to define $G_N(t,T)$ as given by Eq. 3.18

Identification of $G_N(t,T)$

The identification of the parameters of $G_N(t,T)$ is performed by optimisation. It is a classical iterative process where, given a set of parameters $P = \{a_1, a_2, \tau, b\}$, the following operations are performed at each step:

- the partial differential equation Eq. 3.13 is numerically solved (Euler scheme based on a small Δt)
- its result is compared to the reference experimental curve of $\eta_p^{ref}(t,T)$ for T_i = 465°C, 530°C or 600°C and at the different times of the experimental measurements $t^{(j)}$ using a cost function $\mathscr{F}$:

$$\mathscr{F} = \sum_{i,j} \left(\eta_p^{ref}\left(t^{(j)}, T_i\right) - \eta_p\left(t^{(j)}, T_i\right) \right)^2 \tag{3.19}$$

- a variation is introduced on the values of P

The iterative process is stopped as the cost function reaches a minimum.
As a preliminary to the identification process, a quantitative sensitivity analysis has been performed on the parameters of the model. Let P be the set of parameters with $P_{i,0} \in \{a_1, a_2, \tau, b\}$. It was chosen to investigate the influence of the factors on the resulting porosity content by considering an arbitrary variation interval for each parameter so that $P_i \in [\frac{1}{2}P_{i,0}, 2P_{i,0}]$ introducing parameter factors $F_i \in [0.5, 2]$. The porosity content therefore depends on F_i, T and t and can be noted $\eta_p^i(t,T)$. Let the relative error RE of a function f to a reference value f^{ref} be defined as:

$$RE(f) = \left| \frac{f - f^{ref}}{f^{ref}} \right| \times 100 \tag{3.20}$$

Two approaches were considered, having either the temperature or the time set and the other varying to investigate the influence of the parameters on each:

— $\eta_p^i(T,t)$ was calculated according to time or temperature for various parameter factors . The dispersion $d^i(t,T)$ around the reference probability law $\eta_p^{i,0}(T,t)$ was defined as $d^i(t,T) = RE\left(\eta_p^i(t,T)\right)$. The amount of parameter factors was limited to two for curve readability, chosen as the boundaries 0.5 and 2.

— For a complete overview of the parameter factors, the $\eta_p^i(T,t)$ were integrated over time (at fixed temperature) or over temperature (at fixed time) such as $S^i(F_i,T) = \int_0^{t_{final}} \eta_p^i(T,t)\,dt$ and $S^i(F_i,t) = \int_0^{t_{final}} \eta_p^i(T,t)\,dT$. The dispersion around the reference integral value $S^{i,0}(F_i,t)$ according to the chosen parameter factor $D^i(F_i,t,T)$ was defined as $D^i(F_i,T) = RE\left(S^i(F_i,T)\right)$ and $D^i(F_i,t) = RE\left(S^i(F_i,t)\right)$.

Specific cases representative of the general tendencies are presented with set temperature of 600°C and times of 50s, 100s and 300s.
Fig. 3.8 to 3.15 quantify the impact of said parameters according to time and temperature.

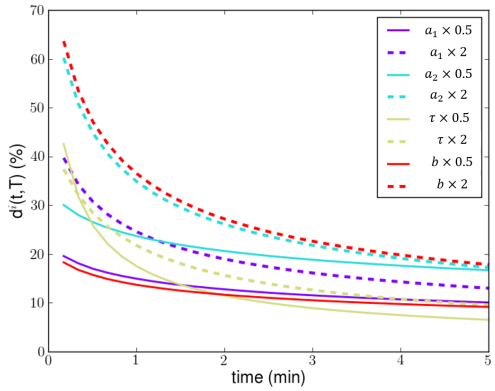

Figure 3.8. – Influence of parameter values on $d^i(t,T)$ according to time at 600°C

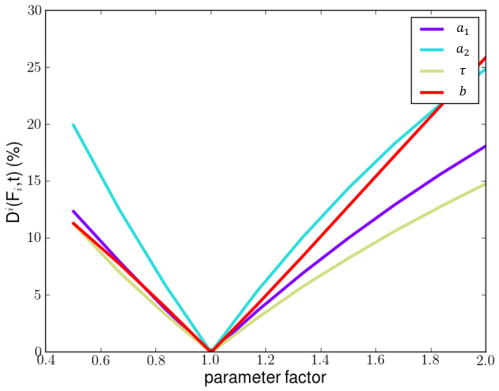

Figure 3.9. – Influence of parameter values on $D^i(F_i,t)$ according to time at 600°C

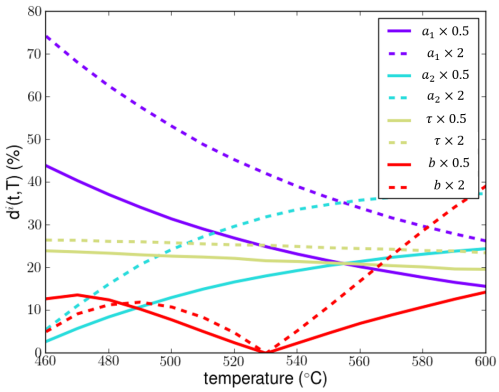

Figure 3.10. – Influence of parameter values on $d^i(t,T)$ according to temperature after 50s

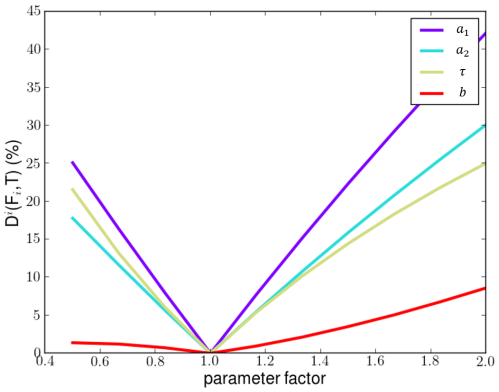

Figure 3.11. – Influence of parameter values on $D^i(F_i,T)$ according to temperature after 50s

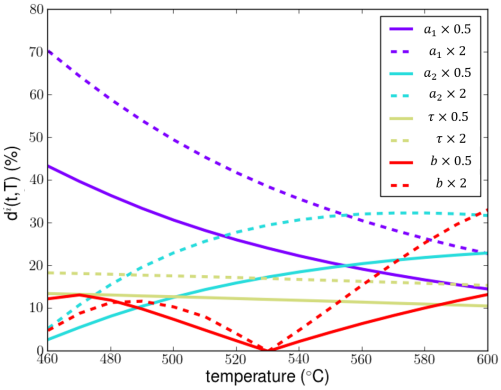

Figure 3.12. – Influence of parameter values on $d^i(t,T)$ according to temperature after 100s

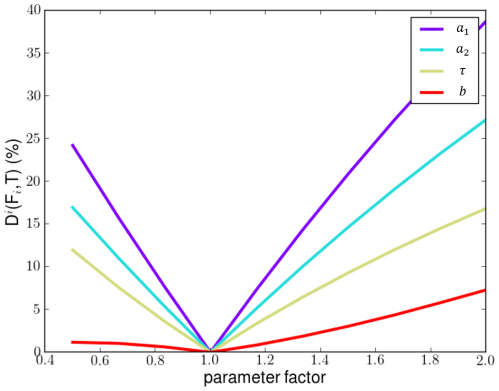

Figure 3.13. – Influence of parameter values on $D^i(F_i,T)$ according to temperature after 100s

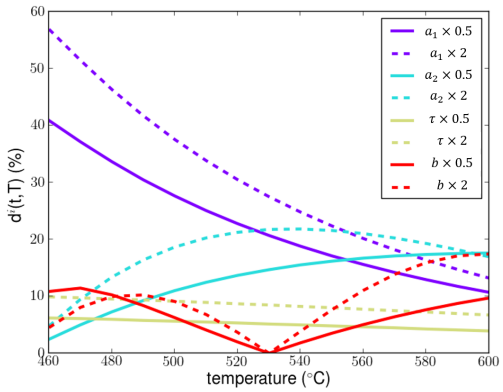

Figure 3.14. – Influence of parameter values on $d^i(t,T)$ according to temperature after 300s

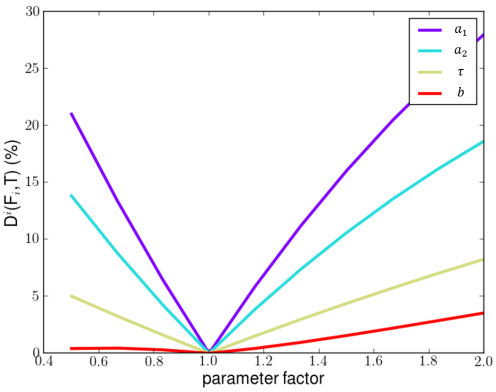

Figure 3.15. – Influence of parameter values on $D^i(F_i,T)$ according to temperature after 300s

This sensitivity analysis shows that any of these parameters have a significant influence which validates the relevance of the proposed form of $G_N(t,T)$. It also enables to determine a reference set of parameters. This iterative process was started from this reference set.

The identified parameters are presented in Table 3.1. The quality of this identification was then validated by comparing the computed kinetics of porosity formation at $T = 500°C$ to the experimental one through a Euler scheme. Furthermore, a Monte-Carlo method was used on a large amount of elements to verify that similar porosity content were obtained. All the computed curves of $\eta_p(t,T)$ can be compared to the experimental ones on Fig. 3.16. Some caution should be taken with temperatures exceeding 600°C as oxidization starts to occur, which alters the internal structure of the yarn, and is not considered by the model.

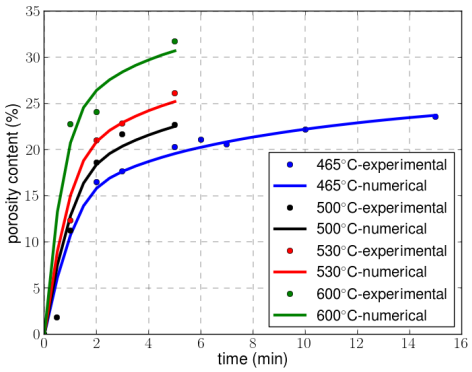

Figure 3.16. – Comparison of the experimental / numerical evolution over time of η_p^* for different temperatures of exposure considering the nucleation process in QI laminates

Probability law: adapted form

Modelling both thermal transfers and mechanical fields under a mechanical load involves dealing with non-linearities originating from the gradients of properties according to temperature and constituent. To this respect, for a good trade-off between accuracy of the porosity kinetics description and efficiency of the numerical analyses, Δt should lie within a range from 10s to 60s. Computing $RE\left(\int_0^t \eta_p(t,T)\,dt\right)$ for different values of Δt, and taking the reference solution as that obtained with $\Delta t = 10^{-3}$s, it is shown that the error becomes significant for time increments larger than 1s, as seen from Fig. 3.17.

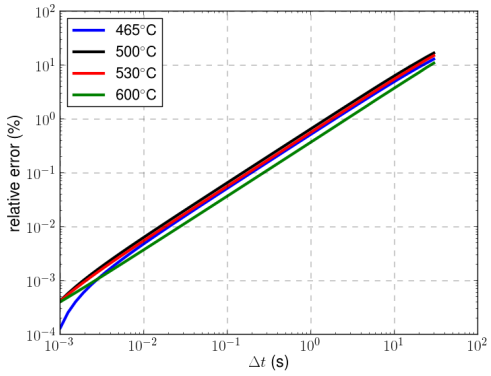

Figure 3.17. – Evolution of the relative error of $\int_0^t \eta_p(t,T)\,dt$ according to Δt for different temperatures of exposure. The reference solution is the one obtained with $\Delta t = 10^{-3}$s

This error originates from the inherent error introduced by the Euler scheme as the small Δt criterion is no longer met. In order to enable the use of $\Delta t \geq 10$s, the definition of $p(t,T,\Delta t) = G_N(t,T)\,\Delta t$ must then be corrected with an adaptation function $f_a(\Delta t)$. The corrected nucleation probabilistic law reads:

$$p(t,T) = G_N(t,T)\,\Delta t \times f_a(\Delta t) \tag{3.21}$$

The time increment correctional factor $f_a(\Delta t)$ is expressed as:

$$f_a(\Delta t) = \frac{1}{\left(0.833 + \left(0.00458 - 0.00167\left(\dfrac{T - T^{ref}}{T^{ref} - T_d}\right)\right)\left(\Delta t^{ref} - \Delta t\right)\right)} \tag{3.22}$$

The reference Δt^{ref} was set at 30s as to conveniently fit the experimental data while not being too large to capture progressive mesostructural changes. Fig. 3.18 shows that results do not depend on Δt, provided it be lower than 60s.

Given the high time-rate of evolution of the porosity content as obtained experimentally, even for the lowest temperature causing the polymer matrix decomposition, Δt larger than 60s would lead to a lack of accuracy. Therefore this upper bound of Δt is not the source of any reduction in the efficiency of the thermomechanical computations.

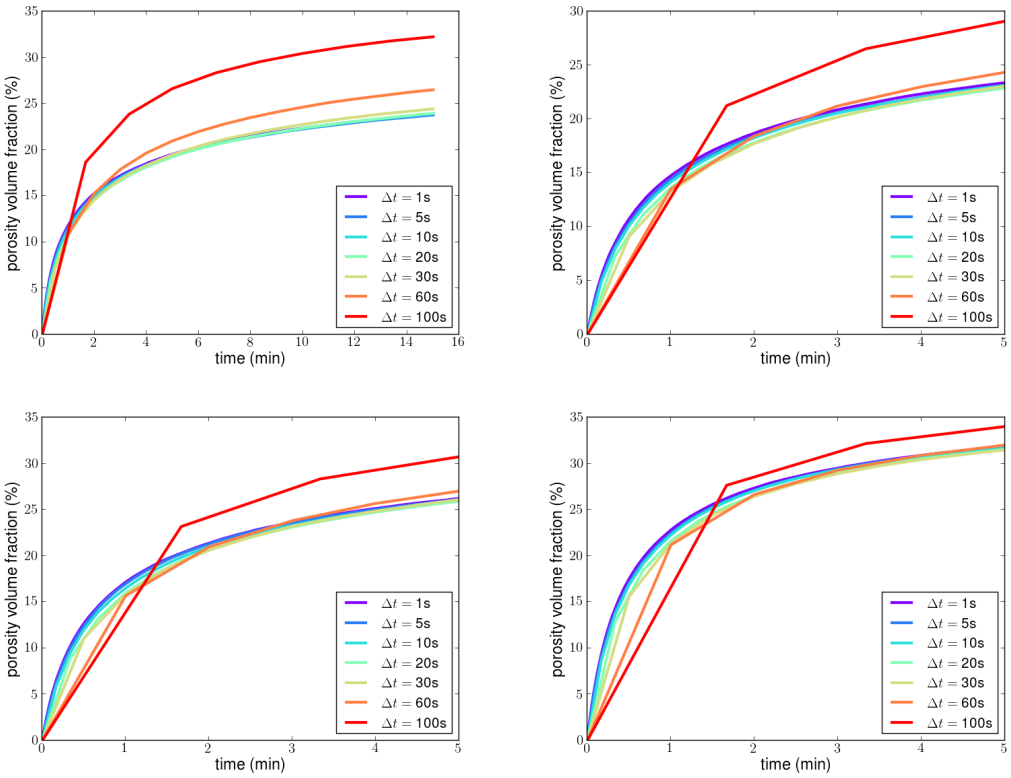

Figure 3.18. – Influence of the dt value on $\eta_p(t,T)$ at 465°C, 500°C, 530°C and 600°C

Sensitivity to mesh size

As the probabilistic approach consists of a series of random draws, a bias might be introduced if the amount of elements is not large enough as it would not result in representative values of the asymptotic behavior. Eq. 3.15 was used to assess the convergence of the probability-based $\eta_p(t,T)$ according to the number of elements N_m^0 used. An arbitrary setting of $T = 530$°C and $\Delta t = 30$s was chosen. Let the deviation from the theoretical value $\eta_p^\infty(t,T)$ be defined as $d\left(N_m^0,t,T\right) = RE\left(\eta_p(t,T)\right)$. As each matrix element undergoes a Bernoulli trial at each time step with a probability $p(t,T)$ to turn into a porosity, the porosity content follows a step-by-step binomial random variable $B\left(n,p\right)$. Let X_n be the amount of successes out of n possibilities so that the probability of achieving it reads:

$$P(X_n = k) = \binom{n}{k} p^k \left(1-p\right)^{n-k} \tag{3.23}$$

Let the mean relative deviation $D_n\left(p\right)$ be defined as

$$D_n\left(p\right) = \mathbb{E}\left(\frac{|X_n - \mathbb{E}(X_n)|}{\mathbb{E}(X_n)}\right) \times 100 \tag{3.24}$$

As for a binomial distribution $B(n,p)$ $\mathbb{E}(X_n) = np$, De Moivre showed in 1730 that $D_n(p)$ can be expressed as

$$\begin{aligned} D_n(p) &= 2n\binom{[np]}{n-1} p^{[np]+1}(1-p)^{n-[np]} \times \frac{100}{np} \\ &= \frac{2n(n-1)!}{[np][np]!(n-np-1)!} p^{[np]+1}(1-p)^{n-[np]} \times \frac{100}{np} \end{aligned} \tag{3.25}$$

As n tends toward high values, Stirling's formula stipulates that $n!$ can be approximated as

$$log(n!) \approx n\,log(n) - n + \frac{1}{2} log(2\pi n)$$

After application of Stirling's formula and developments, Eq. 3.25 becomes

$$log(D_n(p)) = -\frac{1}{2} log(n) + \frac{1}{2} log\left(200\frac{1-p}{2\pi p}\right) \qquad \text{or } d(N_m^0) = \left(\frac{100}{\pi}.\frac{1-p}{pN_m^0}\right)^{\frac{1}{2}} \tag{3.26}$$

For a calculation at 30s, numerical application renders the line equation

$$log(D_n(p)) = -\frac{1}{2} log(n) + 2.11$$

which corresponds to what is observed on Fig. 3.19. It is to be noted that for n values lower than a 100, slight differences appear between the numerical and theoretical values as Stirling formula's assumption of a large N is no longer met.

Fig 3.19 shows the variation of d according to N_m^0 for four exposure times at 530°C. Results show that the porosity content is only lightly affected by the number of elements. It appears that for a model with 10^6 elements, the dispersion is lower than 0.1%. As a realistic amount of matrix elements would be of this magnitude, it can be assumed that the randomness is limited to the location of porosity nucleation and does not reflect at the macroscopic scale.

A view on the decomposed subdomain is shown on Fig. 3.20 for two different refinements. The coarsest mesh corresponds to the one used in (Carpier et al., 2022) for the determination of the laminates axial stiffness evolution in the temperature range from the ambient to the onset of decomposition T_d. Whereas this mesh was fine enough to predict thermoelastic properties of the laminates up to T_d, this qualitative comparison tends to show that the analyses for $T \geq T_d$ are more demanding in terms of mesh size refinement. Further analyses on mesh size effect, from the quantitative point of view, are presented in Section 3.3.4.

3.3.3. Porosity growth

Growth strategy

As microscopic observations have shown, cavities can be present in the form of small of large voids. This latter case is obtained from the mechanism of growth. To model it, it has been

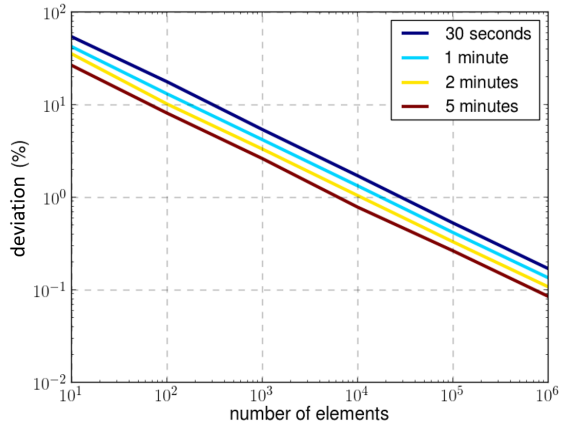

Figure 3.19. – Evolution of the deviation of the porosity content from to the theoretical asymptotic value according to the number of initial matrix elements N_m^0 for different exposure times at 530°C

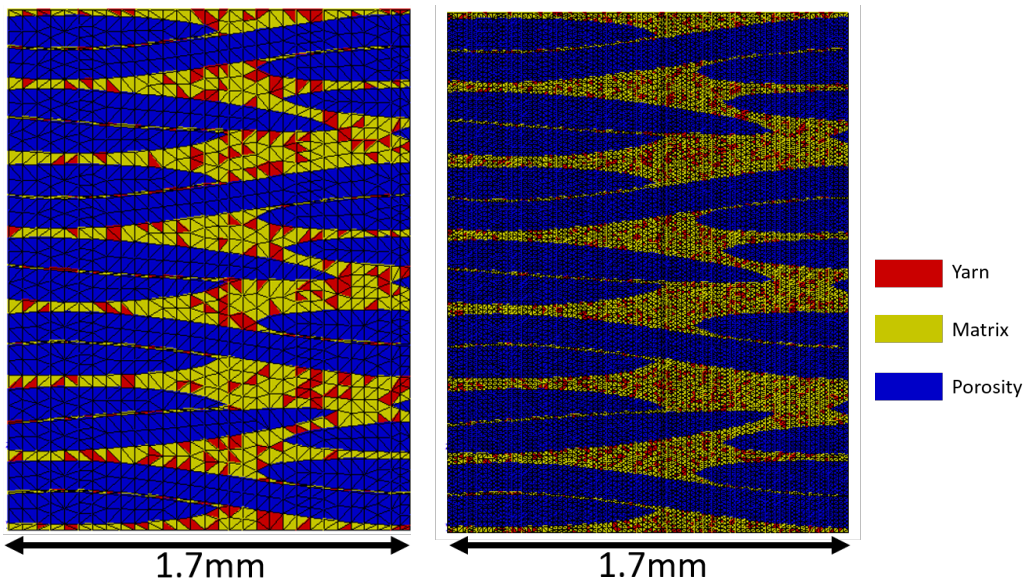

(a) (b)

Figure 3.20. – Simulation of the thermally induced porosity formation in the laminates at 530°C for 5 minutes with explicit porosity distribution. (a) coarse mesh (b) refined mesh

separated from the nucleation one and was accounted for by adapting the probability of porosity formation with a growth probability p_{growth}:

$$p(t,T) = G_N(t,T)\, f_a(\Delta t) + p_{growth}(t,T) \tag{3.27}$$

It can be summarized as:

$$p(t,T) = p_{\text{nucleation}}(t,T) + p_{growth}(t,T) \tag{3.28}$$

p_{growth} is different for each matrix element and depends on the local porosity density: the higher the porosity density around an element, the higher p_{growth} (and hence p) becomes. Let a matrix domain be divided into cubic boxes for the computation of the local porosity densities as represented in Fig. 3.21. All matrix elements belonging to a given cube could be considered to be influenced only by porosities located within the box of interest for the growth mechanism. However, preliminary results showed that such an approach leads to an overly quick saturation. Indeed, once a box is filled with cavities, the growth stops. Furthermore, as the nucleation probability drops, the amount of new porosity elements then becomes too low. Increasing the nucleation probability as a compensation results in a porosity volume fraction significantly higher than expected in the earlier times and a proper equilibrium was not found.
The chosen approach also takes into account the surrounding boxes which are included into the definition of the *local domain*. The three scales of the growth model for each matrix element are then, from smallest to largest:

— Element: matrix/porosity finite element of the model
— Box: cubic domain containing a fixed number of elements defining its size. The example provided in this section considers 5 elements in each box. A difference is made between the box of interest containing the matrix element and the surrounding boxes.
— Local domain: ensemble of boxes surrounding a given matrix element

The surrounding boxes are classified according to their distance from the central domain, i.e the 1^{st} order consists of the box of interest, the 2^{nd} order of the 26 boxes directly surrounding it, the 3^{rd} one the next 37 etc... See Fig. 3.21 for a two-dimensional simplified representation of the discretization up to the 3^{rd} order in which a matrix element and the porosities surrounding it are represented. The other matrix elements are not represented for clarity purposes. The contribution to porosity growth is maximum for the porosities located in the box of interest and the influence is reduced for each order of classification.

Let us note n the number defining the classification order of neighbours and d_i the porosity density in the cubes i forming the local domain of a given matrix element. The global porosity density of this local domain d_p determining the growth probability of the matrix element reads:

$$d_p = \sum_{i=1}^{3^n} \omega_i d_i \tag{3.29}$$

with ω_i the associated weight constant for $i \in \left[3^{k-1}+1, 3^k\right]$, $k \in \{1, ..., n\}$.

Let us assume as an example that each cubic box consists of five elements, being either matrix or porosity. A two-dimensional example is provided in Fig. 3.22 in which $n = 2$, along with the corresponding densities of the constituent boxes of the local domain.

Let us assume further that $\omega_1 = 0.2$ and $\omega_{2...9} = 0.1$. Eq 3.29 then gives a porosity density for the local domain of:

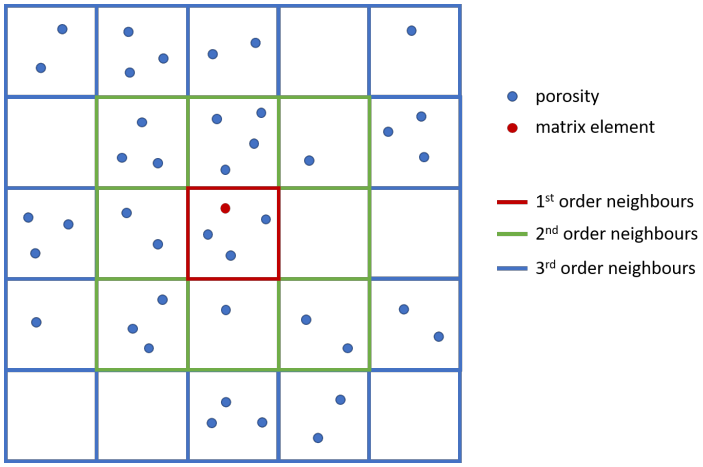

Figure 3.21. – Two-dimensional representation of the *local domain* of a cubic box embedded within its neighbours up to the 3^{rd} order

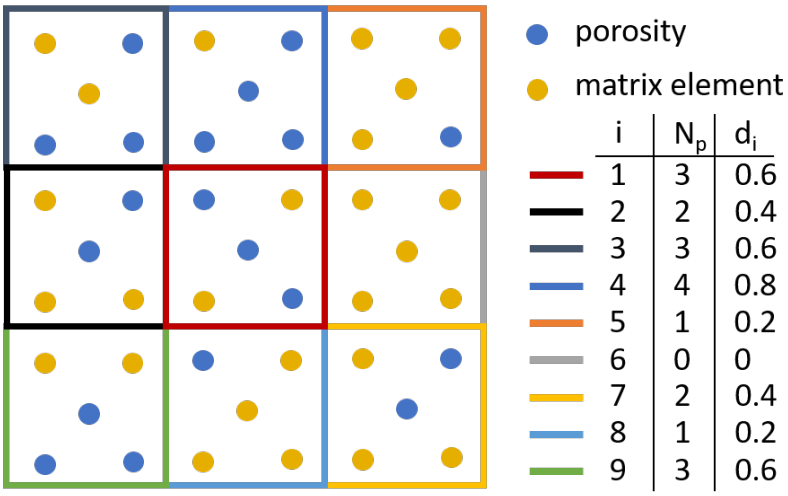

Figure 3.22. – Two-dimensional example of porosity distribution within the boxes of a $2nd$ order domain considering a box size of 5 elements. Calculation of the porosity density of the boxes forming the local domain

$$d_p = 0.38 \tag{3.30}$$

Growth model determination

The question first rests on the compromise between the maximum order of influence considered and the amount of elements placed in each box. These considerations must rely on a reasonable computation time while preserving the chemico-physical aspect of the phenomenon:

— On the one hand, an ideal system would consist of considering each box containing only one matrix element influenced by the other elements directly connected to it. It is however not numerically feasible. On the other hand, an extremely cost effective discretization considering too many elements in each box would not be representative enough.
— Taking into account too many orders would result in (i) large calculation times and (ii) loss of accuracy as elements would interact from a large distance.

It was hence chosen first to use the second order approach. The local domain then consists of the central box and the 26 surrounding it. The impact of the number of elements in each box on the porosity content evolution was then assessed using arbitrary values for the probability and the ω_i. To this end, a cubic domain consisting only of 40,000 matrix elements was created. A 5% porosity content was initially included, and the growth model was tested with a 30s time step using various box sizes. Fig. 3.23 and 3.24 show that the porosity content increases with the number of elements before stabilizing after 10 elements. It can be observed (especially on Fig. 3.24 which represents the porosity content values after 5 minutes) that the porosity content decreases with a large number of elements. It originates from boundary effects: the boxes on the borders are not fully surrounded by matrix and porosity, therefore the local density is necessarily lower. As a result, since with large numbers of elements a majority of the boxes are located on the borders, the porosity content decreases.

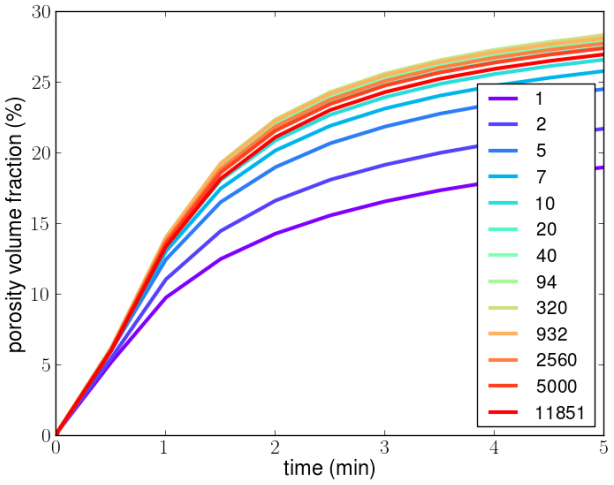

Figure 3.23. – Evolution of the porosity content over time at 530°C for different box sizes defined by the number of elements

The second order approach was then coupled with considering 10 elements in each box, which represents between 2 and 3 elements in each directions of the cubes.

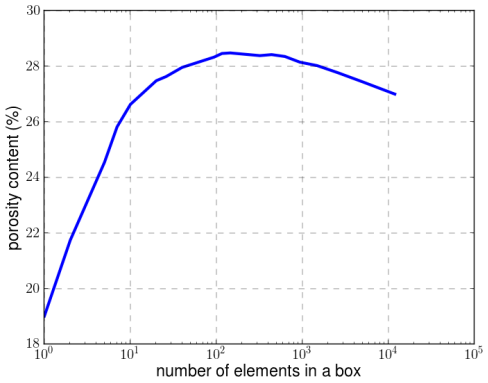

Figure 3.24. – Dependence of the porosity content on the number of elements in each box at 530°C for 5 minutes

Comparison with JMAK growth model

This approach can be compared with the Johnson-Mehl-Avrami-Kolmogorov (JMAK) model, often used to reproduce the phase transformations (especially for crystallization). This model considers the instantaneous nucleation of a certain nuclei content $z(t=0)$, before describing its evolution through growth. The fraction of transformed material over time $z(t)$ (assimilated to $\eta_p(t)$) follows a sigmoidal shape described by the general equation:

$$z(t) = 1 - exp\left(-Kt^n\right) \tag{3.31}$$

where:

— K is a constant depending on $z(t=0)$ and the interface growth velocity

— n is an integer no larger than 4, usually set at $D+1$, D being the dimension of the geometrical model. In the present case, $n=4$ since our model is three-dimensional.

Let us suppose that the nucleation only occurs at the initial time in the proposed growth model so that only the growth governs the porosity content evolution. A cubic domain of matrix containing 1,000,000 elements was used. It was found that the weights of the present approach (as described in Eq. 3.32) can be adjusted as to fit the JMAK-predicted evolution. Fig. 3.25 shows the good agreement for an $z(t=0) = 0.1\%$ (with $K = 1.3E-9$).

The developed model can therefore replicate the evolution described by a theoretical model.

Growth model identification

As a portion of the porosities are formed through the growth mechanism, $G_N(t,T)$ must be adjusted (lowered) to keep a similar porosity content. It was observed that the porosities tend to form large pockets. This led to the assumption that the porosity formation is mostly governed by the growth mechanism. To that end, and as a first approach to demonstrate the capabilities of the growth model, the nucleation probability was arbitrarily divided by 2.5 so that 40% of the

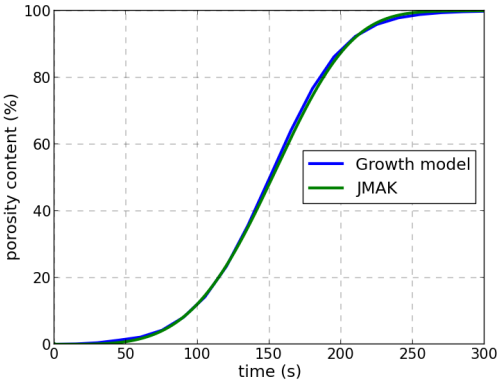

Figure 3.25. – Comparison of the porosity content evolution over time as obtained by the JMAK model and the original approach ($\eta_p(t=0) = 0.1\%$)

porosities are nucleating and 60% originate from the growth.

As it was mentioned in Section 3.3.3, it is necessary to account for the second order neighbours for the welfare of the modelling. However their influence (or weight) can be reduced to a minimum. To that end, it was chosen arbitrarily to set the weight of the central box 80 times higher than the surrounding ones. Doing that, the combined weight of the 26 surrounding boxes is around 3 times lower and represents 25% of the total weight.
As for the determination of G_N, the weights ω_i must follow a similar trend: a high value at the initial times to initiate the growth process, before decreasing with time. The proposed definition of ω_i reads:

$$\omega_i(t,T) = \frac{1}{\left(\tau_{1,i} + \tau_{2,i}\left(\frac{T - T_d}{T^{ref} - T_d}\right)\right) t^c} \qquad \text{with t>0} \tag{3.32}$$

As the growth occurs after the nucleation and the first iteration is at the end of the first time step of the finite element calculation, $t > 0$. The various parameters and their roles are presented in Table 3.2, and the evolution of ω_1 over time for different temperatures is shown of Fig. 3.26. Although it the temperature dependence appears to be limited, the term $\tau_{2,i}\left(\frac{T - T_d}{T^{ref} - T_d}\right)$ is necessary to avoid an overly quick saturation at high temperatures. The evolution of $\omega_{\{2...9\}}$ is similar, only 80 times lower.

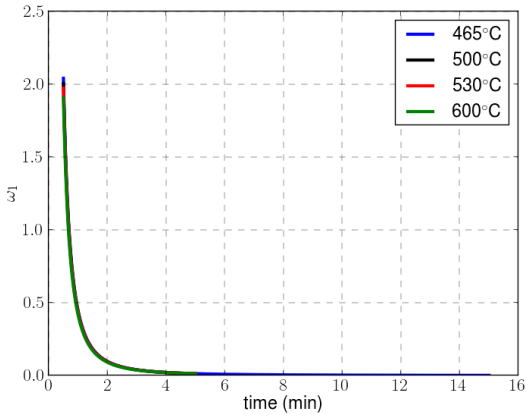

Figure 3.26. – Evolution of the growth weight ω_1 over time for different temperatures of exposure

Parameter	Unit	Value		Main role
		$i = 1$	$i = \{2...9\}$	
τ_1	Time (s)	$1.37e-4$	$1.09e-2$	Affects ω_i for $T = T^{ref}$
τ_2	Time (s)	$5.77e-6$	$4.62e-4$	Dependence of ω_i to T
c	No unit	2.2	2.2	Non-linear dependence of ω_i to t
T^{ref}	Temperature (°C)	530	530	Reference temperature

TABLE 3.2. – Parameters used to define $\omega_i(t, T)$ as given by Eq. 3.32

The parameters from the definition $\omega_i(t, T)$ were identified in order to fit the experimental data, and the obtained porosity content evolution is depicted on Fig. 3.27. It appears that the optimized parameters accurately replicate the experimental results.

Although quantitatively the modelling with or without including the growth process yields similar results, qualitatively major differences in the porosity distribution can be observed. Fig. 3.28 shows the porosity distribution in a simplified cubic domain initially composed only of matrix elements. The first result presented is from a pure nucleation model and the second by initially nucleating a 2% porosity content before letting only the porosity formation through the growth mechanism. For a similar porosity content (around 54%) the nucleation case shows porosity uniformly distributed within the matrix, while the growth mechanism creates large clusters of porosities embedded within large matrix areas as well.

This distribution can be summarized by computing the porosity density in each box. Fig. 3.29 shows the evolution of the different probability distributions of the porosity density over time with and without the growth mechanism. It appears that while the nucleation governed porosity formation yields a normal distribution with a low standard deviation, the standard deviation becomes much larger by considering the growth (especially as time increases). It is the direct statistical effect of the porosity areas observed on Fig. 3.28.

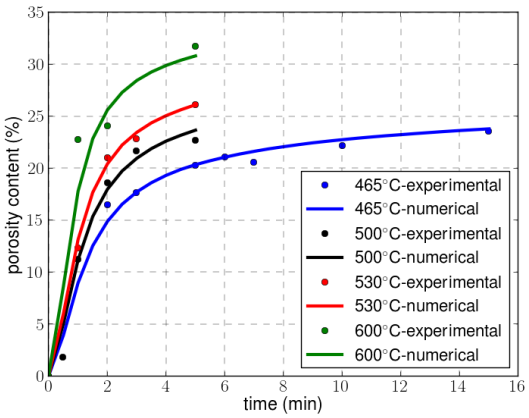

Figure 3.27. – Comparison of the experimental / numerical evolution over time of η_p^* for different temperatures of exposure considering the nucleation and growth processes

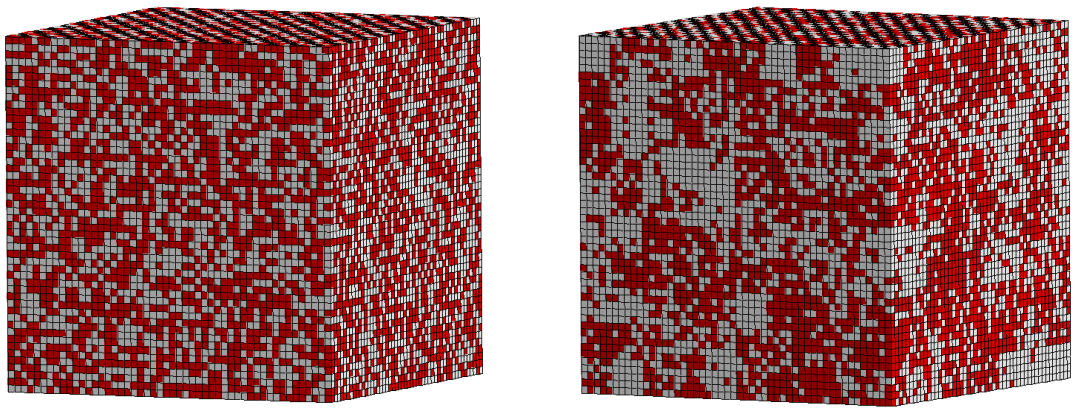

(a) (b)

Figure 3.28. – Porosity distribution for a 54% porosity content in a domain of matrix elements (100%) (a) with nucleation, (b) with initial nucleation followed by growth

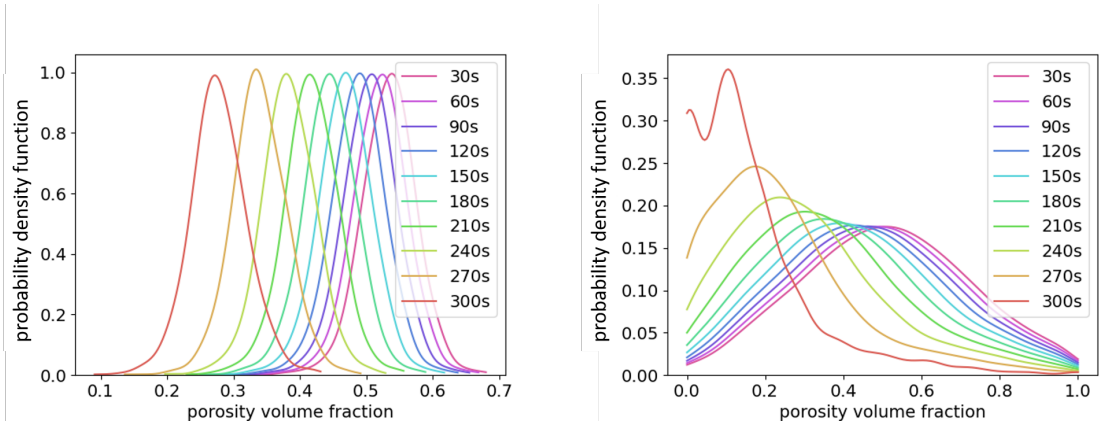

Figure 3.29. – Evolution through time of the distribution of the porosity density in each box over time. Porosities formed through (a) nucleation, (b) nucleation and growth

3.3.4. Thickness expansion: porosity-induced swelling

In order to reproduce the observed macroscopic swelling-induced expansion of the laminates, the simulation of porosity formation has to be completed by a mechanical simulation to include the mechanism of swelling at the scale of porosities. As to mimick a gas, a porosity is treated as a solid isotropic elastic material with a Young Modulus of 10^{-3}MPa. The fiber bundles and the matrix are assigned the same mechanical properties as those used in the previous work (Carpier et al., 2022):

— temperature-independent isotropic transverse elasticity for the fiber bundles; it is assumed that oxidization of the fibers does not occur;
— temperature-dependent isotropic elasticity for the matrix; in the molten state, its Young Modulus is set at 1MPa; it corresponds to the upper bound below which the set value does not impact the mechanical properties of the laminates, as explained in (Carpier et al., 2022).

In this configuration, the value of the imposed internal pressure becomes the only input governing the extent of the macroscopic swelling-induced expansion. Before addressing the question on how the value of the internal pressure was adjusted, a preliminary attention needs to be paid to the effect of mesh refinement.
Fig. 3.30 shows the geometry of the subdomain in its swollen state after a 5 minute exposure at 530°C for two mesh refinements depicted in Fig. 3.20. With the coarse mesh (corresponding to that in (Carpier et al., 2022)), the large size of the voids is at the origin of significant irregularities in the geometrical representation of the fiber bundles. A fine enough mesh, e.g. such as the one in Fig. 3.30(b), should thus be used in order to minimize the sources of artifacts in the thermomechanical modelling during the matrix decomposition.

Having defined the mesh refinement, further analyses were conducted on the qualitative effect of the imposed pressure on the thickness expansion. As a consequence of the rapide decrease of the matrix rigidity upon temperature increase, it was observed that the imposed internal pressure should be defined as a function decreasing through time at rates depending on the temperature of exposure. This function further needs to converge to a saturated value, such as to reproduce the stabilization of the thickness expansion to a constant value.
Let us note P_{int} this imposed internal pressure. The form of P_{int} given in Eq. 3.33 enables to describe these trends:

$$P_{\text{int}}(t) = D_1 exp\left(-D_2 (t-1)^{D_3}\right) + D_4 \tag{3.33}$$

$(D_i)_{i=1,...,4}$ are constant parameters which enable to introduce the dependencies to the temperature of exposure. Table 3.3 defines their respective roles and provide the values which were identified. Fig. 3.31 presents the simulated evolution of thickness expansion over time for three temperatures of exposure, to be compared with the experimental measurements.
The form which has been set for $P_{\text{int}}(t)$ is certainly arbitrary, but it produces a phenomenology which is consistent with physics. And Fig. 3.31 shows that the modelling thereby constructed is capable of correctly representing thickness expansion evolutions for different temperatures of exposure.

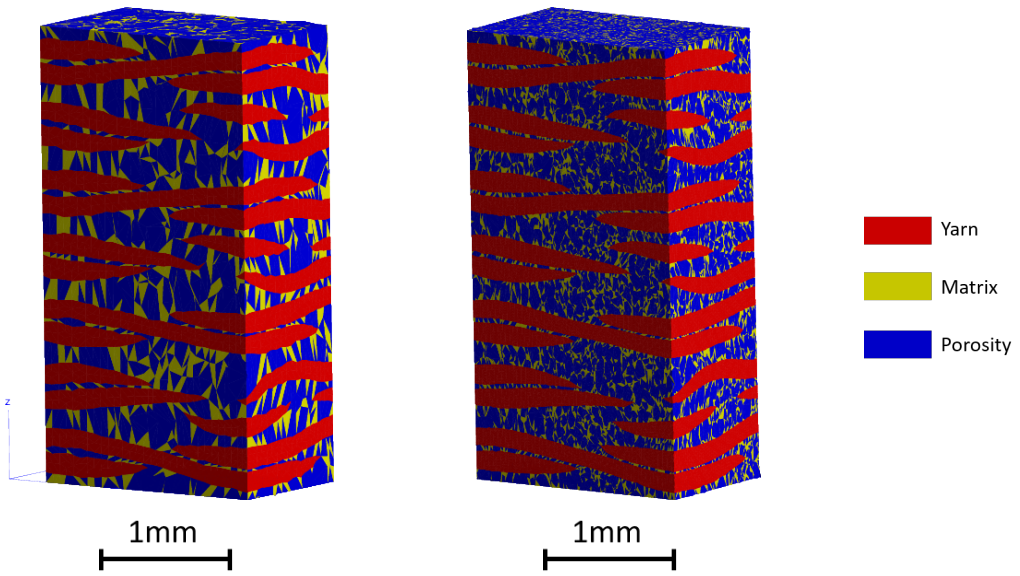

Figure 3.30. – Simulation of the porosity induced swelling on the laminates thermally decomposed for 5 minutes at 530°C. (a) coarse mesh (b) fine mesh

Parameter	Unit	Temperatures			Main role
		465°C	530°C	600°C	
D_1	Pressure (MPa)	0.836	0.590	1.82	Value of P_{int} at the initial time
D_2	Rate (s^{-1})	0.289	3.38	1.23	Dependence of P_{int} to t at the initial time
D_3	No unit	2.05	1.66	1.66	Dependence of P_{int} to t at the intermediate times
D_4	Pressure (MPa)	1.31	1.34	0.320	Asymptotic value of P_{int}

TABLE 3.3. – Parameters used to define $P_{\text{int}}(t)$ as given by Eq. 3.33

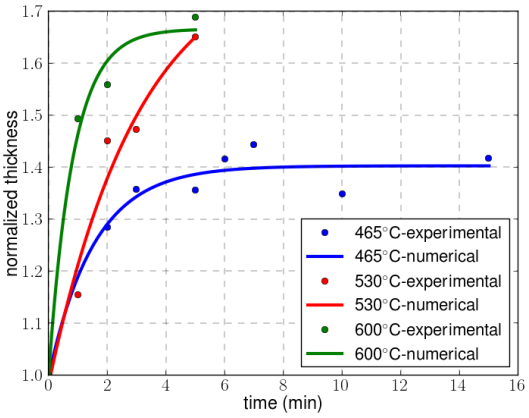

Figure 3.31. – Comparison experimental / numerical of the thickness expansion evolution over time for the different temperatures of exposure

3.3.5. Towards the modelling of the interface debonding

A preliminary experimental study was carried on the third and final identified porosity formation mechanism, i.e. the debonding at the interface between the fiber bundles and the matrix, without pursuing numerical modelling. The main influence of debonding is located at the interply due to the presence of porosities resulting from the processing of the material (Amedewovo et al., 2023). This was also observed in the literature in works such as (Sihn et al., 2023).
The thickness expansion observed on Fig. 3.5a actually originates from (i) the pressurization of the pyrolysis gas within the porosities and (ii) the interface debonding. These two phenomena can therefore be differentiated as to how they influence the swelling of the laminates.
In order to quantify the role of each mechanism, the protocol detailed in Section 3.1.2 was applied to thermal exposures for temperatures in the range from 250°C to 450°C as it was observed that the interface debonding onset is for temperatures lower than that of the thermal decomposition (as it can be observed on Fig. 3.32 at 350°C). The interface decohesion can then be isolated and the trend of its evolution over time and temperature determined. The obtained trend was then assumed to stay similar throughout the decomposition process. As a result, the thickness expansion originating from the interface debonding was obtained for the whole range of temperatures $[250;600]$ °C, and the one resulting from the pressurization was directly deduced.
The experimental results of this method is presented on Fig. 3.33 for various times of exposure. The debonding-related expansion was found to have a converging tendency, while a clear increase was observed at the onset of the thermal decomposition.

Although no numerical modelling of the debonding has been performed, cohesive elements could be used in future works to reproduce this mechanism.

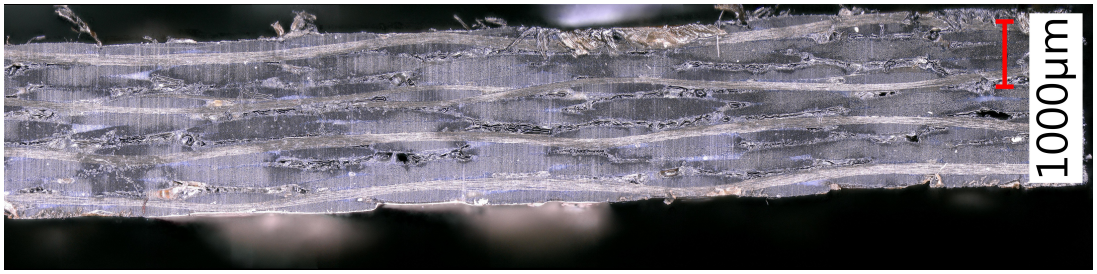

Figure 3.32. – Optical microscope observations of the porosities resulting from the debonding of C/PPS laminates after 5min of thermal exposure at 350°C

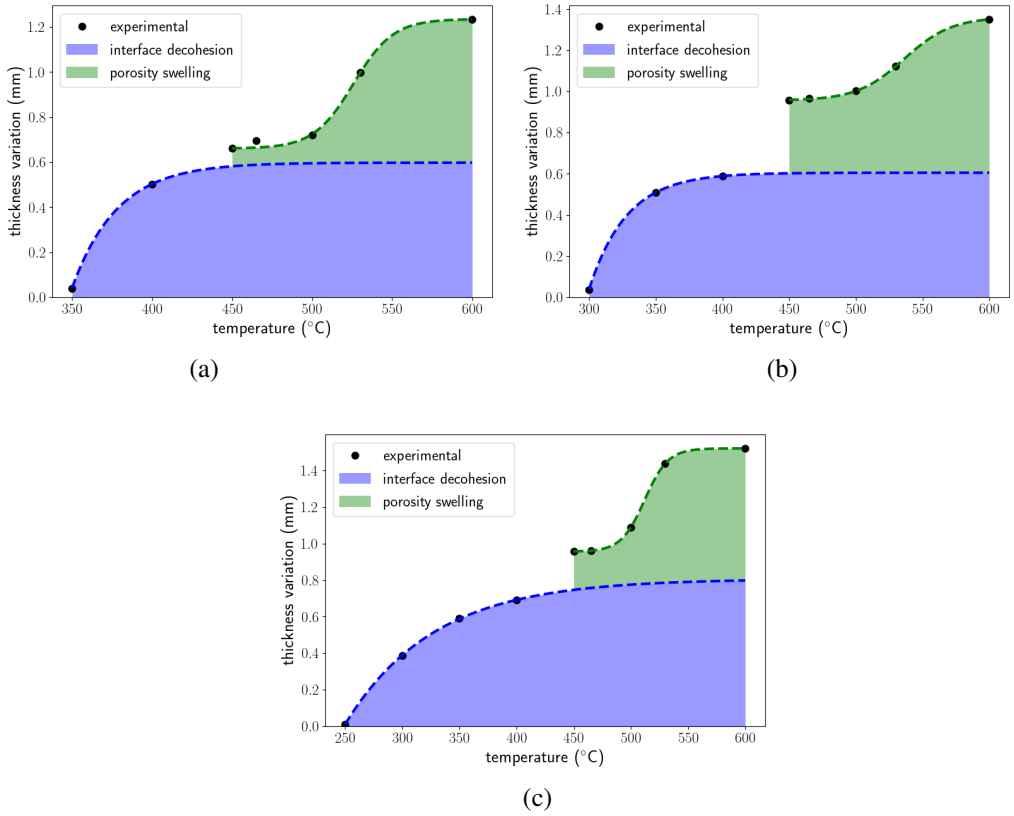

Figure 3.33. – Evolution of the thickness expansion over time, differentiating the pressurization and debonding mechanisms after (a) 2 min, (b) 3min, (c) 5min of exposure

3.4. Conclusion

First, it should be recalled that the present modelling is aimed at describing how through thickness thermal transfers and polymer matrix decomposition evolve concurrently during one-sided thermal irradiation of the laminates. This description is a prerequisite for any representation of

the load transfers and their consequences on the degradation of the mechanical properties of the laminates over time. It requires an accurate spatio-temporal representation of the porosity formation process. Its motivation is not so much to account for thermodynamics based mechanisms of solid-state transformations, but to reproduce the phenomenology of porosity formation kinetics at the mesoscale of the laminates. This is the reason why thermal decomposition mechanims, as enclosed in the modelling, are not fully representative of the involved physico-chemistry. Instead, they are locally incorporated in the numerical modelling according to a phenomenological time and temperature dependent probabilistic law.

Two kinds of porosities are observed experimentally: small ones, heterogeneously distributed, resulting from the nucleation, and large ones resulting from the growth mechanism. Both of these mechanisms were numerically reproduced by progressively transforming matrix elements of finite element model into porosity elements, based on a probabilistic approach. The nucleation law was first implemented and was able to precisely reproduce the porosity content experimentally determined. However, the porosity distribution was not as representative without the growth mechanism, which was then included in the modelling based on local porosity density computation. This porosity distribution should have an influence especially on the thermal transfers, as large porosity areas will act as thermal insulators.

Such an approach has shown its ability and robustness to reproduce both the evolution of the porosity content at different temperatures and the swelling induced expansion. Limitations were found for high temperatures (around 530°C) and times (over 5 minutes), when the laminates collapses. This phenomenon is due to internal structural effects associated with the decomposition of fiber bundles. Neither this intra-bundle decomposition mechanism nor its consequences are included in the numerical model. Such improvements will be the subject of future modelling developments.

The tendency for delamination at the matrix/fiber bundle interface was also noted, for temperatures above 250°C. However, as the current approach results in an accurate porosity content and swelling induced expansion, it fulfills the two main requirements for a correct prediction of the thermomechanical properties evolution of the laminates under thermal irradiation for temperatures up to at least 600°C, which is the ultimate purpose of this study.

From a qualitative point of view, the porosities were found to be homogeneously distributed within the laminates after swelling. This can be compared to micrographs of the laminates decomposed with same temperature (530°C) and time of exposure (5 min), as provided in Fig. 3.34a and 3.34b.

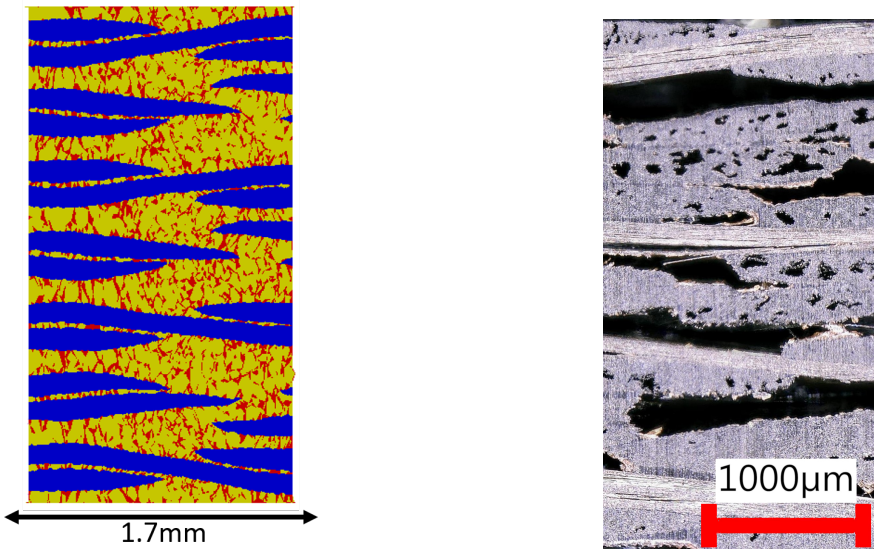

(a) (b)

Figure 3.34. – Observation of the porosity distribution on the contour of QI C/PPS laminates exposed to 530°C during 5 min: (a) as simulated, (b) as observed from optical microscopy

CHAPTER 4

THERMOMECHANICAL RESPONSE TO HIGH TEMPERATURES AND FIRE EXPOSURE

Contents

The changes in the thermal decomposition of QI C/PPS laminates as a function of time and temperature under homogeneous temperature exposure has been investigated in an initial step in Chapter 3. This knowledge can be used to understand the direct influence of the gradual pyrolysis of the polymer matrix on the thermomechanical behavior of the laminates, which is the ultimate purpose of this study. Indeed, the composite part should maintain a sufficient loading capacity to ensure the safety of passengers in a plane. The following sections present experimental and numerical studies on the influence of high temperature exposure on the thermomechanical properties, both in homogeneous and heterogeneous / fire exposure conditions. Post-exposure mechanical tests and combined thermomechanical ones are considered. The focus in terms of mechanical property was set on the axial stiffness as it can be estimated both experimentally and numerically.
Additionally, a preliminary study was carried on the thermomechanical response of a $\pm 45°$ laminates as this stacking configuration highlights the role of the matrix. Therefore, further characterization of the influence of the thermal degradation / decomposition can be performed.

4.1. Mechanical response after homogeneous temperature exposure: case of QI laminates

First, in the continuity of the previous chapter, a homogeneous temperature was considered.

4.1.1. Experimental post-exposure response

The failure mechanisms and residual mechanical properties after thermal decomposition were obtained applying the following protocol:
- Preparation of tensile samples (water cutting, cleaning, drying), as shown in Fig. 4.1
- Exposure in the muffle furnace at the setpoint temperature
- Removal of the sample after a given exposure time
- Post-exposure microscopic observations
- Post-exposure axial tensile tests to failure
- Microscopic observations after failure and assessment of the axial stiffness
- Use of three samples for each (time,temperature) testing conditions

Temperatures and durations of exposure were chosen in agreement with the ones studied in Chapter 3, with temperatures up to 530°C. Therefore, the porosity contents were known and could be directly correlated to the residual properties.

However it is to be noted that a systematic self-ignition of the samples occurred during thermal decomposition. Indeed, the pyrolysis gas concentration increases within the furnace as the sample thermally decompose. At some point, the concentration becomes too important and the ignition occurs. This was not observed during the heating of smaller samples of Chapter 3. Furthermore, the failure primarily occurred within the grip area. These phenomenona significantly influences the reliability of the quantification of stiffness and tensile strength degradation as the

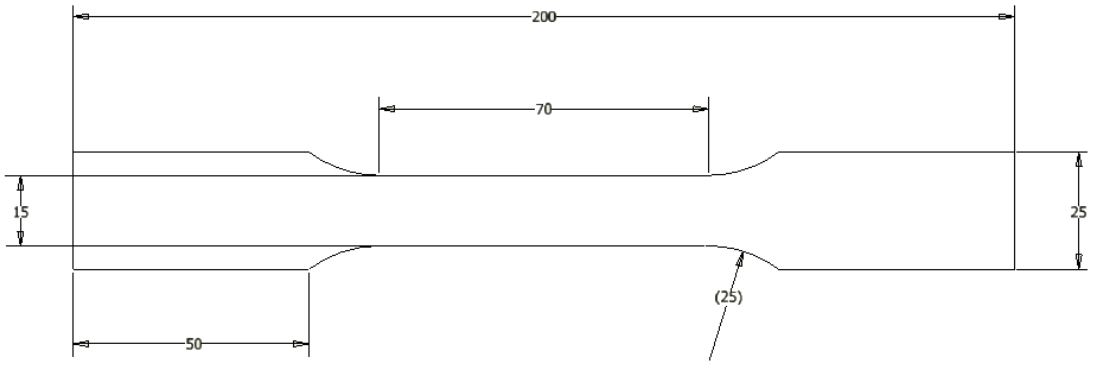

Figure 4.1. – Samples for post-exposure tensile tests

presence of a flame significantly increases the temperature within the furnace (which was not quantified). Hence, the quantitative conclusions of this subsection should be considered with caution.

Qualitative analyses on the failure mechanisms

As a high portion of the matrix (insuring the integrity of both the yarns and the plies) has thermally decomposed, a clear fracture path could not be observed. It was however a combination of a multitude of small fiber bundle fractures which ultimately led to the failure of the samples, as shown in Fig. 4.2. The front view shows the striction, rotation and crushing of the fiber bundles described in Section 1.2.3.
It appears that the thermal decomposition of the matrix does not alter the elastic brittle response to a axial strain loading .

Quantitative analyses of the residual mechanical properties

After thermal degradation/decomposition under homogenous temperature conditions, the residual tensile mechanical behaviour is investigated using a uniaxial servo-hydraulic machine MTS, equipped with hydraulic grips and a load cell with a 100kN capacity. The tensile tests are conducted in displacement-controlled mode (1mm/min) at Room Temperature (RT). The tensile mechanical properties were determined according to the European standards EN 6035 (Test standard EN 6035, 1996). The axial modulus (E^{ax}) and tensile strength (σ^u) were calculated from the following definitions:

$$E^{ax} = \frac{\Delta F}{S \Delta \epsilon^{ax}} \qquad \sigma^u = \frac{F^u}{S} \tag{4.1}$$

with

— ΔF is the difference in the tensile loads at $(\epsilon^a)_2 = 0.25\%$ and $(\epsilon^{ax})_1 = 0.05\%$,

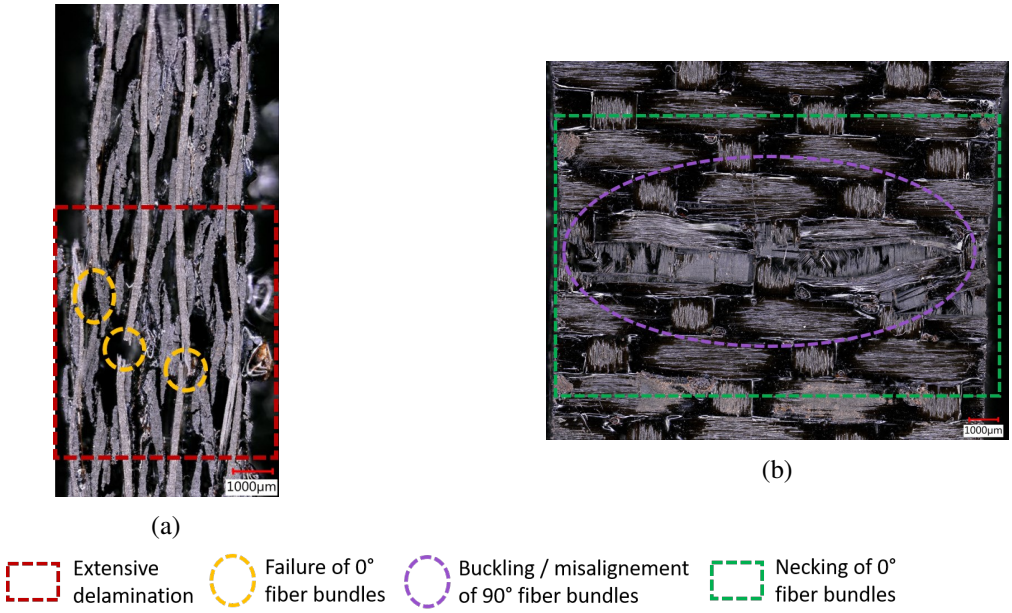

Figure 4.2. – Post-mortem optical microscopy observations of QI laminates after failure under tensile test / exposure to 530°C for 5min. (a) Through-the-thickness view, (b) front view

— S is the specimen cross section,
— $\Delta\epsilon^{ax} = (\epsilon^{ax})_2 - (\epsilon^{ax})_1$ is the difference in the axial strains obtained from a blade extensometer,
— F^u is the maximum force borne by the specimen at failure.

The obtained stress / strain curves are presented on Fig. 4.3 and compared with the behavior at room temperature (RT). The response of QI laminates remains mostly elastic brittle as the load is uniformly borne by the 0° fiber bundles. However for a 5min / 530°C exposure, the mechanical response is no longer purely elastic as the internal structure looses cohesion. Moreover, the failure of the laminates occurs in various steps, the stress decreasing step by step. This behavior is due to the fact that all the plies of the laminates do not fail simultaneously. Indeed, the decomposition of the matrix and its consequences on the internal structure is not fully homogeneous in all the plies. As a result, the 0/90° plies do not fail at the same time. When a ply fails, a drop is observed before it increases again when the remaining plies take up the loading. It replicates itself until the last ply fails.

The axial stiffness resulting from tensile tests conducted after thermal aggression is presented on Fig. 4.4a. Fig. 4.4a shows that this mechanical property is significantly influenced by the exposure to high temperatures. It is first to be noted that the figures only present results up to 3 minutes for the 465°C and 500°C cases due to a lack of sample material. As expected, the higher the temperature and time, the larger the stiffness decrease (see Table 4.1). The residual axial stiffness and the tensile strength even drops below 50% and 75% of their initial value after

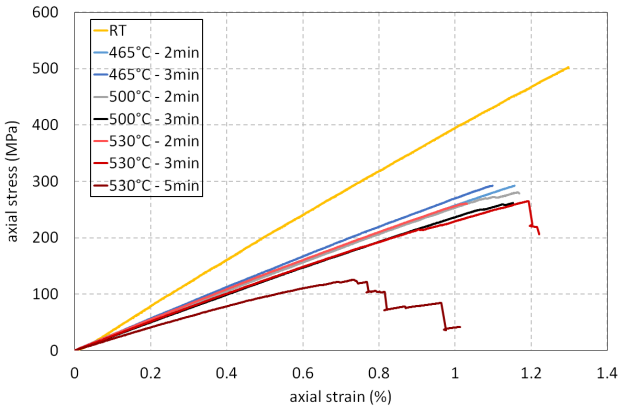

Figure 4.3. – Macroscopic strain / stress curves of QI laminates subjected to a tensile loading after isothermal exposure for different temperatures and durations

a 5min / 530°C exposure 4.2.

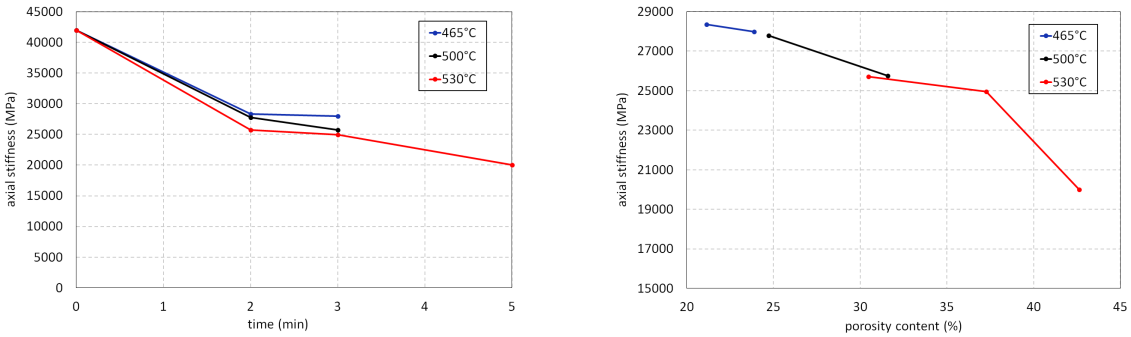

(a) (b)

Figure 4.4. – Evolution of the QI post-exposure axial stiffness over (a) time and (b) porosity content for various temperatures of exposure

	Axial stiffness (MPa) (decrease)		
	465°C	500°C	530°C
2min	28.4 (−32%)	27.8 (−34%)	25.7 (−39%)
3min	28.0 (−33%)	25.8 (−39%)	25.0 (−40%)
5min			20.0 (−52%)

TABLE 4.1. – Evolution of the residual axial stiffness of QI laminates as a function of exposure time and temperature

	Tensile strength (MPa) (decrease)		
	465°C	500°C	530°C
2min	289 (−44%)	272 (−47%)	253 (−51%)
3min	283 (−45%)	259 (−51%)	249 (−52%)
5min			129 (−75%)

TABLE 4.2. – Evolution of the residual tensile strength of QI laminates as a function of exposure time and temperature

As the porosity content was previously identified in Chapter 3 as a function of time and temperature , the stiffness loss can be directly correlated to the increase in the porosity content. Fig. 4.4b shows that the temperature of exposure (at least within the considered range) influences the porosity content but the stiffness evolution is only driven by the porosity formation. It is then possible to reduce the dimension of the function space characterizing the stiffness evolution from (t, T) to η_p.
It is to be noted that the tensile strength follows exactly the same trend.

4.1.2. Numerical modelling

The mesoscopic model described in Chapter 3 was used (using the thermomechanical properties described in Chapter 2) to assess the residual axial stiffness due to the thermal decomposition. It was numerically possible to reproduce post-exposure tensile tests as well as combined thermomechanical loadings. To that end, an axial displacement resulting in an axial strain ε_{11}^{imp} was applied to the $1/28^{th}$ RVE model (see Fig. 3.6) on one of its lateral sides during (combined) or after (post-exposure) the heating process depending on the loading. The numerical loading is applied according to the following procedure:

- Weak thermomechanical coupling
- At each time increment of the calculation:
  - Computation of the thermal problem
  - Extraction of the temperature field
  - Nucleation / growth of the porosities
  - Computation of the temperature-dependent mechanical problem in which the mechanical properties of the matrix vary according to the loading case: solid room temperature properties for post-exposure tests and temperature-dependent properties for combined loading
- Use of different temperatures and times of exposure

Let us denote the axial stiffness of the laminates E_{cl}^{a} defined from the axial stress σ_{11} averaged over the domain volume V:

$$E_{cl}^{a} = \frac{1}{V} \frac{\int_V \sigma_{11} dV}{\varepsilon_{11}^{imp}} \tag{4.2}$$

Preliminary simulations carried on a RVE model (geometry presented in Fig. 1.33) have

estimated a E_{cl}^{a} value of 43.4MPa at room temperature, which can be compared to the 42.0MPa value obtained experimentally (Aucher, 2011). The 3% difference may stem from (i) the chosen mechanical behaviors of the constituents, and (ii) a lack of interaction within the crossing areas of the fiber bundles.
Selecting a $1/28^{th}$ subdomain of the RVE did not influence the representativity of the model as far as the thermal decomposition process was concerned as it is solely influenced by the matrix volume fraction at the pristine state. However, it is not the case for the mechanical properties. 19 additional $1/28^{th}$ subdomains were selected from random positions within the RVE. Their matrix volume fraction as well as their axial stiffness at room temperature and after melting of the matrix (combined thermomechanical loading) were assessed. The results are presented in Fig. 4.5. The matrix volume fraction was normalized according to the RVE one (39.75%), as well as the axial stiffness (42.0MPa at room temperature and 22.9MPa after melting of the matrix). It appeared that only the original subdomain has precisely the same matrix volume fraction at the pristine state, although six others are within a ±5% which confirms the possibility to accurately reproduce the thermal decomposition of the matrix. However, it is quite different in the case of the mechanical response. Results show large differences in the model axial stiffness which are over 10% for every subdomains (apart from the one having a low matrix volume fraction). Stiffnesses associated with pristine and molten matrix present different tendencies:

— In the pristine state, the stiffness evolution over matrix volume fraction seems to follow a linear trend as expected, with the low-percentage matrix domain having higher stiffnesses and vice versa. However the linear curve does not cross the origin at (1.0,1.0), but rather around (1.0,0.85) which means an overall underestimation of 15%.
— In the molten state the differences are more significant and no trend can be observed whatsoever.

These major differences may be attributed to the lack of interaction within the weave pattern. Indeed, as the model domain is too small to consider several fiber bundles in each ply, no influence of the weave pattern on the mechanical behavior is included. This would explain the discrepancies at the molten state. Indeed, the fiber bundle interaction becomes necessary to ensure the cohesion of the laminates as the matrix no longer does.

It was chosen to keep the original subdomain used in Chapter 3 and not to increase its size as it would be too time consuming. Therefore this modelling error must be kept in mind, especially when quantitatively discussing the stiffness decrease due to high temperature exposure. In the remaining sections of the study, two approaches were considered to present the numerical results:

— A normalization by the initial value at room temperature
— An artificial increase in the stiffness to replicate that of the RVE at room temperature. This compensates for the post-processing the difference observed due to the lack of representativity of the $1/28^{th}$ RVE subdomain.

Fig. 4.6 summarizes the evolution of the stiffness as a function of the porosity content for different temperatures (465°C and 530°C), loading nature (post-exposure or combined) and porosity formation mechanism (with or without growth consideration). This figure thereby collects mea-

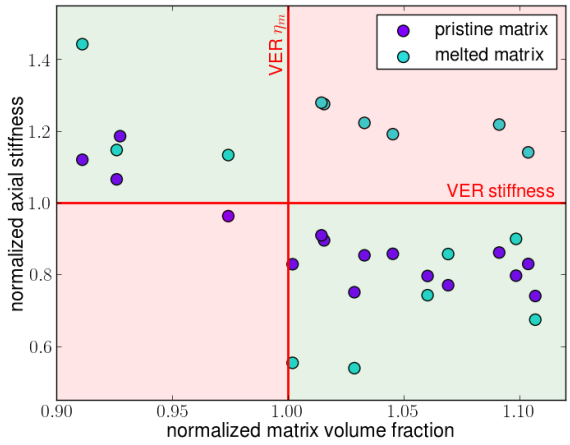

Figure 4.5. – Evolution of the normalized axial stiffness of QI laminates over normalized matrix volume fraction in the pristine state as predicted by the numerical model before and after the melting of the matrix. Each subdomain has two datapoints located at the same matrix volume fraction

surements at different times of exposure in order to cover a wide range of porosity contents. The results show that only the porosity content and the matrix state have a first order effect on the stiffness decrease as little variation is brought by the temperature and the growth process. However higher temperatures mean higher porosity contents and hence a more important property degradation. Quantitatively, the stiffness shows a larger relative decrease with the post-exposure simulations than with the combined ones (10% against 2%). It can be explained by the fact that stiffness decrease resulting from replacing solid matrix by a gas is larger than in the case of liquid matrix replaced by gas.

By comparing the experimental results to the numerical ones obtained with this approach (see Fig. 4.7), the thermal decomposition appears to be less detrimental in the modelling. It is attributed to several reasons:

— On one hand the influence of the decomposition is in the modelling lower as debonding is not fully taken into account as previously explained
— On the other hand the decrease was accentuated in the experiments by the self-ignition of the samples
— The intra-fiber bundle porosities, as observed experimentally on Fig. 3.2, were not modelled. An example of a 530°C exposure for 5min was taken: it was observed that 10% of the fiber bundles consisted of voids. These voids were inserted within the model by randomly transforming 10% of the yarn elements into porosities, and they contributed to decrease the stiffness (about 11%). However this procedure has not yet been automatically implemented.

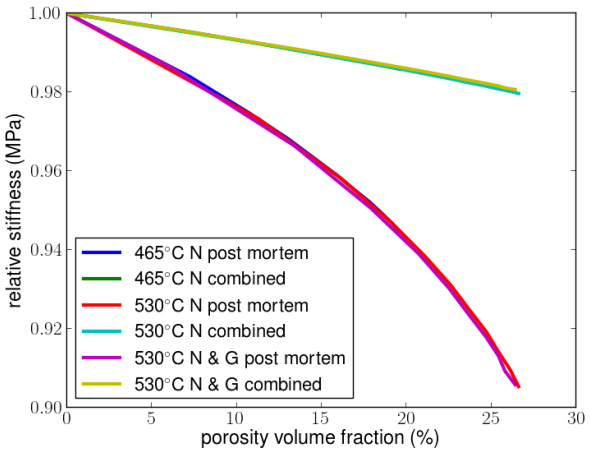

Figure 4.6. – Evolution of the axial stiffness of QI laminates as a function of porosity content as predicted by the numerical model for various temperatures, with (N & G) or without (N) growth mechanism and post-exposure / combined thermomechanical loading. Results at 465°C and 530°C for similar modelling case are juxtaposed

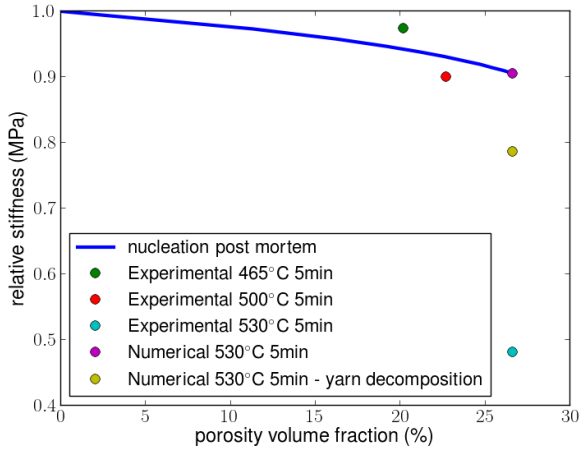

Figure 4.7. – Comparison of the evolution of the post-exposure axial stiffness of QI laminates as a function of porosity content as predicted by the numerical model and experimental data after 5 minutes of exposure at different temperatures. Example of the influence of yarn decomposition included after 5 minute exposure at 530°C

Given that including the growth process does not directly influence the resulting axial stiffness while increasing the computation time, it was chosen not to consider it for pure quantitative simulations. However, it is compulsory for an adequate simulation of the physics put into play.

4.2. Mechanical response after fire exposure: case of QI laminates

In the previous section, isothermal conditions lead to a homogeneous temperature distribution within the laminates' plies. But thermally-induced damages are characterized by heteregeneous effects depending on the plies orientation and the spatial distribution of PPS matrix and carbon fibers. Once the mechanisms of porosity formation is better understood under isothermal conditions, the next step consists in studying the influence of a heterogeneous temperature distribution within the laminates subjected to one-sided fire conditions.

4.2.1. Experimental response to fire exposure

Heterogeneous thermal decomposition

An approach similar to the one used in homogeneous temperature conditions was considered to expose C/PPS samples to a fire scenario. To this end, a small scale kerosene burner was used to apply a localized flame on one side of the samples. The kerosene burner shown in Figure 4.8a is a domestic device (Cuenod manufacturer), built during the AEROFLAMME project and has already been used in previous works (Vieille et al., 2022, 2023). The kerosene is injected in a nozzle generating a hollow cone spray with an angle equal to 80° and a maximum flow rate of 0.3 g/s. This flow rate is controlled with a mass flow meter (MINI CORI-FLOW™ - Bronkhorst), and it can be adjusted. Airflow is also controlled with a mass flow meter (EL-FLOW® Prestige - Bronkhorst). The air to fuel ratio has been selected at 0.85 of the stoichiometric value, in order to obtain heat flux and temperatures values close to the standard values (116kw/m^2 and 1100°C) at the sample location. The flame at the exit of the turbulator is a wide and turbulent jet. Therefore, a 50 mm diameter steel tube is installed after the turbulator to channel the hot combustion gases on the exposed area of the sample. The heat flux applied was measured at 116kw/m^2 as per the FAA instructions. The experimental bench is also equipped with a 100kN tensile load cell which allows a coupling of the thermomechanical loadings, see Fig. 4.8b.

Under fire conditions, the temperature on the back surface is measured by a thermocouple stuck on the laminates with thermal tape. To a first approximation, this allows the back surface of C/PPS laminates subjected to a kerosene flame to be measured as a function of exposure time (Fig. 4.9). After about 10 and 40 seconds, the back surface temperature has reached T_g transition and T_m, respectively. The temperature is stabilized after 120 seconds to reach about 380°C $< T_d$. It therefore suggests that the thermal decomposition has not started in the plies opposed to the flame. In addition, the thermal gradient through the thickness is about 300°C, meaning that the state of the PPS matrix differs from one ply to another. From the load bearing capability standpoint, it also means that the $\pm 45°$ oriented plies have little contribution to bear a tensile load. One may speculate that the portion of the tensile load borne by the 0° plies gradually decreases from the exposed to the back surface. An accurate estimate of these portions cannot be quantified experimentally, but the role played by each of the seven plies of the C/PPS laminates can be determined qualitatively by means of post-mortem fractographic analyses.

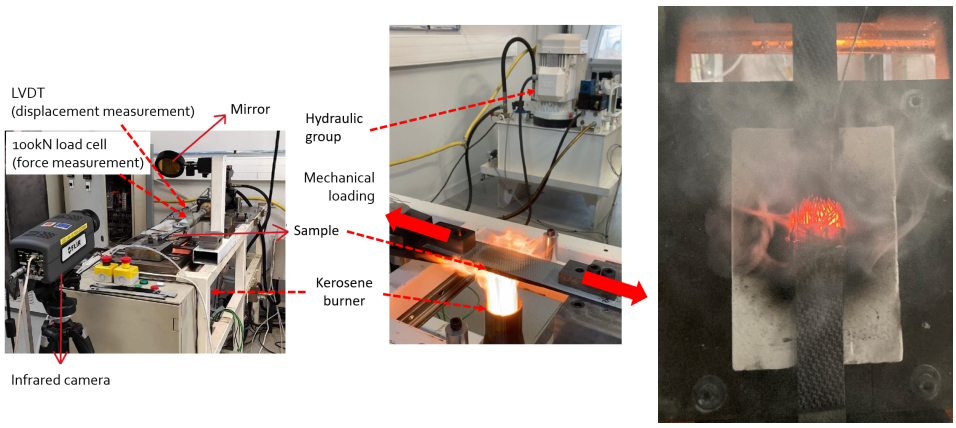

(a) (b)

Figure 4.8. – In situ tensile behaviour of C/PPS laminates subjected to a kerosene flame during mechanical loading: (a) description of the experimental bench, (b) tensile testing during fire exposure

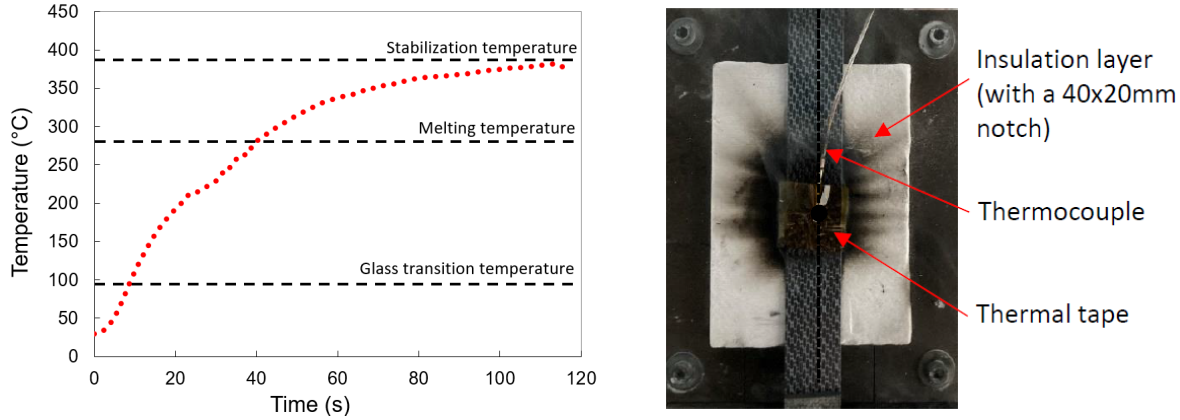

(a) (b)

Figure 4.9. – Measurement of the temperature at the back surface of C/PPS laminates subjected to a kerosene flame: (a) temperature vs exposure time, (b) experimental set-up

Fig. 4.10 and 4.11 present optical microscopy observations on QI laminates for 30s and 60s of flame exposure from different views: (i) through-the-thickness, (ii) exposed surface and (iii) back surface. Results show a clear decomposition gradient through the thickness. About half of the laminates remains at temperatures lower than T_d after 30s of exposure while only the opposed ply seems undamaged after 60s. However matrix rich areas are still embedded between the fiber bundle crossing areas. The microscopic observations show that the back surface is virtually unchanged with respect to its virgin state. On the contrary, the exposed surface is characterized by the occurrence of a few bubbles resulting from the formation of pyrolysis gases

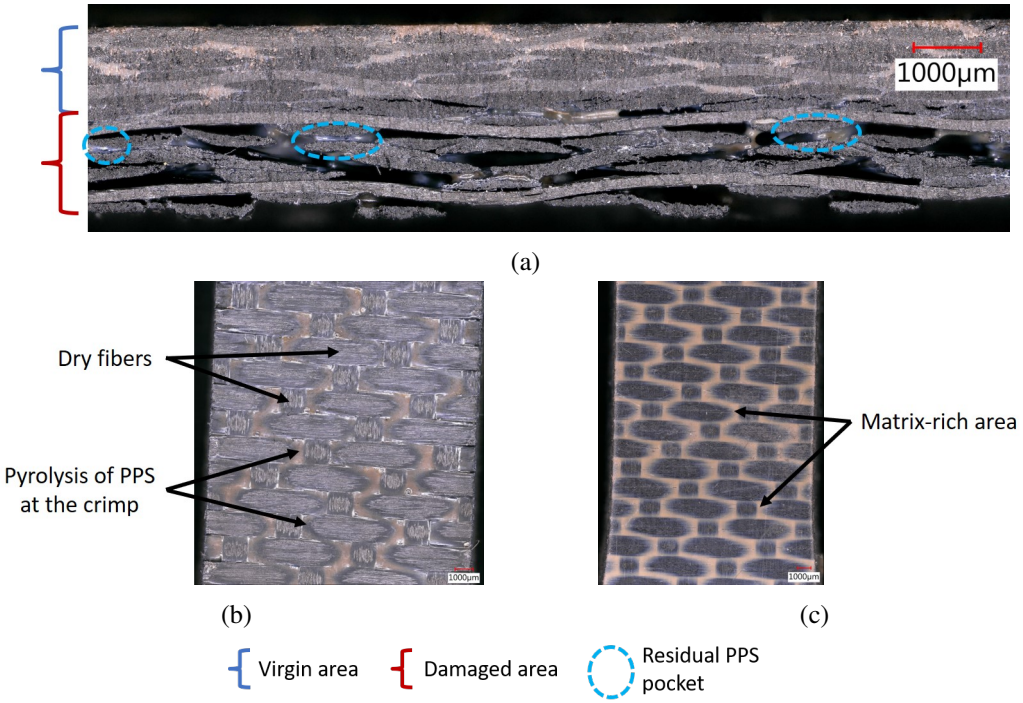

Figure 4.10. – Optical microscopy observations of the heterogeneous thermal decomposition of QI laminates after exposure to a 116kw/m^2 flame heat flux for 30s. (a) Through-the-thickness view, (b) exposed surface, (c) back surface

at the crimp (where the warp fibers undulate over the weft fibers forming matrix-rich areas), see Fig. 4.10b and 4.11b. One may also notice dry carbon fibers suggesting that most of the PPS matrix has been thermally decomposed. The through thickness view reveals that the QI laminates underwent significant delamination along with porosities resulting from the formation of pyrolysis gases. The time-influence can be summarized as follows:

— After 30s, some of the PPS between the fiber bundles has been decomposed. Furthermore, a majority of the matrix embedded within the yarns turned into gas, then exposing the fibers to the flame and possible oxidization.

— After 60s, some fiber debonding is observed. The pyrolysis of the matrix occurred and the matrix was transformed into char due to direct fire exposure. A few pyrolysis gas pockets can be observed at the exposed surface which were formed within the higher plies.

Thermally-induced damages are more extensive under the flame area as was suggested by a more important swelling of the laminates through the thickness and a less extensive delamination along the axial direction. Of course, such thermally-induced damages are expected to have a significant influence on the residual tensile behavior of C/PPS as is discussed in the next section.

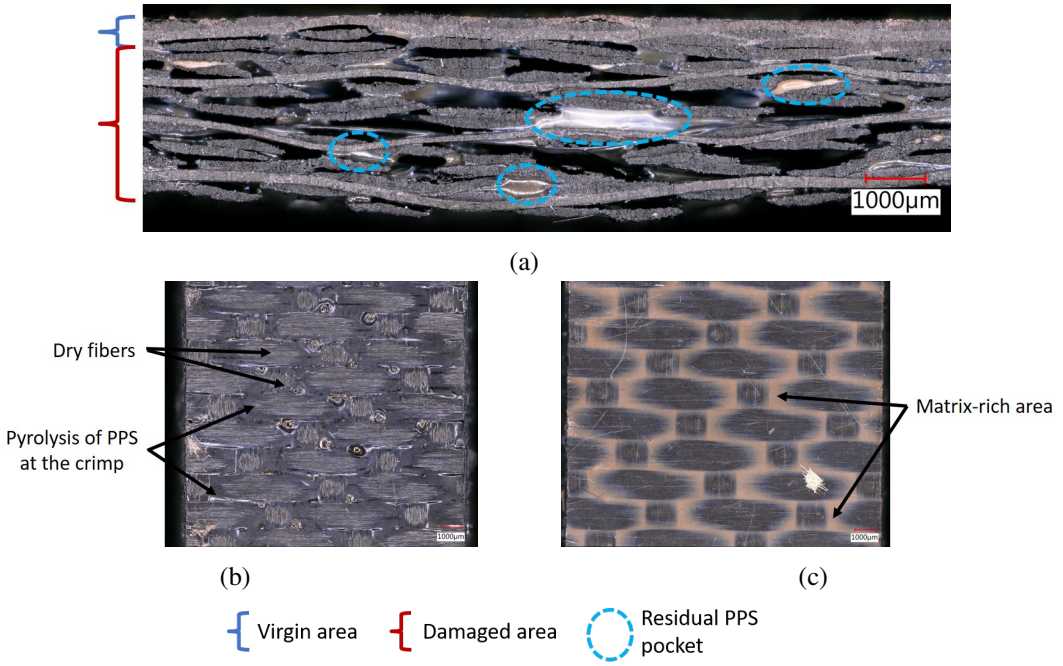

Figure 4.11. – Optical microscopy observations of the heterogeneous thermal decomposition of QI laminates after exposure to a 116kw/m^2 flame heat flux for 60s. (a) Through-the-thickness view, (b) exposed surface, (c) back surface

Post-exposure mechanical behavior

The same mechanical testing protocol as the one described in Section 4.1.1 was used for exposure times of 30s and 60s to a 116kw/m^2 flame heat flux. Fig. 4.12 presents the microscopic observations of the QI samples after 60s of exposure. It appears that the failure occurs in the most decomposed area. Contrary to the post-exposure tests carried out after homogeneous temperature exposure, a clear crack path can be noticed, especially on the back surface. It is due to the fact that the opposed plies are not decomposed, and their structural integrity is rather well preserved.

Quantitatively, the fire exposure appears to have a limited influence on the axial stiffness of the QI laminates for exposure times up to 1min (see Fig. 4.13). It is explained by the fact that the back plies are almost not decomposed and still contribute to maintain a portion of the laminates' stiffness. The tensile strength is however lower as the stresses are extremely concentrated on the back area which induces a faster failure of the material.

4.2.2. Modelling of the thermal decomposition

The experimental setup was numerically reproduced by applying a 116kW/m^2 heat flux and considering the thermal transfers described in Section 2.1.2. First and foremost, the thermal properties of the porosities were set. Although a gas does not physically have a thermal con-

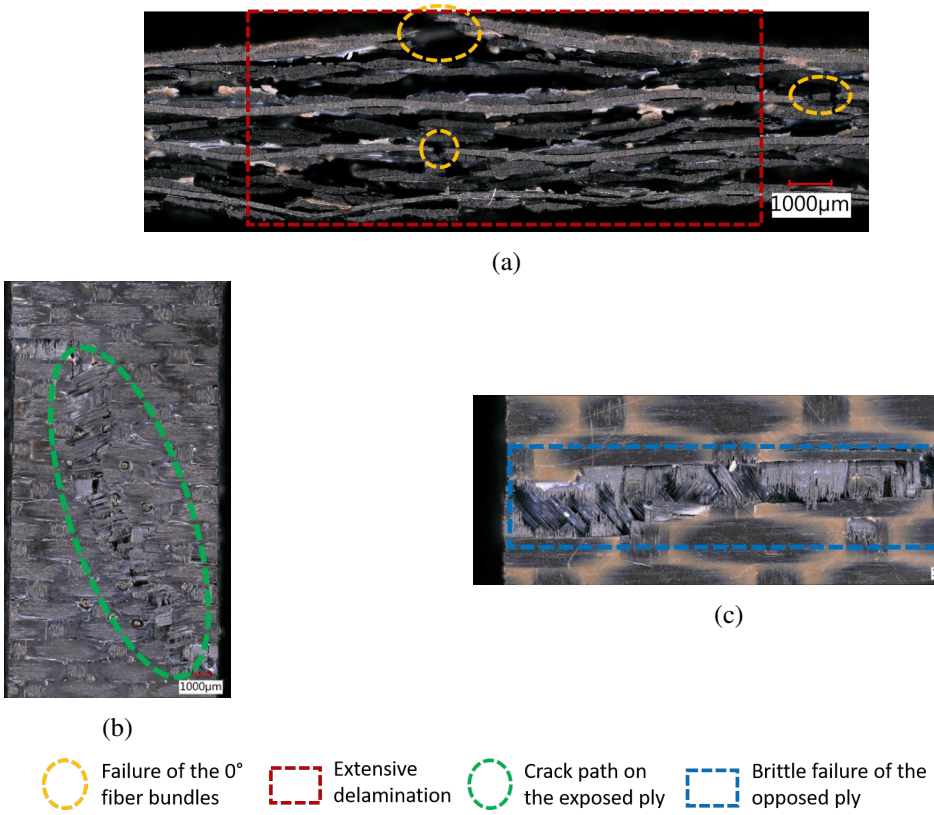

Figure 4.12. – Optical microscopy observations of the post-mortem QI laminates under tensile loading after exposure to a 116kw/m^2 flame heat flux for 60s. (a) Through-the-thickness view, (b) exposed surface, (c) back surface

ductivity coefficient, similarly to Section 3.3.4 the gas was assumed to transfer heat as a solid material. This approach was also used in works such as (Cheung et al., 1962) or (Mirabolghasemi et al., 2019). The selected property and its evolution as a function of temperature was extracted from (The Engineering ToolBox, 2009). Fig. 4.17 shows the selected almost linear evolution of the porosity thermal convection with temperature.

Heterogeneous thermal decomposition

Fig. 4.14 shows the case of a 116kW/m^2 heat flux imposed on the bottom surface during 90s. It presents the distribution of porosities on the contour of the mesh with or without accounting for the porosity-induced swelling through internal pressure. Both numerical decomposition gradient and swelling are in good agreement with those observed experimentally in the same conditions of thermal aggression (see Section 4.2.1).

A more detailed view of the laminates is presented by Fig. 4.15 in the case of porosity formation through the nucleation mechanism only. The through thickness gradient clearly appears,

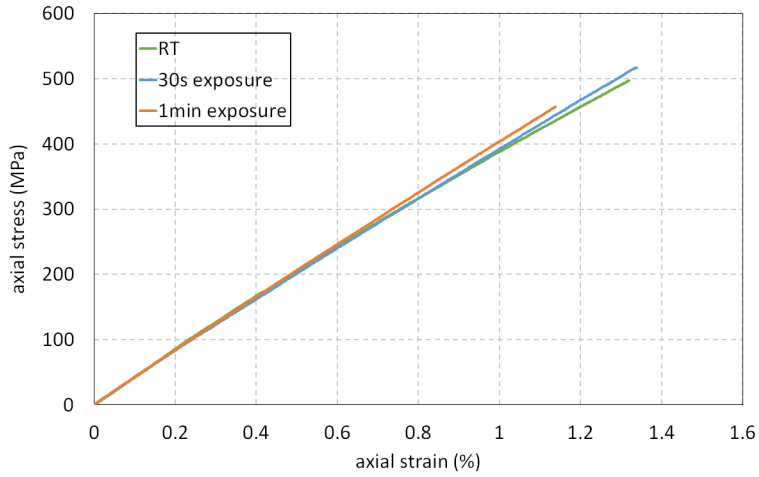

Figure 4.13. – Post-exposure strain / stress curve of QI laminates under tensile loading after exposure to a 116kw/m^2 flame heat flux for different times

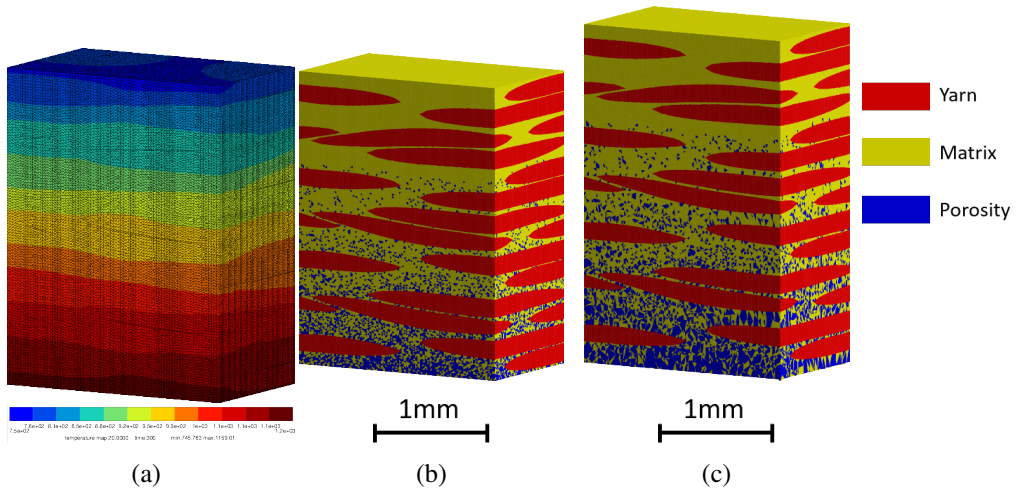

Figure 4.14. – Simulation of thermal decomposition under heterogeneous temperature after exposure to a 116kw/m^2 heat flux for 60s (a) temperature field (°C) ,(b) without swelling ,(c) with swelling

as well as the equi-distribution of the porosities at a given height of the sample. The differences brought by the growth mechanism can be observed in Fig. 4.16 showing that the porosities appear in larger clusters.

From this full-field representation of thermal transfers and porosities, it is possible to extract characteristic measurements of the state of the laminates from ply to ply. Fig. 4.18 depicts the average temperature and induced swelling per ply, highlighting the decomposition state reached

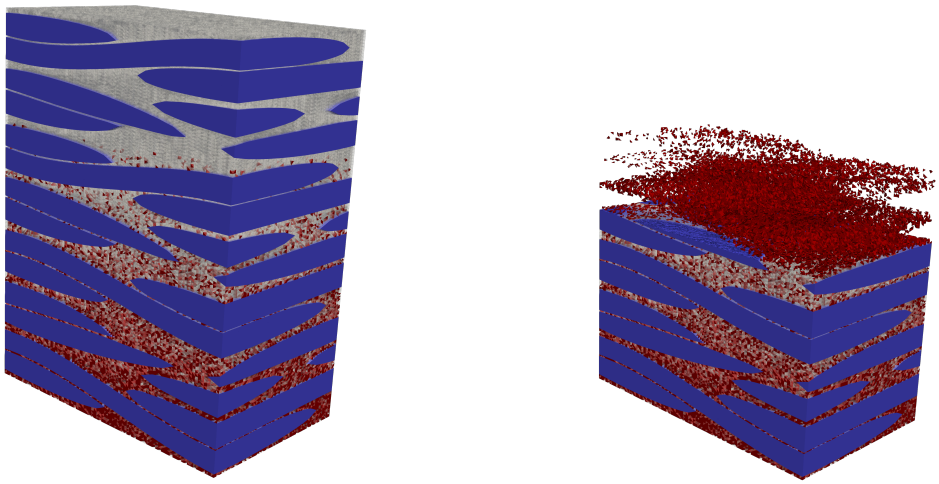

(a) (b)

Figure 4.15. – Simulation of the thermal decomposition by *nucleation* of the porosities caused by exposure to a 116kw/m^2 heat flux for 60s. (a) Whole laminates,(b) volumic view

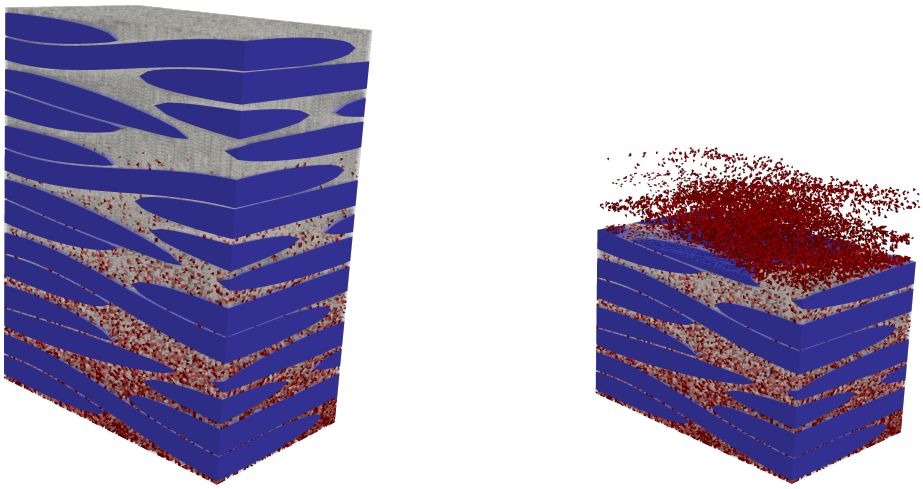

(a) (b)

Figure 4.16. – Simulation of the thermal decomposition by *nucleation and growth* caused by exposure to a 116kw/m^2 heat flux for 60s. (a) Whole laminates, (b) volumic view

in the different plies of the laminates. In order to represent gradients of out-of-plane displacement and porosity content, one can consider the characteristic values of each plies (respectively taking the maximum value or averaging). It is possible to further discretize for a more precise evolution. At the maximum, each ply can be divided into 10 subvolumes in the form of in-plane slices at different heights (10 being in average the number of elements through the thickness of a

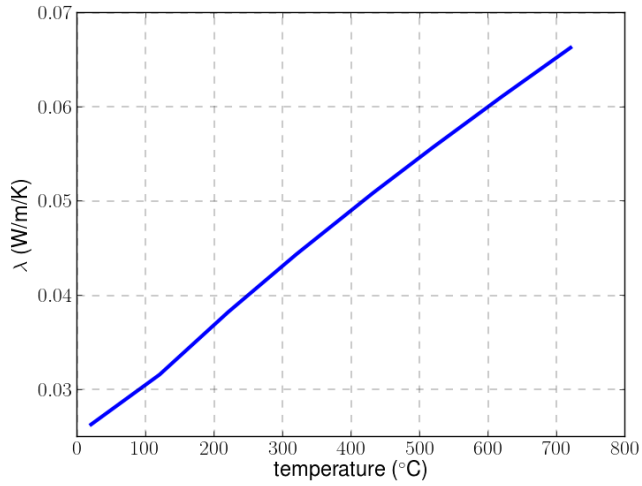

Figure 4.17. – Evolution of the porosity thermal conductivity with temperature

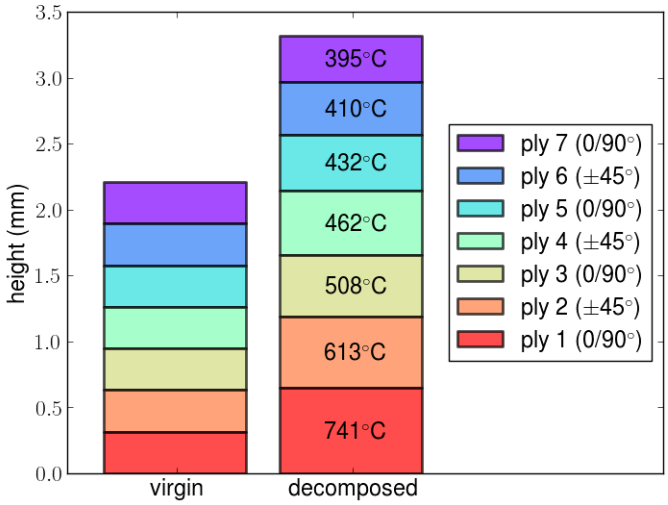

Figure 4.18. – Schematics of the out-of-plane swelling and average temperature after exposure to a 116kw/m^2 heat flux for 60s

ply). Depending on the discretization degree chosen (here 1, 3, 5 and 10), the overall tendencies on the out-of-plane displacement and the porosity content are similar with an increase from one ply to another as temperature increases (from the back surface to the exposed one), see Fig. 4.19. However, to a refinement of the discretization corresponds an increase in the variations within each ply. This variations stem from the mesostructure of the plies, as the matrix is primarily concentrated in the lower and upper parts of each pristine ply. As a result, the porosity con-

tent as well as the out-of-plane displacement are much higher at the ply borders. This intra-ply variation can be overcome by excluding the fiber bundle volume from the total volume used in the calculation of the porosity content so that the porosity content corresponds to the amount of porosities within the matrix (see Fig. 4.20).

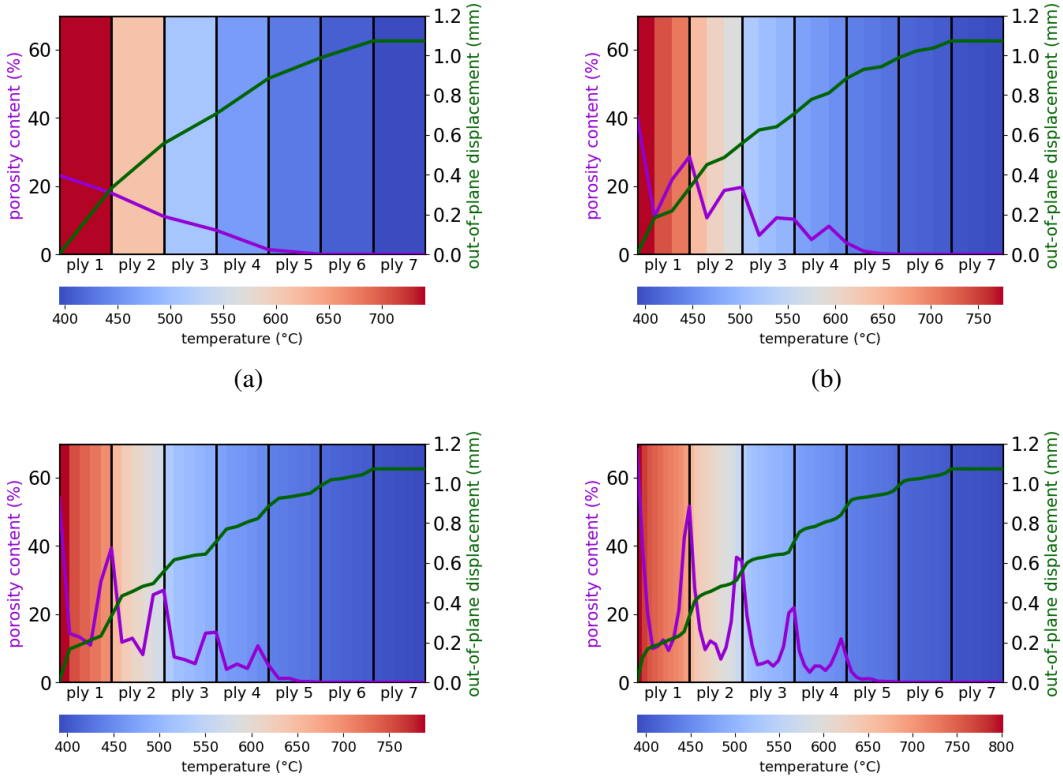

Figure 4.19. – Evolution of the numerically modelled out-of-plane displacement and porosity content in each plies after exposure to a 116kw/m^2 heat flux for 60s. Each ply discretized into a different amount of subvolumes: (a) 1, (b) 3, (c) 5 and (d) 10

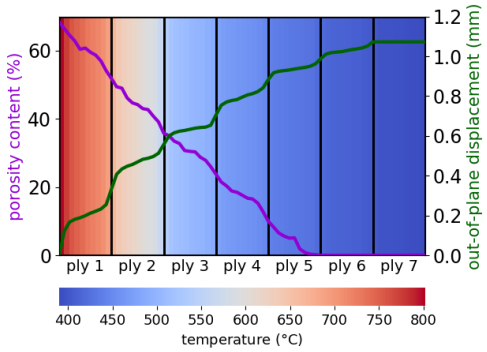

Figure 4.20. – Evolution of the out-of-plane displacement and porosity content (as obtained excluding the fiber bundle volume from the calculation) in each plies after exposure to a 116kw/m^2 heat flux for 60s

4.3. Preliminary study on ±45° laminates

±45° laminates are charaterized by a matrix-dominated thermomechanical response. Some of the experimental tests conducted on QI laminates were also performed on ±45° specimens. The differences observed provide an overview on the possibility to further characterize the influence of the matrix melting and thermal decomposition.
It is to be noted that the microscopic observations presented in this section are based on 0/90° specimens. These samples were used only for the study of the thermal decomposition process, without being subjected to a mechanical loading, in order to spare specimens.

4.3.1. Thermal decomposition process under homogeneous temperature

The same procedure as the one followed with QI specimens (Section 3.1) was used. The self-ignition of a few samples occurred within the furnace due to the high concentration of pyrolysis gas, hence they were removed from the analyses. Suspicion of ignition exists for most of the specimens as large amounts of char has formed on the upper surface, which is a typical consequence of flame exposure. This probably influences the presented results, at least quantitatively. The microscopic observations are shown on Fig. 4.21 for various temperatures. Regarding the influence of the stacking sequence, porosity formation in ±45° laminates is associated with larger gas pockets. It could be explained by the fact that matrix-rich areas are initially localized at the crimp (where weft fibers undulate over warp fiber bundles), which is less noticeable in QI laminates (see Fig. 3.2 for the QI observation in the pristine state). It can also be observed that intra-yarn porosity formation remains almost equivalent between 530°C and 600°C, as opposed to larger porosity content in fiber bundles observed in QI laminates at 600°C.

The porosity content evolution was then determined and its evolution over time for different temperatures is presented on Fig. 4.22 along with the thickness increase and the mass loss on Fig. 4.23. Overall, the results show a higher porosity content in ±45° laminates than in the QI

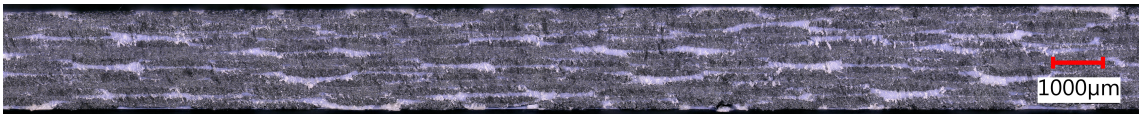

(a) Virgin sample

(b) 465°C – 5min – Porosity content: 32.5%

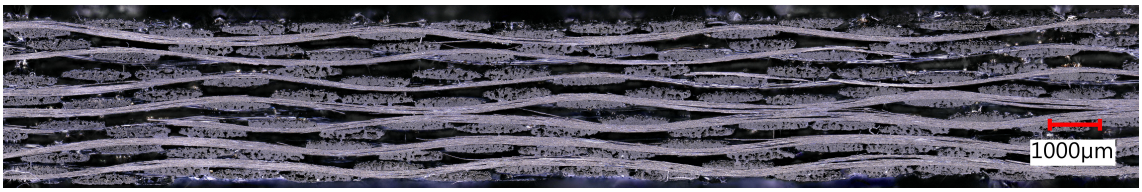

(c) 530°C – 5min – Porosity content: 51.3%

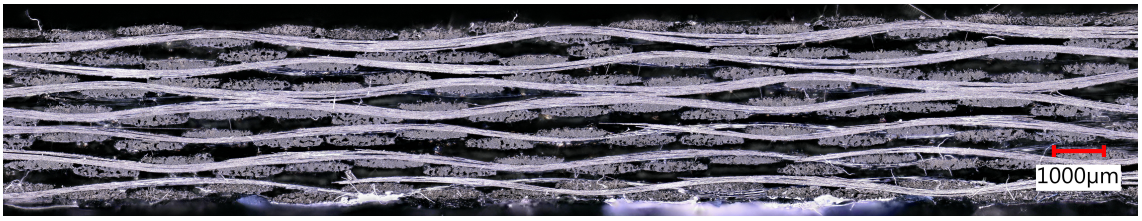

(d) 600°C – 5min – Porosity content: 56.9%

Figure 4.21. – Optical microscope observations of thermally decomposed ±45° C/PPS laminates under homogeneous thermal exposure at different temperatures and exposure times. The plane of observation is a 0° plane

ones (over 10% increase). This originates from the extensive thickness expansion. Indeed, the final thickness is larger and it is to be noted that the thickness collapse does not appear even after 10 minutes. One can assume that the matrix-rich areas at the crimp (responsible for large porosity pockets) are governing this different response, along with a better fiber bundle cohesion observed. Different trends can be observed at different temperatures. While the porosity content converges extremely rapidly during the first 2 minutes at 465°C and 600°C, the 530°C evolution does not allow a faster saturation to be concluded. These differences could be explained as follows:

— At 465°C, the thermal energy is not large enough to promote the decomposition for a porosity content higher than 30%
— At 530°C, the thermal energy is sufficient for the thermal decomposition to carry on at a slow rate
— At 600°C, the temperature is high enough and the material almost instantaneously reaches its maximum decomposition state

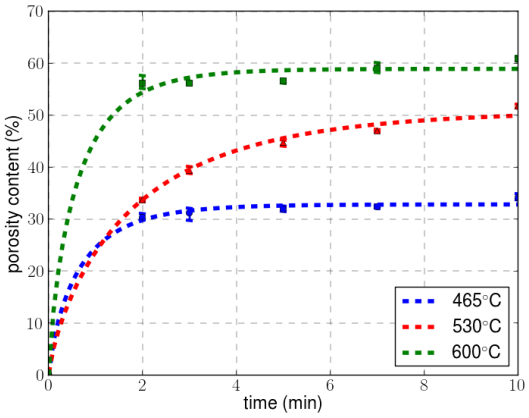

Figure 4.22. – Evolution through time of the porosity content in ±45° laminates for different temperatures of exposure, as measured with the geometry-based method

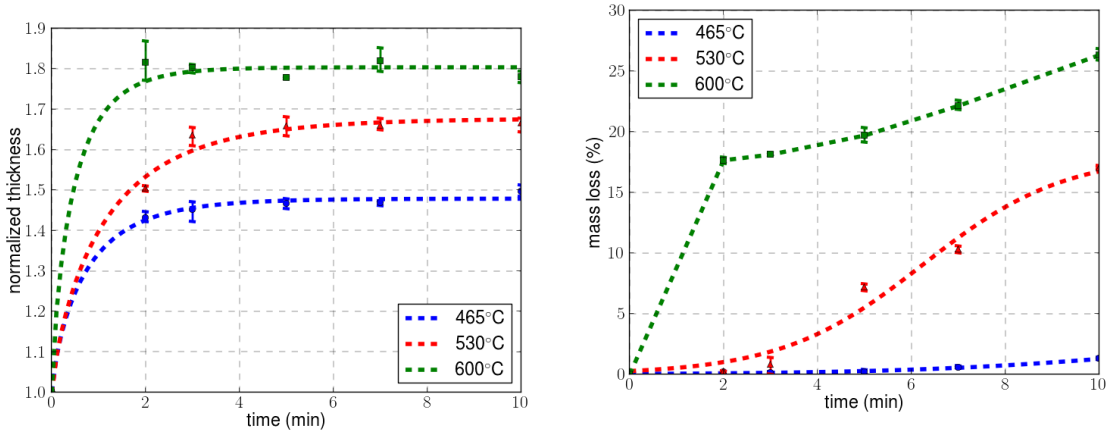

(a) Sample thickness

(b) Sample mass loss

Figure 4.23. – Evolution as a function of time of the geometry-based method characteristic quantities (thickness and mass) in ±45° laminates for different temperatures of exposure

It can also be observed that the pyrolysis kinetics do not depend on the stacking sequence as the mass loss remains quite similar to the one observed in QI laminates. Overall, the experimental results show a lower dispersion in ±45° laminates.

It was attempted to find a probability law reproducing the porosity formation through nucle-

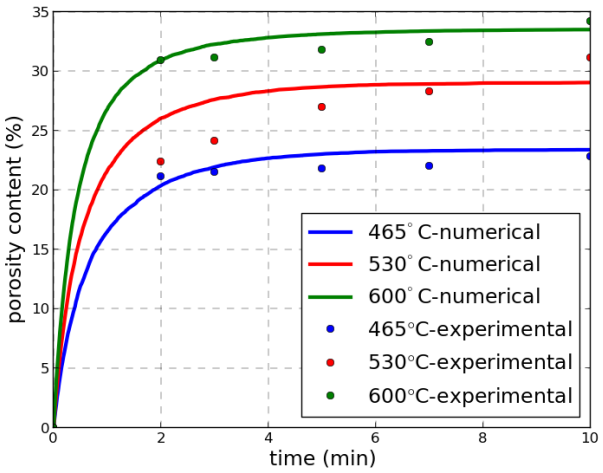

Figure 4.24. – Comparison of the experimental / numerical evolution as a function of time of η_p^* for different temperatures of exposure considering the nucleation process in ±45° laminates

ation as performed in Section 3.3.2 for QI laminates. However, due to the drastically different time-dependence of the 530°C results, a proper fit could not be identified with the simple expression of $G_N(t,T)$ as given in Eq. 3.18. An example of a numerical optimization is shown in Fig. 4.24, which clearly indicates that although the fitting is accurately representing the minimum and maximum temperatures, it is not at all the case at 530°C. One possible solution would be to enrich or improve the $G_N(t,T)$ law by considering new parameters.

4.3.2. Mechanical response after homogeneous temperature exposure

The homogeneous exposure was followed by tensile tests. The deformation leading to fracture appears to be more gradual in ±45° laminates compared to QI ones (Fig. 4.25). Indeed, structural effects allow larger strains to be reached as the fiber bundles reorient themselves along with the loading direction (see Fig. 4.25b). Failure occurs when the intertwined fiber bundle network prevent further rotation to take place.

The fiber bundle rotation was quantified by means of a Digital Image Correlation using the VIC-2D software. A white paint was sprayed on the black surface of a ±45° decomposed laminates and the speckle changes were tracked by a CCD camera during the tensile tests. The software post-processed the images to compute rotation fields similar to the ones shown in Fig. 4.26. The fiber bundle rotation is a direct consequence of the spatial distribution of the +45° and the −45°-oriented fiber bundles which rotate to align with the loading direction.

The thermal decomposition times were limited to only 5min to spare specimens. The obtained stress / strain curves are presented on Fig. 4.27 along with the corresponding fiber bundle rotation. An almost bi-linear behavior is observed, first in the elastic range and then during the

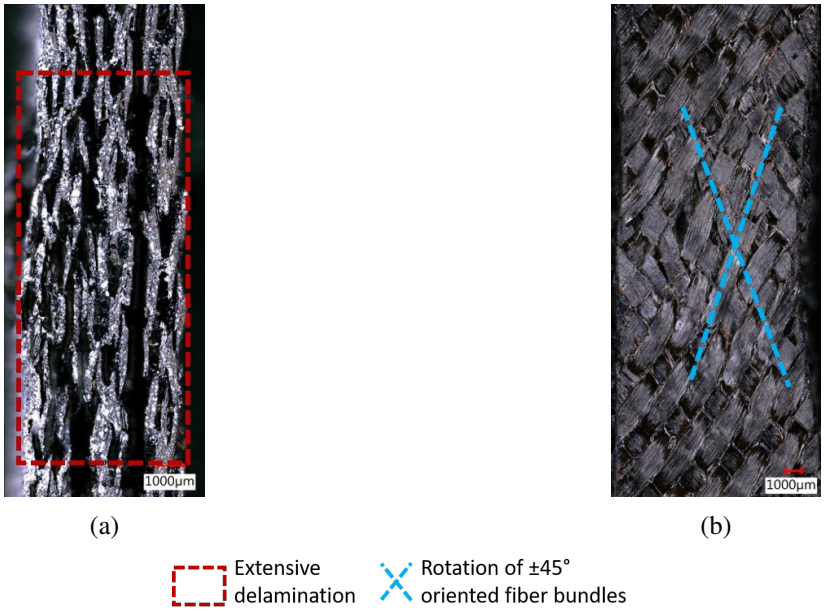

Figure 4.25. – Post-exposure optical microscopy observations of ±45° laminates after failure under tensile test after exposure to 530°C for 5min. (a) Side view, (b) front view

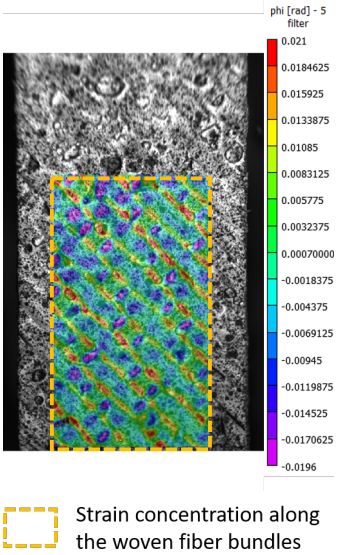

Figure 4.26. – Quantitative determination of the fiber bundle rotation in ±45° laminates during post-exposure tensile loading using DIC

rotation of the fibers. The stress significantly increases due to plastic behavior under shear loading, brought by the fiber bundle rotations. Their loading case goes from shear to a mixed loading mode which is beneficial for the carrying capacity of the yarns.

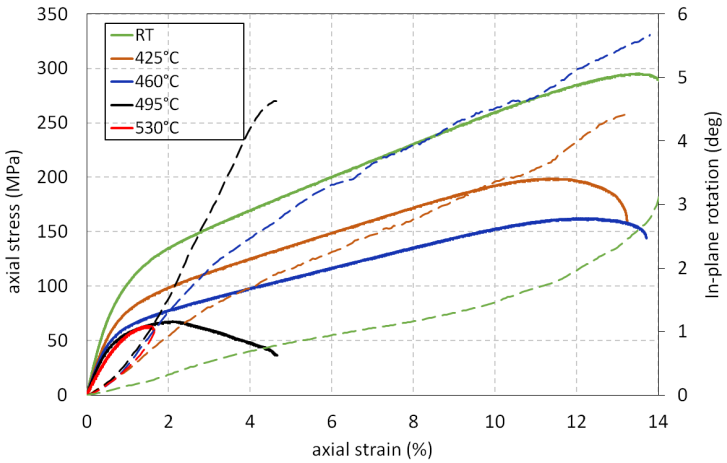

Figure 4.27. – Post-exposure strain / stress curve of ±45° laminates under tensile loading for 5min after an exposure to different temperatures. The fiber bundle rotation is represented along with the tensile loading (doted lines)

Tests at temperatures up to the onset of the thermal decomposition are instrumental to decreasing the stiffness, the stress to failure but not the strain to failure as they enable higher levels of fiber bundle rotations. However, as temperature increases further to 530°C, the behavior is drastically altered with a failure almost instantaneous after the elastic regime.

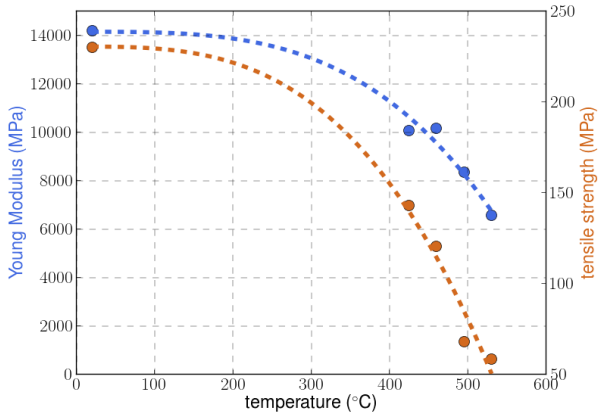

Figure 4.28. – Evolution of the residual axial stiffness and tensile strength of ±45° laminates after 5min as a function of temperature of exposure

The axial stiffness and the tensile strength are highly influenced by the temperature increase, lowering respectively by 44% and 75% at 530°C (see Fig. 4.28). This decrease is of the same order of magnitude as the one observed in QI laminates.

4.3.3. Thermal decomposition process under fire exposure

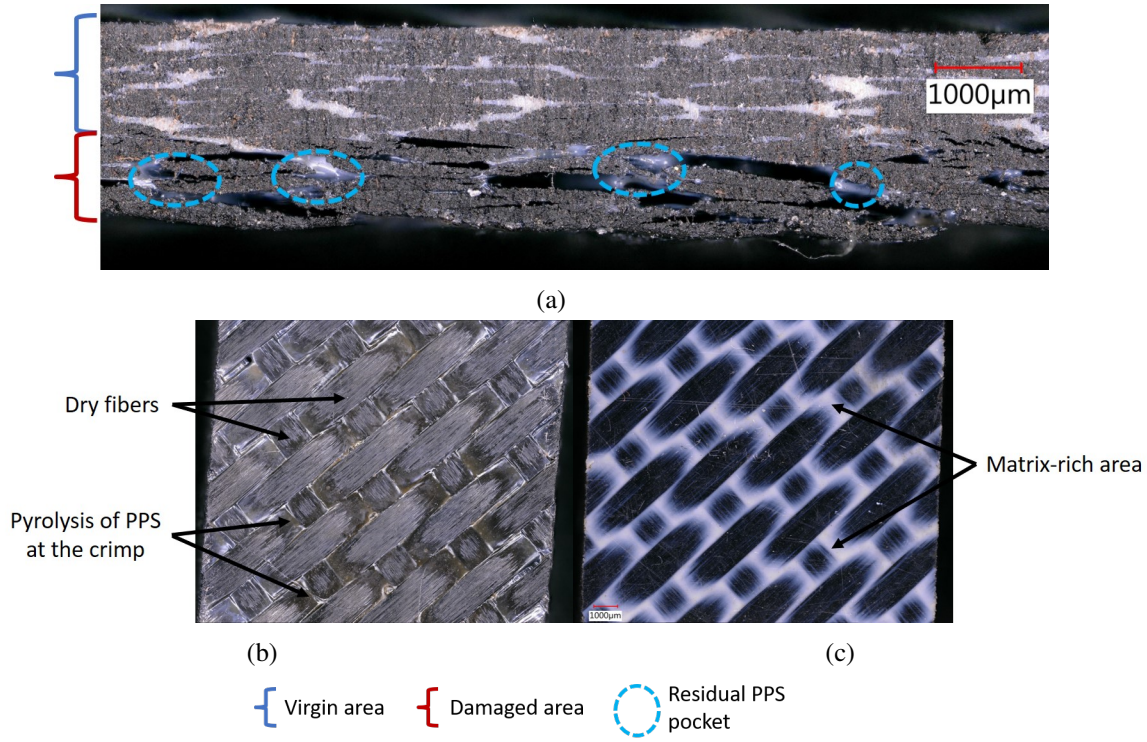

Figure 4.29. – Optical microscopy observations of the heterogeneous thermal decomposition of ±45° laminates after exposure to a 116kw/m^2 flame heat flux for 30s. (a) Through-the-thickness view, (b) exposed surface, (c) back surface

The observations for the ±45° laminates after exposure to the flame for 30s and 60s are presented on Fig. 4.29 and 4.30. Although the overall decomposition gradient is similar to the QI case, the process appears to slightly differ as more residual PPS pockets within the matrix-rich areas remain (Fig. 4.29a and 4.30a). While the void distribution is almost uniform within each ply in the QI, the ±45° voids follow matrix-rich paths in the crimp. Furthermore, the char formation seems to be limited. It can then be speculated that large matrix pockets act as a barrier and delay the direct consequences of fire contact.

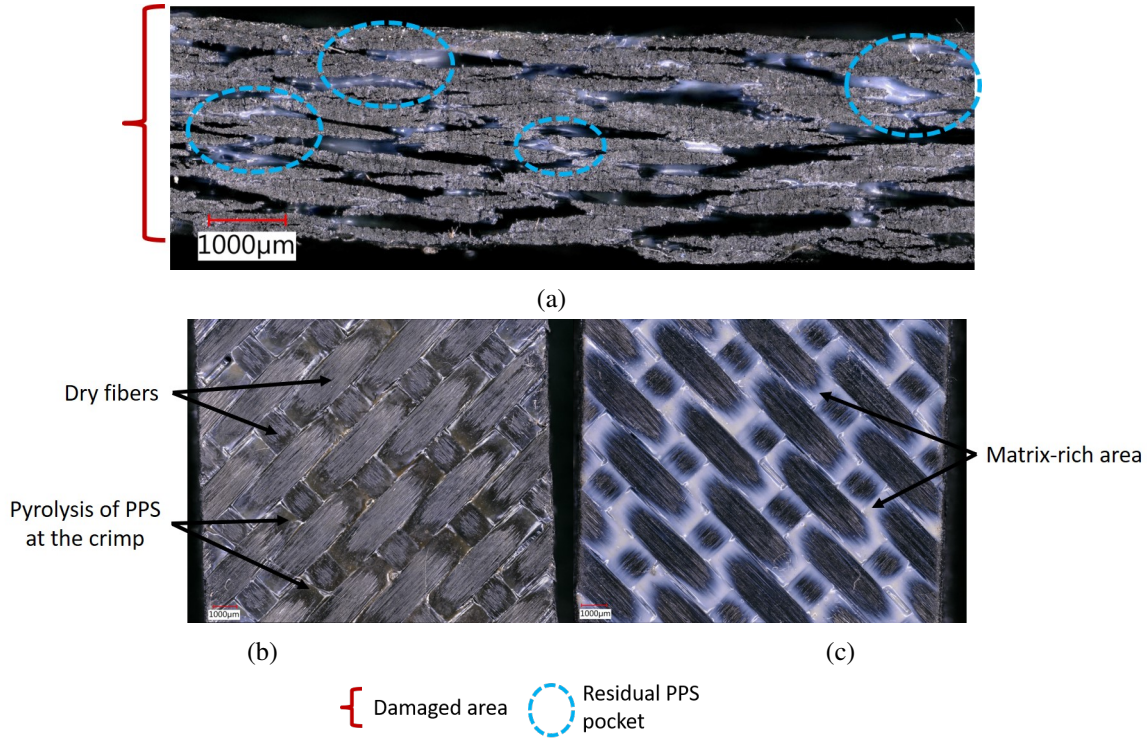

Figure 4.30. – Optical microscopy observations of the heterogeneous thermal decomposition of ±45° laminates after exposure to a 116kw/m^2 flame heat flux for 60s. (a) Through-the-thickness view, (b) exposed surface, (c) back surface

4.3.4. Mechanical behavior after fire exposure

Finally, tensile tests after fire exposure were conducted. Fig. 4.31 shows the failure profile observations. Differences with QI laminates can be noticed as the failure does not occur abruptly but rather by destructuring the weave pattern. Fiber bundles are rotating from their initial position and this scissoring effect results in a larger delamination of the plies.

The fire exposure does not appear to have a significant influence on the residual axial stiffness (at least for these short duration tests), see Fig. 4.32. However, the tensile strength largely decreases as the fiber bundle rotation is increased.

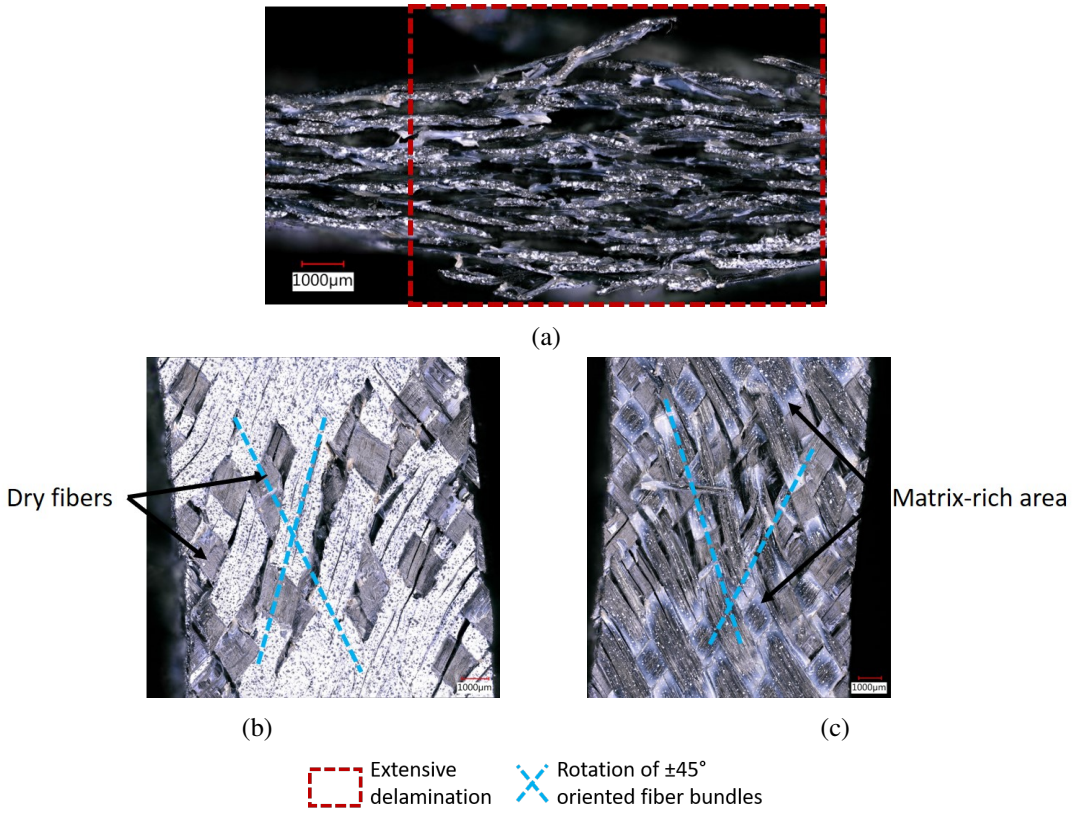

Figure 4.31. – Optical microscopy observations of the post-exposure failure of ±45° laminates under tensile loading after exposure to a 116kw/m^2 flame heat flux for 60s. (a) Through-the-thickness view, (b) exposed surface, (c) back surface

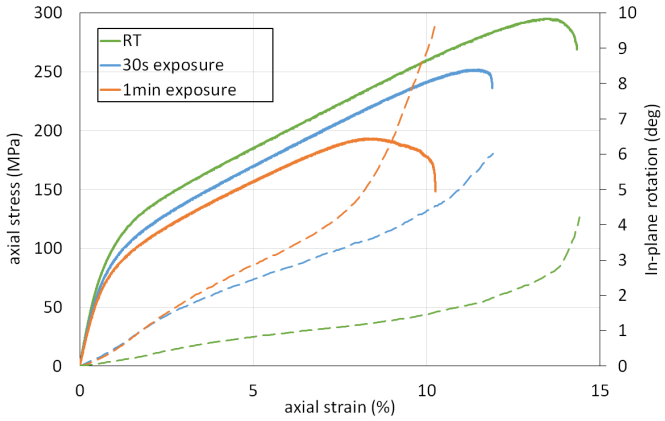

Figure 4.32. – Post-exposure strain / stress curve of ±45° laminates under tensile loading after exposure to a 116kw/m^2 flame heat flux for different times. The fiber bundle rotation is represented along with the tensile loading (doted lines)

4.3.5. Current limitations of the ±45° laminates study

Although this preliminary study has better emphasized the influence of the matrix decomposition on the thermomechanical response (importance of the matrix-rich areas at the crimp, protection of the fiber bundles, rotation of the fiber bundles), the thermomechanical coupling (either under homogeneous temperature or fire exposure conditions) has not been performed yet on ±45° laminates. This limits the comparison with QI laminates.

In addition, the modelling of the thermomechanical behavior of this laminates with an angle ply stacking sequence is more challenging. As explained in Section 4.3.1, the thermal decomposition modelling through nucleation would require important modifications of the probabilistic law. The bigger issue was encountered when performing mechanical tests on the RVE. The axial stiffness appeared to be much larger than expected, especially as the temperature increased and the matrix's stiffness decreased. For instance, at 120°C, the numerical stiffness was 18GPa vs 6GPa experimentally. At this temperature, the Young's modulus of the PPS is of 757MPa (Carpier et al., 2022). To obtain a similar stiffness, the matrix Young's modulus should be around 75MPa (Fig. 4.33). This would mean decreasing the matrix's stiffness by a factor 10.

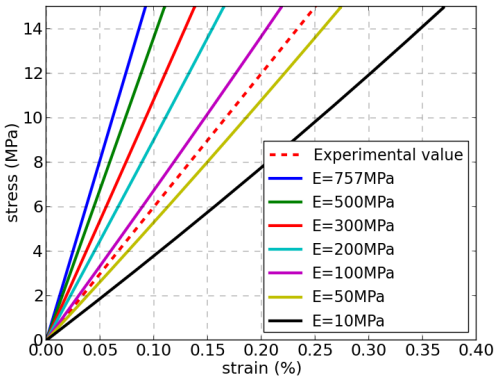

Figure 4.33. – Influence of the PPS Young's modulus on the mechanical behavior of the ±45° laminates numerical model as compared with the experimental reference

It can then be concluded that the numerical model significantly underestimates the influence of the matrix degradation with temperature. It could stem from the very limited fiber bundle rotation in the modelling, contrary to what was observed experimentally, from the earliest stages of the deformation. The question remains opened to know whether the numerical model can simulate fiber bundle rotation (for instance by considering a large strain formulation to allow this structural effect to occur or by introducing the possibility of an easy slip at the interface between fiber bundles and matrix).

4.4. Coupled thermomechanical behavior under fire exposure: case of QI laminates

4.4.1. Experimental results

The remaining of the analyses focus on the QI laminates. The coupling between thermal and mechanical behavior for QI laminates exposed simultaneously to a flame and a mechanical loading was studied. Indeed, although little influence of fire exposure was observed on the axial stiffness during post-exposure tensile tests (as the matrix on the unexposed plies transformed back into the solid state), the load transfer via the molten matrix is not possible anymore during combined fire exposure tests. As a result, it may significantly change the role played by constituents on the mechanical response of composite laminates. Thus, combined thermomechanical tests were carried using the following protocol:

— Preparation of the samples (water cutting, cleaning, drying), see Fig. 4.34 for the geometry
— Exposure to the 116kw/m^2 flame heat flux for 1, 2 and 5 minutes
— Application of the tensile loading to failure

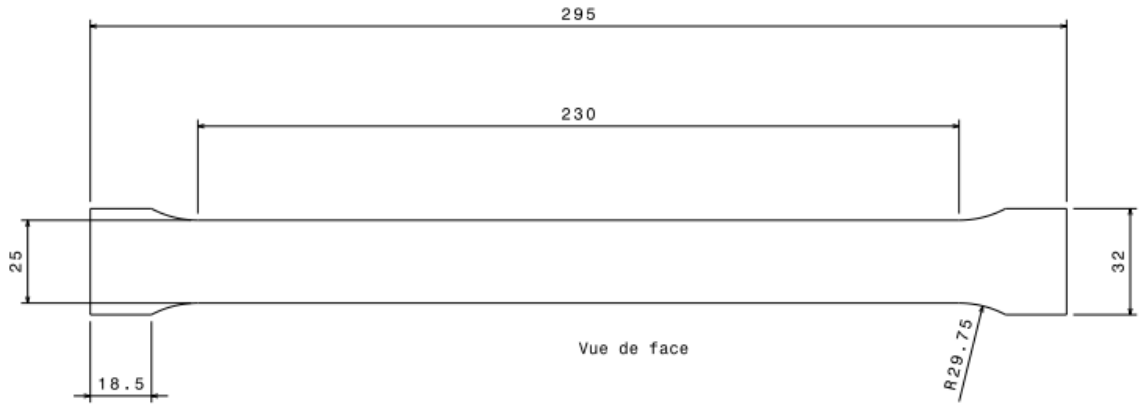

Figure 4.34. – Samples used during combined fire exposure / tensile tests

To better understand the contribution of the plies to the mechanical behavior of quasi-isotropic laminates, it is necessary to know the temperature distribution within the laminates during flame exposure. The temperature changes were monitored on the backside of the specimen by means of thermocouples stuck to the surface. Although this technique provides a reliable and stable measurement, other experimental means are available such as pyrometer, thermoluminescence or infrared camera, which will be used in future studies.

The 2min exposure case shows the evolution of the temperature on the back surface along with the mechanical response (Fig. 4.35). It appears that the 116kw/m^2 heat flux tends to induce a convergence of the temperature of the back surface only up to 380°C after approximately

100s due to the heat flux exchanges with the outside environment combined with the conduction decrease during thermal decomposition (delamination and char production). It is to be noted that this temperature is 70°C below the thermal decomposition onset, confirming the conclusions made from the post-exposure optical microscopy observations that the opposed plies are not decomposed.

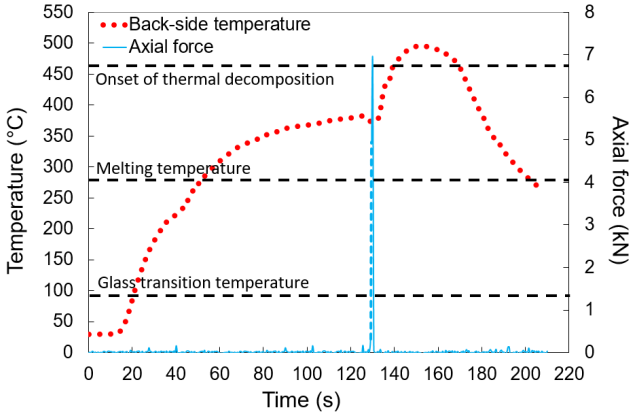

Figure 4.35. – Evolution through time of the temperature on the back surface of C/PPS laminates exposed to a kerosene flame (116kw/m^2) for 2 minutes and a tensile loading

The tensile load was applied after 2min and the failure of the sample results in an increase in the temperature as the flame impacts directly the back surface where the thermocouple is stuck. The temperature measurement on the backside of the specimen provides two important information on the state of the PPS matrix within the laminates. First, all the plies have reached the PPS melting temperature after a 2 min flame exposure and before the application of the mechanical load. Second, the thermal decomposition has not started in the opposed plies until the tensile load is applied. With the present experimental set-up, it is not possible to know the temperature distribution through the thickness of the laminates, and the post-mortem examination of the specimens is the only way to investigate the role played by the constituents within each ply, depending on the fiber bundles orientation and the PPS matrix state. Numerical modelling is required for a sounder understanding of the deformation mechanisms at play in the laminates.

As expected, the mechanical response under combined loading differs a lot from the post-exposure one. Fig. 4.36a shows that the combined loading dramatically decreases the axial stiffness and the tensile strength while the strain to failure remains similar. Furthermore, the tensile behaviour tends to gradually change from elastic-brittle to elastic-plastic depending on the exposure time, though the non-linearity of the behavior remains limited. Fig. 4.36b shows that the first minute of flame exposure is the most degrading for the mechanical properties of the laminates as the axial stiffness decreases by 74% and the tensile strength by 70%. With respect to the initial values, both properties have a similar evolution (see Table 4.3): magnitude, quick decrease within the early stage and a stabilization.

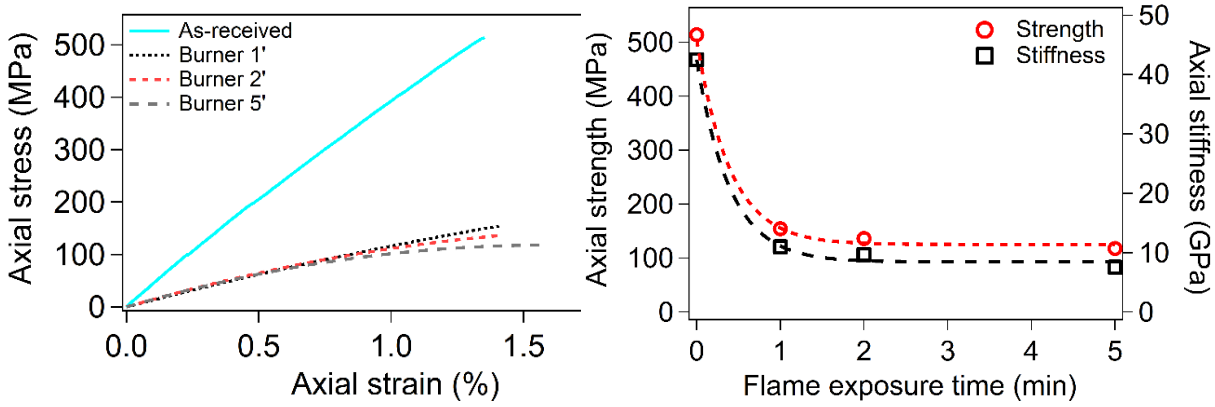

(a) (b)

Figure 4.36. – Mechanical response of QI laminates under combined tensile loading and flame exposure. (a) Stress / strain curve for different times of exposure, (b) evolution of the axial stiffness and tensile strength as a function of time

	Axial stiffness (MPa) (decrease)	Tensile strength (MPa) (decrease)
1min	11.0 (−74%)	154.3 (−70%)
2min	9.7 (−77%)	136.1 (−74%)
5min	7.6 (−82%)	117.8 (−77%)

TABLE 4.3. – Evolution of the axial stiffness and tensile strength as a function of time in QI laminates exposed to a flame combined with a tensile loading

To further analyze these results, it is worth recalling that these tensile tests were conducted on seven plies C/PPS laminates, such as the temperature of the plies are at least above the melting onset. It means that the mechanical properties of the PPS matrix are severely degraded. In agreement with the conclusions drawn in the case of carbon fibers reinforced PPS laminates (Carpier et al., 2020b), for temperatures higher than T_m, significant changes in the mechanical response and failure mechanisms are observed. Before melting, the fibers of 0° fiber bundles are maintained together by the matrix and elongate evenly within the fiber bundles. After melting, the cohesion of the fiber bundles is no longer insured by the matrix, allowing significant transverse contraction of the fibers and a more significant elongation (Fig. 4.37). As tensile load increases, the elongation of the 0° fiber bundles comes along with the generalization of the necking along the 0° direction. This necking ultimately results in a generalized buckling of the 0//90° oriented plies, which significantly increases the bending force at the crimp and leads to the misalignment of 90° fibers bundles (Fig. 4.37c). The generalization of necking is such as the transverse fiber bundles are strongly crushed by the longitudinal fiber bundles. This crushing leads to significant out-of-plane displacements resulting in surface bending effects and extensive delamination. Once the 0° plies fail, the tensile load is taken up by the ±45° plies resulting in the rotation of initially ±45° oriented fibers bundles. This reorientation of fibers comes along with a scissoring

effect (represented by blue dashed lines in Fig. 4.37a) that also contributes to the extensive delamination of the laminates as is clearly shown by the edge's views of the specimens (Fig. 4.37b).

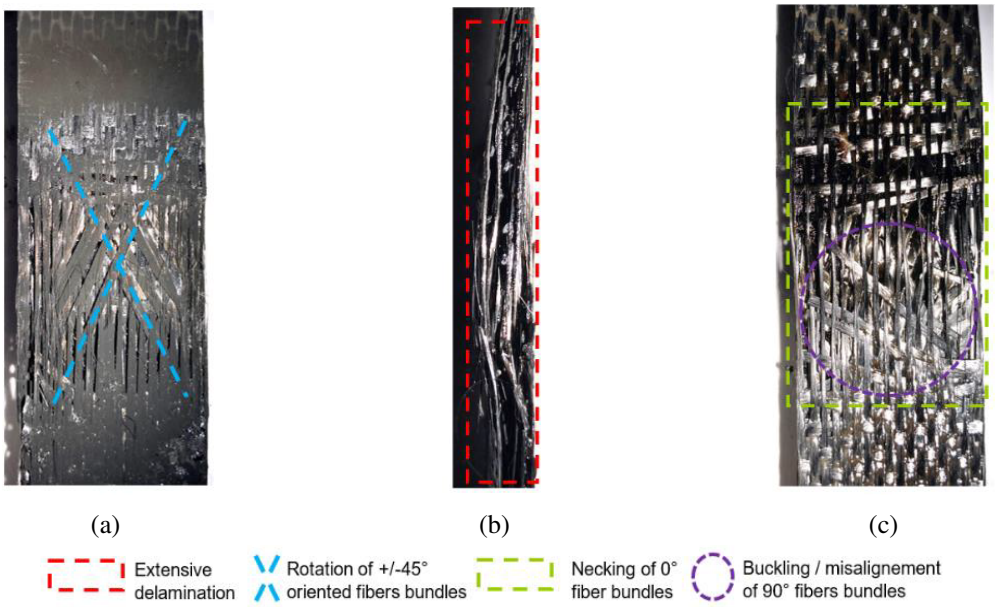

Figure 4.37. – Post mortem observations of C/PPS laminates after tensile testing under kerosene flame (5min exposure case): (a) exposed surface, (b) through-the-thickness view, (c) opposed surface

These combined tests clearly point out the importance and the specific value brought by the investigations on the thermomechanical coupling compared to post-exposure tests which are less representative of critical service conditions.

4.4.2. Numerical modelling

The simulation of the coupled thermomechanical behavior was performed to assess the influence of property degradation and thermal decomposition on the mechanical response of the laminates. The thermal model introduced in Section 4.2.2 was used. A 116kw/m^2 heat flux combined with a 100MPa axial mechanical loading were applied to the $1/28^{th}$ RVE laminates. The focus was put on the first 50 seconds of the exposure as the temperature increase and mechanical behavior were found to be significantly altered within that time range. This quick decrease is in agreement with the experimental conclusions (Section 4.4). Fig. 4.39a shows that the average temperature within each ply gradually decreases from the exposed to the opposed plies. Although it is not possible to compare the temperature of the first ply to experimental results, the temperature of the back surface converges to a value of about 380°C as was observed during the tests. This change in the temperature results in a decrease of the axial stiffness depending on the plies position with respect to heat exposure. The exposed ply's stiffness totally decreases

within the first 10s while it takes up to 30s on the opposed one, see Fig. 4.38. Overall, the laminates stiffness almost linearly decreases until reaching its minimum. Quantitatively, the C/PPS stiffness decreases by 70%, which is similar to experimental tests (82%). The accuracy of the numerical model is acceptable considering its limitations. This decrease mainly occurs due the melting of the matrix. Indeed, the solid-to-liquid transition is critical from the mechanical property standpoint. It is expected that the porosity formation has more influence on the fiber bundle behavior as the resulting fiber debonding leads to an early failure of the laminates. Modelling such debonding could then provide further insights on the role played by the porosities on the mechanical behavior.

Fig. 4.39b shows the axial stress distribution in the plies as a function of the exposure time. It can be divided into two categories: $(0/90°)$, bearing most of the mechanical loading, and $(\pm 45°)$ ensuring the quasi-isotropic behavior. It appears that the axial stress in the first ply (directly exposed to the heat flux) drops drastically during the first 10 seconds, while the other $(0/90°)$ plies tend to take up the axial load. The difference between the plies gradually decreases as the temperature in the plies reaches the melting temperature of the matrix (Fig. 4.39a). Although the load bearing capacity of the $(\pm 45°)$ plies is not significant, a similar trend can be observed.

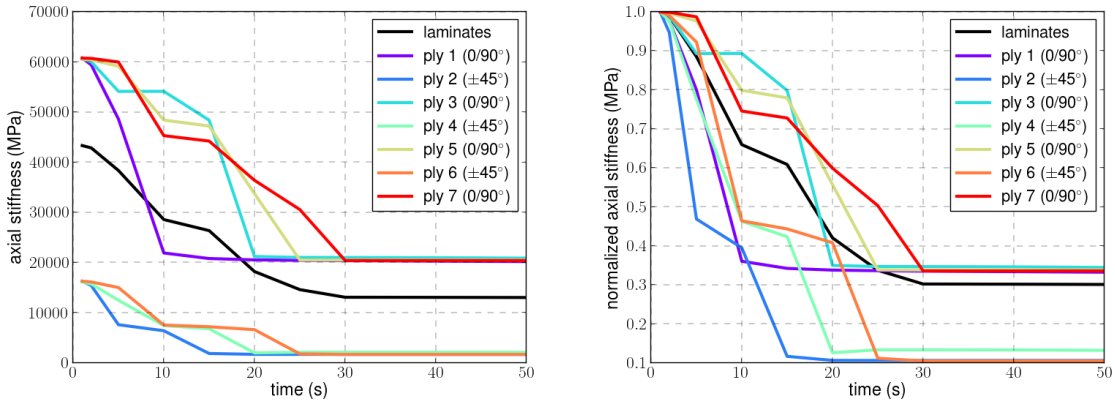

(a) (b)

Figure 4.38. – Simulation of the thermomechanical response of a QI laminates subjected to a 116kw/m^2 heat flux combined with a 100MPa axial mechanical loading. Changes in the axial stiffness of the plies during the first 50s: (a) raw values, (b) normalized values

The stress/strain mechanical fields in the laminates can also be considered. The results are presented after 10s, 20s (initial times during which the fields quickly evolve) and 100s (final stabilized time). The strain values were rescaled by a factor five using a homothety in order to emphasize the local gradients. At first, Fig. 4.40 shows the axial strain distribution in the laminates. A concentration of the axial strains gradually appears in the plies, primarily located in the matrix-rich areas at the crimp (where warp fiber bundles undulate over weft fiber bundles).

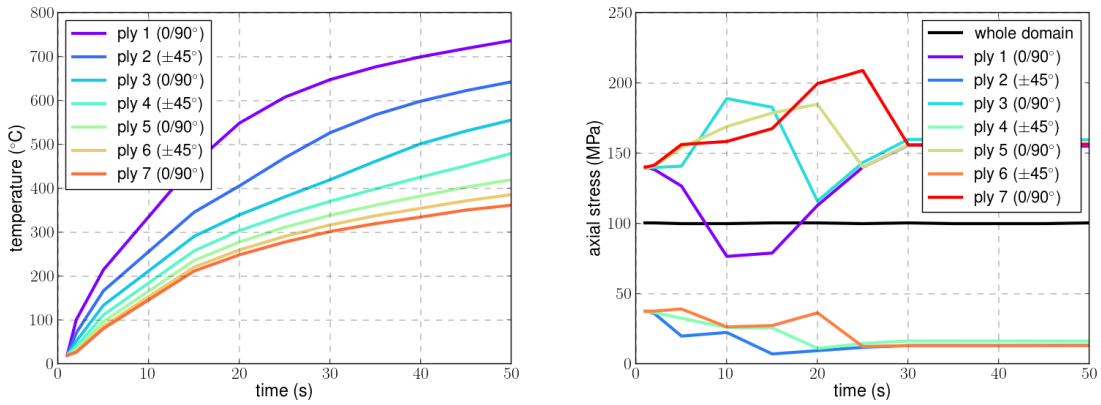

(a) (b)

Figure 4.39. – Simulation of the thermomechanical response of a QI laminates subjected to a 116kw/m^2 heat flux combined with a 100MPa axial mechanical loading during the first 50s: (a) temperature distribution, (b) stress contribution of the plies

This strain concentration is present in the first two, five and all of the plies after respectively 10, 20, and 100s (which is the direct consequence of PPS melting). Moreover, once the laminates is severely decomposed after 100s of exposure, large strain gradients (even compression) appear in the largest of the matrix areas. However, the quantitative strain measurements should be considered with caution due to the small strain formulation and the linear elastic behavior.

Similarly to the axial strain case, Fig. 4.41 shows the out-of-plane strain fields. Large out-of-plane strains (twice as large as the axial ones) appear gradually. However they tend to be localized in the small matrix areas between adjacent fiber bundles. Focusing on the 0° fiber bundles, it appears that the matrix covering them is either in compression (on the inside of the curvature) or in tension (on the external part of the curvature). It shows that the curvature of the 0° fiber bundles gradually decreases as they tend to become straight, fully aligning with the axial loading. A similar behavior is observed for the other orientations of fiber bundles (at a lower scale), although it is not not as easily noticeable as they are not well oriented for a direct visual observation (their longitudinal direction is not in the selected plan).

As expected, it appears from Fig. 4.42 that the 0° fiber bundles mainly bear the axial loading. The stress redistribution shown in Fig. 4.39b points out that the stress carried by the 0° yarns becomes higher as a function of temperature. The effect of the gradual straightening of the fiber bundles (mentioned in the previous paragraph) can also be observed here. Indeed, while the axial stress at the core of the 0° fiber bundles is about 500MPa, significant compression and tensile stresses appear in the curvature areas (about 1.5GPa in compression and 3GPa in tension, values which, as for the strain ones, have to be considered with caution due to the mechanical hypothesis of the model).

From the numerical analysis performed, it is possible to conclude that the numerical model is promising to simulate the thermal transfers within the QI C/PPS laminates, especially consid-

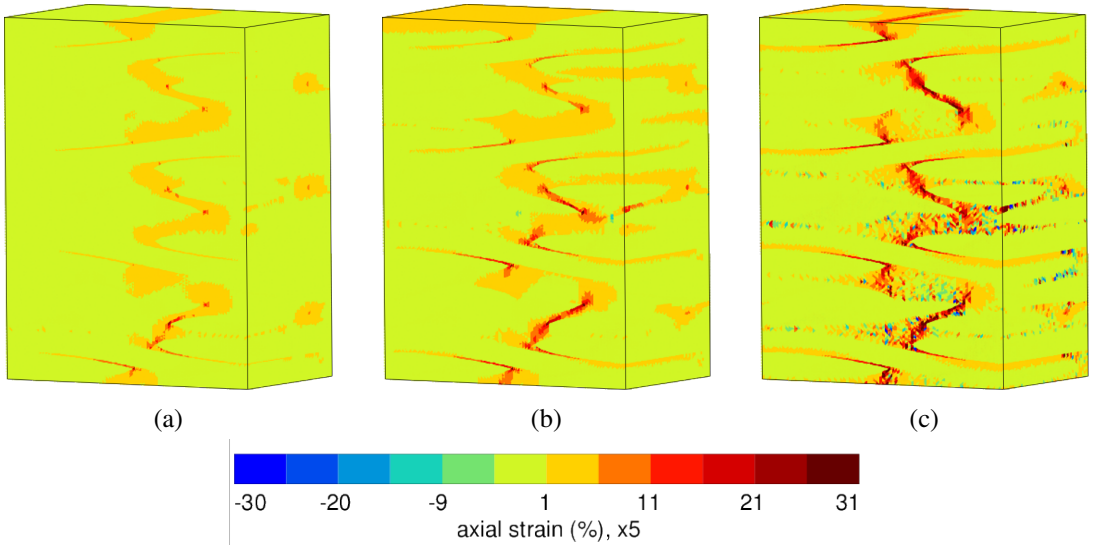

Figure 4.40. – Axial strain field in QI laminates after exposure to a 116kw/m^2 heat flux combined with a 100MPa axial loading. After (a) 10s, (b) 20s, (c) 100s. (The axial loading direction is horizontal)

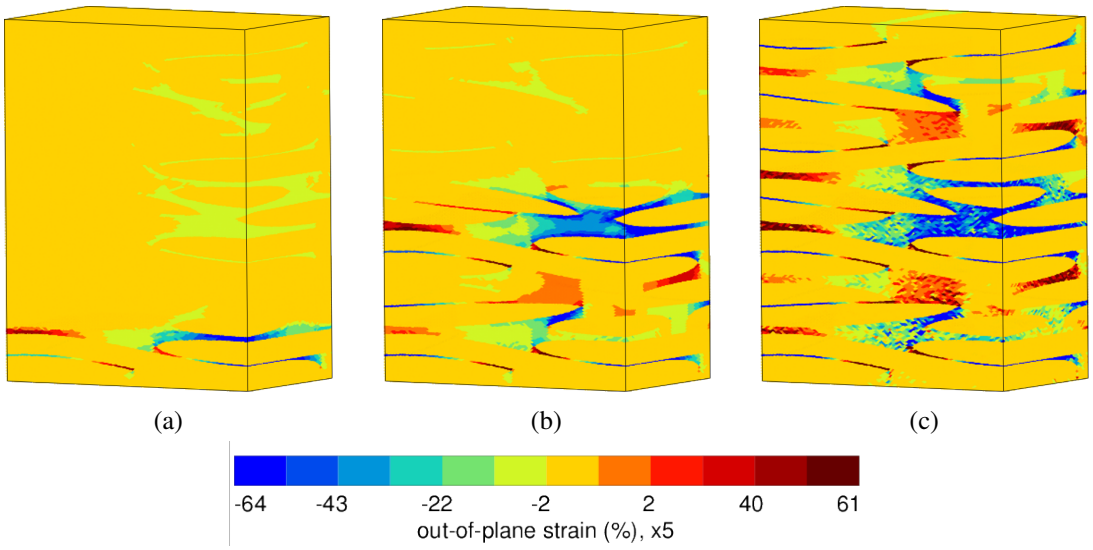

Figure 4.41. – Through-the-thickness strain field in QI laminates after exposure to a 116kw/m^2 heat flux combined with a 100MPa axial loading. After (a) 10s, (b) 20s, (c) 100s. (The axial loading direction is horizontal

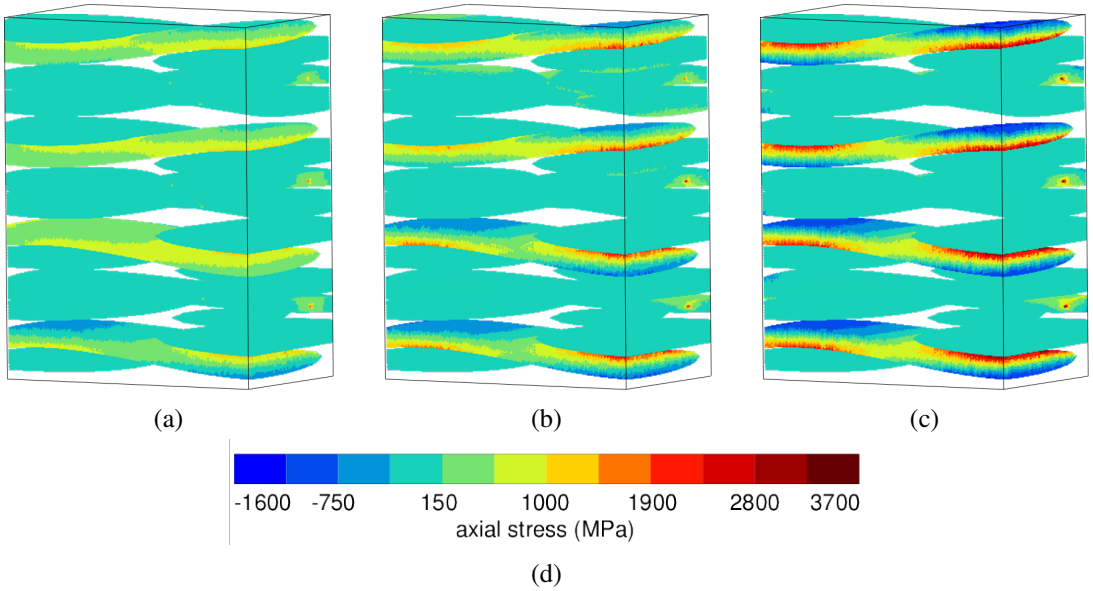

Figure 4.42. – Axial stress field in QI laminates after exposure to a 116kw/m^2 heat flux combined with a 100MPa axial loading. After (a) 10s, (b) 20s, (c) 100s. (The axial loading direction is horizontal

ering the strong assumptions made: the representation of porosities as a solid material and the thermomechanical properties are considered as constants for temperatures above T_d). This temperature gradient induces thermomechanical property degradation and thermal decomposition resulting in a stiffness decrease which is of the same magnitude as the one obtained experimentally. As the load is mainly borne by the $0/90°$ plies, the stiffness error observed with the $\pm 45°$ laminates model is of the second order. Furthermore, the use of a numerical model gives better insight into the understanding of the mechanical response at lower scales as local fields can be computed. However, the predictive capabilities of the model are limited in the present form as damage is not explicitly taken into account, nor viscosity and plasticity.

It is to be noted that in the experiments the temperature exceeds the upper limit of the developed model of 600°, especially in the exposed ply. However it was assumed that, considering an almost instantaneous thermal decomposition in this ply, it should not change significantly the results in terms of matrix behavior. However, a few differences could be observed on the fiber behavior as the temperature reached in the exposed ply is high enough to start their oxidization. The consequences on the local scale of the exposed ply can be studied experimentally by means of X-Ray tomography analyses, as introduced in the next section.

4.5. Towards comprehensive porosity formation analyses through X-Ray tomography

In this section, the first step of the experimental characterization of the thermomechanical response using X-Ray tomography is presented. As a prerequisite to future works focusing on the thermomechanical coupling, tomography analyses were carried out after thermal aggression considering the technical means described in Section 3.1.1. The porosity distribution was determined from the segmentation in the Avizo software (black/white threshold differentiating the components), and then compared with the numerical results. The voxel characteristic dimensions (cubes with side length of 6μm) provides a high resolution (even higher than the numerical model, each finite element having a length of 20μm). It emphasizes the gradual and local decomposition of the laminates' mesostructure.

4.5.1. Porosity formation during fire exposure

First of all, let us focus on the formation of porosities during fire exposure in terms of shape, size, spatial distribution and network. Fig. 4.43 shows a plane parallel to the exposed surface extracted from a tomography reconstruction in which the fibers have been removed to observe more precisely the porosities embedded within the matrix. The observed porosities can be categorized into several categories and it was chosen to highlight four different shapes and sizes:

— 1: Small circular porosities which have just nucleated
— 2: Intermediate circular porosities which have grown/coalesced
— 3: Large macro-porosites which originate (at least partly) from the interface debonding
— 4: Intra-fiber bundle porosities whose shape are mainly longitudinal along the fiber direction

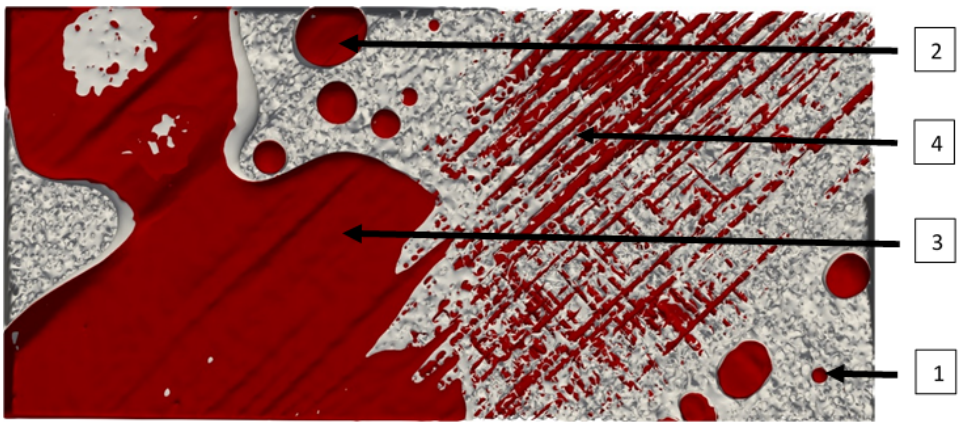

Figure 4.43. – X-Ray tomography observation of porosities with various sizes and shapes embedded in the matrix. Colors represent the constituents (porosities in red, matrix in grey)

Second of all, until they reach a certain size, the porosities located in the matrix-rich areas appear to have a spherical shape, as expected from gas bubbles forming within melted polymer. However, the growth and coalescence processes are not entirely understood, as well as their interaction with the delamination. Is there a minimum/maximum size for a nucleated porosity? Does it occur instantaneously and is followed by the growth? How does the external surface of the porosities exactly grow, or does it consist in a coalescence of many smaller pockets? Hence, the exact contribution of all three porosity formation mechanisms is not fully explained.

All these porosities form a gradient through the thickness, as observed in Fig. 4.44 after 15s and 30s of flame exposure. It is shown that after 15s, the porosities are limited to the first half of the laminates. However, after 30s, porosities have appeared throughout the whole sample despite the temperature being lower than T_d in a large volume of the laminates, as was previously shown. This further highlights the magnitude of the debonding at the matrix / yarn interface.

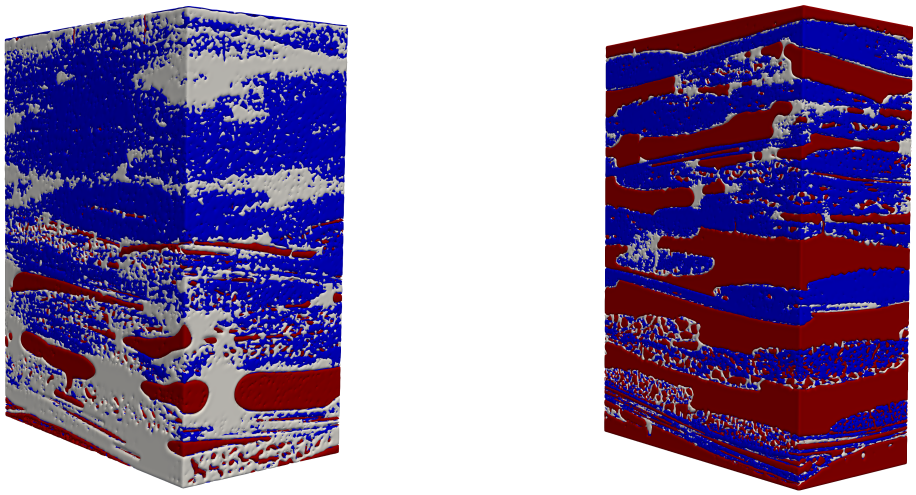

(a) (b)

Figure 4.44. – X-Ray tomography analysis of post-exposure QI laminates subjected to a 116kw/m^2 kerosene flame during (a) 15s, (b) 30s. Colors represent the constituents (porosities in red, matrix in grey, fiber bundles in blue)

One can look at the porosity network building as a function of time, especially when the porosities have appeared throughout the whole sample. Indeed, the porosity network shows the thickness of the connected region starting from the exposed ply in which the pyrolysis gas can circulate. Furthermore, the time to reach a decomposition state in which the porosity network thickness is such that both sides are connected through porosities is of particular interest to the industry as it can be considered as a failure criterion.
To this end, the porosities were isolated in Avizo and their connectivity was processed. The results after 1min of exposure are shown in Fig. 4.45. When the whole sample is considered, the porosity network shows a major connectivity throughout the whole laminates. The volume is large enough to find paths from one ply to another. Small isolated cavities appear in between,

which are the ones located within the fiber bundles and are therefore isolated. However, when the domain of study is limited to a volume similar to the one of the numerical model, no connectivity is detected between the third and fourth plies, and the remaining four plies are mainly divided into two connected regions. It can therefore be concluded that the concept of porosity network length strongly depends on the scale at which the study is conducted.
It is to be noted that a part of what is considered as porosities on the borders of the samples is actually air as it is difficult to properly fully isolate it from actual porosities.

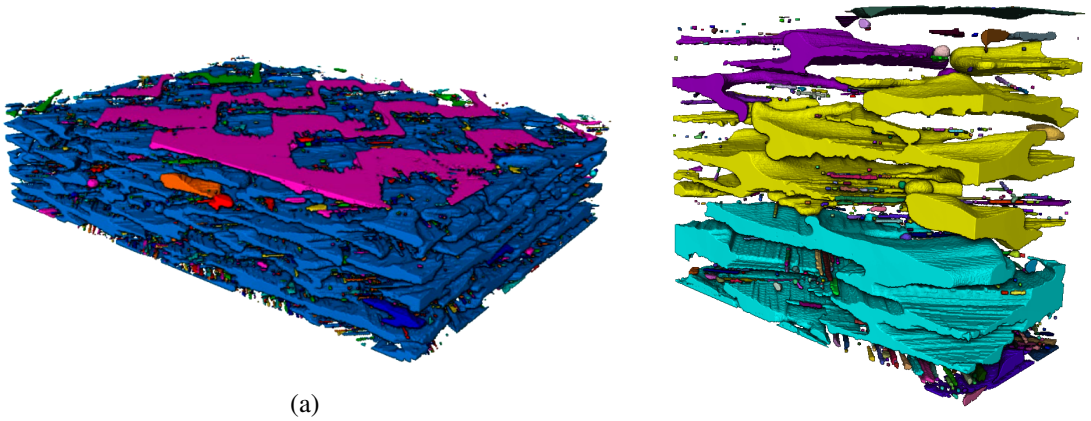

(a) (b)

Figure 4.45. – X-Ray tomography computation of the porosity network after 1min of exposure to a 116kw/m^2 kerosene flame: (a) whole 25×25mm^2 sample, (b) restriction to an equivalent of the numerical model volume ($1/28^{th}$ of an RVE). Each color represents a connected group of porosities.

Finally, the connected porosities can be classified according to their volume. Fig. 4.46 shows, that after a 60s exposure, a large number of small porosities is detected. This number progressively decreases as the volume grows larger and similar trends are observed for QI and ±45° laminates. It is to be noted that the graph does not show porosity networks larger than 500 voxels, as they are not numerous. Fig. 4.47a shows that the contribution of the porosity networks (to the whole porosity volume) as a function of their volume after 60s of exposure almost follows a bilinear trend in logarithmic scales. Indeed, the amount of small porosities counterbalances their low volume, whereas larger ones are not numerous enough. The decrease occurs for volumes up to 1000 voxels, before a significant increase. For clarity purposes, only 2% of the porosity volumes are shown between 20 and 100000 voxels. Overall, the larger porosity network accounts for the majority of the total volume (around 92%). The evolution of the contribution of this macro-porosity with time (and the one of the remaining porosities) in QI and ±45° laminates is presented in Fig. 4.47b. The contributions show a gradual saturation, although quicker for the ±45° laminates. It confirms (with the observations from Section 4.3.1) that the various porosity formation mechanisms occur at a higher rate in ±45° laminates.

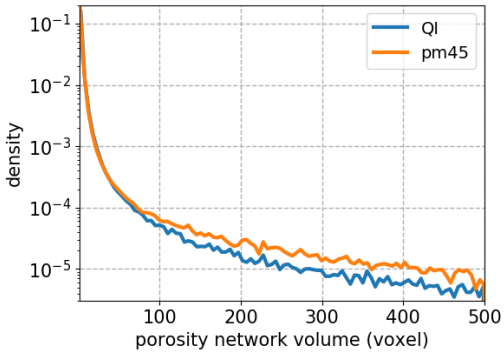

Figure 4.46. – X-Ray tomography computation of the porosity distribution according to their size after 60s of exposure to a 116kw/m^2 kerosene flame. Each voxel represents a $6.5^3 \mu m^3$ cube.

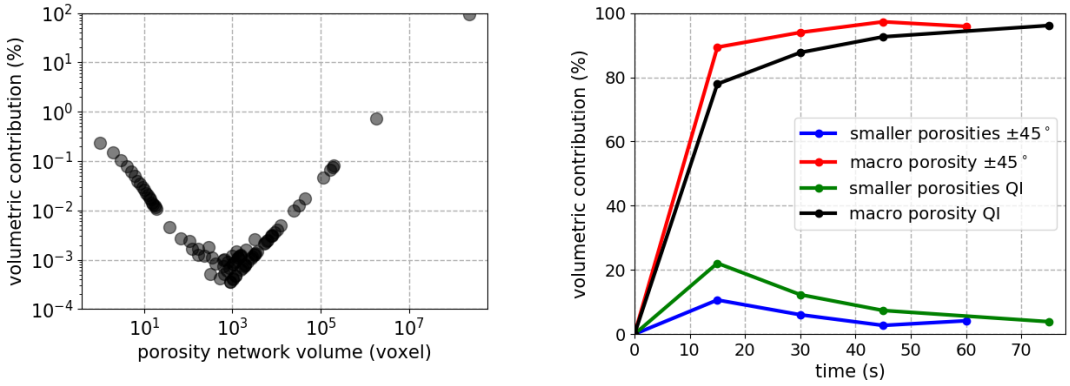

(a) (b)

Figure 4.47. – X-Ray tomography computation of the volumetric contribution of the porosity networks after exposure to a 116kw/m^2 kerosene flame: (a) evolution as a function of the porosity network volume after 60s of exposure in QI laminates, (b) evolution as a function of time of the large macroscopic porosity network and the combination of the smaller ones in QI and ±45° laminates.

4.5.2. Quantification of the porosity content and thickness expansion

The evolution of the porosity content and thickness expansion throughout the thickness can be determined and presented as it was performed for the numerical model in Fig. 4.19. Fig. 4.48 shows their gradient for different exposure times ranging from 15s to 60s of QI laminates. Considering the comparison of the porosity contents obtained by tomography and by the numerical modelling (Fig. 4.49 after 60s of exposure), several observations can be made:

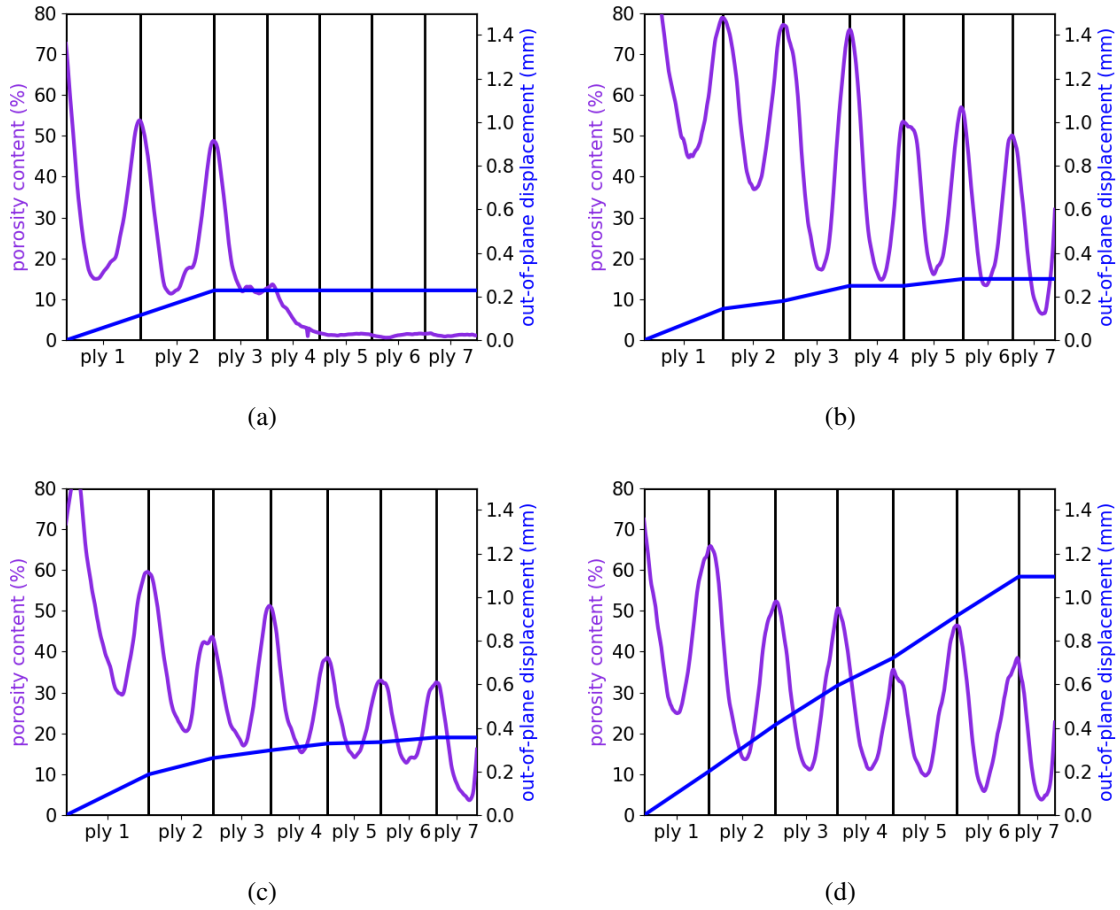

Figure 4.48. – Evolution of the out-of-plane displacement and porosity content in each plies of QI laminates as obtained by X-Ray tomography reconstruction after exposure to a 116kw/m^2 kerosene flame for: (a) 15s, (b) 30s, (c) 45s and (d) 60s

— First, the value of the porosity content on the exposed ply can be slightly overestimated due to the presence of the outside air detected as porosity in the process of selecting phases from the grey levels (as previously mentioned). A few unexpected fluctuations appear which are due to the lack of accuracy in the segmentation.
— The high values at the borders between the plies and the lower ones in the core are obtained again from tomography reconstruction, confirming the influence of the fiber bundle volume fraction on the porosity content.
— The porosity content is similar in the exposed ply when comparing numerical and experimental analyses.
— Discrepancies are also observed, the porosity content being much lower for the numerical model in a majority of the cases. It originates from two identified limitations of the model:
  — The overall underestimation stems from the debonding at the matrix / fiber bundle

interface that is not predicted by the numerical model. Indeed, at lower times and / or for plies further from the flame impact, the temperature is lower than T_d. Experimentally, the porosity formation only results from this debonding in a large part of the laminates. It points out the importance of considering this mechanism in the model as it highly governs the porosity formation under the flame exposure, and the subsequent thermomechanical response of the laminates.

— The lower values at the core of the plies may also result from the porosity formation within the fiber bundles which is not considered by the model. As these areas are mainly filled with fiber bundles, this underestimates the actual porosity content

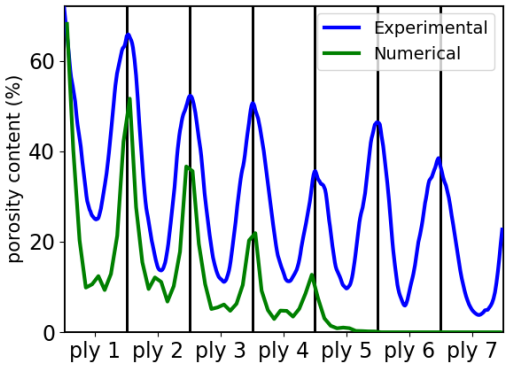

Figure 4.49. – Comparison of porosity content in each plies of QI laminates as obtained by X-Ray tomography reconstruction and numerical modelling after exposure to a 116kw/m^2 kerosene flame for 60s

A few differences can be observed in the ±45° laminates (Fig. 4.50). Overall, the decrease in the porosity content through the thickness of the laminates (and as temperature decreases) seems lower in the ±45° laminates, meaning that the delamination probably contributes more to the thickness expansion. The values are of the same order of magnitude, although they are lower in the ±45° laminates, which may result from the uncertainties of the computation method. It can also be observed that after 15s, 4 plies contain porosities in angle ply laminates as compared to only 3 in QI laminates. It may corroborate the more extensive and faster debonding in ±45° laminates.

This preliminary study on X-Ray tomography analysis emphasizes the potential of this method, as it provides very accurate information on the porosity formation process and the porosity / thickness expansion. In addition, it allows for the numerical model to be compared with experimental results. Ultimately, both the physical representativity and the identification of the model should be improved.
While this first approach has mainly dealt with the observation of porosities after they are formed

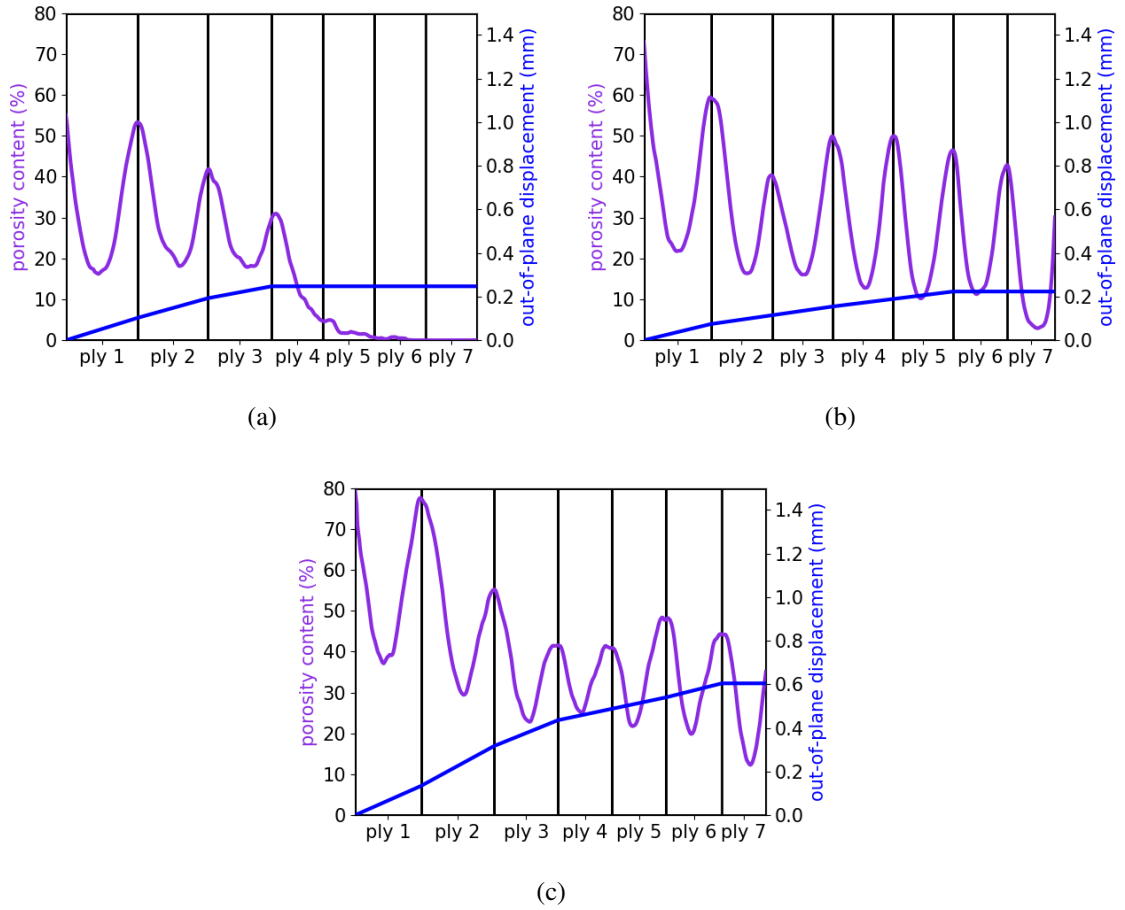

Figure 4.50. – Evolution of the out-of-plane displacement and porosity content in each plies of ±45° laminates as obtained by X-Ray tomography reconstruction after exposure to a 116kw/m^2 kerosene flame for: (a) 15s, (b) 30s and (c) 45s

through their distribution, X-Ray tomography analyses will be very relevant to further understand the porosity formation mechanism in itself.

4.6. Conclusion

This final chapter presents the influence of temperature above the thermal decomposition onset on the mechanical properties of QI C/PPS laminates and the predictive capabilities of the proposed model.

Firstly, tensile tests were performed after a homogeneous temperature exposure. Experimental and numerical results showed that the stiffness decrease can be directly characterized by the

porosity content in the laminates. The model showed a lower influence of porosity content on the axial stiffness than the experimental conclusions. It could result from the model's assumptions (yarn decomposition, representativity of the subdomain) as well as the lack of temperature control due to the self-ignition of the samples in the furnace.

Secondly, the heterogeneous temperature case was studied. It was conducted experimentally by means of a kerosene burner and numerically by applying a 116kw/m^2 heat flux on one side of the laminates. The model is accurate enough to simulate the thermal response as the temperature on the back surface is similar. The temperature gradient leads to a thermal decomposition gradient which can be directly compared to the experimental results.

Thirdly, the coupled thermomechanical tests under flame aggression, which were the ultimate purpose of the study, were performed. The kerosene burner exposure was combined with an axial tensile loading. Contrary to the post-exposure approach, the numerical results are in agreement with the experimental data, albeit some discrepancies on the decomposition influence on the thermomechanical response of the laminates. This suggests that the differences observed in the homogeneous post-exposure simulations mainly stem from the self-ignition of the samples. The results showed that the axial stiffness mainly decreases during the initial 30s of heat flux exposure. During that rapid loss, the stress distribution in the plies changes according to their thermal decomposition state. Although no clear-cut conclusion can be made on the accuracy of the model for strong assumptions reasons (absence of debonding, thermomechanical properties constant for $T > T_d$, fiber bundle decomposition, representativity of the subdomain and linear elastic behavior of the matrix), this model is promising to account for the coupling between thermal and mechanical behaviors.

Preliminary post-exposure tests conducted on $\pm 45°$ laminates showed an influence of temperature exposure on the axial stiffness and tensile strength. They decrease with the same magnitude as in the QI laminates. However, the strain distribution and failure mechanisms differ as the behavior is primarily driven by the reorientation of the fiber bundles. Coupled thermomechanical tests have not been performed yet for practical reasons (availability of $\pm 45°$ laminates) and the modelling is not satisfactory as significant errors are observed in terms of subdomain stiffness.

Finally, a preliminary study based on post-exposure X-Ray tomography provided additional information on the porosity distribution and the induced thickness expansion. It pointed out potential improvements of the numerical model: necessity to consider the fiber bundle / matrix interface debonding and the formation of intra-fiber bundle porosities.

CONCLUSIONS AND PERSPECTIVES

4.7. Conclusions

Under the conditions of a one-sided exposure to a high thermal energy source such as a flame, the tensile strength of a polymer matrix composite laminates is considerably reduced, but it can remain significant for a period of time long enough to avoid a catastrophic outcome. One of the major degradations in thermomechanical properties occurs during the pyrolysis of the matrix. The work presented in this thesis was motivated by previous work carried in the ERMECA team of the GPM laboratory, especially carried out by Carpier Carpier (2018) through a previous PhD study. It has shown promising results in terms of modelling of the thermomechanical behavior of C/PPS QI laminates for temperatures below the onset of the thermal decomposition of the polymer matrix. In particular, it has established a methodology for identifying the full set of thermomechanical parameters and their variations in the considered temperature range. And it has led to a very good agreement with experiments concerning the drastic evolution of the laminates stiffness upon thermal aggression.

This study is then aimed at extending the capabilities of the numerical approach by presenting an original modelling of this progressive thermal decomposition of the polymer matrix within a composite laminate i.e. with new mechanisms, following different stages:

— Accurately reproduce the mechanical behavior of the laminates constituents
— Accurately describe the thermal gradients
— Reproduce the kinetics of porosity formation during the thermal decomposition of the matrix to account for the rapid and dramatic evolution of the polymer state
— Explicitly represent the presence of voids acting as thermal insulators
— Create a model compatible with further coupled thermomechanical considerations

In order to fulfill these requirements, the second and third chapters present the creation and identification of the numerical model while the fourth one uses the developed model to deal with the case of the thermomechanical coupling and the resulting mechanical properties. Comparisons were made with experimental analyses to assess the predictive capabilities of the model.

It is to be reminded that only a model of QI laminates was developed. Indeed, the creation of the model of $\pm 45°$ laminates was not successful as the axial stiffness was over two times higher than what was experimentally expected. It could originate from the lack of fiber rotation in the numerical model, which, as it has been explained, has a major role on its mechanical response.

Firstly, the second chapter presents the influence of temperature on the thermomechanical properties of the laminates constituents. This experimental characterization was required due to the lack of bibliographic information for temperatures above the glass / melting transition of the matrix, depending on the properties. The polymer matrix mechanical behavior was modelled as linear elastic along the fiber bundles, although an elasto-viscoplastic model was developed for the matrix for lower temperature considerations, and the thermal properties were estimated to reproduce the numerically considered thermal transfers.

Secondly, in the third chapter a comprehensive set of experimental analyses has been performed in the regime of polymer matrix decomposition (homogeneous temperature above that of polymer decomposition) for C/PPS laminates. These analyses highlighted the rapidity of the porosity formation process and its strong dependence on exposure temperature. For the targeted case of strong thermal gradients, this implies having a reliable kinetics law of porosity formation through nucleation and growth over the entire temperature range involved. A representation of void formation at the local scale of the laminate must also be possible. Indeed, it is a prerequisite to tackling local heat transfers occurring during a unidirectional thermal aggression, especially considering a strongly heterogeneous material.

A meso-scale FE model where fiber bundles and matrix are explicitly represented has thus been adopted; a kinetics law has been developed and identified from the experimental analyses; each finite element of the matrix phase were attributed temperature-dependent thermomechanical properties and a probability of nucleation determined from the kinetics law; the growth process was implemented by adapting the probability according to the local porosity density; the processes of thermally driven transformation of a matrix element from solid to glassy, liquid and gas state were further completed by the application of an internal pressure to reproduce the mechanism of swelling due to pyrolysis gases. The model replicates correctly the porosity content within the laminates as a function of time and temperature as well as the thickness expansion due to porosity-induced swelling.

In the fourth chapter, the analyses have demonstrated the ability of the model to reproduce a gradient of polymer decomposition through the thickness of the laminates and the corresponding gradient of the swelling from one ply to another. The precision of the meso-scale approach enables to highlights intra-ply inhomogeneity. This results were compared to X-Ray tomography observations which showed similar trends. Differences could however be observed due to the absence in the model of debonding at the matrix / fiber bundle interface and intra-fiber bundle porosities.

The model was used to assess the axial stiffness evolution over time and temperature and the

major decrease it showed was compared to experimental results as a validation. These experimental tests were also used to estimate the failure mechanisms in tension as it is not included in the numerical model. The developed model has shown a promising representativity of the stiffness decrease governed by the porosity content and it has provided insights on the temperature gradient and stress redistribution within a single-sided thermally irradiated laminates.

Preliminary tests on ±45° laminates highlighted the influence on the thermomechanical response of the matrix degrading and decomposing during the heating process. It showed large matrix areas at the crimp inducing a higher porosity content as well as the progressive fiber bundle rotation leading to the failure of the material. The modelling of this stacking sequence was however not performed.

4.8. Perspectives

This manuscript presents the study of the thermomechanical coupling and a numerical model accurately representing the behavior of QI C/PPS laminates during the first instants of a heat flux exposure. Their is still however plenty of possibilities to increase the representativity, the precision and the versatility of the FE model. They can be classified into two categories, detailed below:

— Numerically integrate new thermal decomposition phenomena and their consequences
— Extend the experimental and numerical analyses to new loading cases

First of all, several leads come to mind in order to better represent the thermal decomposition:

— The preliminary steps for the modelling of the decohesion at the matrix / fiber bundle interface were performed by identifying the thickness expansion originating from it. New experiments should be carried out, especially close to the thermal decomposition onset (between 400°C and 450°C) as the thermal decomposition progressively takes over. This could lead to the identification of a proper law depicting the thickness expansion evolution over time and temperature due to the decohesion. Initial simulations on a much simplified model using cohesive elements have shown the feasibility of the method. It however requires to be adapted to tackle the complexity of the laminates geometry, to identify the proper cohesive element constitutive law and to finally fit the numerical expansion to the numerical one.
— The development of voids within the fiber bundle observed in the microscopic observation was reproduced in one example by explicitly representing the embedded porosities. The porosity content within the fiber bundles could be determined, either through 2D microscopic observations or X-Ray tomography. A first estimation was carried out using microscopic observations. The large increase over time and temperature for both QI and ±45° laminates is presented on Fig. 4.51. This approach could then be extended to a probabilistic law similar to the one developed for the porosity formation in the matrix. It may however not be the most representative choice. Indeed, in the numerical model the fibers and the matrix are not differentiated within the fiber bundles. Following that method

would then mean that a large portion of the voids are replacing fibers (representing 83% of a fiber bundle volume), whereas only the matrix is decomposing (at least until the oxidization of the fibers occurs). Another approach would be to alter the thermomechanical properties of the fiber bundles with temperature, which would replicate the behavior but unfortunately not the structural changes. To this effect, a lower scale could be considered, in which only a fiber bundle is represented (a model similar to the one developed for the Chamis model verification). This multiscale approach could lead to the most appropriate method.

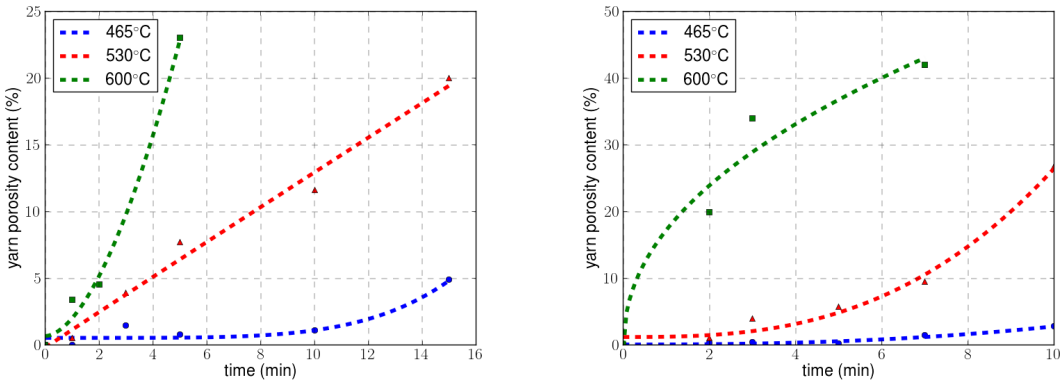

Figure 4.51. – Evolution of the porosity content inside the fiber bundles over time for different temperatures in (a) QI laminates, (b) ±45° laminates, as obtained from 2D optical microscopy observations

The following studies can also be directed towards the inclusion of new loading cases:

— New mechanical behavior could be introduced within the numerical model. Large strain formulation could be used for instance to better represent the fiber bundle rotation during mechanical loading. This approach may solve the issue encountered with the modelling of the ±45° laminates. Moreover, it was experimentally shown for instance that the tensile strength largely decreases with the porosity formation. A failure model could be implemented to account for the brittle failure of the fibers. Large strain formulation could as well to reproduce failure mechanisms relying on large strains (strain localization, fiber bundle rotation, interface debonding). An other interesting point of view, albeit probably difficult to implement both theoretically and in terms of computation time, would be to follow the crack propagation through a decomposed and swollen laminates to assess the influence of the decohesion and the pressurization on this behavior. To that extent, a numerical software such as Z-cracks (an extension of Z-set) could be used, which possesses necessary tools to tackle the problem, such as post-processing, remeshing and field transfer from one mesh to another.

— The study could be extended to new composite material configurations which are used as well in the aeronautical industry. New matrix such as PEEK, changing the number of

layer or adding a glass fiber layer on each sides (usually considered to protect from fire exposure) could highlight the general trends similar between the various TP-based materials and expose the extent of the influence of the material choice on the thermal decomposition and the thermomechanical coupling. Furthermore, the model of ±45° laminates which were experimentally investigated could be further developed as it is ideal to show the matrix-dominated phenomena. Although the precise reason for the stiffness increase was not determined for sure, introducing the fiber rotation may solve the problem.

— Finally, to keep up with the increasing tendency to use hydrogen, a hydrogen burner instead of a kerosene one might be used. If notable differences are observed, the numerical model could be updated to account for this new heat flux source and the specificities of the heat transfers at the exposed surface (convective / radiative contributions, presence of H_2O.

Along with these perspectives, the recently acquired X-Ray tomography equipment could be used further to provide a deeper understanding of the various phenomena and directly obtain more volumetric data which could be directly compared to the numerical results to properly develop the model.
The Avizo software can also reconstruct the fiber within the yarns and highlight their orientation, as is presented on Fig. 4.52a. This will be of particular interest to study the progressive post-exposure failure of the laminates as the X-Ray tomography machine is equipped with a 5kN tensile loading cell. An example of crack observation provided by Avizo developers is shown on Fig. 4.52b, which highlights the large possibilities of this method.

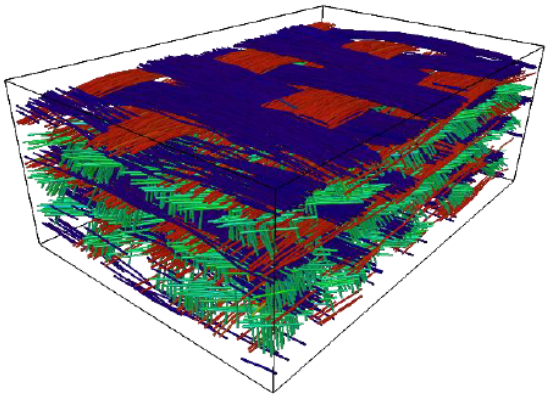

(a)

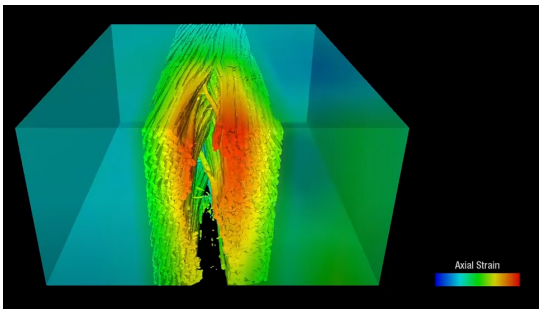

(b)

Figure 4.52. – X-Ray Tomography analysis of fiber orientation after loading (a) in QI laminates after 2 min of exposure to the kerosene flame. Each color represents an orientation. (b) Example provided by Avizo editors of a crack profile

APPENDIX A

DETERMINATION OF AN ELASTO-VISCOPLASTIC MODEL FOR THE PPS MATRIX AT 120°C

A.1. Viscoelastic behavior modelling

A.1.1. Selected model

In order to be able to reproduce the creep behavior of C/PPS and in particular the one of the solid matrix, viscous models were considered, beginning with a viscoelastic one. The chosen model, Generalized Maxwell (GM) which defines a linear viscoelastic behavior, establishes a relashionship between the stress and the strain according to the following expression:

$$\sigma(t) = \int_0^t 2G(t-\tau)\dot{e}(\tau)d\tau + \mathbf{1}\int_0^t K(t-\tau)\mathrm{Trace}(\dot{\epsilon})d\tau \tag{A.1}$$

with e the deviatoric strain tensor ϵ. G and K are relaxtion functions defined by Prony series:

$$\begin{aligned} G(t) &= G_\infty - (G_\infty - G_0)\sum_{i=1}^{n_G}\omega_i^G exp\left(-\frac{-t}{\tau_i^G}\right) \\ K(t) &= K_\infty - (K_\infty - K_0)\sum_{i=1}^{n_K}\omega_i^K exp\left(-\frac{-t}{\tau_i^K}\right) \end{aligned} \tag{A.2}$$

G_0 and G_∞ are shear coefficient whereas K_0 and K_∞ are volumic ones. It must be noted that the sum of the ω_i^G and the ω_i^K must be equal to 1.

These equations are implemented in Z-set with a differential form and internal variables α

and β. The constitutive equations can be expressed as follows:

$$\begin{array}{l}\sigma = \sum_{i=1}^{i=n_\alpha} X_i + \sum_{i=1}^{i=n_\beta} Y_i + 2G_\infty e + K_\infty Trace(\epsilon)\mathbf{1} \\ \text{with} \\ \left\{ \begin{array}{ll} X_i = -2(G_\infty - G_0)\omega_i^G(e - \alpha_i) & 1 \leq i \leq n_\alpha \\ Y_i = -3(K_\infty - K_0)\omega_i^K(Trace(\epsilon)/3 - \beta_i)\mathbf{1} & 1 \leq i \leq n_\beta \end{array} \right. \end{array} \tag{A.3}$$

This model therefore requires a great amount of parameters which need to be determined, depending on the chosen number of relaxation times. These relaxation times are often chosen logarithmically, but other more advanced methods can be found Jalocha et al. (2015).

First of all, it was necessary to select the number of characteristic times considered. The amount of times should be large enough to insure an accurate response of the model while not so much as to overly and unnecessarily complicate the parameter identification. A compromise of three relaxation times was found. Such a number introduces sixteen parameters in the model (Table A.1).

Volumic parameters	K_0	K_∞	ω_1^K	τ_1^K	ω_2^K	τ_2^K	ω_3^K	τ_3^K
Shear parameters	G_0	G_∞	ω_1^G	τ_1^G	ω_2^G	τ_2^G	ω_3^G	τ_3^G

TABLE A.1. – Parameters of the Generalized Maxwell model with three relaxation times

Second of all, to assess the nature of the viscosity introduced by the model, the mechanical properties were defined: the elastic components were selected as to reproduce the stiffness of the PPS at 20°C (i.e. 2.6GPa), while the viscous components were arbitrarily selected to introduce a variety of behaviors ranging from a low viscosity to a higher one. Fig. A.1 shows the comparison between a low/high viscous behavior under a relaxation loading of $1e^{-3}$ applied to the PPS matrix for 100s (see Table. A.2 for the parameter vaules). The obtained results show a gradual decrease in the stress due to the relaxation of the matrix.

	K_0	K_∞	G_0	G_∞	ω_1	τ_1	ω_2	τ_2	ω_3	τ_3
Low viscosity	$2.55e3$	$1.3e3$	$1.2e3$	$6e2$	0.25	1.0	0.35	$1.0e1$	0.4	$1e4$
High viscosity	$2.55e3$	$1.3e3$	$1.2e3$	$6e2$	0.5	1.0	0.3	$1e1$	0.2	$2e1$

TABLE A.2. – Viscoelastic model parameters at 20°C

It was therefore concluded that this model may be used to account for the viscoelasticity of the PPS matrix.

A.1.2. Parameter identification

The identification of the sixteen parameters was performed based on previous creep tests by Albouy (Albouy, 2013) These tests were carried at 120°C and under creep loadings (10, 15 and 20MPa) as shown in Fig. A.2.

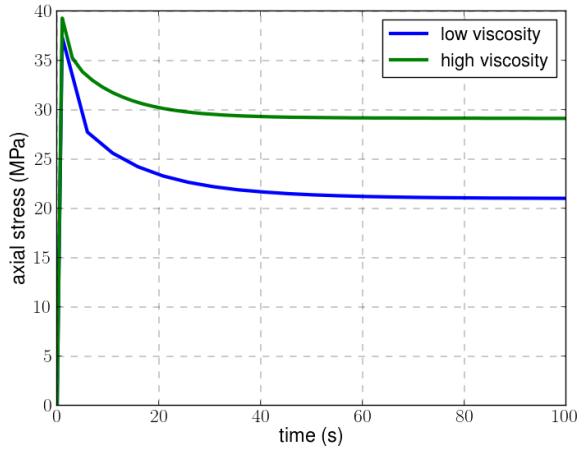

Figure A.1. – Relaxation of the PPS matrix submitted to a $1e-3$ axial strain for two arbitrary viscoelastic parameter sets at 20°C

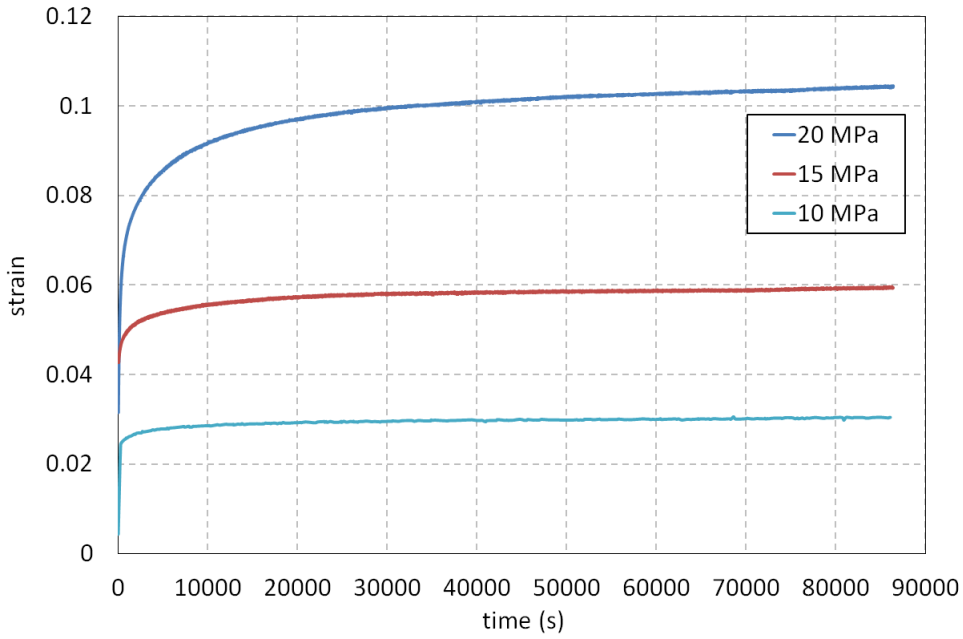

Figure A.2. – Pure PPS polymer creep curves at 120°C under 10, 15 and 20MPa stress for 24h

A first manual optimisation was carried. In order to simplify the identification, the characteristic times and their weight for the volumic and shear components were set as equal, lowering the amount of parameters to ten. It appeared possible to precisely reproduce the experimental curve for a creep loading of 10MPa (Fig. A.3).The identified parameters are presented in Table A.3.

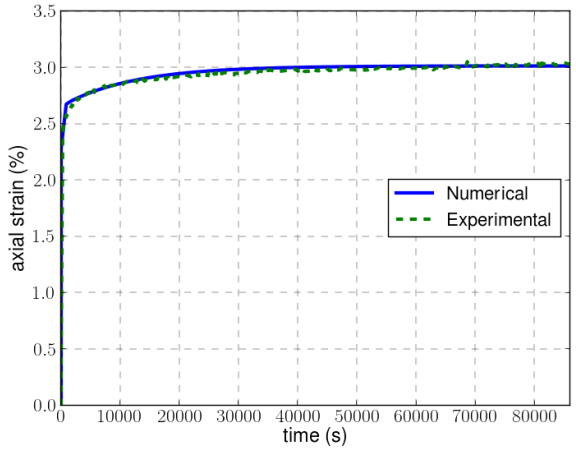

Figure A.3. – Comparison between numerical and experimental results of pure PPS polymer creep behavior at 120°C under 10 MPa stress using a viscoelastic model with optimised parameters

K_0	K_∞	G_0	G_∞	ω_1	τ_1	ω_2	τ_2	ω_3	τ_3
$3.5e2$	$1.75e2$	$1.75e2$	$1.4e2$	0.3	1.0	0.35	$2.0e1$	0.35	$1.5e4$

TABLE A.3. – Optimised viscoelastic parameters of PPS at 120°C

However, it was the model could not replicate higher stress levels, as the numerical results strongly differ from the experimental ones at 15 and 20MPa (see Fig. A.5).

It could be explained on the one hand by an identification process too complicated to be performed manually, which could be solved by using an adapted optimisation algorithm. On the other hand, it could also originates from the fact that the Generalized Maxwell model only considers the viscoelastic behavior and not the viscoplasticity. However, the latter might not be negligible for stresses larger than 10MPa at 120°C as it appears that the PPS is then no longer within its elasticity range (see Fig. A.6).

The first possible explanation was removed from consideration as optimisation through a genetic algorithm implemented in Z-set did not yield more conclusive results. The attention was hence set on including a viscoplastic constitutive model.

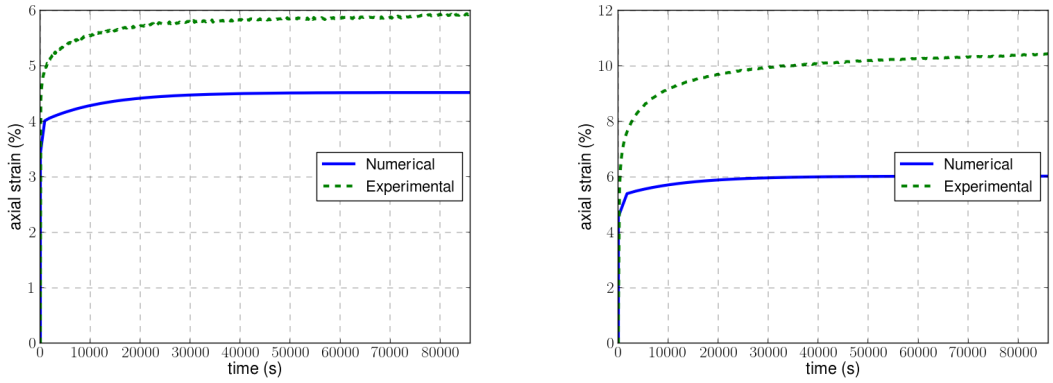

(a) 15MPa (b) 20MPa

Figure A.5. – Comparison between numerical and experimental results of pure PPS polymer creep behavior at 120°C under 15 and 20MPa stress using a viscoelastic model with optimised parameters

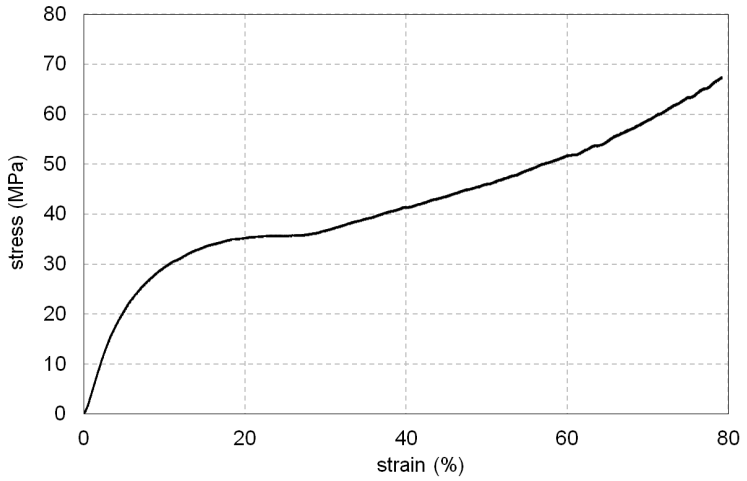

Figure A.6. – Stress / strain curve of pure PPS polymer at 120°C (Albouy, 2013)

A.2. Viscoplastic behavior modelling

A.2.1. Selected model

The considered elasto-viscoplastic model consists of different behavior which are implemented in Z-set:

— A simplified GM model for the viscoelastic component

— A Gsell flow defined, using the cumulated viscoplastic multiplier μ, by:

$$\dot{\lambda} = [\frac{f}{K(1-e^{-w\nu})} e^{h\nu^n}]^{m_1} \qquad \text{with} \quad K,\ w,\ h,\ n \quad \text{model coefficients}$$

In order to avoid a numerical issue for v=0, an ϵ_0 term is added so that the $m\nu$ product becomes $m(\nu+\epsilon_0)$

— A Drucker Prager criterion which is a non-associated criterion (meaning that the flow direction is not the same as the normal to the yield surface $\frac{\partial f}{\partial \sigma}$. Let us note (i) K the tension to compression yield ratio, (ii) β the internal friction angle and (iii) ψ the dilatation angle. Let us define the following intermediate variables:

$$\begin{cases} \sigma_{eq} = (\frac{3}{2}\sigma' : \sigma')^{1/2} \\ r^3 = (\frac{9}{2}\sigma'.\sigma' : \sigma') \\ d = (1+\frac{1}{3}tan\beta)\sigma_t \quad \text{and} \quad c = \frac{1}{K}(1+\frac{1}{3}tan\psi) \quad \text{in tension with} \quad \sigma_t \quad \text{the tensile yield} \\ d = (1-\frac{1}{3}tan\beta)\sigma_c \quad \text{and} \quad c = 1-\frac{1}{3}tan\psi \quad \text{in compression with} \quad \sigma_c \quad \text{the compression yield} \\ d = \frac{\sqrt{3}}{2}\tau\left(1+K^{-1}\right) \quad \text{and} \quad c = \left(\frac{5}{2}+\frac{5}{2K^2}-\frac{4}{K}\right)^{1/2} \quad \text{in shear with} \quad \tau \quad \text{the shear yield} \\ t = \frac{\sigma_{eq}}{2}(1+\frac{1}{K}-(1-\frac{1}{K})\frac{r^3}{q^3} \\ g(\sigma) = t + \frac{tr(\sigma)}{3}tan\psi \end{cases}$$

The flow and normal are then expressed as:

$$f(\sigma) = t(\sigma) + \frac{tr(\sigma)}{3}tan\beta - d(\sigma)$$
$$n = \frac{1}{c}\frac{\partial g}{\partial \sigma}$$

— A non-linear isotropic hardening whose radius according to the cumulated plastic strain equivalent p is expressed as:

$$R = R_0 + Q(1-e^{-bp}) \qquad \text{with} \quad R_0,\ Q,\ b \quad \text{model coefficients}$$

A.2.2. Parameter identification

The same genetic algorithm provided with Z-set was used to optimize the various parameters based on the creep tests at 10MPa and 20MPa while the results at 15MPa were used as a verification of the optimisation process. The optimized parameters at 120° C are depicted in Table A.5. Results show on Fig. A.7 that this new viscoplasticity consideration allows the model to accurately reproduce the creep behavior of the PPS matrix for a wider range of stresses up to 20MPa.

It was therefore proven that such a constitutive model can numerically reproduce the material's viscosity. However, the identification was not extended to a wide set of temperature as it was chosen to focus this study on temperatures above T_m. In these cases the matrix is either molten or decomposed, either case leading to negligible bearing capabilities of the matrix,

K (MPa)	$1.94e2$
G (MPa)	$4.31e2$
ω_1^K	$1.85e2$
τ_1^K (s)	0.64
ω_2^K	$8.54e5$
τ_2^K (s)	0.11
ω_3^K	$8.70e8$
τ_3^K (s)	0.15
ω_1^G	$3.74e3$
τ_1^G (s)	0.22
ω_2^G	$2.0e5$
τ_2^G (s)	0.18
ω_3^G	$6.57e8$
τ_3^G (s)	0.6

(a) Viscoelastic parameters

flow gsell	
e0	$1.0e-5$
K (MPa)	$2.0e2$
w	$1.5e2$
h	1.0
n	10.0
m	0.3
criterion Drucker-Prager	
friction angle	15.3
dilatation angle	11.0
K	1.0
non-linear isotropic hardening	
R0 (MPa)	12.0
Q (MPa)	20.0
b	14.0

(b) Viscoplastic parameters

TABLE A.5. – Optimised elasto-viscoplastic parameters of PPS at 120°C

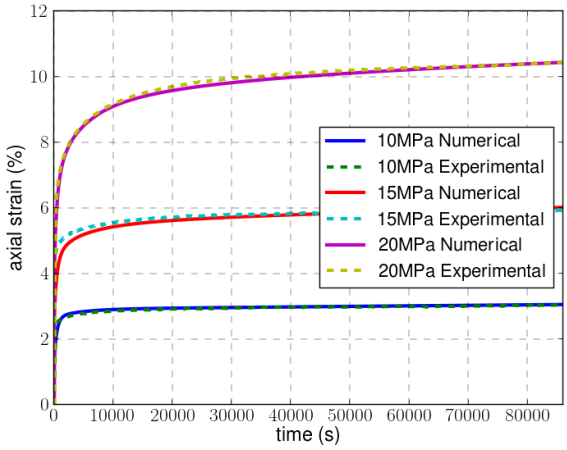

Figure A.7. – Comparison between numerical and experimental results of PPS creep behavior at 120°C under 10 MPa loading using an elasto-viscoplastic model with optimised parameters

making viscous considerations unnecessary.

LIST OF FIGURES

LIST OF TABLES

BIBLIOGRAPHY

Addiego, F., Di Martino, J., Ruch, D., Dahoun, A., Godard, O., Lipnik, P., and Biebuyck, J.-J. (2010). Cavitation in unfilled and nano-caco(3) filled hdpe subjected to tensile test: Revelation, localization, and quantification. *Polymer Engineering & Science*, 50:278 – 289. 37

Alan, B. T. N. (2006). *A model for the structural integrity of composite laminates in fire*. PhD thesis, Newcastle University. 35

Albouy, W. (2013). *De la contribution de la visco-élasto-plasticité au comportement en fatigue de composites à matrice thermoplastique et thermodurcissable*. Theses, INSA de Rouen. 53, 168, 171, 182

Amedewovo, L., Levy, A., de Parscau du Plessix, B., Aubril, J., Arrive, A., Orgéas, L., and Le Corre, S. (2023). A methodology for online characterization of the deconsolidation of fiber-reinforced thermoplastic composite laminates. *Composites Part A: Applied Science and Manufacturing*, 167:107412. 44, 111

Assael, M., Antoniadis, K., Metaxa, I., Mylona, S., Assael, Y., Wu, J., and Hu, M. (2015). A novel portable absolute transient hot-wire instrument for the measurement of the thermal conductivity of solids. *International Journal of Thermophysics*, 36:3083–3105. 21

Atreya, A. and Agrawal, S. (2002). An experimental and theoretical investigation into burning characteristics of pps-glass fiber composites. 37

Aucher, J. (2011). *Etude comparative du comportement composites à matrice thermoplastique ou thermodurcissable*. PhD thesis, INSA de Rouen. 9, 34, 40, 48, 122, 174, 175

AZO Materials (2018). Thermal analysis in practice – polymers. `https://www.azom.com/article.aspx?ArticleID=16410`. 28, 174

Berreur, L., de Maillard, B., and Nösperger, S. (2002). L'industrie française des matériaux composites. 9

Beyler, C. and Hirschler, M. (2002). *Thermal Decomposition of Polymers*, pages 111–131. 30

Biasi, V. (2014). *Thermal Modelling of Decomposing Composite Materials Submitted to Fire*. PhD thesis. 49, 74

Biasi, V., Leplat, G., Feyel, F., and Beauchêne, P. (2014). Heat and mass transfers within decomposing carbon fibers/epoxy resin composite materials. 35, 49

Blaise, A. (2011). *Caractérisation microstructurale d'un PEHD semi-cristallin déformé, par tomographie X et diffusion de lumière polarisée*. Theses, Université Henri Poincaré - Nancy 1. 36

Bonnet, B. (2005). *Comportement au choc de matériaux composites pour applications automobiles*. Theses, École Nationale Supérieure des Mines de Paris. 37

Boubakar, M., Vang, L., Trivaudey, F., and Perreux, D. (2003). A meso–macro finite element modelling of laminate structures: Part ii: time-dependent behaviour. *Composite Structures*, 60(3):275–305. 53

Bouscarrat, D. (2019). *Time-dependent damage in woven-ply thermoplastic composites above glass transition temperature*. PhD thesis. Thèse de doctorat dirigée par Vieille, Benoit et Lévesque, Martin Mécanique Normandie 2019. 10, 29, 39, 48, 175, 183

Braiek, S., Ben Khalifa, A., Zitoune, R., Zidi, M., and Salem, M. (2020). Fire behaviour of hybrid filament-wound single and adhesively bonded composites tubes under static pressure. *Polymer Testing*, 91:106815. 23

Budrugeac, P. (2000). The evaluation of the non-isothermal kinetic parameters of the thermal and thermo-oxidative degradation of polymers and polymeric materials: its use and abuse. *Polymer Degradation and Stability*, 71(1):185–187. 50

Cain, C. and Lattimer, B. (2009). Measuring properties for material decomposition modeling. *Journal of ASTM International*, 7(1):1–26. 74

Canal, L. P., Segurado, J., and LLorca, J. (2009). Failure surface of epoxy-modified fiber-reinforced composites under transverse tension and out-of-plane shear. *International Journal of Solids and Structures*, 46(11):2265–2274. 50

Carbillet, S. (2005). *Contribution aux calculs fiabilistes sur des structures composites*. PhD thesis. Thèse de doctorat dirigée par Boubakar, Mohamed Lamine Sciences pour l'ingénieur Besançon 2005. 29

Carpier, Y. (2018). *Contribution à l'analyse multi-échelles et multi-physiques du comportement mécanique de matériaux composites à matrice thermoplastique sous températures critiques*. Theses, Normandie Université. 34, 38, 39, 40, 41, 42, 43, 44, 45, 46, 47, 48, 50, 61, 63, 64, 80, 161, 175, 176

Carpier, Y., Alia, A., Vieille, B., and Barbe, F. (2021). Experiments based analysis of thermal decomposition kinetics model. case of carbon fibers polyphenylene sulfide composites. *Polymer Degradation and Stability*, 186:109525. 12, 92

Carpier, Y., Vieille, B., Barbe, F., and Coppalle, A. (2022). Meso-structure-based thermomechanical modelling of thermoplastic-based laminates subjected to combined mechanical loading and severe thermal gradients. *Composites Part A: Applied Science and Manufacturing*, 162:107165. 23, 53, 54, 55, 56, 57, 61, 64, 69, 74, 75, 88, 99, 109, 143, 174, 175, 176

Carpier, Y., Vieille, B., Coppalle, A., and Barbe, F. (2020a). About the tensile mechanical behaviour of carbon fibers fabrics reinforced thermoplastic composites under very high temperature conditions. *Composites Part B: Engineering*, 181:107586. 35, 175

Carpier, Y., Vieille, B., Coppalle, A., and Barbe, F. (2020b). Study of thermomechanical coupling in carbon fibers woven-ply reinforced thermoplastic laminates: Tensile behavior under radiant heat flux. *Polymer Composites*, 41(9):3552–3563. 80, 146

Castagnet, S., Girault, S., Gacougnolle, J., and Dang, P. (2000). Cavitation in strained polyvinylidene fluoride: mechanical and x-ray experimental studies. *Polymer*, 41(20):7523–7530. 37

Cayzac, H.-A. (2014). *Analyses expérimentale et numérique de l'endommagement matriciel d'un matériau composite : Cas d'un pultrudé thermoplastique renforcé de fibres de verre*. Theses, Ecole Nationale Supérieure des Mines de Paris. 53

Chae, S.-H., Zhao, J.-H., and Edwards, Darvin R. Ho, P. S. (2010). Characterization of the Viscoelasticity of Molding Compounds in the Time Domain. *Journal of Electronic Materials*, 39(4):419–425. 53, 175

Chamis, C. (1989). Mechanics of composite materials: Past, present and future. *Journal of Composites Technology & Research*, 11:3–14. 64, 65, 183

Chang, C. (1986). Thermal effects on polymer composite structures. *Theoretical and Applied Fracture Mechanics*, 6(2):113–120. 44

Chaudemanche, S. (2013). *Caractérisation in situ de l'endommagement volumique par spectroscopie Raman et rayon X de différents polypropylènes déformés en traction uniaxiale*. Theses, Université de Lorraine. 36

Chazelle, T., Perrier, A., Schuhler, E., Cabot, G., and Coppalle, A. (2019). Fire Response of a Carbon Epoxy Composite: Comparison of the Degradation Provided with Kerosene or Propane Flames. In *Ninth International Seminar on Fire and Explosion Hazards (ISFEH9)*, Saint Petersburg, Russia. 24, 25, 174

Cheng, X., Shi, L., Liu, Q., and Liu, Z. (2020). Heat effects of pyrolysis of 15 acid washed coals in a dsc/tga-ms system. *Fuel*, 268:117325. 22

Cheung, H., Bromley, L. A., and Wilke, C. R. (1962). Thermal conductivity of gas mixtures. *AIChE Journal*, 8(2):221–228. 129

Choudhuri, A. R. and Gollahalli, S. (2003). Characteristics of hydrogen–hydrocarbon composite fuel turbulent jet flames. *International Journal of Hydrogen Energy*, 28(4):445–454. 24, 26, 174

Christian, O. (1994, cop. 1993). *Polymères : structure et propriétés*. Sciences des matériaux. Masson, Paris. 29, 175

Christöfl, P., Czibula, C., Berer, M., Oreski, G., Teichert, C., and Pinter, G. (2020). Comprehensive investigation of the viscoelastic properties of pmma by nanoindentation. *Polymer Testing*, 93:106978. 52

Combette, P. and Ernoult, I. (2005). *Physique des polymères . Tome II . Propriétés*. Collection Enseignement des sciences. Hermann, Paris. 32

Day, M. and Budgell, D. (1992). Kinetics of the thermal degradation of poly(phenylene sulfide). *Thermochimica Acta*, 203:465–474. 50

Duquesne, S. and Bourbigot, S. (2009). *Char Formation and Characterization*, pages 239–259. 30

Dörr, D., Schirmaier, F. J., Henning, F., and Kärger, L. (2017). A viscoelastic approach for modeling bending behavior in finite element forming simulation of continuously fiber reinforced composites. *Composites Part A: Applied Science and Manufacturing*, 94:113–123. 52

Eiermann, K. (1964). Thermal conductivity of high polymers. *Journal of Polymer Science Part C: Polymer Symposia*, 6(1):157–165. 43

Fahmy, A. A. and El-Lozy, A. R. (1974). *Thermally Induced Stresses in Laminated Fiber Composites*, pages 245–259. Springer US, Boston, MA. 44

Federal Aviation Administration (2023). Faa regulations. `https://www.faa.gov/regulations_policies/faa_regulations`. 84

Feih, S., Mathys, Z., Gibson, A., and Mouritz, A. (2007a). Modelling the compression strength of polymer laminates in fire. *Composites Part A: Applied Science and Manufacturing*, 38(11):2354–2365. CompTest 2006. 44

Feih, S. and Mouritz, A. (2012). Tensile properties of carbon fibres and carbon fibre–polymer composites in fire. *Composites Part A: Applied Science and Manufacturing*, 43(5):765–772. Office of Naval Research (ONR): Composites in Fire. 32, 47

Feih, S., Mouritz, A., Mathys, Z., and Gibson, A. (2007b). Tensile strength modeling of glass fiber—polymer composites in fire. *Journal of Composite Materials*, 41(19):2387–2410. 32

Fisher, B., Eaton, M., and Pullin, R. (2023). A novel multi-scale modelling approach to predict the reduction of transverse strength due to porosity in composite materials. *Composite Structures*, 312:116861. 44

Flynn, J. and Wall, L. (1966). General treatment of the thermogravimetry of polymers. *J Res Natl Bur Stand - Phys Chem*, 70A:487–523. 92

Frederick Jr., W. J. and Mentzer, C. C. (1975). Determination of heats of volatilization for polymers by differential scanning calorimetry. *Journal of Applied Polymer Science*, 19(7):1799–1804. 42

Friedrich, K. (1983). Crazes and shear bands in semi-crystalline thermoplastics. In Kausch, H. H., editor, *Crazing in Polymers*, pages 225–274, Berlin, Heidelberg. Springer Berlin Heidelberg. 36, 37

Ge, Q., Yu, K., Ding, Y., and Qi, H. (2012). Prediction of temperature-dependent free recovery behaviors of amorphous shape memory polymers. *Soft Matter*, 8:11098–11105. 52

Gendre, L. (2011). Matériaux composites et structures composites. `https://eduscol.education.fr`. 8, 174

Gibson, A., Torres, M. O., Browne, T., Feih, S., and Mouritz, A. (2010). High temperature and fire behaviour of continuous glass fibre/polypropylene laminates. *Composites Part A: Applied Science and Manufacturing*, 41(9):1219–1231. Special Issue on 10th Deformation & Fracture of Composites Conference: Interfacial interactions in composites and other applications. 34, 175

Gibson, A. G., Wright, P. N. H., Wu, Y. S., Mouritz, A. P., Mathys, Z., and Gardiner, C. P. (2004). The integrity of polymer composites during and after fire. *Journal of Composite Materials*, 38(15):1283–1307. 22

Gigliotti, M., Pannier, Y., Gonzalez, R. A., Lafarie-Frenot, M. C., and Lomov, S. V. (2018). X-ray micro-computed-tomography characterization of cracks induced by thermal cycling in non-crimp 3d orthogonal woven composite materials with porosity. *Composites Part A: Applied Science and Manufacturing*, 112:100–110. 37

González, C. and LLorca, J. (2007). Mechanical behavior of unidirectional fiber-reinforced polymers under transverse compression: Microscopic mechanisms and modeling. *Composites Science and Technology*, 67(13):2795–2806. 50

Grange, N. (2018). *Étude du comportement au feu de matériaux composites destinés à des applications aéronautiques : expériences et Modélisations*. PhD thesis, INSA Centre Val de Loire. Thèse de doctorat dirigée par Chetehouna, Khaled et Gascoin, Nicolas Energétique Bourges, INSA Centre Val de Loire 2018. 86

Grape, J. A. and Gupta, V. (1998). The effect of temperature on the strength and failure mechanisms of a woven carbon/polyimide laminate under compression. *Mechanics of Materials*, 30(3):165–180. 34

Guo, Z., Zhuang, C., Li, Z., and Chen, Y. (2021). Mechanical properties of carbon fiber reinforced concrete (cfrc) after exposure to high temperatures. *Composite Structures*, 256:113072. 32

Halm, D., Fouillen, F., Lainé, E., Gueguen, M., Bertheau, D., and van Eekelen, T. (2017). Composite pressure vessels for hydrogen storage in fire conditions: Fire tests and burst simulation. *International Journal of Hydrogen Energy*, 42(31):20056–20070. 22, 49

Hariharan, R., Test, F., Florio, J., and Henderson, J. (1990). Internal pressure and temperature distribution in decomposing polymer composites. In *the Ninth International Heat Transfer Conference*, Israël. 45, 175

Haudin, J. (2008). Matériaux pour l'ingénieur. `http://mms2.ensmp.fr/ressources/ens_polycopies.php`. 10

Henderson, J., Tant, M., Doherty, M., and O'Brien, E. (1987). Characterization of the high-temperature behaviour of a glass-filled polymer composite. *Composites*, 18(3):205–215. 44

Henderson, J., Wiebelt, J., and Tant, M. (1985). A model for the thermal response of polymer composite materials with experimental verification. *Journal of Composite Materials*, 19(6):579–595. 49

Henderson, J. and Wiecek, T. (1987). A mathematical model to predict the thermal response of decomposing, expanding polymer composites. *Journal of Composite Materials*, 21(4):373–393. 49

Hermans, P. H. and Weidinger, A. (1961). On the determination of the crystalline fraction of polyethylenes from x-ray diffraction. *Die Makromolekulare Chemie*, 44(1):24–36. 32

Hirsekorn, M., Marcin, L., and Godon, T. (2022). Thermo-viscoelastic homogenization of 3d woven composites with time-dependent expansion coefficients. *International Journal of Solids and Structures*, 244-245:111569. 51

Hull, T. R. and Baljinder, K. K. (2009). *Fire Retardancy of Polymers New Strategies and Mechanisms*. Cambridge: Royal Society of Chemistry. 18

Humbert, S., Lame, O., Chenal, J.-M., Rochas, C., and Vigier, G. (2010). New insight on initiation of cavitation in semicrystalline polymers: in-situ SAXS measurements. *Macromolecules*, pages 7212–7221. 37

Höhne, G., Breuer, K.-H., and Eysel, W. (1983). Differential scanning calorimetry: Comparison of power compensated and heat flux instruments. *Thermochimica Acta*, 69(1):145–151. 21

Jalocha, D., Constantinescu, A., and Neviere, R. (2015). Revisiting the identification of generalized maxwell models from experimental results. *International Journal of Solids and Structures*, 67-68:169–181. 168

Jean-Marie, B. (2012). *Matériaux composites : comportement mécanique et analyse des structures*. Éditions Tec & Doc Lavoisier, Londres Paris New-York, 5e édition edition. 8

Kazemi, M., Kabir, S. F., and Fini, E. (2021). State of the art in recycling waste thermoplastics and thermosets and their applications in construction. *Resources, Conservation and Recycling*, 174:105776. 9, 174

Kolařík, J. and Pegoretti, A. (2006). Non-linear tensile creep of polypropylene: Time-strain superposition and creep prediction. *Polymer*, 47(1):346–356. 32

Kourtides, D., Gilwee Jr., W. J., and Parker, J. (1979). Thermochemical characterization of some thermally stable thermoplastic and thermoset polymers. *Polymer Engineering & Science*, 19:24 – 29. 30

Ladeveze, P. and LeDantec, E. (1992). Damage modelling of the elementary ply for laminated composites. *Composites Science and Technology*, 43(3):257–267. 47

Lagrée, P. (2023). Equation de la chaleur. 41

Legrand, V., TranVan, L., Casari, P., and Jacquemin, F. (2020). Structure-properties relationships of moisturized sandwich composite materials under extreme temperature conditions (fire resistance). *Composite Structures*, 235:111774. 22

Leplat, G., Huchette, C., and Biasi, V. (2016). Thermal and damage analysis of laser-induced decomposition within carbon/epoxy composite laminates. *Journal of Fire Sciences*, 34. 23, 174

Levchik, G. F., Si, K., Levchik, S. V., Camino, G., and Wilkie, C. A. (1999). The correlation between cross-linking and thermal stability: Cross-linked polystyrenes and polymethacrylates. *Polymer Degradation and Stability*, 65(3):395–403. 30

Linseis (2021). `https://linseis.jp/en/products/dilatometer/l75-pt-horizontal/`. 21, 174

Liu, L., Holmes, J., Kardomateas, G., and Birman, V. (2011). Compressive response of composites under combined fire and compression loading. *Fire Technology*, 47:985–1016. 45

Lomov, S., Boisse, P., Deluycker, E., Morestin, F., Vanclooster, K., Vandepitte, D., Verpoest, I., and Willems, A. (2008). Full-field strain measurements in textile deformability studies. *Composites Part A: Applied Science and Manufacturing*, 39(8):1232–1244. Full-field Measurements in Composites Testing and Analysis. 38

Loukil, M. (2013). *Experimental and Numeriacal Studies of Intralaminar Cracking in High Performance Composites*. PhD thesis. 7, 174

Loverich, J., Russell, B., Case, S. W., and Reifsnider, K. (2000). Life prediction of pps composites subjected to cyclic loading at elevated temperatures. 32

Luche, J., Rogaume, T., Richard, F., and Guillaume, E. (2011). Characterization of thermal properties and analysis of combustion behavior of pmma in a cone calorimeter. *Fire Safety Journal*, 46(7):451–461. 22

Ma, C.-C. M., Hsia, H.-C., Liu, W.-L., and Hu, J.-T. (1988). Studies on thermogravimetric properties of polyphenylene sulfide and polyetherether ketone resins and composites. *Journal of Thermoplastic Composite Materials*, 1(1):39–49. 12, 30, 84

Marcin, L. (2010). *modélisation du comportement, de l'endommagement et de la rupture de matériaux composites à renforts tissés pour le dimensionnement robuste de structures*. Theses, Université Bordeaux 1. 53

Mirabolghasemi, A., Akbarzadeh, A., Rodrigue, D., and Therriault, D. (2019). Thermal conductivity of architected cellular metamaterials. *Acta Materialia*, 174:61–80. 129

Moldoveanu, S. C. (2005). Chapter 2 thermal decomposition of polymers. In *Analytical Pyrolysis of Synthetic Organic Polymers*, volume 25 of *Techniques and Instrumentation in Analytical Chemistry*, pages 31–107. Elsevier. 30

Montaudo, G., Puglisi, C., and Samperi, F. (1994). Primary thermal degradation processes occurring in poly(phenylenesulfide) investigated by direct pyrolysis–mass spectrometry. *Journal of Polymer Science Part A: Polymer Chemistry*, 32(10):1807–1815. 27, 183

Mouritz, A. and Gibson, A. G. (2006). *Fire Properties of Polymer Composite Materials*, volume 143 of *Solid Mechanics and Its Applications*. Springer. 18, 24, 28, 30, 174

Mouritz, A. P. and Mathys, Z. (2000). Mechanical properties of fire-damaged glass-reinforced phenolic composites. *Fire and Materials*, 24(2):67–75. 22

Naghipour, P. (2011). *Simulation and Experimental Evaluation of Mixed Mode Delamination in Multidirectional CF/PEEK Laminates under Quasi-Static and Fatigue Loading*. PhD thesis. 8, 174

Nawab, Y., Jacquemin, F., Casari, P., Boyard, N., Borjon-Piron, Y., and Sobotka, V. (2013). Study of variation of thermal expansion coefficients in carbon/epoxy laminated composite plates. *Composites Part B: Engineering*, 50:144–149. 21

Nawaz, N. (2011). Modelling and experimental analysis of aerospace composites in fire. 35, 48

Needleman, A. and Tvergaard, V. (1984). An analysis of ductile rupture in notched bars. *Journal of the Mechanics and Physics of Solids*, 32(6):461–490. 53

Osada, T., Nakai, A., and Hamada, H. (2003). Initial fracture behavior of satin woven fabric composites. *Composite Structures*, 61(4):333–339. 38

Ostrach, S. (1952). Laminar natural-convection flow and heat transfer of fluids with and without heat sources in channels with constant wall temperatures. 74

Papanicolaou, G. and Zaoutsos, S. (2019). 1 - viscoelastic constitutive modeling of creep and stress relaxation in polymers and polymer matrix composites. In Guedes, R. M., editor, *Creep and Fatigue in Polymer Matrix Composites (Second Edition)*, Woodhead Publishing Series in Composites Science and Engineering, pages 3–59. Woodhead Publishing, second edition edition. 52

Patel, P., Hull, T. R., Lyon, R. E., Stoliarov, S. I., Walters, R. N., Crowley, S., and Safronava, N. (2011a). Investigation of the thermal decomposition and flammability of peek and its carbon and glass-fibre composites. *Polymer Degradation and Stability*, 96(1):12–22. 30

Patel, P., Hull, T. R., Lyon, R. E., Stoliarov, S. I., Walters, R. N., Crowley, S., and Safronava, N. (2011b). Investigation of the thermal decomposition and flammability of peek and its carbon and glass-fibre composites. *Polymer Degradation and Stability*, 96(1):12–22. 31, 175

Patel, P., Hull, T. R., McCabe, R. W., Flath, D., Grasmeder, J., and Percy, M. (2010). Mechanism of thermal decomposition of poly(ether ether ketone) (peek) from a review of decomposition studies. *Polymer Degradation and Stability*, 95(5):709–718. 27, 183

Pawlak, A. and Galeski, A. (2008). Cavitation during tensile deformation of polypropylene. *Macromolecules*, 41(8):2839–2851. 37

Pawlak, A., Galeski, A., and Rozanski, A. (2013). Cavitation during deformation of semicrystalline polymers. *Progress in Polymer Science*, 39. 37

Pering, G. A., Farrell, P. V., and Springer, G. S. (1980). Degradation of tensile and shear properties of composites exposed to fire or high temperature. 63

Philippe, D., Vieille, B., and Barbe, F. (2023). Modelling the gradual through thickness porosity formation and swelling during the thermal aggression of thermoplastic based laminates. *Composites Part B: Engineering*, 266:111026. 80

Plaseied, A. and Fatemi, A. (2008). Deformation response and constitutive modeling of vinyl ester polymer including strain rate and temperature effects. *Journal of Materials Science*, 43:1191–1199. 52

Plastics, R. L. . and rubber (2004). *Handbook of building materials for fire protection*. McGraw-Hill handbooks. McGraw-Hill, New York. 42

Plummer, C. J. G., Cudré-Mauroux, N., and Kausch, H.-H. (1994). Deformation and entanglement in semicrystalline polymers. *Polymer Engineering & Science*, 34(4):318–329. 36

Poulet, P.-A. (2017a). *Effet de la variabilité microstructurale sur le comportement d'un composite UD verre/PA11 : de la caractérisation expérimentale à la modélisation multi-échelle*. Theses, Université Paris sciences et lettres. 53

Poulet, P.-A. (2017b). *Effet de la variabilité microstructurale sur le comportement d'un composite UD verre/PA11 : de la caractérisation expérimentale à la modélisation multi-échelle*. PhD thesis. Thèse de doctorat dirigée par Laiarinandrasana, Lucien et Joannès, Sébastien Mécanique Paris Sciences et Lettres (ComUE) 2017. 37

Pradère, C., Batsale, J.-C., Goyhénèche, J.-M., Pailler, R., and Dilhaire, S. (2009). Thermal properties of carbon fibers at very high temperature. *Carbon*, 47(3):737–743. 36, 43, 175

Pradère, C. (2004). *Caractérisation thermique et thermomécanique de fibres de carbone et céramique à très haute température*. PhD thesis. Thèse de doctorat dirigée par Batsale, Jean-Christophe Mécanique. Énergétique Paris, ENSAM 2004. 36, 175

Progelhof, R. C., Throne, J. L., and Ruetsch, R. R. (1976). Methods for predicting the thermal conductivity of composite systems: A review. *Polymer Engineering & Science*, 16(9):615–625. 43

Reifsnider, K. and Caset, S. (1998). Strength-based predictive methods for large-scale combined degradation effects. 32

Remy-Petipas, C. (2000). *Analyse et prévision du comportement à long terme des composites fibres de carbone : matrice organique*. PhD thesis. Thèse de doctorat dirigée par Perreux, Dominique Sciences pour l'ingénieur Besançon 2000. 53

Rizk, G., Legrand, V., Khalil, K., Casari, P., and Jacquemin, F. (2018). Durability of sandwich composites under extreme conditions: Towards the prediction of fire resistance properties based on thermo-mechanical measurements. *Composite Structures*, 186:233–245. 49

Rizk, G., Nahas, R., Khalil, K., Challita, G., Legrand, V., Casari, P., and Jacquemin, F. (2019). Durability of composite assemblies under extreme conditions: Thermomechanical damage prediction of a double-lap bonded composite assembly subject to impact and high temperature. *Composite Structures*, 213:58–70. 49

Rosenberg, E., Brusselle-Dupend, N., and Epsztein, T. (2011). A mesoscale quantification method of cavitation in semicrystalline polymers using x-ray microtomography. *Materials Science and Engineering: A*, 528(21):6535–6544. 37

Rowe, D. (2006). *Thermoelectrics Handbook: Macro to Nano*. CRC/Taylor & Francis. 21

Rozanski, A., Galeski, A., and Debowska, M. (2011). Initiation of cavitation of polypropylene during tensile drawing. *Macromolecules*, 44(1):20–28. 37

Rutherford, E. and Soddy, F. (1902). Xli. the cause and nature of radioactivity part i and ii. *The London, Edinburgh, and Dublin Philosophical Magazine and Journal of Science*, 4(21):370–396. 91

Samaro (2022). Samaro vous propose une mise à jour de son guide de sélection dédié aux composites. `https://samaro.fr/fr/blog/3328-samaro-vous-propose-une-mise-a-jour-de-son-guide-de-selection-dedie-aux-composites`. 11, 174

Sauder, C. (2001). *Relation microstructure/propriétes à haute temperature dans les fibres et matrices de carbone*. PhD thesis. Thèse de doctorat dirigée par Lamon, Jacques et Pailler, René Sciences chimiques. Physicochimie de la matière condensée Bordeaux 1 2001. 36

Sauder, C., Lamon, J., and Pailler, R. (2002). Thermomechanical properties of carbon fibres at high temperatures (up to 2000 °c). *Composites Science and Technology*, 62(4):499–504. 32, 33, 175

Schapery, R. (1969). On the characterization of nonlinear viscoelastic materials. *Polymer Engineering & Science*, 9(4):295–310. 53

Schefer, R., Houf, W., Bourne, B., and Colton, J. (2006). Spatial and radiative properties of an open-flame hydrogen plume. *International Journal of Hydrogen Energy*, 31(10):1332–1340. 24, 26, 174

Schirrer, R. and Fond, C. (1995). Quelques aspects de la rupture des polymères : craquelures, microcisaillements et renforcement aux chocs. *Rev. Met. Paris*, 92(9):1027–1042. 36

Schulte-Fischedick, J., Seiz, S., Lützenburger, N., Wanner, A., and Voggenreiter, H. (2007). The crack development on the micro- and mesoscopic scale during the pyrolysis of carbon fibre reinforced plastics to carbon/carbon composites. *Composites Part A: Applied Science and Manufacturing*, 38(10):2171–2181. 36, 175

Schuster, J., Heider, D., Sharp, K., and Glowania, M. (2008). Thermal conductivities of three-dimensionally woven fabric composites. *Composites Science and Technology*, 68(9):2085–2091. 42

Selezneva, M., Montesano, J., Fawaz, Z., Behdinan, K., and Poon, C. (2011). Microscale experimental investigation of failure mechanisms in off-axis woven laminates at elevated temperatures. *Composites Part A: Applied Science and Manufacturing*, 42(11):1756–1763. 38

Sherburn, M. (2007). Geometric and mechanical modelling of textiles. 61, 88

Sihn, S., Pitz, J., and Vernon, J. P. (2023). Laser-induced heating, property changes, and damage modes in carbon fiber reinforced polymer matrix woven composites. *Composite Structures*, 322:117422. 23, 48, 49, 111

Somarathna, H., Raman, S., Mohotti, D., Mutalib, A., and Badri, K. (2020). Hyper-viscoelastic constitutive models for predicting the material behavior of polyurethane under varying strain rates and uniaxial tensile loading. *Construction and Building Materials*, 236:117417. 53

Stacking sequence (2023). `https://doc.comsol.com/5.5/doc/com.comsol.help.compmat/compmat_ug_modeling.3.09.html`. 11, 174

Staggs, J. (2004). The heat of gasification of polymers. *Fire Safety Journal*, 39(8):711–720. 42

Stoliarov, S. I., Safronava, N., and Lyon, R. E. (2009). The effect of variation in polymer properties on the rate of burning. *Fire and Materials*, 33(6):257–271. 42

Stoliarov, S. I. and Walters, R. N. (2008). Determination of the heats of gasification of polymers using differential scanning calorimetry. *Polymer Degradation and Stability*, 93(2):422–427. 42

Swanson, D. and Wolfrum, J. (2018). Time to failure modeling of carbon fiber reinforced polymer composites subject to simultaneous tension and one-sided heat flux. *Journal of Composite Materials*, 52:002199831774971. 23

Takagi, H., Takahashi, M., Maeda, R., Onishi, Y., Iriye, Y., Iwasaki, T., and Hirai, Y. (2008). Analysis of time dependent polymer deformation based on a viscoelastic model in thermal imprint process. *Microelectronic Engineering*, 85(5):902–906. Proceedings of the Micro- and Nano-Engineering 2007 Conference. 52

Test standard EN 6035 (1996). *Determination of notched and unnotched tensile strength*. Aerospace series - Fiber-reinforced plastics - Test Method. European Association of Aerospace Industries (AECMA). 118

The Engineering ToolBox (2003). Convective heat transfer. `https://www.engineeringtoolbox.com/convective-heat-transfer-d_430.html`. 74

The Engineering ToolBox (2009). Air - thermal conductivity vs. temperature and pressure. `https://www.engineeringtoolbox.com/air-properties-viscosity-conductivity-heat-capacity-d_1509.html`. 129

Totry, E., Molina-Aldareguía, J. M., González, C., and LLorca, J. (2010). Effect of fiber, matrix and interface properties on the in-plane shear deformation of carbon-fiber reinforced composites. *Composites Science and Technology*, 70(6):970–980. 38, 50

Van Hartingsveldt, E. and Van Aartsen, J. (1991). Strain-rate dependence of interfacial adhesion in particle-reinforced polymers. *Polymer*, 32(8):1482–1487. 51, 175

Vaughan, T. and McCarthy, C. (2011). Micromechanical modelling of the transverse damage behaviour in fibre reinforced composites. *Composites Science and Technology*, 71(3):388–396. 50

Vieille, B., Alia, A., Coppalle, A., and Lin, L. (2023). In situ tensile behavior of hybrid carbon and glass fibers reinforced peek laminates: Isothermal or fire testing conditions. *Composites Part B: Engineering*, 262:110807. 125

Vieille, B., Coppalle, A., Keller, C., Garda, M.-R., Viel, Q., and Dargent, E. (2015). Correlation between post fire behavior and microstructure degradation of aeronautical polymer composites. *Materials & Design*, 74:76–85. 80

Vieille, B., Coppalle, A., Le Pluart, L., Schuhler, E., Chaudhary, A., Rijal, B., Alia, A., Delpouve, N., and Bourdet, A. (2022). Influence of a flame-retardant on the fire-behaviour and the residual mechanical properties of c/pekk composite laminates exposed to a kerosene flame. *Composites Part A: Applied Science and Manufacturing*, 152:106720. 125

Vieille, B. and Taleb, L. (2011). About the influence of temperature and matrix ductility on the behavior of carbon woven-ply pps or epoxy laminates: Notched and unnotched laminates. *Composites Science and Technology*, 71(7):998–1007. 38

Vincent, C., Corn, S., Longuet, C., Aprin, L., Rambaud, G., and Ferry, L. (2019). Experimental and numerical thermo-mechanical analysis of the influence of thermoplastic slabs installation on the assessment of their fire hazard. *Fire Safety Journal*, 108:102850. 22

Vyazovkin, S. and Wight, C. A. (1999). Model-free and model-fitting approaches to kinetic analysis of isothermal and nonisothermal data. *Thermochimica Acta*, 340-341:53–68. 50

Walther, B. M. (1998). An investigation of the tensile strength and stiffness of unidirectional polymer-matrix, carbon-fiber composites under the influence of elevated temperatures. 27, 48, 183

Wang, H., Chu, W., and Chen, G. (2019). A brief review on measuring methods of thermal conductivity of organic and hybrid thermoelectric materials. *Advanced Electronic Materials*, 5(11):1900167. 20

Westover, C. (2012). The compressive behavior of glass fiber reinforced composites subjected to local thermal loading. page 95. 23

Yang, L., Yan, Y., Liu, Y., and Ran, Z. (2012). Microscopic failure mechanisms of fiber-reinforced polymer composites under transverse tension and compression. *Composites Science and Technology*, 72(15):1818–1825. 50

Yao, F., Zheng, J., Qi, M., Wang, W., and Qi, Z. (1991). The thermal decomposition kinetics of poly(ether-ether-ketone) (peek) and its carbon fiber composite. *Thermochimica Acta*, 183:91–97. 30

Z-set (2023). Z-set | non-linear material & structure analysis suite. `http://www.zset-software.com/`. 88

Zerbe, P., Schneider, B., Moosbrugger, E., and Kaliske, M. (2017). A viscoelastic-viscoplastic-damage model for creep and recovery of a semicrystalline thermoplastic. *International Journal of Solids and Structures*, 110-111:340–350. 52

Zhang, B., Yang, Z., Sun, X., and Tang, Z. (2010). A virtual experimental approach to estimate composite mechanical properties: Modeling with an explicit finite element method. *Computational Materials Science*, 49(3):645–651. 50

Zhang, C., Duan, Y., Xiao, H., Wang, B., Ming, Y., Zhu, Y., and Zhang, F. (2022). Effect of porosity and crystallinity on mechanical properties of laser in-situ consolidation thermoplastic composites. *Polymer*, 242:124573. 44

Zhao, D., Qian, X., Gu, X., Jajja, S., and Yang, R. (2016). Measurement techniques for thermal conductivity and interfacial thermal conductance of bulk and thin film materials. *Journal of Electronic Packaging*, 138. 20